



Faculteit Wetenschappen

Departement Fysica

**Mechanics of a single-ossicle ear:
optical measurements and finite-element modeling
of the avian middle ear**

**Mechanica van een éénbeentjesoor:
optische metingen en eindige-elementenmodellering
van het vogelmiddenoor**

Proefschrift voorgelegd tot het behalen van de graad van

Doctor in de Wetenschappen: Fysica

aan de Universiteit Antwerpen te verdedigen door

Pieter MUYSHONDT

Promotoren

Prof. Dr. Joris Dirckx

Prof. Dr. Peter Aerts

Antwerpen 2018

The candidate was financially supported by the Research Foundation – Flanders
(FWO)

De kandidaat werd financieel ondersteund door het Fonds voor Wetenschappelijk
Onderzoek – Vlaanderen (FWO)



DOCTORAL COMMITTEE

Chair

Prof. Dr. Jan Sijbers: *Department of Physics, University of Antwerp*

Supervisors

Prof. Dr. Joris J. J. Dirckx: *Department of Physics, University of Antwerp*

Prof. Dr. Peter Aerts: *Department of Biology, University of Antwerp; Department of Movement and Sport Science, University of Ghent*

Internal members

Prof. Dr. Joke Hadermann: *Department of Physics, University of Antwerp*

External members

Prof. Dr. Steve J. A. Vanlanduit: *Department of Mechanical Engineering, Free University of Brussels; Department of Electromechanics, University of Antwerp*

Prof. Dr. Michael J. Fagan: *School of Engineering and Computer Science, University of Hull (UK)*

Prof. Dr. Magnus von Unge: *Department of Otorhinolaryngology, Akershus University Hospital and University of Oslo (Norway); Department of Clinical Science, Intervention and Technology, Karolinska Institute, Stockholm (Sweden); Center for Clinical Research, University of Uppsala (Sweden)*

Private PhD defense

Monday, 12 March 2018, 14h30
Meeting room De Rede, office U.338
Campus Groenenborger, University of Antwerp

Public PhD defense

Wednesday, 18 April 2018, 17h00
Auditorium A.143
Campus Middelheim, University of Antwerp

PREFACE

Hearing is an essential aspect in daily life. According to the World Health Organization, over 5% of the world's population – 360 million people – suffer from disabling hearing loss. Finding adequate treatment for hearing loss is therefore one of the most relevant medical challenges of our time. There are many different types of hearing loss, with degrees ranging from mild to profound, and they can be divided into two main categories. Sensorineural hearing loss is characterized by a problem with the sensory organ in the inner ear or with the auditory nerve. Such hearing loss is mostly permanent, and though there are many causes most cases are related to old age where hearing can often be restored by using a hearing aid.

There are also hearing impairments that find their origin in the outer ear or middle ear. The human middle ear contains an eardrum or tympanic membrane and three tiny bones, called the ossicles. When somewhere along this mechanical chain sound waves are not properly conducted to the inner ear, one speaks of conductive hearing loss. Such a type of hearing loss is often temporary and can be caused by, for example, fluid accumulation in the middle ear or an ear infection. Sometimes, however, the chain of ossicles is permanently disrupted, which can only be solved by surgically recoupling or replacing the ossicles. In some cases, a partial ossicular replacement prosthesis (PORP) is implanted to replace one or two of the ossicles. A total ossicular replacement prosthesis (TORP), on the other hand, replaces the entire chain of ossicles; as a TORP directly couples the tympanic membrane to the inner ear, it is also called a single-ossicle or piston prosthesis. Although reasonably effective, such prostheses miss the flexibility of the three-ossicle chain to handle large and sudden pressure variations occurring in daily life. This lack of compliance increases the risk of the prosthesis to penetrate too deep into the inner ear, and even to dislocate from the chain.

Mammals, like humans, are actually the only class of vertebrates that have three ossicles in their middle ears. Amphibians, reptiles and birds only use a single ossicle – the columella – to transport sound energy from the outer ear to the inner ear. So far, it remains a mystery how nature succeeded in generating a single-ossicle ear that possesses the flexibility to handle large pressure changes, without affecting the ability to conduct sound from the outer ear to the inner ear. This PhD dissertation focuses on the middle ear of birds to investigate the mechanical functioning of single-ossicle ears. Among the classes of vertebrates with a single ossicle, birds largely have the best hearing ability, while being the most subjected to external pressure variations.

However, the mechanical behavior and material parameters values of this ear in response to quasi-static and dynamic loading are largely unknown. New insights in the mechanical function of the bird middle ear could even prove to be very valuable for designing improved single-ossicle prostheses for humans.

This dissertation is divided into two main parts. **Part I** contains two chapters that provide a general introduction to the topics and techniques that are covered in the five chapters of Part II. Chapters 1 and 2 can be consulted by the reader as a reference guide to the terminology, theoretical principles and research techniques that are used in the later chapters. In **Part II**, the main research results of this dissertation are discussed in five chapters that are very closely based on different research papers.

Chapter 1 introduces the basic principles of sound and hearing, and a brief overview of the structure and function of the avian ear. The anatomy and physiology of the outer ear, middle ear and inner ear are discussed, although the middle ear is described in more detail than the other two parts. **Chapter 2** presents an overview of the theory of structural mechanics, the techniques used for computational modeling of the middle ear, and the experimental methods used in this work to measure middle-ear morphology and vibrations. The first research chapter, **Chapter 3**, investigates the acoustic response and mechanical properties of the middle ear of the mallard duck. The most influential material parameter values of the tympanic membrane are determined by updating the outcome of a computational model to vibration measurement data of the middle ear. **Chapter 4** presents the first data of the acoustic input impedance of the bird inner ear, measured in ostrich. The inner ear is filled with fluids that pose a certain load or impedance on the middle-ear components, which is an important quantity as it influences the vibration behavior and sound transmission performance of the middle ear. In **Chapter 5**, the quasi-static and dynamic motions of the single ossicle of birds are determined in ostrich. The dynamic vibration motion is measured after destroying the inner ear. A computational model is created to validate the observed motions and determine the effect of the inner-ear load on these motions. **Chapter 6** investigates the effect of beak opening on acoustic transmission in the ear of chickens. The change in vibration response of the middle ear is measured after fully opening the beak, and a comparison is made between roosters and hens. The hypothesis is tested that the attenuation is larger in males than in females, given the difference in vocalization capacity between the sexes. The sound intensity of a rooster's crow is measured close to its own ears to illustrate the need of a putative protective mechanism for self-generated sounds. **Chapter 7** studies the effect of a fracture in the manubrium or handle of the malleus – the first ossicle in the human middle ear – on sound transmission. Vibration measurements are performed on human ear specimens, and different surgical methods to restore the fraction are compared. This chapter differs from the others in that it focuses on the human middle ear, but it illustrates the use of prosthetic ossicles to restore the middle-ear apparatus, which may benefit from understanding of the bird ear.

CONTENTS

| | |
|---|-----------|
| Doctoral committee | 5 |
| Preface | 7 |
| Contents | 9 |
| Part I: Introduction | 15 |
| Chapter 1: The avian hearing organ | 17 |
| 1.1 Sound and hearing..... | 17 |
| 1.1.1 The properties of sound..... | 17 |
| 1.1.2 The perception of sound..... | 18 |
| 1.2 Structure and function of the ear..... | 19 |
| 1.2.1 The outer ear..... | 20 |
| 1.2.2 The middle ear..... | 21 |
| 1.2.2.1 Middle-ear structure..... | 21 |
| 1.2.2.2 Middle-ear function..... | 26 |
| 1.2.3 The inner ear..... | 30 |
| Chapter 2: The middle ear: mechanics, modeling and measurement | 33 |
| 2.1 Mechanics of the middle ear..... | 33 |
| 2.1.1 Elasticity theory..... | 33 |
| 2.1.1.1 Stresses and strains..... | 34 |
| 2.1.1.2 Linear isotropic elasticity..... | 35 |
| 2.1.2 Viscoelasticity..... | 37 |
| 2.1.2.1 Linear viscoelasticity..... | 37 |
| 2.1.3 Vibration theory..... | 40 |
| 2.1.3.1 The harmonic oscillator..... | 40 |

| | | |
|--|---|-----------|
| 2.1.3.2 | Characterization of damping..... | 42 |
| 2.2 | Modeling of the middle ear..... | 44 |
| 2.2.1 | The finite-element method..... | 44 |
| 2.2.1.1 | The finite-element formulation | 45 |
| 2.2.2 | Modeling procedures | 49 |
| 2.2.2.1 | Geometry modeling..... | 49 |
| 2.2.2.2 | Model validation..... | 50 |
| 2.3 | Measurement of the middle ear | 52 |
| 2.3.1 | Morphological measurement | 52 |
| 2.3.1.1 | X-ray computed tomography | 53 |
| 2.3.2 | Vibration measurement | 54 |
| 2.3.2.1 | Laser Doppler vibrometry..... | 54 |
| 2.3.2.2 | Digital stroboscopic holography | 56 |
| Part II: My Research | | 59 |
| Chapter 3: Middle-ear acoustic response and mechanical properties in duck | | 61 |
| | Abstract | 61 |
| 3.1 | Introduction | 62 |
| 3.2 | Materials and methods..... | 63 |
| 3.2.1 | Experiments | 63 |
| 3.2.1.1 | Sample preparation | 63 |
| 3.2.1.2 | Stroboscopic holography | 63 |
| 3.2.1.3 | Laser Doppler vibrometry..... | 64 |
| 3.2.2 | Finite-element modeling | 64 |
| 3.2.2.1 | Morphology..... | 64 |
| 3.2.2.2 | Model description and boundary conditions | 66 |
| 3.2.2.3 | Material properties | 66 |
| 3.2.2.4 | Inverse analysis | 67 |
| 3.3 | Results..... | 68 |

| | | |
|---|--|-----------|
| 3.3.1 | Experimental results..... | 68 |
| 3.3.1.1 | Stroboscopic holography | 68 |
| 3.3.1.2 | Laser Doppler vibrometry..... | 70 |
| 3.3.2 | Model results..... | 71 |
| 3.3.2.1 | Sensitivity analysis..... | 71 |
| 3.3.2.2 | Inverse analysis | 72 |
| 3.4 | Discussion..... | 73 |
| 3.4.1 | Avian middle-ear mechanics | 73 |
| 3.4.1.1 | Material stiffness..... | 73 |
| 3.4.1.2 | Tympanic membrane displacements..... | 73 |
| 3.4.1.3 | Extrastapedial tip / columellar footplate velocity | 74 |
| 3.4.2 | Method considerations | 74 |
| 3.5 | Conclusion..... | 75 |
| Chapter 4: Acoustic input impedance of the ostrich inner ear | | 77 |
| | Abstract | 77 |
| 4.1 | Introduction | 78 |
| 4.2 | Materials and methods..... | 78 |
| 4.2.1 | Acoustic impedance | 78 |
| 4.2.2 | Sample preparation | 79 |
| 4.2.3 | Experiments in the acoustic regime | 80 |
| 4.2.3.1 | Laser Doppler vibrometry..... | 80 |
| 4.2.3.2 | Digital stroboscopic holography | 81 |
| 4.2.4 | Experiments in the quasi-static regime..... | 81 |
| 4.2.5 | Columellar footplate surface area | 82 |
| 4.3 | Results..... | 82 |
| 4.3.1 | Columellar footplate surface area | 82 |
| 4.3.2 | Experiments in the acoustic regime | 83 |
| 4.3.2.1 | Laser Doppler vibrometry..... | 83 |
| 4.3.2.2 | Digital stroboscopic holography | 84 |

| | | |
|--|--|-----------|
| 4.3.3 | Experiments in the quasi-static regime..... | 85 |
| 4.3.4 | Acoustic impedance analysis..... | 86 |
| 4.4 | Discussion..... | 87 |
| 4.4.1 | Experimental approach..... | 87 |
| 4.4.1.1 | Sample preparation..... | 87 |
| 4.4.1.2 | Experiments in the acoustic regime..... | 88 |
| 4.4.1.3 | Experiments in the quasi-static regime..... | 88 |
| 4.4.2 | Experimental results..... | 89 |
| 4.4.2.1 | Acoustic impedance analysis..... | 89 |
| 4.4.2.2 | Comparison with measurements in mammals..... | 90 |
| 4.4.2.3 | Comparison with measurements in birds..... | 91 |
| 4.4.2.4 | Scaling to smaller bird species..... | 92 |
| 4.5 | Conclusion..... | 92 |
| Chapter 5: Quasi-static and dynamic columella footplate motion in ostrich | | 95 |
| | Abstract..... | 95 |
| 5.1 | Introduction..... | 96 |
| 5.2 | Materials and methods..... | 97 |
| 5.2.1 | Quasi-static motion..... | 97 |
| 5.2.1.1 | Sample preparation..... | 97 |
| 5.2.1.2 | Micro-computed tomography..... | 98 |
| 5.2.1.3 | Image analysis..... | 99 |
| 5.2.2 | Dynamic motion..... | 100 |
| 5.2.2.1 | Experiments..... | 100 |
| 5.2.2.2 | Finite-element modeling..... | 101 |
| 5.3 | Results..... | 106 |
| 5.3.1 | Quasi-static motion..... | 106 |
| 5.3.2 | Dynamic motion..... | 107 |
| 5.3.2.1 | Model validation..... | 107 |
| 5.3.2.2 | Velocity response..... | 108 |

| | | |
|--|--|------------|
| 5.3.2.3 | Rocking-to-piston ratio..... | 111 |
| 5.3.2.4 | Full-field displacement | 114 |
| 5.4 | Discussion..... | 116 |
| 5.4.1 | Quasi-static motion..... | 116 |
| 5.4.1.1 | Experiments in literature | 116 |
| 5.4.1.2 | Experimental results..... | 116 |
| 5.4.2 | Dynamic motion | 118 |
| 5.4.2.1 | Experiments in literature | 118 |
| 5.4.2.2 | Experimental results..... | 119 |
| 5.4.2.3 | Model results..... | 119 |
| 5.5 | Conclusion..... | 121 |
| Chapter 6: Sound attenuation in the chicken ear as a result of beak opening | | 123 |
| | Abstract | 123 |
| 6.1 | Introduction | 124 |
| 6.2 | Materials and methods..... | 126 |
| 6.2.1 | Middle-ear vibration experiments | 126 |
| 6.2.1.1 | Sample preparation | 126 |
| 6.2.1.2 | Experimental setup..... | 127 |
| 6.2.1.3 | Statistical analysis..... | 127 |
| 6.2.2 | Rooster vocalization experiments..... | 128 |
| 6.3 | Results..... | 128 |
| 6.3.1 | Middle-ear vibration experiments | 128 |
| 6.3.1.1 | Female specimens..... | 128 |
| 6.3.1.2 | Male specimens..... | 129 |
| 6.3.1.3 | Statistical analysis..... | 129 |
| 6.3.2 | Rooster vocalization experiments..... | 132 |
| 6.4 | Discussion..... | 133 |
| 6.4.1 | Middle-ear vibration experiments | 133 |
| 6.4.1.1 | Experimental approach..... | 133 |

| | |
|---|------------|
| 6.4.1.2 Experimental results..... | 135 |
| 6.4.2 Rooster vocalization experiments..... | 137 |
| 6.5 Conclusion..... | 137 |
| Chapter 7: Laser vibrometry to study the repair of human malleus fractures | 139 |
| Abstract | 139 |
| 7.1 Introduction | 140 |
| 7.2 Materials and methods..... | 141 |
| 7.2.1 Description of the laser Doppler vibrometry method | 142 |
| 7.3 Results..... | 144 |
| 7.4 Discussion..... | 147 |
| 7.5 Conclusion..... | 148 |
| General conclusions | 149 |
| Nederlandstalige samenvatting | 155 |
| Bibliography | 157 |
| Abbreviations | 171 |
| Publications | 173 |
| Dankwoord – Acknowledgments | 177 |

PART I
INTRODUCTION

CHAPTER 1 THE AVIAN HEARING ORGAN

1.1 Sound and hearing

This section handles the basic concepts of sound and hearing. We will look at how properties of sound are defined, and how sound is perceived by birds. The section about the properties of sound is partially based on the work of previous colleagues, Jan Buytaert (Buytaert, 2010) and Jef Aernouts (Aernouts, 2012). The section on sound perception in birds is based on Dooling (2000, 2002) and Köppl et al. (2014).

1.1.1 *The properties of sound*

The environment we live in is an ocean of air molecules that are in constant motion and collision. Air pressure is created by the collective effect of colliding air molecules. At sea level, the air pressure is equal to 1013 hPa. What we perceive as sound is an oscillation of air pressure around the atmospheric pressure, which travels as a pressure wave through the air. The weakest acoustic pressure that a human can hear is approximately 20 μ Pa, which is around five billion times smaller than the atmospheric pressure around us. Without difficulties we can hear sounds of increasing pressure that are more than ten million times larger than the threshold. Because of this large dynamic range, the pressure of sound is often represented on a logarithmic scale – the decibel (dB) scale, by using the sound pressure level (SPL) L_p :

$$L_p = 20 \cdot \log_{10} \left(\frac{p}{p_0} \right) \text{ dB.} \quad (1.1)$$

In this equation, p is the sound pressure calculated as the root mean square of the pressure signal, and p_0 is the chosen reference pressure of 20 μ Pa that corresponds to the lower threshold of human hearing. The logarithmic scale proved to be natural for the perception of loudness, as the brain perceives changes in amplitude of sound pressure logarithmically. The sound level can also be expressed with respect to the intensity of sound $I = p^2/z$, with z the specific acoustic impedance of the medium (see Section 1.2.2.2). By substituting this relation into (1.1), the sound intensity level L_I becomes

$$L_I = 10 \cdot \log_{10} \left(\frac{I}{I_0} \right) \text{ dB,} \quad (1.2)$$

which is equivalent to L_p . In (1.2), $I_0 = p_0^2/z$ is chosen equal to 10^{-12} W/m² given that z is approximately 400 Pa·s/m in air. Sound pressure and intensity usually depend on the distance from the sound source. To have a measure for the sound level that does not depend on distance, we use the sound power level L_W defined as

$$L_W = 10 \cdot \log_{10} \left(\frac{P}{P_0} \right) \text{ dB.} \quad (1.3)$$

In this equation, P is the sound power of the source and $P_0 = I_0/A_0 = 10^{-12}$ W is the reference sound power in air with $A_0 = 1 \text{ m}^2$. When sound is produced by a point source in a completely free field, a progressive spherical pressure wave emerges for which the sound intensity I depends on the distance from the source r by $I(r) = P/(4\pi r^2)$. The sound pressure p follows the relation $p \propto 1/r$. For a progressive spherical wave, the relation between L_W and L_p thus becomes

$$L_W = L_p + 10 \cdot \log_{10} \left(\frac{4\pi r^2}{A_0} \right) \text{ dB.} \quad (1.4)$$

Therefore, the sound power of the source can be obtained when the sound pressure in a point at a distance r from the source is known.

1.1.2 *The perception of sound*

The auditory world of birds is rich. Birds are very vocal, and they communicate by a large repertoire of vocalizations, ranging from simple calls and cries to extremely variable vocalizations. Hearing clearly plays an important role in a bird's life. In many standard behavioral auditory tests, such as frequency or intensity discrimination, birds perform as well as mammals, including humans. In some aspects, such as perceiving fast-fluctuating sounds, birds often outperform mammals. Localizing sounds is more difficult for birds. Typically, birds can localize sounds in azimuth as well as mammals of comparable size. However, with the exception of owls (Klump, 2000), birds cannot localize in elevation. Birds have been shown to group complex sounds into patterns, much like humans do with speech syllables, or group concurrent sounds in a complex scene into different 'auditory objects', for instance to distinguish different birds singing.

Obviously, the hearing ability of birds is different from humans and other mammals. Birds hear in a different frequency range, and the minimal pressure at which birds are able to hear also differs. As may be expected, the bandwidth and threshold of hearing also varies greatly between avian species. The variation of hearing in birds can be roughly divided into three groups of birds: the songbirds or Passeriformes, the evolutionary older orders of birds constituting of many of the non-Passeriformes, and the owls or Strigiformes. Figure 1.1 displays the median audiogram of these three avian groups compared to the mean audiogram of humans. An audiogram or audibility curve represents the threshold pressure of hearing as a function of sound frequency.

The audiograms in Figure 1.1 (a) demonstrate that most birds hear best at frequencies between about 1 and 5 kHz, with absolute sensitivities often approaching 0–10 dB SPL at the most sensitive frequency, which is usually in the region of 2–3 kHz. Hearing sensitivity falls off at the rate of about 15 dB SPL/octave below 1 kHz and about 35–40 dB SPL/octave above 3 kHz. Songbirds tend to hear better at high frequencies than

the non-Passeriformes, while the non-Passeriformes present lower hearing thresholds at lower frequencies than songbirds. There are exceptions to this homogenous picture of avian hearing. In general, owls have a very strong auditory sensitivity over the entire frequency range. Common pigeons (*Columba livia*), on the other hand, have an unusual auditory sensitivity to very low frequency sounds (Quine, 1978; Yodlowski, 1980), which can be almost 50 dB more sensitive than humans in the range of 1–10 Hz (Kreithen and Quine, 1979). When comparing different orders of birds, it seems that the center frequency and the high-frequency cutoff of hearing are inversely correlated with a bird's size and weight. In comparison to humans, as shown in Figure 1.1 (b), most birds do not hear well at either high or low frequencies. At the high-frequency end of the audiogram, even with the noted exceptions, there are no cases in which birds hear at frequencies higher than about 15 kHz. Only in the region of 2–3 kHz hearing thresholds are comparable.

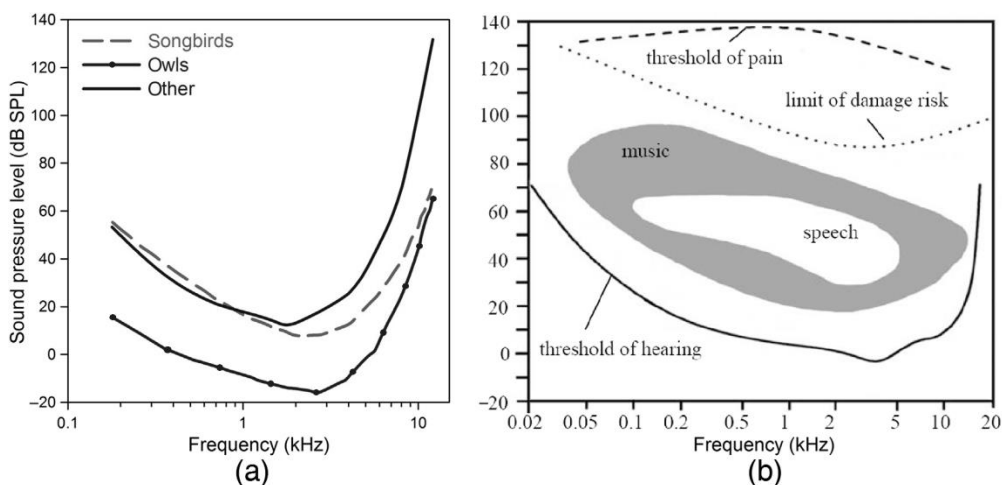


Figure 1.1. Comparison of the hearing ability of birds and humans. (a) Median audiograms of three main groups of bird. Figure modified from Dooling (2000). (b) Mean audiogram of humans (solid line). The graph also displays the threshold of pain, the limit of risk to hearing damage, and the frequency and pressure range of music and speech. Figure from Buytaert (2010).

1.2 Structure and function of the ear

Even though sizes and shapes of the components in the avian ear differ greatly between species, the structural organization of the avian ear is relatively consistent (Saunders et al., 2000). This makes it possible to provide a brief but general overview of the ear structure that applies to most birds. This observation is different from what is found in reptiles, for instance, which have a similar ear design to birds but with much more interspecific variation. Just like for humans and other mammals, the ear of birds can be divided into three main parts: the outer ear, the middle ear, and the inner ear. These parts are described in the following three sections. The descriptions

are primarily based on the overview of Saunders et al. (2000) for the outer and middle ear, and on Manley (1990a) and Köppl (2014) for the inner ear.

1.2.1 The outer ear

The outer ear in birds consists of the ear canal or auditory meatus. Unlike many mammals, birds don't have auricles or pinnae. Some owls, however, have asymmetrical outer ear structures such as a facial ruff, skin flaps, and asymmetrical bony ear canals (Norberg, 2002), as shown in Figure 1.2. These structures allow them to localize the elevation of sound sources. The ear canal of birds serves to guide sound waves from outside to the tympanic membrane, and at the same time it also protects the membrane. The external opening of the canal is typically smaller than the area of the tympanic membrane, which is oriented obliquely at the base of the canal. The walls of the canal are defined by muscles associated with the jaws, but also by the quadrate bone and the end of the lower jawbone. The epidermal layer of the canal wall is continuous with the outer surface of the tympanic membrane. The length of the canal is typically short (2–7 mm), and its shape varies considerably between species. Given that birds in general do not hear above 10 kHz, it is safe to assume that the ear canal provides no meaningful pressure amplification at the tympanic membrane through resonance.

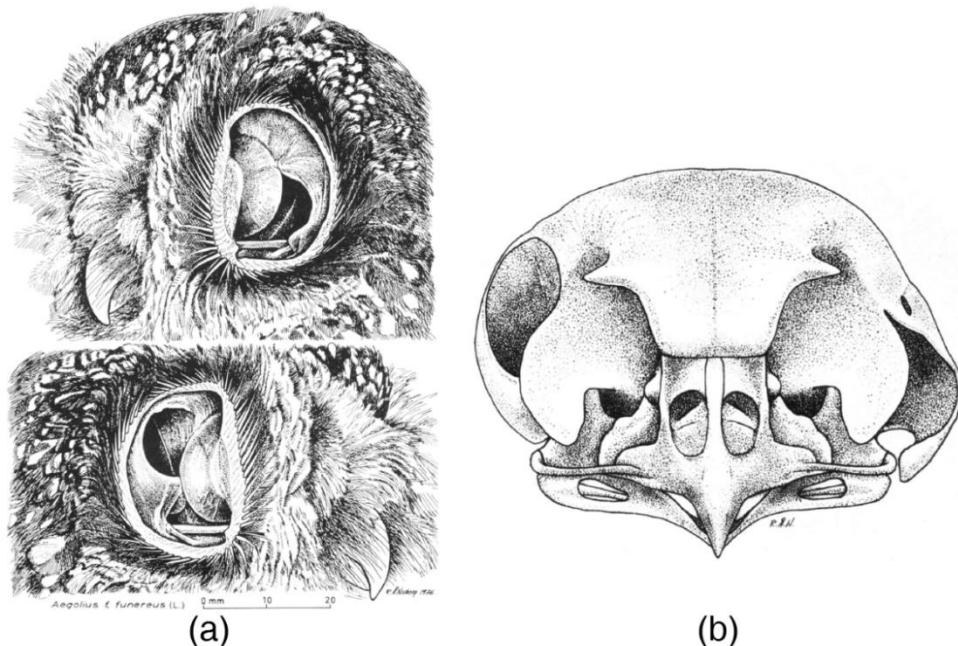


Figure 1.2. Outer ear organization in Tengmalm's owl. (a) Lateral view of the head and ear. The head and ears are intact, but two skin flaps have been displaced to expose underlying structures in the ear canal. (b) Frontal view of the skull. Asymmetry of the ear canal openings in (a) is caused by asymmetric positioning and orientation of the skull structures forming the wall of the ear canal. Figures from Norberg (2002).

1.2.2 The middle ear

The middle ear (ME) is a complicated three-dimensional (3D) system between the outer and inner ear, the primary function of which is to bridge the acoustic impedance difference between pressure waves in air and fluid waves in the fluid-filled inner ear. The structure and function of this system are discussed in the following two subsections.

1.2.2.1 Middle-ear structure

The main components of the avian ME are the tympanic membrane, or eardrum, and the single hearing bone, called the columella. The avian ME has several other components and features, which are described and discussed in the current section. A drawing of the ME organization in parakeet is shown in Figure 1.3

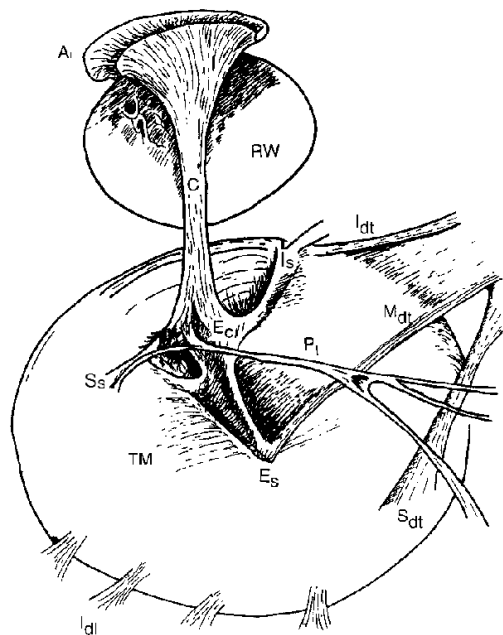


Figure 1.3. Drawing of the ME in parakeet. TM, tympanic membrane; C, columella; E_c , extracolumella; E_s , extrastapedial process; I_s , infrastapedial process; S_s , suprastapedial process; A_b , annular ligament; RW, round window; P_b , Platner's ligament; I_{dt} , intrinsic drum-tubal ligaments; I_{db} , inferior drum-tubal ligament; M_{dt} , medial drum-tubal ligament; S_{dt} , superior drum-tubal ligament. Figure modified from Saunders (1985).

1.2.2.1.1 The middle-ear cavity

The components of the ME are located inside an air-filled cavity, called the ME cavity or tympanic cavity. This cavity is relatively spacious compared to head size and has a very irregular shape. It is mostly surrounded by bony structures, except at the boundary with the ear canal where the TM is found. The cavity is not only surrounded by the bone of the skull but also by the kinetic quadrate bone, which is a part of the beak suspension.

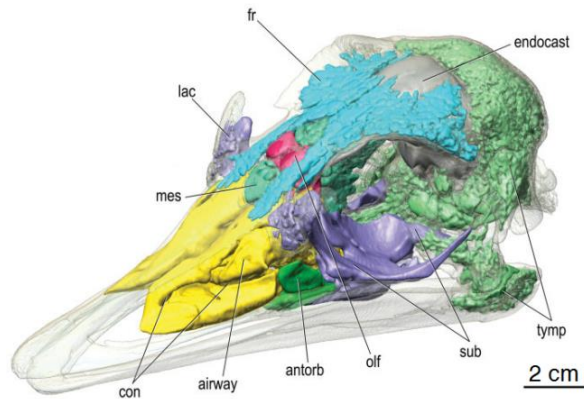


Figure 1.4. Air-filled spaces in the ostrich skull. The air space connecting the MEs (tymp) is shown in light green. Figure from Witmer and Ridgely (2008).

Unlike mammals, the avian ME cavity does not fully enclose the ME structures, but it is pneumatically connected to the corresponding cavity on the other side of the head: both cavities are connected by a complicated network of air-filled passages in the skull that together form one air space. This network can be very different between species. Birds also possess an equivalent to the human Eustachian tube, called the pharyngotympanic tube, which joins with the tube on the opposite side of the head in the middle plane. At the connection of both tubes, a common extension enters the roof of the pharynx where muscle contractions control venting into the oral cavity. The joining tubes have been referred to as the interaural pathway, which also connects both MEs pneumatically. The interaural pathway, together with the other passages that connect the MEs, were shown to play a role in the localization of sound (e.g., Larsen et al., 2016). Figure 1.4 shows the air space that connects both MEs in the ostrich.

1.2.2.1.2 The tympanic membrane

The eardrum or tympanic membrane (TM) is a multilayered membrane that forms the natural boundary between the ear canal and the ME cavity. The surface of the TM is shaped as cone – in some species it is highly conical while in others it is almost flat – and the tip of the cone points towards the ear canal. This is different from mammals, where the conical tip points towards the ME cavity. The conical tip of the TM corresponds to the point of insertion of the extrastapedial process of the extracolumella (see further). The perimeter of the TM is more or less shaped as an oval, and is surrounded by bone of the skull and the kinetic quadrate. However, in some species connective and muscular tissue is found between the TM perimeter and the bony surroundings.

The TM is composed of three layers. The outer layer is an epithelial layer similar to that of the body surface, but much thinner. As explained in Section 1.2.1, this layer is continuous with the epidermal layer covering the wall of the ear canal. The middle

layer of the TM, called the lamina propria, is a connective tissue layer composed of collagen fibers. In chickens, radially and circumferentially oriented fibers were distinguished (Chin et al., 1997). The ME muscle and three processes of the extracolumella insert in this middle layer, and the ascending ligament is entirely embedded in it (see further). The middle layer has a nonuniform thickness: at the margins and insertions it is relatively thick, while at the central parts it is thinner. The inner layer of the TM is also an epithelial layer that continues over the other structures of the ME.

1.2.2.1.3 *The columella*

An interesting fact is that birds only have a single hearing bone, which is called the columella or stapes. This is different from mammals that have three hearing bones, i.e., the ossicles. The columella of birds is the homologue of the stapes in mammals, which is the third and final ossicle in the mammalian ME chain. The two other mammalian ossicles, the malleus and incus, are homologous to the avian articular and quadrate bone, respectively. In birds, these bones are a part of the beak suspension.

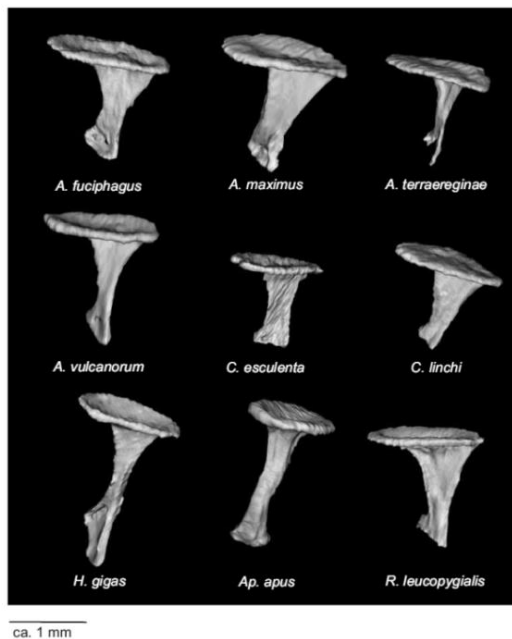


Figure 1.5. 3D reconstructions of the columella of nine different bird species. Figure from Thomassen et al. (2007).

The columella is shaped as a flattened beam or shaft, and curls about 90° around its longitudinal axis. The shaft of the columella is positioned at an acute angle relative to the plane of the TM. The bony shaft can be partially hollow, reducing its mass. On the medial side, the columella ends in a disk-shaped expansion called the columellar footplate (CFP) or clipeolus. The CFP has an oval appearance and is bounded in the oval window by the annular ligament, which allows the CFP to move and vibrate. The

ligament is made of collagen fibers and often has a variable width and thickness. In a lot of species, the CFP has an out-of-center positioning with respect to the columellar shaft. The shaft either attaches to the CFP in one piece, or by multiple branches that extend from the end of the shaft to the CFP plane. Figure 1.5 shows the columella of nine different bird species.

1.2.2.1.4 The extracolumella

The columella does not directly communicate with the TM, but by way of the cartilaginous extracolumella. The extracolumella is made of hyaline cartilage and is bound to the columella by a flexible synchondrosal connection, often referred to as the intracolumellar joint. The extracolumella consists of three arms: the supra-, infra- and extrastapedial processes (Pohlman, 1921), of which the lateral ends insert in the middle layer of the TM (see Section 1.2.2.1.2). The three processes serve to stabilize the columella and tense the TM. The central arm of the extracolumella, the extrastapedial process, presses on the TM giving it a conical appearance. The supra- and infrastapedial processes arise from the shaft of the extrastapedial process and often extend to the rim of the TM.

1.2.2.1.5 Ligaments of the middle ear

The extrastapedial process is not in direct contact with the TM, but communicates with it through the ascending ligament. This ligament starts at the margin of the TM, passes between the infra- and suprastapedial processes, and extends to the conical tip of the TM under the extrastapedial process. The ligament is composed of collagen fibers that together form a string in the middle layer of the TM. It protects and stabilizes the membrane in the region of the extracolumella, and may also serve to transfer motion from the TM to the extrastapedial process. An additional series of drum-tubal ligaments attach the TM to its bony perimeter and serve to keep the membrane taut. Another ligament, called Platner's ligament, arises at the junction between the supra- and extrastapedial processes and extends to ME cavity wall. There it is attached to the junction of the bones of the skull and the quadrate, or directly on the quadrate (Starck, 1995). The presumed function of the ligament is to additionally stabilize the columella.

1.2.2.1.6 The middle-ear muscle

A single muscle is associated with the ME. The muscle was given different names, i.e., the stapedius, stapedial muscle, columellar muscle, middle-ear muscle, tensor tympani and laxor tympani. In this work, the term 'middle-ear (ME) muscle' is adopted. The ME muscle is located for the largest part outside of the ME cavity. The muscle tendon passes through an opening in the ME cavity and splits into several tendons that reach to the margins of the TM. One tendon attaches to the posterior edge of the TM between the supra- and infrastapedial processes, while the other extends across the inner surface of the TM and attaches to the extrastapedial process. Electrical stimulation of the muscle causes the ME volume to increase due to a net

outward displacement of the TMs, leading to a change of the tension in the TM and the columellar apparatus. Measurements of the microphonic potential in the cochlea of the inner ear in chickens and starlings have shown a decrease of the potential as a function of muscle tension (e.g., Counter and Borg, 1982). The function of the muscle is not entirely clear. Activation as part of an acoustic reflex in response to external sounds was demonstrated in owls (Golubeva, 1972), but was absent in pigeon, chicken and starling (Wada, 1924; Counter and Borg, 1979; Oeckinghaus and Schwartzkopff, 1983). However, the muscle was shown to contract in response to self-generated sounds in chickens, suggesting that it functions as protection for self-generated vocalization. Other proposed functions are protection from low-frequency wind noise during flight, masking of undesired low-frequency sounds to improve communication, or provide necessary feedback for vocal development.

1.2.2.1.7 *The paratympanic organ*

The paratympanic organ is a small sense organ in the ME of many birds (von Bartheld and Giannessi, 2011). The location of the organ in the ME is shown in Figure 1.6. The organ contains a sensory epithelium with typical mechanoreceptive hair cells, just like the hair cells in the cochlea of the inner ear (see further). The function of the organ is still unknown. One possible explanation is that it detects height-dependent atmospheric pressure changes, thus functioning as an altimeter for migrating birds (Kreithen and Keeton, 1974). It has also been suggested to function as a detector of infrasound, potentially guiding migratory birds (Kreithen and Quine, 1979). von Bartheld and Giannessi (2011) proposed that the organ may function as a sensory relay together with the ME muscle to control TM tension. Larsen et al. (2016) additionally suggested that it could be the normal sensory relay to regulate the frequency and duration of ME pressure equalizations by opening and closing of the pharyngotympanic tubes. So far, none of the proposed explanations has been demonstrated.

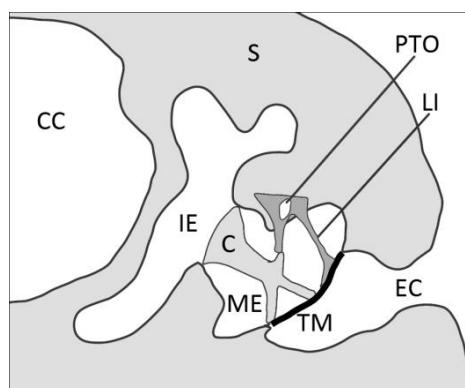


Figure 1.6. Drawing of the location of the paratympanic organ (PTO) in a cross section of the avian ear. EC, ear canal; TM, tympanic membrane; ME, middle-ear cavity; C, columellar apparatus; IE, inner ear; LI, ligament; PTO, paratympanic organ; S, skull; CC, cranial cavity. Figure modified from von Bartheld and Giannessi (2011).

1.2.2.2 Middle-ear function

The main function of the ME is concerned with the transmission of sound from the outer ear to the IE. The transmission of sound pressure is situated in the range of auditory frequencies perceivable by the animal (Figure 1.1 (a)), and the mechanisms behind it are discussed in the current section. However, pressure waves with frequencies outside of this range also exist and may have an influence on the acoustic performance of the ME. Pressure waves with higher frequencies than sound (ultrasound) do generally not have sufficient amplitude to interact meaningfully with the hearing organ. On the low end of the frequency spectrum, however, quasi-static pressure variations with usually large magnitude can cause sufficient deformations of the ME. Such pressure changes (of 100 Pa or more) are typically much larger than acoustic waves (in the order of 1 Pa). Our ears are continuously subjected to quasi-static pressure variations, for instance due to changes in atmospheric pressure. Presumably this is even more important for flying birds, who continuously encounter atmospheric pressure variations due to changes in altitude.

The ME uses different mechanisms to overcome quasi-static pressure differences between the air-filled ME cavity and the atmospheric environment. Even though the avian ME cavity is normally isolated from the atmosphere (e.g., Larsen et al., 2016), venting of the cavity may occur by opening of the pharyngotympanic tube (see Section 1.2.2.1.1), which partially or completely neutralizes the quasi-static pressure difference. Deformation of the TM may also contribute to pressure equilibration by changing the volume of the ME cavity (e.g., Padurariu et al., 2016). Additionally, the ME cavity and the air space connecting both MEs is covered with a mucosa layer, which is perfused with blood vessels. Gas exchange between dissolved gases in the blood and the air in the ME cavity may increase or decrease the pressure. Altogether, these effects partially or completely balance the quasi-static pressure difference over the TM, so the transmission of sound pressures through the ME is minimally affected.

1.2.2.2.1 Acoustic impedance

There are different ways to study the acoustic function of the ME. One of them considers the overall response of the system by measuring the flow of energy through the conductive apparatus. The resistance to transport of acoustic energy through a surface in a medium is represented by the acoustic impedance Z , which is defined as the ratio of sound pressure p to the acoustic volume flow U ,

$$Z = \frac{p}{U}. \quad (1.5)$$

The acoustic volume flow U is the volume of the acoustic wave passing through the surface per unit of time, which depends on the surface area. To define the impedance as a property of the medium alone, we use the specific acoustic impedance z defined as

$$z = \frac{p}{u}, \quad (1.6)$$

with u the acoustic flow velocity, which is the acoustic volume flow U per unit area. When we consider an acoustic wave traveling across the barrier between two media, a combination of reflection and transmission of the wave will occur at the boundary. The amount of reflection can be represented by the intensity reflection coefficient R , which depends on the specific acoustic impedance of the two media z_1 and z_2 through

$$R = \left(\frac{z_2 - z_1}{z_2 + z_1} \right)^2. \quad (1.7)$$

The intensity transmission coefficient T can be calculated by $T = 1 - R$. In the hearing organ, the ear canal is filled with air and the inner ear with fluid. Air has a specific acoustic impedance of $z_{\text{air}} = 415 \text{ Pa}\cdot\text{s}/\text{m}$ and the specific acoustic impedance of the inner-ear fluid is similar to that of water, namely $z_{\text{water}} = 1.48 \cdot 10^6 \text{ Pa}\cdot\text{s}/\text{m}$, which is four orders of magnitude higher than that of air. If the outer ear was directly connected to the inner ear, then according to (1.7) a sound wave reaching the boundary between air and fluid would be reflected by 99.89% due to a higher impedance of the fluid, so the major part of the sound information would be lost. Therefore, a system is needed to bridge the difference of acoustic impedance between air and inner-ear fluid, so that a larger part of the acoustic wave is transmitted. The system that achieves this is the ME. Traditionally, three mechanisms of the ME are assumed to contribute to impedance matching, as discussed below.

1.2.2.2.2 The hydraulic lever

The TM and CFP can be considered as the input and output surfaces of sound pressure in the ME. The acoustic waves in air that penetrate the ear canal exert a certain pressure on the TM, and with this pressure a certain force is associated. If we suppose that the force on the TM is perfectly transmitted to the CFP by the ME, then the same force will act on the fluid in the inner ear. As the surface area of the CFP A_{CFP} is always smaller than the surface area of the TM A_{TM} , the pressure over the ME is amplified by the following relation:

$$\frac{p_{\text{CFP}}}{p_{\text{TM}}} = \frac{A_{\text{TM}}}{A_{\text{CFP}}}. \quad (1.8)$$

This ratio is often called the hydraulic ratio (Figure 1.7). From (1.5)–(1.7) it becomes clear that an amplification of the input pressure p_{TM} leads to an increase of the corresponding impedance over the ME, resulting in an improved transmission of sound energy. The hydraulic ratio of birds varies greatly among species, ranging from 14 for the common pigeon to 40 for the long-eared owl (*Asio otus*). However, this ratio assumes that both the TM and CFP perform perfectly piston-like motions. At low frequencies below 1 kHz this is a reasonable approximation, but for higher frequencies it becomes increasingly inaccurate, as the TM starts showing very complicated vibration patterns.

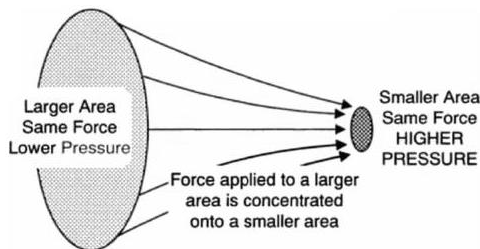


Figure 1.7. Illustration of the hydraulic lever of the avian ME. Figure from Gelfand (2009).

1.2.2.2.3 The catenary lever

The catenary lever action or curved membrane effect was first proposed by von Helmholtz (1873) and is based on the catenary principle, considering that the TM has a curved shape. The TM is fixed at its perimeter, and displacements of the TM are larger in the body of the membrane than at the tip of the cone where the extrastapedial process is attached (Figure 1.8). According to this principle, smaller displacements are associated with larger forces, leading to an amplification of the input pressure over the ME and hence impedance, according to (1.5). Tonndorf and Khanna (1970) suggested that catenary action could produce a transformer ratio of about a factor of 2.

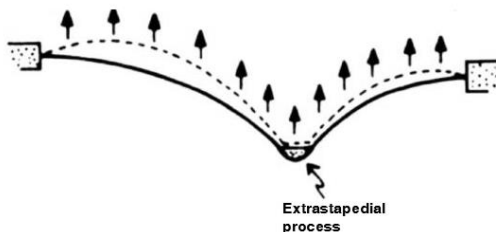


Figure 1.8. Illustration of the catenary lever in the avian ME. Figure modified from Zwislocki (1965).

1.2.2.2.4 The ossicular lever

When acoustic pressures reach the TM, the membrane undergoes transverse displacements that are maximal in the center and zero at the margin. Motion of the extrastapedial tip causes the extrastapedial process to move up and down with respect to the hinge points of the supra- and infrastapedial process. As such, the extrastapedial process partially rotates around an axis at the TM margin that runs through the attachments of the supra- and infrastapedial processes. With this rotation a lever advantage is obtained due to the relative length of two lever arms: the (long) force lever arm of length l_{TM} related to the input (the TM), and the (short) resistance lever arm of length l_{CFP} related to the output (the CFP). Forces associated with these lever arms are related by

$$\frac{F_{CFP}}{F_{TM}} = \frac{l_{TM}}{l_{CFP}}. \quad (1.9)$$

As $l_{TM} > l_{CFP}$, the input force F_{TM} increases over the ME and thus also the pressure and impedance, according to (1.5). Multiple definitions of the lever arms have been proposed for the avian ME, which are illustrated in Figure 1.9.

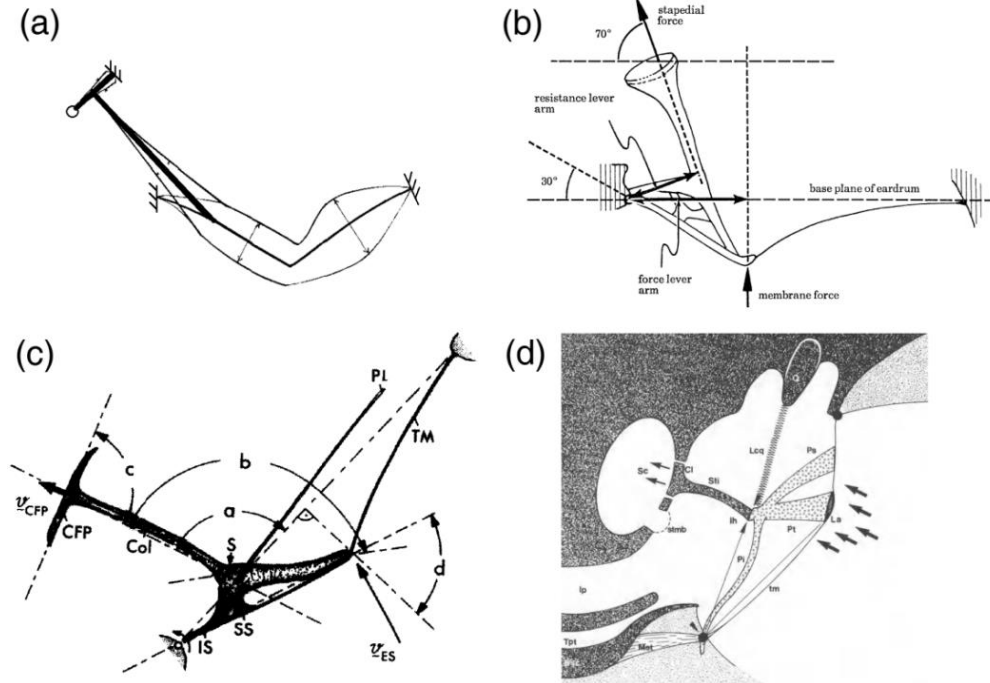


Figure 1.9. Different definitions of the lever arms in the avian ME associated with ossicular lever action. Drawings show cross sections of the ME in a plane perpendicular to the rotation axis of the extracolumella. (a) Representation by Gaudin (1968), with resting and extreme ME configurations indicated. Bold lines show the input and output lever arms. (b) Interpretation of Norberg (1978) in Tengmalm's owl, showing the input and output lever arms. (c) Interpretation of Gummer et al. (1989a) in pigeon. The ossicular lever ratio is a goniometric function of the angles indicated in the figure. (d) Representation by Starck (1995). Straight lines show the input and output lever arms.

In Gaudin (1968) (Figure 1.9 (a)), l_{TM} is the combined length of the columella and extrastapedial process, and l_{CFP} is the longitudinal diameter of the CFP. This definition is based on the assumption that the CFP performs largely rocking motions, rotating around the edge of the oval window. In Norberg (1978) (Figure 1.9 (b)), l_{TM} is the orthogonal distance from the rotation axis at the TM margin to the extrastapedial tip projected onto the base plane of the TM, and l_{CFP} is the orthogonal distance from the rotation axis to the intracolumellar joint. Gummer et al. (1989a) calculated the ossicular lever ratio r_{OL} by

$$r_{OL} = \frac{\cos \theta}{\sin(d - \theta)} \frac{\sin c}{\sin a}, \quad (1.10)$$

where $\theta = \pi/2 - (b - a)$. The angles a , b , c and d are indicated in Figure 1.9 (c). Starck (1995) described the lever arms similarly to Norberg (1978), but he defined l_{TM} as the

distance from the distal end of infrastapedial process to the extrastapedial tip, and l_{CFP} as the distance from the end of the infrastapedial process to the intracolumellar joint (Figure 1.9 (d)). The definitions of Norberg (1978), Gummer (1989a) and Starck (1995) are based on the assumption that the CFP performs largely piston-like motion in the oval window.

High-frequency hearing in most birds is limited to 8–10 kHz, which is generally lower than in mammals. This restriction is also reflected in the frequency response of the extrastapedial tip and CFP, which display a rapid deterioration of sound conduction above 3–4 kHz. One possible reason is related to the mass reactance of the ME, which traditionally controls the high-frequency response of a vibrating system. In mammals, the axis of rotation of the ossicular lever passes through the malleus and incus. Their mass is thus more or less compacted around the axis of rotation, which greatly reduces the moment of inertia. In birds, the rotation axis is located at the margin of the TM, so the columellar apparatus is located at considerable distance from the axis of rotation. As a consequence, the moment of inertia is large and the high-frequency response of the extrastapedial tip and CFP is greatly reduced. Another possibility could arise from flexion in the extrastapedial process. This possible flexion is caused by the cartilaginous nature of the extracolumella and may result in a considerable absorption of the driving force between the TM and columella, leading to a decreased response at the CFP.

1.2.3 *The inner ear*

The CFP is bounded in the oval window, forming the sound input to the inner ear (IE), as shown in Figure 1.10 for the chicken. The IE consists of two parts: the vestibular organ and the cochlear duct. The vestibular organ, which is composed of the three semicircular canals, is responsible for balance and motion awareness and is not involved in the perception of sound. The part of the IE that contributes to hearing is called the cochlea or cochlear duct, which is correct in the sense that it is homologous to the mammalian cochlea. In birds and other non-mammals, the cochlear duct is not coiled, so the term cochlea (“snail”) is not entirely appropriate. From here on, the term cochlear duct is used.

The cochlear duct contains two fluid-filled membranous systems, the otic and periotic labyrinths, which are filled with endolymph and perilymph fluid, respectively. Mechanical vibrations of the CFP in the oval window generate a pressure wave in the periotic labyrinth. First, the wave travels through the scala vestibuli across the basilar membrane. At the distal end of the cochlear duct the wave enters the scala tympani where it travels back across the basilar membrane. Eventually, it reaches the round window or secondary tympanic membrane, where the remaining pressure is released into the ME cavity. The basilar membrane contains a basilar papilla, which is a sensory organ composed of short and tall hair cells. The basilar papilla is tonotopically organized, such that hair cells located at the distal end of the duct are maximally

sensitive to low frequencies, and those at locations close to the oval window are maximally sensitive to high frequencies (Gleich et al., 2004). When set into motion, these tiny sensory cells send an electric potential to the auditory nerve, which transmits it further to the brain. This electric signal contains information of the loudness and pitch of the acoustic signal collected by the hearing organ. The distal end of the cochlear duct also houses the vestibular lagenar macula, which has disappeared in mammals and does not respond to sound.

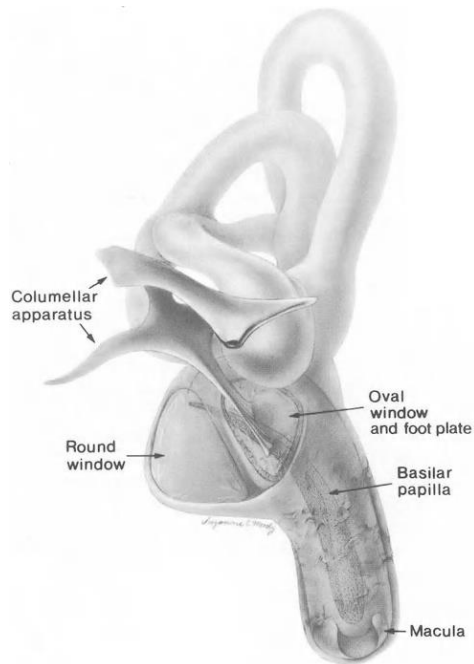


Figure 1.10. Drawing of the IE of the chicken in relation to the columellar apparatus. The oval window, over the scala vestibuli, and the round window, over the scala tympani, are shown. The cochlear duct is drawn as if partially transparent, and the position of the basilar papilla and lagenar macula are visible. Figure modified from Tanaka and Smith (1978).

CHAPTER 2 THE MIDDLE EAR: MECHANICS, MODELING AND MEASUREMENT

2.1 Mechanics of the middle ear

When a structural or solid material is subjected to external forces, internal forces will build in the material and the structure will undergo displacements and deformations. The field that studies the deflections and deformations and the internal forces or stresses within structures is called structural mechanics. The ME is a good example of a structural material, as it experiences internal forces and deformations due to static and dynamic pressure loading. Of course there are more aspects to the ME than just the mechanics: physiological processes (e.g., muscle contraction) and biochemical processes (e.g., gas exchange) exist that affect its mechanical behavior. However, by studying the mechanics of this ME we can learn a lot about its function. The external loading of a structural material can be stationary or time dependent. Elasticity theory describes the deformations and stresses in a material under static external loading. Many structures are also subjected to external forces that vary with time. Typically, structures that undergo time-dependent deformations exhibit internal energy losses during the loading process – i.e., the material shows viscous behavior. When these effects are relevant, this behavior needs to be included in the mathematical description, which is done by the theory of viscoelasticity. Viscoelastic material models are often required when the structure is subjected to time-dependent harmonic loadings, as is the case for the ear. In the latter situation, the structure will exhibit vibration behavior, which is described by the theory of vibration. This section gives a general introduction to elasticity, viscoelasticity and vibration theory which are important to study the mechanics of the avian ME. It is partially based on Sadd (2005), Fletcher (1992) and Banks (2010), and on the work of my previous colleagues, Jef Aernouts (Aernouts, 2012) and Daniël De Greef (De Greef, 2017)

2.1.1 *Elasticity theory*

As a result of external loadings, elastic structures will change shape or deform. An elastic body is said to be deformed or strained when the relative positions between points in the body change. This is different from rigid body motion, where the relative position between points remains the same. The work done by the external loadings is stored inside the body in the form of strain energy. For an ideal elastic body, this stored energy is completely recovered when the structure returned to its original configuration. When the deformations are small, they can usually be described

relative to the original configuration, which is done in linear elasticity. When deformations are large this approximation is often no longer appropriate. In such case a nonlinear elastic description is required. In the current work, we limit ourselves to linear elasticity as it is mostly sufficient to describe the mechanical behavior of the avian ME in response to sound pressure loading.

2.1.1.1 Stresses and strains

Any deformation of an elastic body can be described by the displacements of all the points belonging to the body. The displacement of two points in a body is illustrated in Figure 2.1.

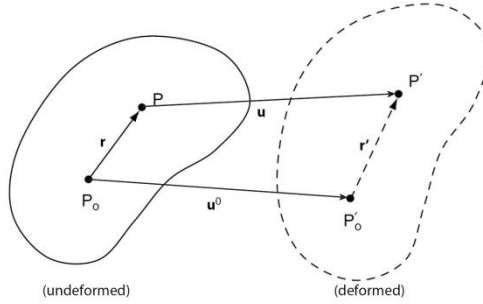


Figure 2.1. General deformation of two points in a body. Figure modified from Sadd (2005).

The points P_o and P are displaced along the displacement vectors \mathbf{u}^o and \mathbf{u} , respectively. When P_o and P are neighboring points, a first-order Taylor expansion around P_o can be applied to express the components of \mathbf{u} :

$$u_i = u_i^o + \frac{\partial u_i}{\partial x_j} r_j, \quad (2.1)$$

with $x_j = \{x, y, z\}$, representing the Cartesian coordinates. As r is small, the higher-order terms of the Taylor expansion are neglected. In (2.1), the Einstein notation was used: when in one term an index appears twice, the term is summed over all possible values of that index. E.g.:

$$a_i b_i = \sum_{i=1}^3 a_i b_i = a_1 b_1 + a_2 b_2 + a_3 b_3. \quad (2.2)$$

The factors $\partial u_i / \partial x_j$ can be regarded as elements of a tensor called the displacement gradient tensor. It can be decomposed into a symmetric and antisymmetric part as follows:

$$\frac{\partial u_i}{\partial x_j} = \varepsilon_{ij} + w_{ij} = \frac{1}{2} \left(\frac{\partial u_i}{\partial x_j} + \frac{\partial u_j}{\partial x_i} \right) + \frac{1}{2} \left(\frac{\partial u_i}{\partial x_j} - \frac{\partial u_j}{\partial x_i} \right), \quad (2.3)$$

The tensor ε_{ij} is called the (small) strain tensor and w_{ij} the rotation tensor. ε_{ij} describes the deformation of an infinitesimal element in the body. As ε_{ij} is symmetric it contains six independent strain components: three normal strains $\varepsilon_{ii} = \varepsilon_i = \partial u_i / \partial x_i$ and three shear strains $\varepsilon_{ij} = 1/2(\partial u_i / \partial x_j + \partial u_j / \partial x_i)$ with $i \neq j$.

Internal forces arise in the interior of a body when it is subjected to external forces. Within elasticity theory it is assumed that these forces are distributed continuously within the body. When a body is subjected to external forces, the internal forces can be investigated by making a virtual cross section through the body, as illustrated in Figure 2.2 (a). In this cross section, consider a small area ΔA with normal vector \mathbf{n} . The resultant internal force acting on ΔA is given by $\Delta \mathbf{F}$. The stress or traction vector \mathbf{t} acting on ΔA is defined as

$$\mathbf{t}(\mathbf{n}) = \lim_{\Delta A \rightarrow 0} \frac{\Delta \mathbf{F}}{\Delta A}. \quad (2.4)$$

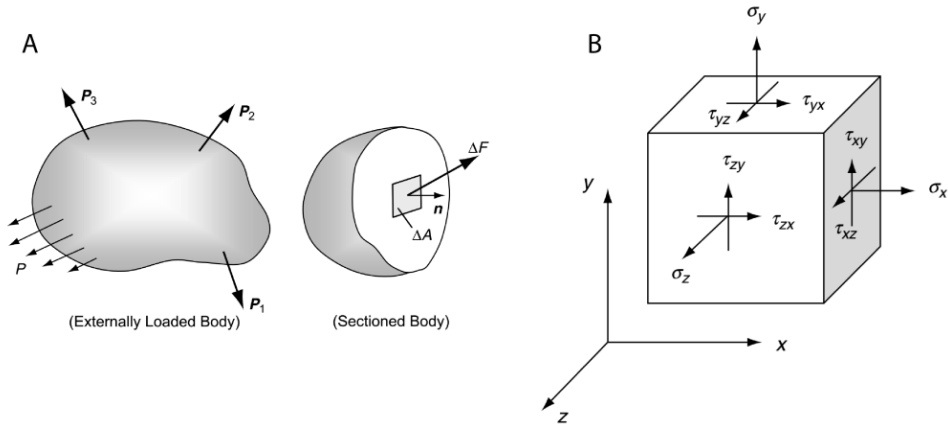


Figure 2.2. (a) Sectioned body under external loading. (b) Components of the stress tensor. Figures from Sadd (2005).

The traction vector depends on the normal vector \mathbf{n} of the surface. Consider the special cases for which ΔA coincides with the three coordinate planes with normal vectors pointing along the positive Cartesian axes, as shown in Figure 2.2 (b). The traction vectors on each face can be written as:

$$\mathbf{t}(\mathbf{n} = \mathbf{e}_i) = \sigma_{ij} \mathbf{e}_j, \quad (2.5)$$

with $\mathbf{e}_i = \{\mathbf{e}_1, \mathbf{e}_2, \mathbf{e}_3\}$ the unit vectors of the Cartesian axes. The nine quantities σ_{ij} are the components of the traction vector and can be represented by a 3×3 tensor, the (Cauchy) stress tensor. Just as for the strain tensor, it can be proven that the stress tensor is symmetric (Sadd, 2005). This implies that the stress tensor also has six independent components: three normal stresses $\sigma_{ii} = \sigma_i$ and three shear stresses σ_{ij} or τ_{ij} with $i \neq j$.

2.1.1.2 Linear isotropic elasticity

Equations that describe the response of a material in response to external stimuli are called constitutive equations. An example is the relation between the stress and strain in a structure. In general, the stress depends on the strain, strain rate, strain history, temperature and material properties. In this section, the description is limited to

linear elasticity, in which strain rate, strain history and temperature are disregarded. In linear elasticity, the second-order strain and stress tensors are linearly related through the fourth-order elasticity tensor ζ by

$$\sigma_{ij} = \zeta_{ijkl}\varepsilon_{kl}. \quad (2.6)$$

In general, the elasticity tensor has 81 components, but this number reduces to 36 independent components due to the symmetry of the strain and stress tensors. The fourth-order elasticity tensor can be condensed into the second-order reduced elasticity tensor \mathbf{C} , which contains the coefficients that express each independent component of the stress tensor as a linear combination of the independent strain tensor components:

$$\begin{bmatrix} \sigma_x \\ \sigma_y \\ \sigma_z \\ \tau_{yz} \\ \tau_{zx} \\ \tau_{xy} \end{bmatrix} = \begin{bmatrix} C_{11} & C_{12} & \dots & C_{16} \\ C_{21} & C_{22} & \dots & \\ \vdots & \vdots & \ddots & \\ C_{61} & & & C_{66} \end{bmatrix} \begin{bmatrix} \varepsilon_x \\ \varepsilon_y \\ \varepsilon_z \\ 2\varepsilon_{yz} \\ 2\varepsilon_{zx} \\ 2\varepsilon_{xy} \end{bmatrix}, \quad (2.7)$$

In compact form this expression becomes $\sigma_i = C_{ij}\varepsilon_j$. Inverting this relation reveals the reduced compliance tensor \mathbf{S} : $\varepsilon_i = S_{ij}\sigma_j$. Using the concept of strain energy, it can be demonstrated that these tensors are symmetric as well, reducing the total number of independent coefficients for a linear elastic material to 21 (Sadd, 2005). When a linear elastic material is isotropic, the elasticity tensor is invariant to all rotations. Hence, the constitutive equation simplifies further so that only two independent coefficients are required to describe the stresses and strains of the material under external loading:

$$\sigma_{ij} = \lambda\varepsilon_{kk}\delta_{ij} + 2\mu\varepsilon_{ij}. \quad (2.8)$$

In this equation, λ is Lamé's constant and μ the shear modulus. Together, these coefficients are called Lamé's coefficients. The equation is known as the generalized Hooke's law for linear isotropic elastic structures. Alternatively, the strain components can be expressed as a function of the stress components:

$$\varepsilon_{ij} = \frac{1+\nu}{E}\sigma_{ij} - \frac{\nu}{E}\sigma_{kk}\delta_{ij}, \quad (2.9)$$

where $E = \mu(3\lambda + 2\mu)/(\lambda + \mu)$ is the modulus of elasticity or Young's modulus, and $\nu = \lambda/[2(\lambda + \mu)]$ is Poisson's ratio of the material. They can be intuitively understood by means of a uniaxial tensile test, in which a sample is subjected to tension in the x direction (see Figure 2.3). The stress tensor is then closely represented by

$$\sigma_{ij} = \begin{bmatrix} \sigma & 0 & 0 \\ 0 & 0 & 0 \\ 0 & 0 & 0 \end{bmatrix}. \quad (2.10)$$

Using this in (2.9) gives a corresponding strain tensor of

$$\varepsilon_{ij} = \begin{bmatrix} \frac{1}{E} & 0 & 0 \\ 0 & -\frac{\nu}{E} & 0 \\ 0 & 0 & -\frac{\nu}{E} \end{bmatrix} \cdot \sigma. \quad (2.11)$$

This result illustrates that the Young's modulus is a measure for the resistance of strain to stress in the direction of the external force. In the transverse direction, this measure is multiplied with $-\nu$. As such, Poisson's ratio represents the ratio of transverse to axial strain.

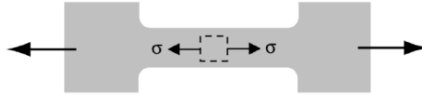


Figure 2.3. Uniaxial tensile test on a sample subjected to tension in the x direction. Figure modified from Sadd (2005).

2.1.2 Viscoelasticity

Materials that exhibit both elastic and viscous behavior are called viscoelastic materials. For these materials, the stress not only depends on the strain and material properties, but also in the strain rate and strain history. Therefore, time becomes a parameter in the material's constitutive equations. In a purely elastic material, the strain always shows the same dependence on time as the stress. In viscoelastic materials, however, they exhibit a different dependence on time. For instance, when a viscoelastic material is suddenly strained and maintained at constant strain, the corresponding stress induced in the material decreases gradually over time. This phenomenon is called stress relaxation. Alternatively, when the material is stressed instantaneously and the stress is maintained constant, the material will gradually deform until it reaches a constant strain. This effect is called creep. When the material is subjected to a cyclic loading, the stress-strain relation during the positive loading process will be different from the relation during the unloading process. This phenomenon is called hysteresis.

2.1.2.1 Linear viscoelasticity

When strains are small, linear viscoelasticity is suited to describe the behavior of a viscoelastic material. Linear viscoelastic behavior is often represented by a model composed of linear springs (for the elastic part) and dashpots (for the viscous part) in different configurations. When the strain becomes large, linear viscoelasticity is often no longer appropriate, and nonlinear viscoelastic models should be employed. In the current work, the description is limited to linear viscoelasticity. For a linear spring, the relation between the stress σ and strain ε is given by $\sigma = R\varepsilon$, with R the spring constant. For a linear dashpot, however, the stress depends on the strain rate $\dot{\varepsilon} = d\varepsilon/dt$ by $\sigma = c\dot{\varepsilon}$, with c the coefficient of viscosity of the material.

2.1.2.1.1 The Maxwell and Kelvin-Voigt model

The most simple viscoelastic material models are the Maxwell and Kelvin-Voigt models. They represent the combination of one spring and one dashpot element placed in series and parallel, respectively, as illustrated in Figure 2.4.

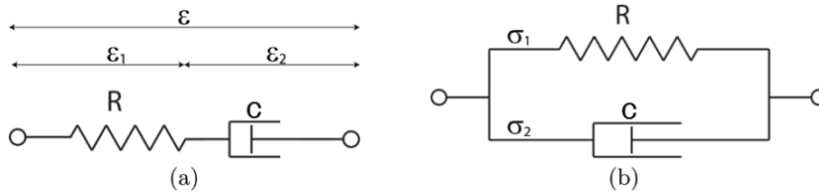


Figure 2.4. Two simple models of a viscoelastic material. (a) Maxwell model, combining a spring and dashpot in series. (b) Kelvin-Voigt model, combining the same elements in parallel. Figure from Aernouts (2012).

For the Maxwell model, the stress-strain relations of the spring and dashpot are $\sigma = R\epsilon_1$ and $\sigma = c\dot{\epsilon}_2$ respectively. Because the elements are connected in series, they experience the same stress σ . Similarly, the total strain is the sum of the strain in each component: $\epsilon = \epsilon_1 + \epsilon_2$. The constitutive equation of the Maxwell model is then:

$$\dot{\epsilon}(t) = \frac{\dot{\sigma}(t)}{R} + \frac{\sigma(t)}{c}. \tag{2.12}$$

For the Kelvin-Voigt model, the stress-strain relations are $\sigma_1 = R\epsilon$ and $\sigma_2 = c\dot{\epsilon}$ respectively. Because the elements are connected in parallel, they experience the same strain. Similarly, the total stress is the sum of the stress in each component: $\sigma = \sigma_1 + \sigma_2$. The constitutive equation of the Kelvin-Voigt model is then given by

$$\dot{\epsilon}(t) + \frac{R}{c}\epsilon(t) = \frac{\sigma(t)}{c}. \tag{2.13}$$

Both of these models are useful in some situations, but under certain circumstances they display unphysical behavior, as illustrated in Figure 2.5.

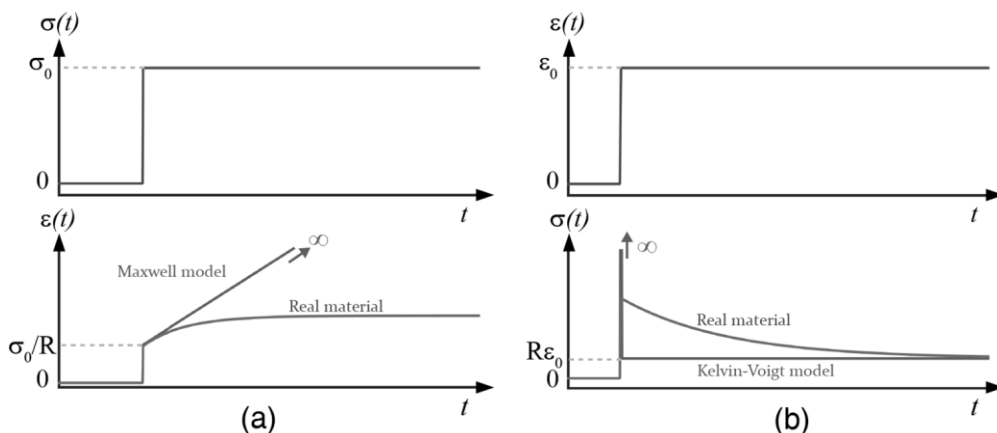


Figure 2.5. (a) Creep in a real viscoelastic material and in the Maxwell model. (b) Stress relaxation in a real viscoelastic material and in the Kelvin-Voigt model. Figure from De Greef (2017).

The Maxwell model is a poor model for creep. It continues to deform indefinitely towards infinity when it is subjected to a sudden constant stress, which is in contradiction with real viscoelastic materials. The Kelvin-Voigt model, on the other hand, is a poor model for stress relaxation. In a real viscoelastic material, the initially high but finite stress, right after the onset of the strain, gradually decreases over time. However, an instantaneous strain applied to the Kelvin-Voigt model induces an infinite stress in the model, which is also unrealistic.

2.1.2.1.2 The generalized Maxwell model

To model phenomena such as creep and stress relaxation more realistically, the viscoelastic model needs more elements. The standard linear solid model adds a spring in parallel to the original Maxwell model. This is the simplest model that can simulate both creep and stress relaxation. A more general model is the generalized Maxwell model, as shown in Figure 2.6. In this model, a spring is placed in parallel with m Maxwell models, all of which can possess different parameter values for the springs and dashpots.

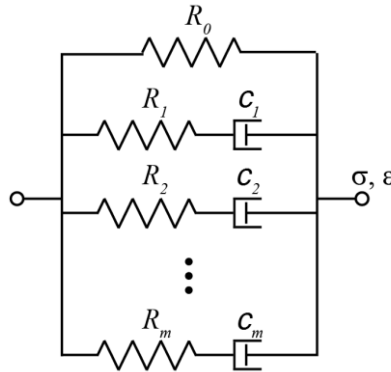


Figure 2.6. Generalized Maxwell model with m branches. Figure from Aernouts (2012).

The total stress in this model is the sum of the stresses in each branch. The stress in the first branch σ_0 due to a strain ε is $\sigma_0 = R\varepsilon$. For the j -th branch, we find from (2.12) that

$$\sigma_j(t) = \frac{D}{D/R_j + 1/c_j} \varepsilon(t), \quad (2.14)$$

where $D = d/dt$ denotes differentiation with respect to time. The total stress σ of the generalized Maxwell model is then given by

$$\sigma(t) = \sum_{j=0}^m \sigma_j(t) = \left(R_0 + \sum_{j=1}^m \frac{R_j D}{D + R_j/c_j} \right) \varepsilon(t). \quad (2.15)$$

The large number of material parameters for the generalized Maxwell model allows the model to characterize different viscoelastic properties on different relaxation time scales, and thus also on different frequency ranges.

2.1.3 Vibration theory

When structures are driven by a harmonic loading, they will vibrate. When studying vibration systems, three basic properties of the structure need to be taken into account: a stiffness which provides a restoring force when the structure is displaced, a viscous damping force that accounts for the energy losses in the structure, and mass or inertia which causes the resulting motion to overshoot the resting position. In this section, some basic properties of vibration systems are discussed. We will also look at how damping is characterized in vibration systems.

2.1.3.1 The harmonic oscillator

A basic example of a vibrating system is the one-dimensional (1D) damped harmonic oscillator, which will be used to illustrate the theory of vibrations in this section. The 1D damped harmonic oscillator can be represented by an object with a certain mass that is attached to a fixed wall by a spring and dashpot arranged in parallel. The equation of motion for this system is:

$$m \frac{d^2x}{dt^2} + c \frac{dx}{dt} + Rx = F(t), \quad (2.16)$$

with m the mass of the object, c the damping coefficient, R the spring constant or stiffness of the spring, x the displacement of the object relative to its resting position, and $F(t)$ a time-dependent external force on the object. We distinguish two cases for this linear differential equation, one in which there is no external force, and another in which the external force is harmonic.

2.1.3.1.1 The free damped harmonic oscillator

When there is no external force ($F(t) = 0$), we can solve (2.16) by assuming a solution of the form $x = Ae^{st}$, in which A is real and s complex. This results in a quadratic equation for s , which is solved to give $s = i\omega_d - \alpha$, with

$$\omega_d = \omega_0 \sqrt{1 - \frac{\alpha^2}{\omega_0^2}}, \quad (2.17)$$

representing the natural or resonance frequency of the damped system, $\omega_0 = \sqrt{R/m}$ the resonance frequency of the undamped system, and $\alpha = c/(2m)$ the damping factor. The solution of (2.16) is then given by

$$x(t) = Ae^{-\alpha t} \sin(\omega_d t + \phi), \quad (2.18)$$

with A and ϕ real-valued constants determined by the initial conditions. The amplitude of the motion $Ae^{-\alpha t}$ is not constant but decreases exponentially with time. If $\alpha/\omega_0 \ll 1$, the damping is small and the frequency of the damped system is close to the frequency of the undamped system ($\omega_d \approx \omega_0$). When the damping is increased, however, ω_d will decrease. If $\alpha/\omega_0 = 1$, the damping is termed critical and the object returns to its resting state without any oscillation. When damping is greater than the

critical value ($\alpha/\omega_0 > 1$), the object will return to the resting state more slowly. The motion of the oscillator for these different situations is shown in Figure 2.7.

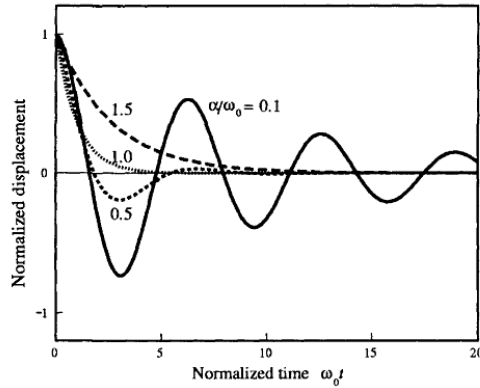


Figure 2.7. Decay of the free damped harmonic oscillator. When $\alpha/\omega_0 < 1$, the damping is small and the decay is oscillatory. If $\alpha/\omega_0 = 1$, the damping is critical and the motion tends to zero in the shortest time possible. When $\alpha/\omega_0 > 1$, the damping is large and the motion towards zero is prolonged. Figure from Fletcher (1992).

2.1.3.1.2 The driven damped harmonic oscillator

Consider that the external force in (2.16) is nonzero and harmonic, i.e., $F(t) = |F|e^{i\omega t}$, with $|F|$ the amplitude and ω the angular frequency of the harmonic force. The general solution to (2.16) is a linear combination of two solutions: a transient solution, given by (2.18), and a steady-state solution. As (2.16) represents a linear differential equation, we can propose a steady-state solution of the form $x(t) = Ae^{i(\omega t + \phi)} = \tilde{x}e^{i\omega t}$, with $\tilde{x} = Ae^{i\phi}$ and ω the same angular frequency as the external force. Substituting this expression into (2.16) and omitting the factor $e^{i\omega t}$ yields

$$-\omega^2 m \tilde{x} + i\omega c \tilde{x} + R \tilde{x} = |F|. \quad (2.19)$$

This equation can be regarded as the expression of the equation of motion in the frequency domain. By isolating \tilde{x} and returning to the time-dependent displacement $x(t)$, the solution turns out to be

$$x(t) = \frac{F/m}{\omega_0^2 - \omega^2 + 2i\alpha\omega} e^{i\omega t}, \quad (2.20)$$

with α and ω_0 as defined before. The amplitude and phase of this motion are given by

$$A = \frac{F/m}{\sqrt{(\omega_0^2 - \omega^2)^2 + 4\alpha^2\omega^2}}, \quad (2.21)$$

$$\phi = \text{atan}\left(-\frac{2\omega\alpha}{\omega_0^2 - \omega^2}\right). \quad (2.22)$$

Figure 2.8 shows the amplitude and phase of the steady-state response for the damped harmonic oscillator. Displacement (x) and velocity ($dx/dt = i\omega x$) responses are shown for a system with a set of reference parameters, and for systems with either increased

stiffness, increased mass or decreased damping. From the amplitude plot, it can be inferred that the response of a 1D driven damped oscillator is stiffness dominated at low frequencies (i.e., frequencies below the resonance frequency), mass dominated at high frequencies (i.e., frequencies above the resonance frequency), and damping dominated around the resonance frequency. In the phase plot, it can be noticed that the force and displacement are in phase at low frequencies. The phase of the displacement undergoes a gradual transition around the resonance, while at high frequencies it lags behind the phase of the force by half a period.

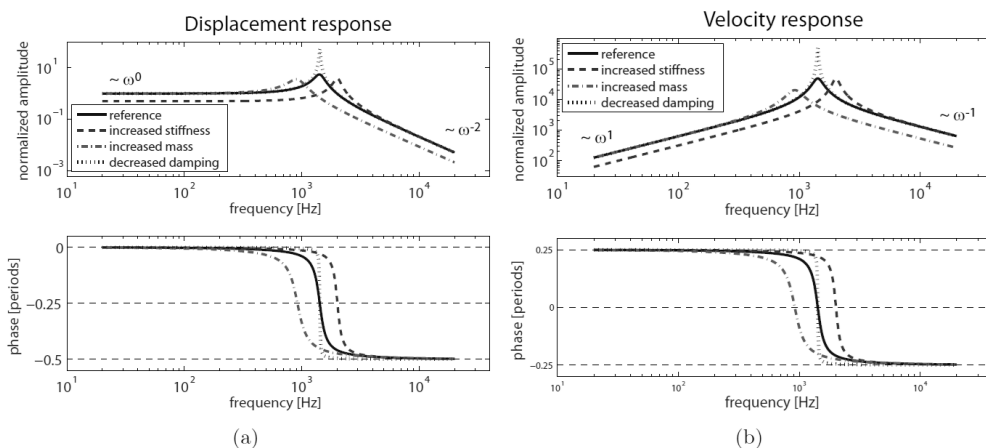


Figure 2.8. Steady-state (a) displacement and (b) velocity response of a 1D damped harmonic oscillator driven by a harmonic external force F with amplitude $|F| = 10^{-3}$ N. The parameters for the reference model are $R = 400$ N/m, $c = 8.13 \cdot 10^{-3}$ N·s/m, $m = 50 \cdot 10^{-7}$ kg. For the model with increased stiffness, R is equal to 800 N/m. For the model with increased mass, m has a value of $120 \cdot 10^{-7}$ kg. For the model with decreased damping, c is equal to $0.813 \cdot 10^{-3}$ N·s/m. Figure from Aernouts (2012).

2.1.3.2 Characterization of damping

Different methods exist to characterize damping in vibration systems. In (2.16), damping is represented by the damping coefficient c , but the form of c has not yet been specified. In this section, three methods that were used in this work to characterize the damping are discussed: Rayleigh damping, loss factor damping and viscoelastic damping. These methods will be described for a 1D system with a single degree of freedom, but they can easily be extended to 3D structures with multiple degrees of freedom.

2.1.3.2.1 Rayleigh damping

In Rayleigh damping, the damping coefficient c in (2.16) is defined as a linear combination of the mass and stiffness of the system:

$$c = \alpha m + \beta R. \quad (2.23)$$

In this expression, α and β are two real-valued parameters, which can be selected to match the modal damping of two different modes. Rayleigh damping, however, is not directly related to any physical property. Historically, it was introduced as it was numerically attractive to have damping terms which are a linear combination of the mass and stiffness terms.

2.1.3.2.2 Loss factor damping

Rather than to include a separate damping term in the equation of motion, as in (2.16) or (2.19), damping can be taken into account by replacing the real-valued stiffness R by a complex or dynamic modulus R^* in the frequency domain expression of the equation of motion in (2.19):

$$-\omega^2 m \tilde{x} + R^* \tilde{x} = |F|, \quad (2.24)$$

with R^* defined by

$$R^* = R' + iR'' = R'(1 + i\eta). \quad (2.25)$$

In this expression, R' is the storage modulus, R'' the loss modulus, and $\eta = R''/R'$ the damping loss factor. The storage modulus measures the maximal stored energy in one vibration cycle, representing the elastic portion, and the loss modulus determines the energy dissipated as heat over one cycle, representing the viscous portion.

Sometimes, the storage modulus and the loss factor are defined as constant quantities, and the loss modulus can be extracted from them. In more complicated models, the complex modulus is frequency dependent. For instance, when relating (2.19) and (2.24), we see that $R' = R$ and $R'' = c\omega$, and thus $\eta = c\omega/R$. Therefore, the loss factor increases linearly with frequency when c is constant. In the case of Rayleigh damping, as formulated in (2.23), the loss factor becomes $\eta = \alpha\omega/\omega_o^2 + \beta\omega$ with ω_o the resonance frequency as defined before. At the resonance frequency, this relation becomes $\eta = \alpha/\omega_o + \beta\omega_o$. This expression is often extended to other frequencies, yielding $\eta = \alpha/\omega + \beta\omega$, which is an assumption.

2.1.3.2.3 Viscoelastic damping

We can also calculate the complex modulus of a viscoelastic model such as the generalized Maxwell model, for which the time-dependent relation between stress and strain is given by (2.15). If the applied load is an oscillatory strain with angular frequency ω , the strain in the system can be expressed as: $\varepsilon(t) = \varepsilon_o e^{i\omega t}$. In the case of a linear harmonic system, the stress response is also oscillatory with the same frequency and with phase angle δ :

$$\sigma(t) = \sigma_o e^{i(\omega t + \delta)} = \sigma^* e^{i\omega t}, \quad (2.26)$$

with $\sigma^* = \sigma_o e^{i\delta}$. For a purely elastic system, the stiffness R was the ratio of the stress σ to the strain ε (see Section 2.1.2.1). Similarly, the complex modulus R^* of a viscoelastic system can be defined as the ratio of the complex-valued amplitudes of the stress σ^* and strain ε_o in the frequency domain. For the generalized Maxwell model, this ratio is

obtained by substituting the harmonic expressions for $\varepsilon(t)$ and $\sigma(t)$ into (2.15). After reordering and omitting the factor $e^{i\omega t}$, it is found that

$$R^*(\omega) = \frac{\sigma^*}{\varepsilon_0} = \frac{\sigma_0}{\varepsilon_0} e^{i\delta} = R_0 + \sum_{j=1}^m \frac{i\omega R_j}{i\omega + R_j/c_j}, \quad (2.27)$$

where we used that $D\varepsilon(t) = d(\varepsilon_0 e^{i\omega t})/dt = i\omega\varepsilon_0 e^{i\omega t}$. The storage modulus R' and loss modulus R'' are then given by:

$$R'(\omega) = R_0 + \sum_{j=1}^m \frac{R_j \tau_j^2 \omega^2}{1 + \tau_j^2 \omega^2}, \quad (2.28)$$

$$R''(\omega) = \sum_{j=1}^m \frac{R_j \tau_j \omega}{1 + \tau_j^2 \omega^2}, \quad (2.29)$$

with $\tau_j = c_j/R_j$ the characteristic time of the j -th branch. From this example it can be seen that both the storage and loss modulus of the generalized Maxwell model are frequency dependent, which is also the case for many other viscoelastic models.

2.2 Modeling of the middle ear

In general, modeling can be used for purposes of understanding, prediction and control of a system. Construction and exploration of a model can summarize what is known about a system, and can lead to a better understanding of how it works. Once a model has been validated to some extent, it can be used for prediction. Finally, models can be used for purposes of control. For instance, they can be used to examine and manipulate variables that are not accessible (observable) or manipulable (controllable) in the real system. A quantitative model can often be used to perform computational experiments that are not feasible with the real system: too expensive, too small, too big, too fast, too slow, too many confounding factors, and so on. Models of the mechanics of the ME exist in many different incarnations, from very simple to very sophisticated. This section focuses on modeling of the ME by means of the finite-element method. The content of this section is based on Zienkiewicz and Taylor (2000a,b), Funnell et al. (2012, 2013), Aernouts (2012) and De Greef (2017).

2.2.1 The finite-element method

Simple boundary-value problems can be solved by formulating the differential equations that describe the system, and then solving the equations analytically with the appropriate boundary conditions. For more complicated shapes and structures, analytically solving the equations is often impossible and numerical methods become necessary. The main methods for solving multidimensional partial differential equations are the finite-difference method, the finite-element (FE) method, and the boundary-element method. Over the last decades, the FE method has been developed so extensively that it is not possible to give a brief overview in the present work. What follows is a short introduction to the basics of FE modeling. For a more elaborate

overview of the subject, the reader is referred to De Arantes E Oliviera (1968), Bonet and Wood (1997) and Zienkiewicz and Taylor (2000a,b), although this list is certainly not comprehensive.

2.2.1.1 The finite-element formulation

The theory of FE modeling can be presented by a weak formulation of the governing differential equations, one of which is based on the weighted residual approach. The development for structural analysis follows the more traditional approach via the virtual work principle or the principle of minimum total potential energy.

2.2.1.1.1 Static analysis

The total potential energy of a body Π is the sum of the elastic strain energy stored in the deformed body U and the potential energy W associated with the applied forces on the body. This energy is at a stationary position when a virtual displacement δu_i from the current position of the body involves no change in energy:

$$\delta\Pi = \delta U + \delta W = 0, \quad (2.30)$$

in which

$$\delta U = \int_V \delta\varepsilon_{ij} \sigma_{ij} dV, \quad (2.31)$$

$$\delta W = - \int_V \delta u_i b_i dV - \int_{S_t} \delta u_i t_i dS. \quad (2.32)$$

In these expressions, σ_{ij} and ε_{ij} are the stress and strain tensors of the body, b_i the volume forces acting on the volume V of the body, and $t_i = \sigma_{ji} n_j$ the traction forces acting on the part of the body surface S_t defined by stress boundary conditions. According to (2.3), the virtual strain $\delta\varepsilon_{ij}$ can be related to the virtual displacement δu_i as follows:

$$\delta\varepsilon_{ij} = \frac{1}{2} \left(\frac{\partial \delta u_i}{\partial x_j} + \frac{\partial \delta u_j}{\partial x_i} \right). \quad (2.33)$$

Let us now consider the vector form of the stress and strain as in (2.7), which will be denoted by small boldface symbols $\boldsymbol{\sigma}$ and $\boldsymbol{\varepsilon}$, respectively. By using the vector notation of the strain, the strain-displacement relation can be converted into the following matrix multiplication:

$$\boldsymbol{\varepsilon} = \begin{bmatrix} \partial/\partial x & 0 & 0 \\ 0 & \partial/\partial y & 0 \\ 0 & 0 & \partial/\partial z \\ \partial/\partial y & \partial/\partial x & 0 \\ 0 & \partial/\partial z & \partial/\partial y \\ \partial/\partial z & 0 & \partial/\partial x \end{bmatrix} \begin{bmatrix} u \\ v \\ w \end{bmatrix} \equiv \mathbf{D}\mathbf{u}, \quad (2.34)$$

where we assumed the 3D case with $\mathbf{u} = (u,v,w)$. The same relation holds for virtual strains and displacements:

$$\delta \boldsymbol{\varepsilon} = \mathbf{D} \delta \mathbf{u}. \quad (2.35)$$

At the same time, (2.30)–(2.32) can be expressed in matrix form as

$$\int_V \delta \boldsymbol{\varepsilon}^T \boldsymbol{\sigma} dV - \int_V \delta \mathbf{u}^T \mathbf{b} dV - \int_{S_t} \delta \mathbf{u}^T \mathbf{t} dS = 0, \quad (2.36)$$

where small boldface symbols again denote vector quantities. Matrix quantities will be denoted by capital boldface symbols. To solve (2.36) for \mathbf{u} , we perform a FE approximation for \mathbf{u} of the form

$$\mathbf{u}(\mathbf{x}) \approx \mathbf{N}_i(\mathbf{x}) \mathbf{u}_i = [\mathbf{N}_1(\mathbf{x}) \quad \mathbf{N}_2(\mathbf{x}) \quad \cdots] \begin{bmatrix} \mathbf{u}_1 \\ \mathbf{u}_2 \\ \vdots \end{bmatrix}. \quad (2.37)$$

In this approximation, the original displacement field \mathbf{u} is only considered in specific points with coordinates \mathbf{x}_i , called nodes: $\mathbf{u}_i = \mathbf{u}(\mathbf{x}_i)$. The $\mathbf{N}_i(\mathbf{x})$ are shape function matrices and represent prescribed functions of position, each of which corresponds to one of the nodes by which the geometry is approximated. As such, $\mathbf{N}_i(\mathbf{x})$ interpolates the nodal displacements \mathbf{u}_i to the regions in between the nodes, called finite elements. The functions $\mathbf{N}_i(\mathbf{x})$ are generally matrices and have to be chosen in such a way that they give appropriate nodal displacements when the nodal positions \mathbf{x}_j are inserted in (2.37). The following conditions need to be satisfied:

$$\mathbf{N}_i(\mathbf{x}_i) = \mathbf{I}, \quad (2.38)$$

$$\mathbf{N}_i(\mathbf{x}_j) = \mathbf{0} \text{ for } i \neq j. \quad (2.39)$$

with \mathbf{I} the identity matrix. Let us assume that all components of the displacement field are specified in an identical manner by \mathbf{N}_i . Then we can write

$$\mathbf{N}_i(\mathbf{x}) = N_i(\mathbf{x}) \mathbf{I}. \quad (2.40)$$

If \mathbf{x} is contained within an element surrounding node i (i.e., node i is one of the nodes belonging to the element), then $N_i(\mathbf{x})$ is a scalar piecewise function of position. For all coordinates outside of this region we have $N_i(\mathbf{x}) = 0$. The expression for $N_i(\mathbf{x})$ can be obtained from (2.37) by noting that $N_i(\mathbf{x}_i) = 1$, and $N_i(\mathbf{x}_j) = 0$ for $i \neq j$. For example, in the case of a plane geometry with coordinates $\mathbf{x} = (x, y)$ and a displacement field having only one component ($\mathbf{u} = w$), we can build a FE mesh composed of triangular elements defined by linear shape functions. The appearance of such a shape function N_i is shown in Figure 2.9. If desired, higher-order polynomial basis functions can be used as well. By using higher-order polynomials, the number of unknown variables increases. The number of equations is increased accordingly, depending on the order of the polynomial, by introducing additional nodes at specific locations in the elements. From here on, FE discretizations of boldface vector and matrix quantities will be denoted by indices.

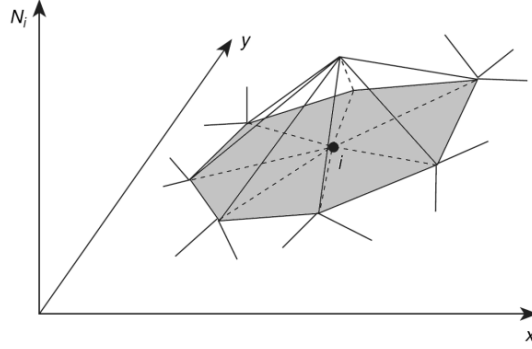


Figure 2.9. Shape function of a triangular finite element in a plane geometry. Inside the gray region the shape function is a piecewise linear function of x and y , forming a heptagonal pyramid. Outside this region the shape function is zero. Figure from Zienkiewicz and Taylor (2000a).

The FE approximation can also be applied to the virtual strain $\delta\epsilon$ in (2.36) by using the relation of the strain to the displacement field in (2.34). By inserting (2.37) into (2.34) we obtain

$$\boldsymbol{\epsilon} = \mathbf{D}\mathbf{u} \approx (\mathbf{D}\mathbf{N}_i)\mathbf{u}_i \equiv \mathbf{B}_i\mathbf{u}_i = [\mathbf{B}_1 \quad \mathbf{B}_2 \quad \dots] \begin{bmatrix} \mathbf{u}_1 \\ \mathbf{u}_2 \\ \vdots \end{bmatrix}. \quad (2.41)$$

In the 3D case, the \mathbf{B}_i are defined as

$$\mathbf{B}_i = \begin{bmatrix} \partial N_i / \partial x & 0 & 0 \\ 0 & \partial N_i / \partial y & 0 \\ 0 & 0 & \partial N_i / \partial z \\ \partial N_i / \partial y & \partial N_i / \partial x & 0 \\ 0 & \partial N_i / \partial z & \partial N_i / \partial y \\ \partial N_i / \partial z & 0 & \partial N_i / \partial x \end{bmatrix}. \quad (2.42)$$

The approximation in (2.41) can also be applied to the virtual strain and displacement fields, i.e., $\delta\epsilon = \mathbf{B}_i\delta\mathbf{u}_i$. This expression can be substituted into (2.36), yielding

$$\delta\mathbf{u}_i^T \left(\int_V \mathbf{B}_i^T \boldsymbol{\sigma} dV - \int_V \mathbf{N}_i^T \mathbf{b} dV - \int_{S_t} \mathbf{N}_i^T \mathbf{t} dS \right) = 0. \quad (2.43)$$

This relation is true for any value of the virtual nodal displacements $\delta\mathbf{u}_i$, so it must also hold for the multipliers. For each node i we thus obtain

$$\int_V \mathbf{B}_i^T \boldsymbol{\sigma} dV = \int_V \mathbf{N}_i^T \mathbf{b} dV + \int_{S_t} \mathbf{N}_i^T \mathbf{t} dS. \quad (2.44)$$

In linear elasticity, the stress $\boldsymbol{\sigma}$ is related to the strain $\boldsymbol{\epsilon}$ by the elasticity tensor \mathbf{C} of (2.7) ($\boldsymbol{\sigma} = \mathbf{C}\boldsymbol{\epsilon}$). By using this relation together with (2.34) and (2.41), the left-hand term in (2.44) becomes

$$\left(\int_V \mathbf{B}_i^T \mathbf{C} \mathbf{B}_j dV \right) \mathbf{u}_j \equiv \mathbf{K}_{ij} \mathbf{u}_j, \quad (2.45)$$

in which \mathbf{K}_{ij} are the elements of the so-called linear stiffness matrix. Expression (2.44) then becomes

$$\mathbf{K}_{ij}\mathbf{u}_j = \mathbf{f}_i, \quad (2.46)$$

where

$$\mathbf{f}_i = \int_V \mathbf{N}_i^T \mathbf{b} dV + \int_{S_t} \mathbf{N}_i^T \mathbf{t} dS. \quad (2.47)$$

Expression (2.46) represents an algebraic equation, which can be simply solved for \mathbf{u}_j . In many situations, however, it is necessary to use nonlinear or time-dependent stress-strain (constitutive) relations, and in these cases other solution strategies need to be developed for the left-hand term of (2.44).

2.2.1.1.2 Dynamic analysis

The FE derivation we have just discussed is meant for static problems. For dynamic problems we need to include contributions of inertia and damping, such as in (2.16). To achieve this, the following transformation is done in (2.32):

$$b_i \rightarrow b_i - \rho \frac{d^2 u_i}{dt^2} - \mu \frac{du_i}{dt}. \quad (2.48)$$

with ρ the mass density and μ a viscosity parameter. The difference with static problems is that the displacement field now becomes a function of time. Similarly to (2.46), one can obtain a discretized matrix equation for the dynamic problem of the form

$$\mathbf{M}_{ij} \frac{d^2 \mathbf{u}_j}{dt^2} + \mathbf{H}_{ij} \frac{d\mathbf{u}_j}{dt} + \mathbf{K}_{ij} \mathbf{u}_j = \mathbf{f}_i, \quad (2.49)$$

where

$$\mathbf{M}_{ij} = \int_V \mathbf{N}_i^T \rho \mathbf{N}_j dV, \quad (2.50)$$

$$\mathbf{H}_{ij} = \int_V \mathbf{N}_i^T \mu \mathbf{N}_j dV. \quad (2.51)$$

\mathbf{M}_{ij} are the elements of the so-called mass matrix and \mathbf{H}_{ij} of the damping matrix. \mathbf{K}_{ij} and \mathbf{f}_i are defined in (2.45) and (2.47), respectively. If one is interested in the steady-state response to harmonic loading with angular frequency ω , a harmonic analysis can be done via the substitutions $\mathbf{f}_i = |\mathbf{f}_i| e^{i\omega t}$ and $\mathbf{u}_i = |\mathbf{u}_i| e^{i(\omega t + \phi)} = \tilde{\mathbf{u}}_i e^{i\omega t}$ in (2.49), yielding

$$(-\omega^2 \mathbf{M}_{ij} + i\omega \mathbf{H}_{ij} + \mathbf{K}_{ij}) \tilde{\mathbf{u}}_j = |\mathbf{f}_i|, \quad (2.52)$$

which is solved for $\tilde{\mathbf{u}}_j$. One can implement different damping models in (2.52). For example, Rayleigh damping can be modeled by way of the substitution $\mathbf{H}_{ij} = \alpha \mathbf{M}_{ij} + \beta \mathbf{K}_{ij}$, which is a FE extension of (2.23) in the 3D case. Damping can also be modeled by replacing the stiffness matrix with a complex modulus and omitting the term related to the damping matrix \mathbf{H}_{ij} , as was done in (2.25) for the 1D situation. For a linear

isotropic viscoelastic material, the stiffness matrix \mathbf{K}_{ij} (or the elasticity tensor \mathbf{C}) is multiplied with the complex factor $(1+i\eta)$, which is equivalent to multiplying the Young's modulus with this factor. For anisotropic viscoelastic material models, it is possible to supply each entry in the elasticity tensor with an individual loss factor.

2.2.2 *Modeling procedures*

When doing FE modeling, it is important to follow certain procedures in order to make sure the model describes reality as adequately as possible. These procedures involve operations on the model geometry and validation of the physical description of the model. These actions are frequently applied in the modeling parts of this thesis, and are briefly discussed here.

2.2.2.1 *Geometry modeling*

Realistic FE modeling requires more or less accurate 3D shapes. Typical FE analyses in engineering start from a computer-aided design drawing of the geometry of interest. In biomechanical problems, however, the geometry is usually not drawn, so it must first be measured. In the current work, micro-computed tomography was used to measure the geometrical shape of ME structures, which will be discussed in Section 2.3.1.1. Such measurements yield a 3D matrix, the elements of which are called voxels (volume pixels) containing gray-scale values.

2.2.2.1.1 *Image segmentation*

Once a 3D voxel data set has been obtained, the outlines of the structures of interest in the data set can be identified, a procedure which is called image segmentation. Automatic segmentation techniques can be used, such as automatic thresholding of gray-scale values, threshold-based region growing, etc. Usually, however, some degree of manual intervention of the user is required to identify the outlines of structures and the shared surfaces between adjoining structures.

2.2.2.1.2 *Surface generation*

Once a segmentation model has been created, a surface model of the geometry is generated, which is usually a triangular mesh. The number of triangles must be large enough to maintain enough details of the surface geometry, but at the same time small enough to avoid a needlessly large data set that will eventually result in an excessive computation time. The smoothness of the surface mesh is critical for the mechanical behavior, especially for thin structures like the TM, as any artificial local curvature will have a strong influence on the model output.

2.2.2.1.3 *Volume mesh generation*

In a subsequent step a volume mesh is constructed, which involves creating a mesh of solid elements (e.g., tetrahedra) to fill the volume enclosed by the surface mesh. The elements must not be too long and thin, because this leads to numerical problems in the FE calculations. The mesh must be fine enough to avoid excessive discretization

errors but not so fine as to require excessive computation time. Often it is desirable to make the mesh finer in some parts of the model than in others. It is important to do a convergence analysis, i.e., to test a model with varying mesh resolutions under different of load conditions, to ensure that the size of the mesh is acceptable.

2.2.2.2 *Model validation*

Once a geometrical model with appropriate volume mesh has been generated, a physical model can be applied to the geometry. Model validation is an evaluation of how closely the physical behavior of a model matches the experimentally measured behavior of the system. The match is expressed in terms of an appropriate validation metric, which quantifies the difference between a certain output measure or feature of the model and the same measure or feature of the experimental data. There are many ways of formulating validation metrics, including correlations and sums of differences. If it is decided that the match is not good enough, then either the model or the experiment may be revised and refined. ASME (originally known as the American Society of Mechanical Engineers) has formulated general guidance for the iterative verification and validation of computational models (ASME, 2006; Schwer, 2007).

2.2.2.2.1 *Sensitivity analysis*

Ideally the match is expressed not only as a measure of the difference, but also with a measure of uncertainty and confidence level of the results. Uncertainty analysis allows to characterize a model's uncertainty, and to determine which model parameters are mainly responsible for that uncertainty. The latter procedure is called sensitivity analysis, and is important because it gives guidance on how to improve the FE model. The improvement can be made by adjusting parameter values or, preferably, by obtaining better a-priori estimates of the parameter values. If a model is very sensitive to a particular parameter, then that parameter is a good candidate for additional experiments to determine its value.

Sensitivity analysis is formulated in terms of a parameter space. If the model has k parameters then one has a k -dimensional parameter space. For each parameter there will be a best-guess estimate value (the baseline value) and a range of reasonable values it might have. To estimate the uncertainty of a model, one should ideally run simulations for all possible combinations of many different parameter values to see how the model output changes. If one uses n different values of each of k parameters, one would need n^k model runs. This method of choosing combinations of parameter values quickly becomes impractical for the number of parameters often encountered, given that FE models are frequently computationally intensive. Therefore, it is desirable to reduce the number of parameter combinations. The most common approach is the one-at-a-time method: first, one parameter is varied over its range with all of the other parameters at their baseline values; then, that parameter is returned to its baseline value and a second parameter is varied, and so on. This

approach reduces the number of simulations, but the drawback is that it doesn't give information about parameter interactions. For example, suppose that parameter a is at its baseline value, and that increasing parameter b from its baseline value increases the model output. However, when a has a different value, increasing b happens to decrease the model output. In such case, there is an interaction between the two parameters. Interactions are not uncommon in complicated systems and they will contribute to the model's uncertainty. To incorporate such effects, a more complete sampling of the parameter space is needed than in a one-at-a-time analysis. A number of strategies for selecting points have been used, such as Latin Hypercube sampling or the one that is used in the elementary-effects method. For a more elaborate overview of the existing types of sensitivity analyses and sampling methods, the reader is referred to Pianosi et al. (2016).

2.2.2.2.2 *Parameter identification*

Parameter fitting is part of model updating and consists of trying to find the set of parameter values that causes a model to best fit some experimental data, a procedure often referred to as inverse analysis or inverse engineering. For a small number of parameters it may be feasible to find the best fit by manually adjusting parameters, but it is often necessary to use some algorithmic approach. This involves two steps: choice of an objective (or cost) function and the actual algorithm for minimizing that function.

For most optimization algorithms, the objective function to be minimized must be a single number, so when multiple validation metrics are used to optimize a model the metrics must be combined in some sort of weighted average. In the best possible scenario, an objective optimum will be found such that all of the validation metrics have small values. In reality, however, the minimum often corresponds to parameter values that make some of the metrics good and others bad, so the formulation of an objective function becomes more difficult.

One can visualize the optimization problem for two parameters as searching for the lowest point on a surface, with the x and y coordinates representing the parameter values, and the z value corresponding to the value of the objective function. The optimization can be done in a brute-force manner by calculating the objective function at closely spaced points over the whole surface. However, this is impractical for more than a few parameters or for objective functions of any complexity. As a result, different strategies have been developed to reduce the number of parameter-value combinations that need to be calculated. A major problem is the distinction between the global minimum of a function and possible local minima. The minimization strategy may appear to have found a minimum, but it may be just a small valley on a high plateau, with a much lower minimum in some unexplored region. Another problem is in deciding what step sizes to use when varying parameters. If the step size is too large, some narrow deep valleys may be missed, but

too small step sizes will be impractically time consuming. There are many optimization algorithms available. One major subdivision is between those that require an explicit formulation of the derivative of the objective function with respect to each parameter, and those that do not. For models of any complexity, it is much easier if explicit derivatives are not needed, but the price is generally increased computation time. Another major division is between deterministic algorithms, which use a sequential strategy to seek locations with lower objective values, and stochastic algorithms using a shotgun approach.

2.3 Measurement of the middle ear

Studying the properties of a system by means of computational models is definitely a valuable approach, but to investigate its behavior it is primarily important to obtain measurement data of the real-life system under study. For instance, in order to create a computational model of a system it is often necessary to have a-priori knowledge of physical parameter values, which have to be determined by measurements in advance. FE models also need information of the geometry of the system, and for biological systems like the ME this requires measuring the 3D shape of the structure. Even in the presence of a-priori material parameter values and geometrical data, the model requires validation to experimental data before it can be used for purposes of understanding, prediction or control. In ME research, a wide range of techniques have been used to measure the geometry and mechanical behavior of the ME or a part of it. This section presents a brief description of the morphological and vibration measurement techniques that were used in this work. The content is partially based on Aernouts (2012), Funnell et al. (2013) and De Greef (2017).

2.3.1 Morphological measurement

To perform realistic numerical modeling of the ME, accurate 3D morphological information of the structure is needed. There are different techniques to retrieve such information, which can be divided into profilometry methods that only measure the object's surface profile and tomographic methods that image the interior of the object, usually by making cross-sectional images of the structure. Many profilometric techniques have been used to measure the surface of ME structures, such as moiré profilometry for the TM. Tomographic methods include different light-microscopy techniques, such as serial-section histology, confocal microscopy, optical coherence tomography (OCT) and orthogonal-plane fluorescence optical sectioning (OPFOS). Electron microscopy can be used for mapping fine details of the ME tissues, which provides a much higher spatial resolution than light-microscopy methods. Another tomographic technique is magnetic resonance imaging (MRI), which provides good contrast between different types of tissues. A common technique for measuring the interior of structures in the ME is X-ray computed tomography, which was used in the

current work to create geometrical models of the ME used as input for FE modeling. The basic principles of this technique are briefly discussed here.

2.3.1.1 *X-ray computed tomography*

X-ray computed tomography (CT) uses X-rays to create cross sections of a physical object, which can be used to reconstruct a virtual 3D model of the object. One usually speaks of micro-computed tomography (micro-CT or μ CT) when the pixel sizes of the cross-sectional images are in the micrometer range, as opposed to most clinical CT scanners having a lower resolution.

2.3.1.1.1 *Experimental setup*

In the CT technique, the object to be measured is positioned in the path of a wide X-ray beam emitted by an X-ray source. A part of the X-rays is attenuated by the object and another part is transmitted, creating an 'X-ray shadow image' of the object onto an X-ray sensitive detector. This procedure is repeated for different measurement angles, either by rotating the object relative to the source and the detector, or vice versa. The sequence of shadow images is then 'back-projected' onto the imaged volume by using certain image processing methods, resulting in a stack of virtual tomographic slices through the object.

2.3.1.1.2 *Physical principle*

X-rays interact with the atoms of the object in a number of ways. For X-rays with energies below about 30 keV, attenuation is mainly obtained by the photoelectric effect: an incident X-ray photon is absorbed by a tightly bound electron in the atom, and the electron is ejected from the atom. The effect is proportional to $(Z/E)^3$, with Z the atomic number and E the X-ray energy. The effect is stronger for bone than for soft tissue, as bone contains more elements with higher atomic numbers, and therefore it is possible to distinguish these tissues in reconstructions of the scan. For X-ray energies higher than 30 keV, the Compton effect dominates: an incoming X-ray photon collides with an outer-shell electron, causing the photon to be scattered and the electron to be ejected. This effect is proportional to ρ_e/E , with ρ_e the electron density and E the X-ray energy. Because the effect does not depend on the atomic number Z , it provides less tissue contrast than the photoelectric effect.

2.3.1.1.3 *Types of systems*

A distinction can be made between fan-beam and cone-beam systems, as illustrated in Figure 2.10. A fan-beam system uses a 1D X-ray source and detector, creating a two-dimensional (2D) cross section of the object. By sequentially directing the incident beam via a collimator onto different cross-sectional heights of the sample, a complete series of 2D cross sections of the object can be created. A cone-beam system, on the other hand, uses a 2D X-ray source and detector, creating 2D shadow images of the object that are used to reconstruct the entire set of 2D cross sections of the object. Mathematically, this stack of 2D images can be combined into a 3D tensor of gray-

scale values, which are a measure for the amount of X-rays that have been attenuated at the corresponding physical locations in the object.

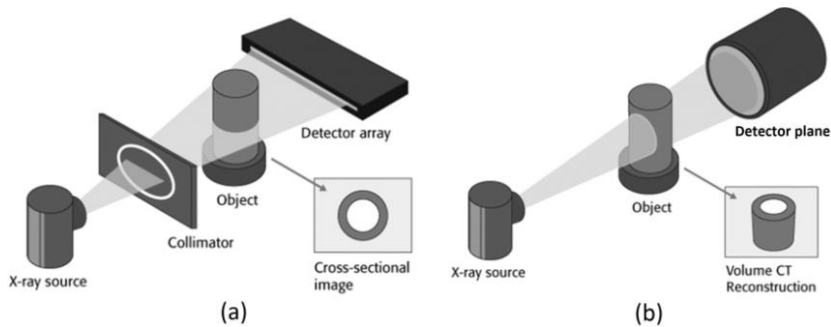


Figure 2.10. Schematic overview of (a) a fan-beam CT system and (b) a cone-beam CT system.

The great majority of CT systems use X-ray tubes, which produce a fairly broad band of frequencies. The fact that softer (lower-frequency) X-rays are absorbed more than harder ones leads to a phenomenon known as beam hardening, which causes image artifacts that are difficult to avoid. This problem can be avoided by using synchrotron radiation, which provides very bright and highly collimated X-ray beams with a practically monochromatic frequency range. However, this technique is currently only available in a few centers.

2.3.2 Vibration measurement

In ME research, various methods have been used to measure the vibration response of parts of the system. Within the range of methods, a separation can be made between techniques that require to making contact with the system, such as Mössbauer spectroscopy, and noncontact techniques that traditionally rely on optical interferometry of laser light. In the case of noncontact methods, single-point and full-field techniques can be distinguished, which respectively measure the vibration response in a single point and on an entire surface. In this work, use has been made of both a single-point technique, i.e., laser Doppler vibrometry, and a full-field method, i.e., digital stroboscopic holography, to measure the vibration of ME structures.

2.3.2.1 Laser Doppler vibrometry

Laser Doppler vibrometry (LDV) is a noncontact optical technique that is used to measure the velocity response on the surface of a vibrating object. LDV achieves this by measuring the frequency Doppler shift of a laser beam that is reflected on the vibrating surface.

2.3.2.1.1 Experimental setup

A typical LDV measurement setup is shown in Figure 2.11. In this setup, the beam of a laser with frequency f_0 is split up by a first beam splitter (BS 1) into an illumination beam and a reference beam. After passing through a second beam splitter (BS 2), the

illumination beam is focused onto the surface of the measurement object, and scattered light from the vibrating object is reflected back onto the beam splitter. Light scatters from the object in all directions, but some portion of the light is collected by the LDV system, which is called the object beam. Before the object beam reaches the photodetector, it passes through a third beam splitter (BS 3) where it recombines with the reference beam.

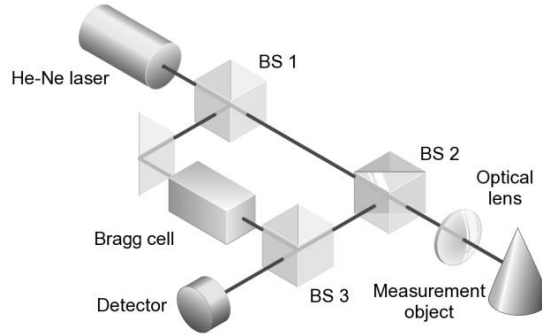


Figure 2.11. Schematic overview of a LDV setup.

2.3.2.1.2 Physical principle

The motion of the object adds a Doppler shift to the object beam of $f_d = 2v(t)\cos(\alpha)/\lambda$, where $v(t)$ is the velocity of the object's surface as a function of time, α is the angle between the laser beam and the velocity vector, and λ is the wavelength of the light. As such, the frequency of the object beam is shifted relative to the frequency of the reference beam. The initial frequency of the laser is very high ($f_o > 10^{14}$ Hz), which is higher than the response of the photodetector. The difference in frequency between the object and reference beam, on the other hand, causes a detectable amplitude modulation of the interference signal at the photodetector, which can be used to calculate the velocity of the measured object. However, the modulation frequency of the modulated signal contains only information of the velocity amplitude of the object but not of its direction: a shift of equal amplitude in either direction (above or below the frequency of the reference beam) causes a modulation of the same frequency. To solve this problem, a Bragg cell is placed in the path of the reference beam (or the illumination beam), which is an optoacoustic modulator that shifts the frequency of the corresponding beam by a certain amount f_b . This introduces a modulation frequency in the signal measured at the detector, even if the measurement object is at rest. Now, the movement of the object causes a change in this known reference modulation frequency. If the object moves towards the interferometer, the modulation frequency is reduced to $f_m = f_b - f_d$, and if it moves away from the vibrometer, the detector receives a higher frequency of $f_m = f_b + f_d$. The recorded intensity profile $I(t)$ on the photodetector due to interference of the object and reference beam is

$$I(t) = I_o + I_r + \sqrt{I_o I_r} \cos(2\pi f_m t + \phi), \quad (2.53)$$

with I_o the intensity of the object beam, I_r the intensity of the reference beam, and ϕ the phase difference between the object and reference beam. This amplitude-modulated signal is converted by the photodetector into a frequency-modulated signal, with the Bragg-cell frequency as the carrier frequency and the Doppler shift as the modulation frequency. This signal can be demodulated to derive the vibration velocity of the object.

2.3.2.1.3 *Types of systems*

There are different types of LDV systems. The most common type is a single-point vibrometer, which can measure 1D out-of-plane motion. Also scanning vibrometers exist, which serve to measure the vibrations at a series of points sequentially across the surface of interest. This is achieved by moving a single laser beam across the surface using a set of controllable movable mirrors and sequentially measuring the vibration in every point. If one is interested in measuring vibrations on multiple points but when the vibrations themselves are unrepeatable, a scanning vibrometer is inadequate. In such case, a multipoint vibrometer can be used, which is simply a set of multiple single-point vibrometers that measure the vibration on multiple points simultaneously. A LDV system can also be constructed to measure motions in 3D. To realize this, three separate laser beams are directed onto the measurement point under different directions. This allows a determination of the complete in-plane and out-of-plane vibration velocity of the object.

2.3.2.2 *Digital stroboscopic holography*

To measure the vibration of an object's surface in multiple points, it is possible to use the scanning LDV technique, as explained in the previous section. However, a large number of points increases the time required to do the measurements and so increases the chance that dehydration effects of the biological sample will influence the results. A method to measure the full-field displacement response in a single measurement is holography.

2.3.2.2.1 *Experimental setup*

The basic idea of holography is to expand the width of the laser beam, split up this beam into a reference and an illumination beam, to direct the illumination beam to the object, and to measure the interference pattern of the reflected object beam with the reference beam on a recording plane, as depicted in Figure 2.12. The interference pattern of the object and reference beams is stored on the recording plane, forming a hologram. By illuminating the recorded hologram with either of the two beams, the other beam gets reconstructed by diffraction of the illuminating beam on the hologram. This creates the illusion that both beams are still present in front of the hologram, while in reality only one of the two beams is present.

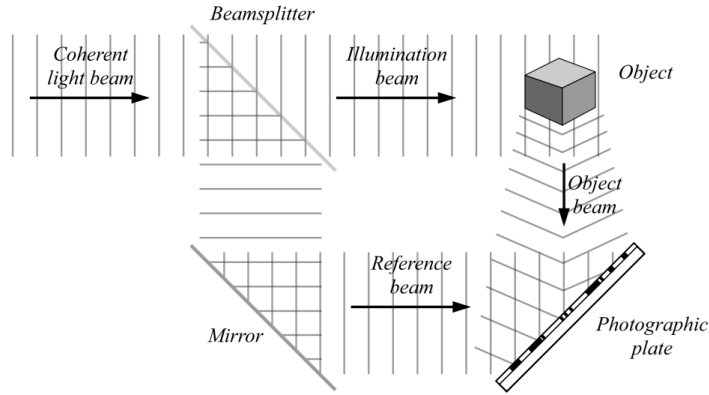


Figure 2.12. Schematic overview of a typical (analog) holography setup.

2.3.2.2.2 Physical principle

An important characteristic of holography is that not only the intensity of the object beam is recorded, but also the optical phase. This phase contains depth information of the recorded object and can be used to determine the shape of the object's surface. Likewise, the displacement between two recorded states of a moving object can be determined by subtracting the reconstructed object-beam phase maps of the two holograms. The result is a wrapped phase-difference map. By applying a 2D phase-unwrapping algorithm, the actual (unwrapped) phase difference between the two object beams is obtained. The change in optical path length $\Delta\delta$ of the beam between the two states is related to the phase difference $\Delta\phi$ by $\Delta\delta = \lambda\Delta\phi/(2\pi)$, with λ the optical wavelength. Therefore, the displacement can be immediately obtained from the optical wavelength.

When an interference pattern of the object and reference beam is recorded on a CCD, this information can be used to numerically reconstruct a 3D image of the object. This reconstruction is based on Fresnel diffraction theory, and uses the central reconstruction formula of digital holography. Without going through the derivation, the formula for calculating the reconstructed image b is given by:

$$b(n\Delta\xi, m\Delta\eta) = \exp\left\{-i\pi\lambda d' \left[\left(\frac{n}{N\Delta\xi}\right)^2 + \left(\frac{m}{M\Delta\eta}\right)^2 \right]\right\} \cdot \sum_{k=0}^{N-1} \sum_{l=0}^{M-1} h(k, l) \exp\left\{-\frac{i\pi}{\lambda d'} [(k\Delta\xi)^2 + (l\Delta\eta)^2]\right\} \exp\left\{i2\pi \left(\frac{kn}{N} + \frac{lm}{M}\right)\right\}. \quad (2.54)$$

In this equation, λ is the wavelength of the laser beam; d' is the reconstruction distance; $\Delta\xi$ and $\Delta\eta$ are the pixel distances on the CCD along the two pixel directions ξ and η in the hologram plane, and N and M are the total pixel numbers in these respective directions; $h(k, l)$ is the intensity distribution of the interference pattern in the hologram plane; n and m are the indices corresponding to the measurement

points in the plane of the reconstructed image (with respective coordinates x and y), and Δx and Δy are the physical distances in the reconstruction plane between neighboring measurement points for these coordinates. The physical distances Δx and Δy in the reconstruction plane are related to the pixel distances $\Delta\xi$ and $\Delta\eta$ in the hologram plane by $\Delta x = d'\lambda/(N\Delta\xi)$ and $\Delta y = d'\lambda/(M\Delta\eta)$.

The summation term in (2.54) can be calculated by performing a Fourier transform on the recorded hologram $h(k,l)$, multiplied with the function $\exp\left\{-\frac{i\pi}{\lambda d'}[(k\Delta\xi)^2 + (l\Delta\eta)^2]\right\}$. The prefactor $\exp\left\{-i\pi\lambda d'\left[\left(\frac{n}{N\Delta\xi}\right)^2 + \left(\frac{m}{M\Delta\eta}\right)^2\right]\right\}$ does not depend on the specific hologram and influences only the absolute phase at each location; when only the phase difference of the reconstructed holograms between two recorded states of the object is relevant, this factor can be omitted. Still, a value for the reconstruction distance d' needs to be chosen. It can be shown that the optimal reconstruction distance is equal to the recording distance d , i.e., the distance between the object and the CCD. At this distance, one of the two first-order diffraction beams will be in focus. When choosing $d' = -d$, the other first-order beam will be in focus. As both beams contain identical information, the result will be equivalent. In order to determine the displacement between two states of the object, the phase is extracted from the complex field b of the two recorded states, while the amplitude is disregarded. For the derivation of (2.54) and a more in-depth analysis on the subject, the reader is referred to, e.g., Schnars and Jüptner (2002), Kreis (2005) and Poon (2007).

2.3.2.2.3 Types of systems

As for LDV, there are different types of holography. In an analog holography setup, the interference of the object and reference beam is recorded on a holographic plate, as depicted in Figure 2.12. After recording, a reconstructed image of the object can be viewed by the inverse process of illuminating the holographic plate with the same reference beam as during recording. In digital holography, the holographic plate is replaced by a CCD and the reconstruction is done in a computer based on (2.54). In time-average holography, an object is set in vibration and the laser is shuttered on and off to expose the holographic plate during a multiple number of periods. In this way, the average vibration amplitude during one period can be obtained. A time-average hologram only provides information of the vibration amplitude, but does not contain any information on the relative vibration phase between the points on the surface. In stroboscopic holography, an object is set in vibration and the laser is shuttered on and off at several specific phase instants in the vibration period. In this way, holograms at multiple phases in one period are obtained, and the displacement relative to the resting position can be calculated at all of these phase instants. By combining these images, the vibration amplitude and phase over the entire surface can be calculated.

PART II
MY RESEARCH

CHAPTER 3 MIDDLE-EAR ACOUSTIC RESPONSE AND MECHANICAL PROPERTIES IN DUCK

Abstract

So far, the quasi-static and acoustic functional principles of the avian ME are poorly understood. This chapter aims to improve understanding of this system by studying the acoustic response and mechanical properties of the ME of the mallard duck. Aside of being a well available species, the mallard was chosen because it encounters quasi-static pressure variations occurring in daily life, for example when flying or when dabbling in the water. Being able to deal with such pressure variations is an important characteristic for potential new single-ossicle prostheses. Two optical techniques were used to assess the sound-induced vibrations of the ME: stroboscopic holography was used to measure full-field TM vibrations, and LDV was used to measure the frequency response of the columella at the connection with the TM and the IE. Due to the lack of a-priori knowledge of mechanical parameters, the value of the most important material parameter was determined in this study, which happened to be the Young's modulus of the TM. To achieve this, a FE model of the ME based on μ CT data was created and matched to the experimental results. In summary, our results indicate which mechanical parameters are essential to the good functioning of the avian ME and provide a first estimation of their values.

This chapter is based on:

Muyshondt, P.G.G., Soons, J.A.M., De Greef, D., Pires, F., Aerts, P., Dirckx, J.J.J., 2016.

A single-ossicle ear: Acoustic response and mechanical properties measured in duck, *Hear. Res.* 340, 35–42. doi:10.1016/j.heares.2015.12.020.

Muyshondt, P., De Greef, D., Soons, J., Dirckx, J.J.J., 2014. Optical techniques as validation tools for finite element modeling of biomechanical structures, demonstrated in bird ear research. *AIP Conf. Proc.* 1600, 330–337. doi:10.1063/1.4879599.

Muyshondt, P., De Greef, D., Soons, J., Peacock, J., Dirckx, J.J.J., 2014. Determination of the mechanical properties in the avian middle ear by inverse analysis. *Proceedings of the COMSOL Conference, Cambridge, UK.*

3.1 Introduction

The avian ME uses the TM, a cartilaginous unit (the extracolumella) and a single ossicle (the columella) to bridge the acoustic impedance difference between air and the fluids of the IE. Although the hearing frequency range in birds is generally smaller than in mammals, with an upper frequency limit around roughly 10 kHz (Dooling et al., 2000), hearing thresholds in both classes are mostly comparable. Just as in mammals, impedance matching in avian species is obtained by three mechanisms: (1) a hydroacoustic transformation represented by the TM-to-CFP area ratio, (2) a mechanical lever action based on rotations around a fulcrum (Saunders et al., 2000), and (3) a curved membrane effect. The mechanical lever is supposed to go along with a tilting motion of the columella and the CFP, given the acute angle between the ossicle and the TM plane (Gaudin, 1968), although detailed measurements are missing. A piston-like motion has been reported in one owl species, which was attributed to an additional flexing motion of the extracolumella (Norberg, 1978).

It is not well understood how the avian ME deals with quasi-static pressure changes. It has been suggested that the intracolumellar joint plays a role by performing a buckling motion, which is identified as a synchondrosis that functions as a ball joint (Mills and Zhang, 2006; Arechvo et al., 2013). To understand this quasi-static and vibroacoustic behavior, a thorough knowledge is needed of the mechanical parameters that describe the columellar bird ear. Understanding the functioning of the single-ossicle avian ear may eventually contribute to the improvement of current single-ossicle prostheses.

Studies of the mechanical properties of the avian ME are scarce, and only describe (quasi-)static characteristics (e.g., Thomassen et al., 2007). Moreover, a-priori knowledge of material parameters is lacking entirely. In this study, the acoustic response and mechanical properties were investigated in mallard duck (*Anas platyrhynchos*) by means of optical interferometry and FE modeling. Sound-induced motions of the TM were measured with stroboscopic holography to obtain its full-field displacement, and the sound-induced velocities of the CFP and the conical tip of the TM were measured using a LDV system. A 3D FE model of a duck's ME is constructed, based on the geometry obtained from μ CT scans. Using this model, the mechanics of the ME are simulated under acoustic stimulation of the TM. Because initially defined material parameters are uncertain, a sensitivity analysis is performed to quantify their relative influence on the model output. Afterwards, the most influential parameter is determined in inverse analysis for different specimens, which allows us to study the vibroacoustic behavior and viscoelastic properties of the TM at multiple frequencies.

3.2 Materials and methods

3.2.1 Experiments

3.2.1.1 Sample preparation

Measurements were performed on three dissected left ears of defrosted mallard duck heads (S₁, S₂ and S₃). S₁ and S₂ were male and S₃ female. Under the operation microscope, no signs of pathology were detected. During preparation, a part of the left side of the skull containing the ME was dissected from the head, which opened the bilaterally connected ME cavities. The quadrate, which is a part of the beak suspension connected to the ME, was partially removed and the major part of the ear canal was drilled away to expose the TM. After a first set of measurements, the IE load on the ME was removed by drilling away its medial wall and draining the IE fluid. The samples were kept moist by use of a vaporizer (BU-1300, Bonaire, Salisbury, Australia) and by putting them in hydrated paper between the preparation and the measurements. In between measurements, samples were stored in refrigerated saline solution.

3.2.1.2 Stroboscopic holography

Digital stroboscopic holography enables the quantitative measurement of full-field displacement of a vibrating object as a function of time. This is realized by synchronizing very short laser pulses (8 ns) to the vibration phase so that the object's motion is 'frozen in time'. The full-field displacement at the chosen phase is then calculated by comparing the displaced hologram to a reference hologram of the object in rest. By cycling the laser pulses stepwise through the vibration period at evenly spaced phase instants, the entire time-resolved transverse motion of the surface is obtained. After Fourier analysis of the time-dependent displacement waveforms, the displacement magnitude and phase maps can be obtained. The exact phase difference between the incident sound waves and the vibrating surface is monitored with an oscilloscope. For a more detailed description of this technique, see Cheng et al. (2010, 2013), Khaleghi et al. (2013) and De Greef et al. (2014a). Sound pressures of eleven frequencies ranging from 0.05 to 12.8 kHz, two per octave, were applied to the lateral side of the TM with pressure amplitudes between 90 and 110 dB SPL. The actual sound pressure at the TM was recorded with a probe microphone. During the measurement, the samples were placed inside a fixture with the TM plane positioned perpendicular to the illumination beam of the laser. On S₃, the motion was measured with both intact and removed IE to measure the effect of the IE impedance on the TM response. To enhance reflectivity of the TM, the membrane was painted with a thin layer of either of two different coatings: a suspension of 5% TiO₂ in deionized water for S₁ and white make-up liquid (Aquacolor Soft Cream – White Wet Make-up, Product Code 01129/00, Kryolan, Berlin, Germany) for S₂ and S₃. Tests showed that the latter gives the best combination of reflectivity, ease of application and delay of dehydration.

3.2.1.3 *Laser Doppler vibrometry*

The sound-induced motions of the ossicle were measured on S₂ and S₃ using a LDV system (OFV-534 sensor head and OFV-5000 controller, Polytec, Waldbronn, Germany) that is mounted on a surgical microscope (OPMI Sensera/S7, Carl Zeiss, Jena, Germany). Sound-induced velocities were divided by the sound pressure measured in front of the TM, defining the ME transfer functions. To enhance light reflectivity, a little piece of reflective tape was placed onto the point of measurement, small enough to minimize inertial effects. During measurement, the laser beam was pointed perpendicularly to the object's surface. Pure-tone sinusoidal pressures, sixteen per octave, with amplitude levels of 90 dB were presented to the lateral TM surface. A probe microphone was placed in front of the TM to measure the actual pressure. Experimental control and signal processing was done in Matlab. Because it was not feasible to have optical access to the CFP from the lateral side, the following approach was applied: first, the velocity response was measured at the conical tip of the TM from the lateral side with IE intact. Then, the IE was opened and drained and the transfer function was measured again at the TM to examine the effect of the IE impedance. Finally, the response was measured at the CFP in the oval window from the medial side.

3.2.2 *Finite-element modeling*

3.2.2.1 *Morphology*

The geometry of the FE model is based on μ CT images of a dissected left ear of a mallard duck, different from the ones used in the experiments. The μ CT scan was executed at the University of Ghent Computer Tomography (UGCT) facility (Masschaele et al., 2007). To enhance soft tissue contrast, the ME sample was stained during two days before scanning using a daily refreshed 2.5% phosphotungstic acid (PTA) solution in deionized water, which limits tissue shrinkage most (Buytaert et al., 2014). The resulting data set is built up of $2000 \times 2000 \times 1640$ cubic voxels with a voxel size of $7.5 \mu\text{m}$. Image segmentation of the CT data was carried out in Amira 5.3 (FEI, Hillsboro, OR, USA). An automatic seed-fill algorithm was applied together with an interpolation method to obtain the segmentation, although manual intervention was required to detect boundaries of soft tissue structures. After segmentation the different geometric components were converted separately into triangulated surface objects (STL: stereolithography file format), which were recombined in FE software (COMSOL Multiphysics 5.0, Burlington, MA, USA). The final triangulated surface contains the ME structures shown in Figure 3.1, but the ear canal, the ME cavity wall and the IE were not considered, in order to not overcomplicate the model and to obtain well-defined boundary conditions. The geometry includes the following objects: a slightly conical TM with the apex pointing outwards into the ear canal, the columella bounded by an annular ligament, the extracolumella considered as a single

unit comprising three arms (the infra-, extra- and suprastapedial processes), and Platner's ligament made of collagen fibers which extends across the ME cavity onto the otic process of the quadrate (Starck, 1995). The extrastapedial process ends in the apex of the conical TM, which is referred to as the extrastapedial tip. The ratio of the TM-to-CFP surface area is equal to 23.2 and the columella is tilted at an angle of 59.6° relative to the TM plane. Several ligaments and muscles mentioned in literature (Pohlman, 1921) were not apparent in the scan and were not considered in the final geometry. This includes the columellar muscle which inserts onto the columella, the drum-tubal ligaments that run through the TM, and the ascending ligament which connects the TM to the extrastapedial process.

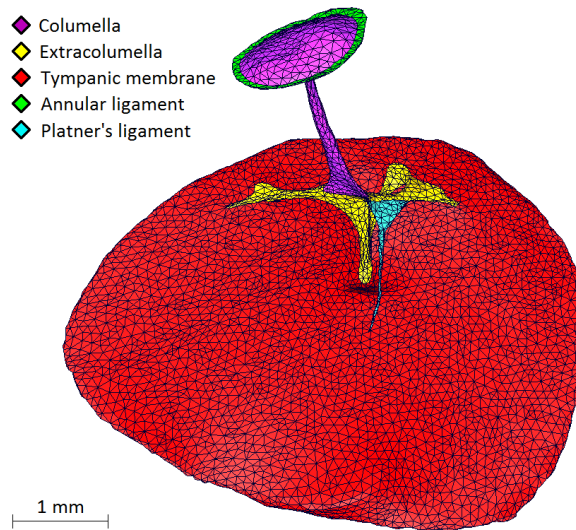


Figure 3.1. Triangulated surface model of the left ME of a mallard duck. All different components are indicated in color.

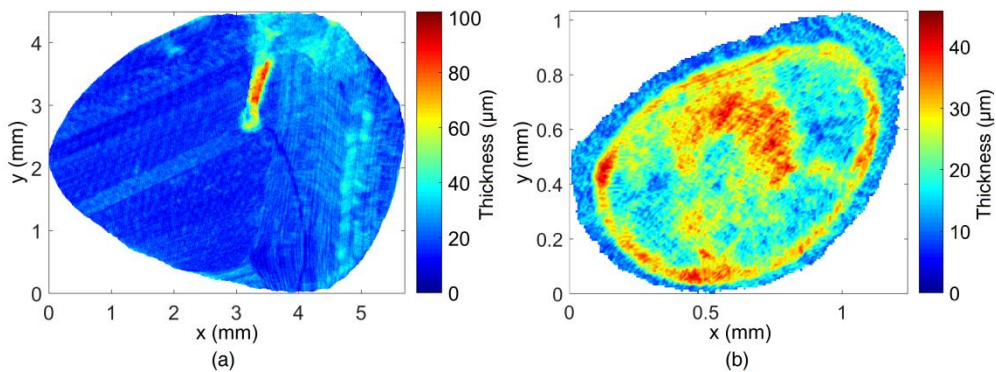


Figure 3.2. Thickness distributions of (a) the TM and (b) the CFP. The TM thickness is largest near the attachment of the extrastapedial process of the extracolumella, which corresponds to the location of the ascending ligament. The CFP thickness is largest around the connection with the annular ligament.

3.2.2.2 Model description and boundary conditions

In the FE mesh, the TM is described as a shell structure and was meshed using triangular elements. To take into account the nonuniform thickness distribution of the TM, the original segmentation data was used to calculate the full-field thickness of the membrane by adaptation of Van der Jeught et al. (2013), which is defined as the perpendicular distance from the medial to the lateral TM plane, as depicted in Figure 3.2 (a). Platner's ligament was modeled by triangular shell elements near the connection with the extracolumella, and by beam elements along the length of the ligament, having a uniform thickness and diameter as calculated from the segmentation data. The shaft of the bony columella and the cartilaginous extracolumella were meshed using tetrahedral solid elements. For the CFP and annular ligament, shell elements were used with nonuniform thickness distribution as shown in Figure 3.2 (b). Adjacent solid and shell objects were rigidly connected, which means that shared nodes yield equal displacements, also at the intracolumellar joint. In addition, beam-shell connections shared rotational degrees of freedom. As a boundary condition, the outer rim of the TM and the annular ligament were fully constrained, allowing neither rotations nor displacements. Also, Platner's ligament was fully constrained at the border with the quadrate. At the medial surface of the CFP, a viscoelastic load was applied to model the impedance of IE fluids, with a total spring constant of 525.8 N/m and damping coefficient of 0.771 N·s/m, adapted from Merchant et al. (1996). Modeling was done in the frequency domain to calculate the steady-state response of the entire geometry at individual frequencies. To simulate the acoustic stimulus of the TM, a uniform harmonic pressure of 1 Pa (i.e., 94 dB SPL) was applied at the lateral TM surface.

3.2.2.3 Material properties

All objects made of soft tissue were treated as viscoelastic materials. Only the bony columella was treated as a purely elastic material. Viscoelasticity in the frequency domain was modeled by a complex modulus E^* defined as

$$E^*(\omega) = E_1(\omega) + iE_2(\omega) = E_1(\omega)[1 + i\eta(\omega)], \quad (3.1)$$

in which ω represents the angular frequency, i the imaginary unit, E_1 the storage or Young's modulus (unit: Pa; further on assigned by E) that accounts for the elastic part, E_2 the loss modulus that takes into account the viscous portion (unit: Pa), and $\eta = E_2/E_1$ the loss factor, which is a dimensionless quantity equal to zero for purely elastic materials. As no a-priori avian ME parameter values are available, they were initially taken from other literature values, given in Table 3.1, which are all considered homogeneous and isotropic.

To describe the frequency dependence of the viscoelastic TM, three model descriptions were applied that were used in De Greef et al. (2014b). Model 1: constant

values for E and η for the TM, given in Table 3.1. Model 2: a third-order generalized Maxwell model, comprised of a spring in parallel with three spring-dashpots in series, and characterized by a frequency-dependent storage and loss modulus (Zhang and Gan, 2010). Model 3: a Rayleigh damping model with frequency-dependent loss factor (Vollandri et al., 2011) and constant Young's modulus.

Table 3.1. Material parameter values used in the initial FE model. All mass densities ρ , Poisson's ratios ν , and values indicated with ^a are taken from (Homma et al. 2010), being frequently used in current human ME models. ^b is taken from (Spahn and Wittig, 2003), which is based on hyaline cartilage values in the knee of a domestic pig. ^c is taken from (Homma et al., 2009) and comes from values of the human anterior malleolar ligament. ^d is taken from (Aernouts et al., 2012) and represents a constant loss factor derived for the human TM, here used for all soft tissue structures. ^e is taken from (Thomassen et al., 2007) and was used to model the annular ligament in birds that consists of collagen.

| Component | ρ (10^3kg/m^3) | E (MPa) | η | ν |
|--------------------|--------------------------------|--------------------|--------------------|-------|
| Columella | 2.2 | 14100 ^a | 0 | 0.3 |
| Extracolumella | 1.2 | 39.2 ^b | 0.078 ^d | 0.3 |
| Tympanic membrane | 1.2 | 20 ^a | 0.078 ^d | 0.3 |
| Platner's ligament | 1.2 | 21 ^c | 0.078 ^d | 0.3 |
| Annular ligament | 1.2 | 20 ^e | 0.078 ^d | 0.3 |

3.2.2.4 Inverse analysis

Because no a-priori knowledge is available of the avian ME parameters, there is a considerable uncertainty on the initial values defined in Table 3.1. To characterize which parameters have the largest influence on the model output, a sensitivity analysis was performed using the technique of Oakley and O'Hagan (2004). The values for the two most influential material parameters that follow from the sensitivity analysis are used as input for an inverse optimization routine. In this procedure, the model is fitted to the experimental data by minimizing a least-squares objective function defined by

$$\chi^2(p) = \sum_i [f_{\text{mod}}(x_i, p) - f_{\text{exp}}(x_i)]^2. \quad (3.2)$$

In this expression, f_{mod} stands for the model output and f_{exp} for the experimental output, x_i represents a variable on which the output depends and over which the output is summed, and p is the set of model parameters to be determined. Surrogate modeling (Gorissen et al., 2010) was used to perform the optimization. In this technique, the parameter space defined by p is initially sampled using a Maximin Latin Hypercube design to ensure maximal space filling. At the sampled points, objective function (3.2) is evaluated through which a surrogate model is built. Then, the minimum of the current surrogate model is determined and new samples are selected and evaluated according to the location of the current minimum. This procedure is repeated until a satisfying representation is found for the objective

function and when an optimum can be identified. This optimum or minimum indicates the optimized combination of parameter values.

3.3 Results

3.3.1 Experimental results

3.3.1.1 Stroboscopic holography

In Figure 3.3, experimentally obtained displacement maps of the lateral TM surface are shown for S_1 , S_2 and S_3 at 1.6 kHz. The magnitude is normalized to incident pressure and the phase is taken relative to the phase of the incoming sound wave (negative phase denotes motion lagging behind sound pressure). In some cases the TM could not be fully illuminated, so that the TM displacement map is partially missing. In S_3 , the effect of removing the IE on TM displacements was assessed and found to be small. TM displacement maps of the different samples show some differences: absolute displacements and phase patterns in S_1 are different from S_2 and S_3 , and the magnitude profile in S_3 differs slightly from S_1 and S_2 , having different locations of maximal displacement with different orientations. In S_3 , a line of small displacement is apparent that corresponds to the location of the middle drum-tubal ligament (MDT, Figure 3.3 – left), but it is much less prominent in other samples. Nevertheless, TM displacements evolve similarly with frequency and the number of vibration maxima differs little or not at all between samples. They are further discussed for the example of S_2 .

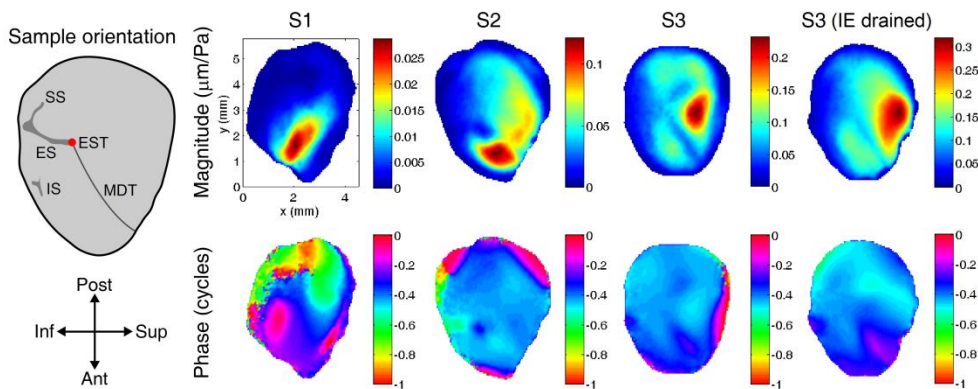


Figure 3.3. Experimental (S_1 , S_2 and S_3) displacement magnitudes ($\mu\text{m}/\text{Pa}$) and phases (cycles) of the lateral TM surface at 1.6 kHz. The last column shows TM displacements of S_3 after draining the IE. Anatomical orientations and attachment locations of the infra- (IS), extra- (ES), and suprastapedial (SS) processes are indicated. The extrastapedial tip (EST) is annotated by a red dot and the middle drum-tubal ligament (MDT) by a diagonal line.

In Figure 3.4, the displacement maps of the lateral TM surface of S_2 are shown in the first column, for selected stimulus frequencies of 0.4, 1.6 and 6.4 kHz. For all frequencies, the magnitude is smallest on the inferior part of the TM, which

corresponds to the attachment location of the extracolumella. At 0.4 kHz, the phase is uniform and the magnitude shows one area of larger displacement. At 1.6 kHz, different parts of the TM start to move out of phase with each other. These spatial transitions of the phase occur continuously at some TM locations and more abruptly at others. Around 6.4 kHz, the displacement pattern becomes more complex and starts to form ring patterns around the extrastapedial tip.

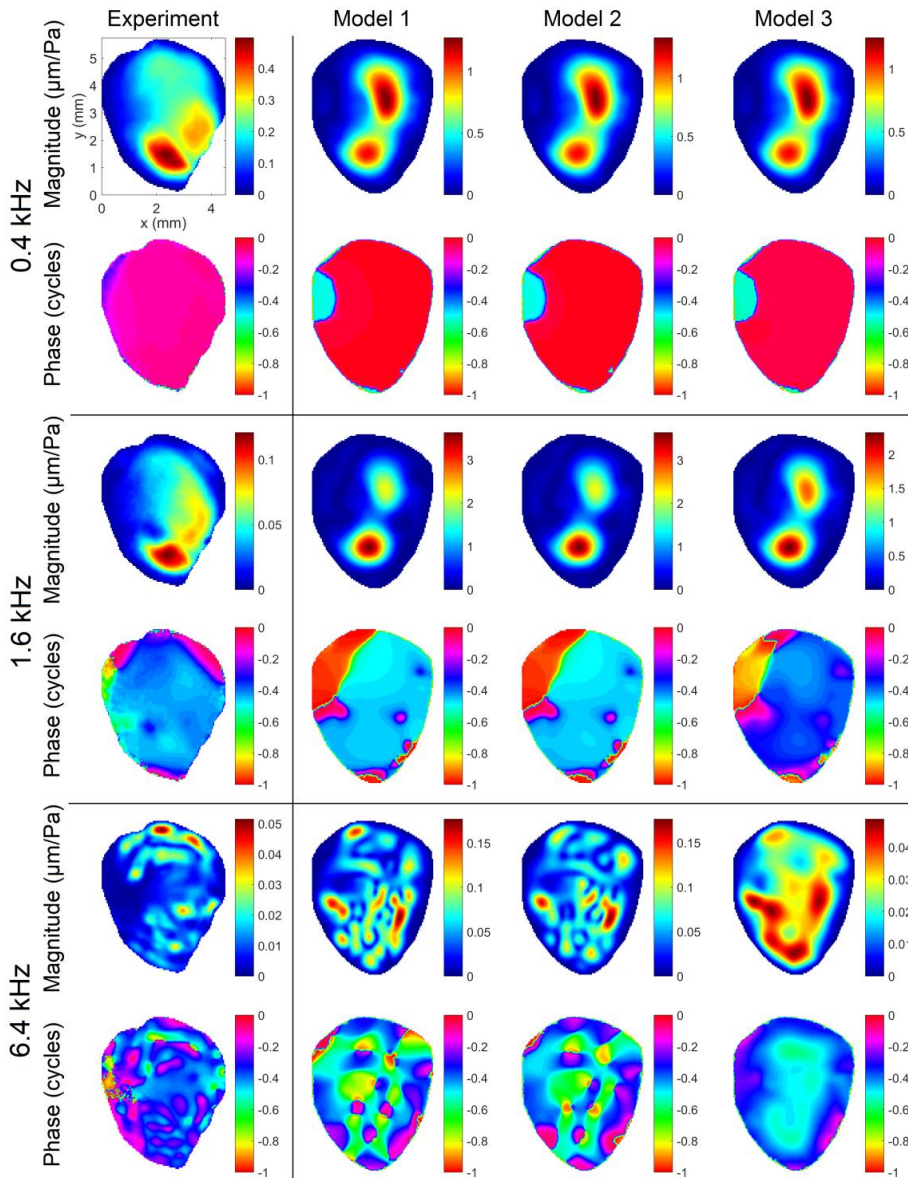


Figure 3.4. Displacement magnitudes ($\mu\text{m}/\text{Pa}$) and phases (cycles) of the lateral TM surface at 0.4, 1.6 and 6.4 kHz, for both the experiment (S2, left) and the three optimized models (right). Displacement phases are taken relative to the phase of the incident pressure wave. The models are described in Sections 3.2.2.2 and 3.3.2.2.

3.3.1.2 Laser Doppler vibrometry

Figure 3.5 shows the vibrometry data measured on S₂ (gray) and S₃ (black). The top panel represents the transfer function plotted as velocity magnitude normalized to pressure, as a function of input frequency. Solid lines stand for the response measured on the extrastapedial tip and dashed lines represent the CFP response. All measurements were done after removal of the IE, except for the thin black line which shows the extrastapedial tip response with intact IE. The bottom panel depicts the extrastapedial tip-to-columellar footplate (EST-to-CFP) velocity ratio of S₂ and S₃. First of all we notice an offset in response between the two samples. Nevertheless, both samples show the same damped resonance near 1.5 kHz after removal of the IE. Around 6 kHz, S₂ reaches a second resonance, while in S₃ the response is mainly flat but higher on average. Removing the IE in S₃ leaves the low-frequency response unaltered, but shifts the first resonance frequency to the right and increases the high-frequency response, which resembles the effect of removing inertial impedance from the system. In both samples, the EST-to-CFP velocity ratio varies between 1.5 and 2.5 for most frequencies. The velocity ratio drops below 1 above 6 kHz (S₂) and 8 kHz (S₃).

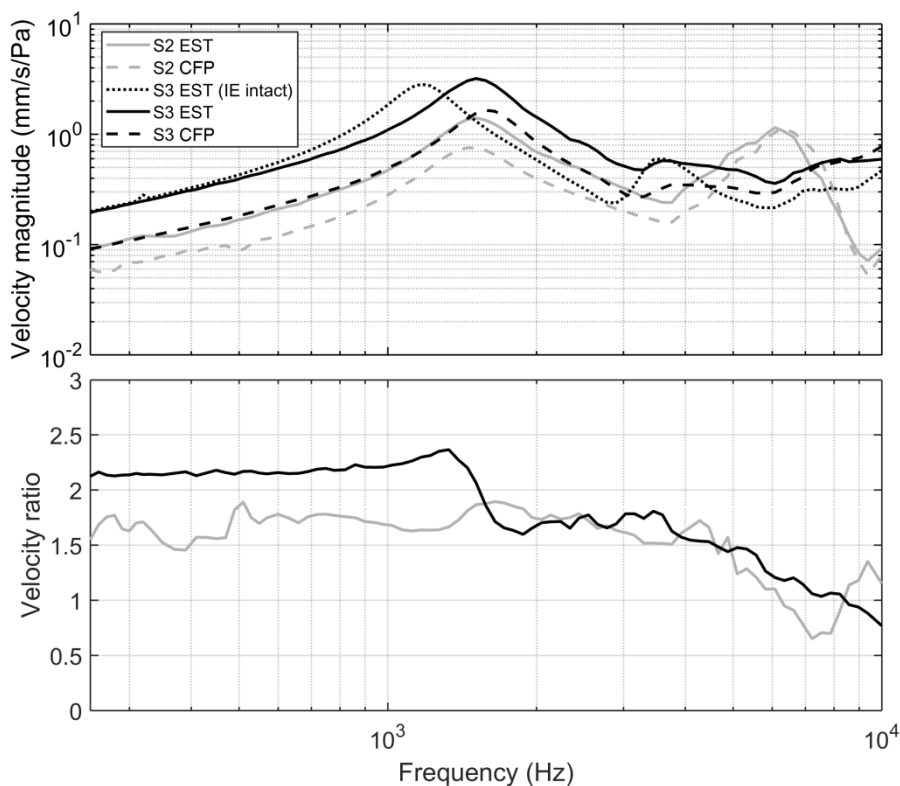


Figure 3.5. Top: Normalized velocity magnitude of the extrastapedial tip (EST) and CFP as a function of stimulus frequency, measured on S₂ and S₃. Bottom: EST-to-CFP velocity ratio of S₂ and S₃.

3.3.2 Model results

3.3.2.1 Sensitivity analysis

All material parameters were subjected to a sensitivity analysis with the exception of the Young's modulus of Platner's ligament, because it solely serves for stabilization (Saunders et al., 2000), and all Poisson's ratios, which have been shown to be unimportant (Funnel and Laszlo, 1977). First, parameter uncertainty intervals were chosen with uniform probability distribution. If p_o is the base value of each parameter (see Table 3.1), the lower bound p_l and upper bound p_u are defined as follows: $p_l = 0.1 \cdot p_o$ and $p_u = 10 \cdot p_o$ for all Young's moduli, $p_l = 0.5 \cdot p_o$ and $p_u = 1.5 \cdot p_o$ for all loss factors, and $p_l = p_o - 100 \text{ kg/m}^3$ and $p_u = p_o + 100 \text{ kg/m}^3$ for all mass densities. Subsequently, 400 samples were generated within the defined parameter space of the sensitivity analysis. At these samples, the full-field displacement of the TM and the EST-to-CFP velocity ratio were evaluated when using model 1 at 1.6 kHz, which is near the resonance frequency (Figure 3.5). The results of the sensitivity analysis are shown in Table 3.2, in which effects are quantified by relative variances expressed in percentages. Total effects are not necessarily equal to the sum of individual and interaction effects, as higher-order terms may be present in which a parameter is involved.

Table 3.2. Individual, interactive and total effects of material parameters on the TM displacement and the EST-to-CFP velocity ratio at 1.6 kHz. Effects are expressed as variances in percentage. Individual effects on the TM displacement (resp. velocity ratio) are given in the upper row (resp. leftmost column) and interactions in the upper-right (resp. bottom-left) part of the middle table. Total effects are shown in the rightmost column (resp. bottom row). ME components are indicated with lowercase symbols for the material parameters. VR = velocity ratio, ST = soft tissue structures, C = columella, EXC = extracolumella.

| (%) | | ρ_C | ρ_{ST} | E_{TM} | E_C | E_{EXC} | E_{CAL} | η_{ST} | |
|-------------|-------------|----------|-------------|----------|-------|-----------|-----------|-------------|-------------|
| | Ind. | 0.08 | 0.15 | 71.49 | 0.13 | 0.89 | 0.61 | 0.82 | TM |
| ρ_C | 0.12 | | 0 | 0.04 | 0 | 0.01 | 0 | 0.11 | 0.26 |
| ρ_{ST} | 0.15 | 0.02 | | 2.5 | 0.1 | 0.17 | 0.03 | 0.23 | 9.59 |
| E_{TM} | 10 | 0.13 | 0.53 | | 0.91 | 2.7 | 0.94 | 1.65 | 94.79 |
| E_C | 1.6 | 0.16 | 0.55 | 2.51 | | 0.18 | 0.04 | 0.11 | 9.4 |
| E_{EXC} | 7.45 | 0.05 | 0.31 | 2.86 | 1.22 | | 0.05 | 0.63 | 15.76 |
| E_{CAL} | 15.08 | 0.08 | 0.39 | 5.25 | 2.28 | 4.38 | | 0.03 | 4.18 |
| η_{ST} | 0.12 | 0 | 0 | 0 | 0 | 0 | 0 | | 12.73 |
| | VR | 4.25 | 17.01 | 59.54 | 42.88 | 46.09 | 62.44 | 0.13 | Tot. |

Investigating the results on the TM displacement, E_{TM} has the highest influence, whereas other parameters only have negligible effect and mostly contribute through interactions with E_{TM} . Following E_{TM} , E_{EXC} has the second largest effect ($EXC =$

extracolumella). Other material parameters, such as ρ_{ST} and η_{ST} (ST = soft tissue structures), have smaller effect given their small initial uncertainty. For the EST-to-CFP velocity ratio, the influence of E_{CAL} is highest, followed closely by E_{TM} , E_{EXC} and E_C (C = columella; CAL = columellar annular ligament). It is noted that most total effects of parameters are much larger than individual effects, for instance with E_C , which suggests that interactions between parameters and higher-order effects are very important.

3.3.2.2 Inverse analysis

First, holography data of the TM displacement at 1.6 kHz are used as experimental input for inverse analysis. The parameter with largest influence on the TM displacement is chosen as the first parameter to determine, which turns out to be E_{TM} . For the second parameter we choose E_{EXC} because it has the second largest effect, although we expect it to have limited influence on the overall TM displacements when compared to E_{TM} . For the optimization, objective function (3.2) is defined as

$$\chi^2(p) = \sum_i \left\{ [M_{\text{mod}}(\mathbf{r}_i, p) - M_{\text{exp}}(\mathbf{r}_i)]^2 + [\phi_{\text{mod}}(\mathbf{r}_i, p) - \phi_{\text{exp}}(\mathbf{r}_i)]^2 \right\}. \quad (3.3)$$

In this expression, $\mathbf{r}_i = (x_i, y_i)$ are the 2D TM coordinates and $p = (E_{TM}, E_{EXC})$ are the parameters to be determined. M represents the displacement magnitude and ϕ the displacement phase at 1.6 kHz. M and ϕ are both normalized to 1 in model and experiment, meaning that only displacement patterns are considered and not absolute displacements. For the TM stiffness, the objective functions for different experimental data sets reached minima at $E_{TM} = 41.9$ MPa (S1), $E_{TM} = 33.0$ MPa (S2) and $E_{TM} = 72.6$ MPa (S3). For extracolumella stiffness, the resulting value was too uncertain to be determined precisely using any of S1, S2 or S3.

In Figure 3.4, the optimized result of model 1 as obtained for S2 is compared with the experimental outcome for S2 at 0.4, 1.6 and 6.4 kHz. To study the frequency dependence of the viscoelasticity of the TM, model 2 and 3 are applied. For model 2, a prefactor c is multiplied with the frequency-dependent storage modulus in De Greef et al. (2014b) such that $E_{TM}(\omega) = c \cdot E_1(\omega) = 33.0$ MPa at 1.6 kHz. For model 3, $E_{TM} = 33.0$ MPa and constant. Comparing the three models, similar results are obtained at 0.4 and 1.6 kHz. The models show a large area of maximal displacement on the posterior part of the TM that is not seen in S2 but only in S3 (Figure 3.3 – S3). Also, the model phase undergoes a sudden half-cycle jump near the extracolumella that is not seen in the experimental data. At 6.4 kHz, the larger damping in model 3 at higher frequencies leads to a poorer match between the displacement patterns predicted by that model and the experiment. Model 1 and 2 better predict the displacement patterns at 6.4 kHz, though the clearer spatial phase variations they predict are larger than those seen in the data at 6.4 kHz. Furthermore, the experimentally obtained phase map shows a little more ring structures than the model predictions. Absolute

displacements are well described at 0.4 and 6.4 kHz. Only at 1.6 kHz the model displacements are one order of magnitude too high.

3.4 Discussion

3.4.1 Avian middle-ear mechanics

In the past, the mechanics of the avian ME have been modeled as a series of mathematical equations (Relkin, 1988; Starck, 1992) and a 2D rigid-rod model (Thomassen et al., 2007) that only describe the behavior of the ME in (quasi-)static circumstances under the assumption of a-priori parameter values. Because of this scarcity of literature data, current results are also compared to existing data of mammal ME mechanics.

3.4.1.1 Material stiffness

The central layer of the TM in chickens is composed of radial and circular collagen fibers with possibly different properties (Chin et al., 1997). In the current study, the TM Young's modulus in duck was chosen isotropic as a first approximation to not increase the number of unknown parameters. Using the holography data as experimental input for inverse analysis, the TM Young's modulus in three samples was respectively found to be 33.0, 41.9 and 72.6 MPa at 1.6 kHz. Currently, our findings can only be compared to mammals, which already show a great variety between different species, studies and specimens (e.g., Vollandri et al., 2011). For instance, the values found in our study vary by a factor 2, whereas in human, fitting vibrometry measurements on two temporal bones yields a variation of a factor 4 (De Greef et al., 2014b), which clearly indicates the presence of interindividual differences. Nevertheless, our results are within the range of what is generally found in most mammal species (~ 10–100 MPa). Furthermore, the sensitivity analysis shows that elasticities of the annular ligament, extracolumella and columella have a large effect on the EST-to-CFP velocity ratio, which implies that their values will be needed to describe the ME transfer function and the 3D motions of the columella in future studies.

3.4.1.2 Tympanic membrane displacements

As was found in human (De Greef et al., 2014b), observed TM motions suggest the presence of internal damping in the membrane: a certain amount of damping is needed to describe the continuous phase variations over the membrane at different frequencies. This amount should be small enough to allow for the complicated displacement patterns on the membrane at higher frequencies (Figure 3.4), which tend to form ring patterns around the center, but it needs to be high enough to smooth out nonexistent sharp resonances in the frequency-dependent response of the TM, which may explain why absolute displacements in the vicinity of the resonance at 1.6 kHz are poorly predicted by the models. TM displacements show that a membrane

with constant Young's modulus and loss factor gives almost the same results as a TM described by a third-order Maxwell model. When comparing the experimental and numerical results of displacements at low frequencies, we observe that the models show a nonexistent phase jump near the extracolumella, which is possibly caused by not considering the ascending ligament as a separate structure. This ligament is generally found to be stiffer than the rest of the TM due to a thicker layer of collagen fibers (Chin et al., 1997; Vallejo Valdezate et al., 2007).

3.4.1.3 *Extrastapedial tip / columellar footplate velocity*

First of all, the frequency of the peak velocity corresponds closely to the most sensitive frequency in mallard ducks (Trainer, 1946). The velocity transfer function of the avian ME has also been measured at both the extrastapedial tip and CFP in the ringed turtledove (*Streptopelia risoria*) (Saunders and Johnstone, 1972) and the common pigeon (Gummer et al., 1989a,b). These experiments yielded peak amplitudes of 1–10 mm/s/Pa between 0.8–2 kHz, and an EST-to-CFP velocity ratio of 2.2–2.5 between 0.125–4 kHz. These results are similar to our findings in that they denote a positive lever action, while compared to mammals (e.g., Rosowski et al., 2007; Ravicz et al., 2007) amplitudes are around ten times higher. At frequencies higher than 4 kHz, the velocity ratio was earlier found to increase above a value of 5, for which two possible explanations were suggested (Manley, 1972a, 1990b): either the complicated motions of the TM significantly change displacements at the extrastapedial tip, or an additional flex in the extrastapedial process absorbs the TM motions. However, in our measurements, a decrease was observed above 7 kHz. Thus, an acoustic impedance mismatch at the oval window near the upper frequency limit in birds seems to take place in opposite directions for different species. Removal of the IE shifts the resonance frequency to the right in the extrastapedial tip velocity and increases the high frequency response. This suggests that the IE impedance is mass dominated.

3.4.2 *Method considerations*

In the optimization process of the FE model, only material parameters were considered but not the system's geometry and boundary conditions. However, it is known that for instance TM thickness has a strong influence on TM stiffness and hence the overall ME response (Aernouts et al., 2012). The same holds for the IE load, which influences motions of the columella at the extrastapedial tip (Figure 3.5) and certainly at the CFP. The reason for disregarding these parameters is that each newly added parameter would drastically increase the number of required function evaluations in the sensitivity analysis and hence the total calculation time. On the other hand, sensitivities were only determined at a single frequency, while the influence of parameters can change with frequency. Nonetheless, optimization of the most influential parameters using the holography data, which was done at the same

frequency as the sensitivity analysis, well predicted TM displacements at other frequencies. In each optimization, only two parameters were considered simultaneously, of which eventually only one parameter was determined. A larger number of parameters would increase the total calculation time but also the risk of overfitting the experimental data. Even our approach has some limitations: the FE geometry is based on a different sample than the ones used in the experiments, and measurements performed on three specimens show some differences. For instance, small differences in ME geometry may cause the optimized parameters to be slightly over- or underestimated, and because only three samples were studied, definite conclusions may not be drawn yet. Nevertheless, we expect that the effect of geometrical variations is small when compared to the interindividual variances on the obtained material parameters themselves.

3.5 Conclusion

In this study, the acoustic response and mechanical properties of the single-ossicle ME of birds were studied for the first time by combining the results of vibration experiments with FE simulations. From the analysis we found that TM displacements are mainly influenced by the TM Young's modulus, whereas the ME transfer function mostly depends on the Young's moduli of the annular ligament, the TM and the extracolumella, in that order.

Using holography measurements at 1.6 kHz, the TM Young's modulus was found equal to 33.0, 41.9 and 72.6 MPa in three samples respectively, showing a considerable interindividual variability. Our results suggest that in birds, similar to mammals, moderate damping in the TM material properties produces better fits between predicted and measured phases of the TM motion patterns.

The velocity transfer functions of the extrastapedial tip and CFP are around ten times higher in magnitude than what is generally found in mammals. The EST-to-CFP velocity ratio is equal to 1.5–2.5 denoting a positive lever action, but at higher frequencies this ratio dropped corresponding to an increase in CFP response relative to extrastapedial tip response and a loss of lever function.

CHAPTER 4 ACOUSTIC INPUT IMPEDANCE OF THE OSTRICH INNER EAR

Abstract

Motions of the columella are influenced by the presence of the IE fluid. In the Chapter 3, the loading of the IE on the columella was modeled by a viscoelastic pressure load on the CFP with a quantitative value derived from measurements on human ears. The IE load affects vibrations of the columella by turning piston-like motion partially into rocking motion. However, the precise impedance of the IE in birds is unknown and may be very different from the impedance of mammals due to differences in IE size, shape and structure between both classes. In this chapter, the acoustic input impedance of the IE is measured in ostrich. The ostrich was chosen because it has very large ears compared to most other birds, in which the needed sample manipulations and experimental procedures would be impossible. The IE impedance was determined by comparing the vibration response of the columella with intact IE and with drained IE. For acoustic frequencies, the columella was stimulated electromagnetically and the vibration response was measured with LDV. For quasi-static frequencies, columellar displacements were induced with a piezo transducer and the force response was measured with a force sensor. As a result, we found that values of the IE impedance in the ostrich are one to two orders of magnitude smaller than what is found in mammal ears.

This chapter is based on:

Muyshondt, P.G.G., Aerts, P., Dirckx, J.J.J., 2016. Acoustic input impedance of the avian inner ear measured in ostrich (*Struthio camelus*). *Hear. Res.* 339, 175–183. doi:10.1016/j.heares.2016.07.009.

Muyshondt, P.G.G., Pires, F., Dirckx, J.J.J., 2016. LDV measurement of bird ear vibrations to determine inner ear impedance and middle ear power flow. *AIP Conf. Proc.* 1740, 050001. doi:10.1063/1.4952665.

4.1 Introduction

To date, there are two conflicting theories regarding the motions of the columella in the bird ME: the first theory proposes that the ossicle performs side-to-side or rocking movements under stimulation of the TM (Gaudin, 1968), while the other theory proposes piston-like motions (Norberg, 1978). The nature of this motion is important as it influences the lever function of the ossicle that contributes to the impedance matching function of the ME.

Studies in human (e.g., Hato et al., 2003) have shown that the IE influences motions of the stapes. The predominant piston-like motions of the stapelial footplate are converted into rocking motions to some extent at higher stimulus frequencies, which is partially due to the presence of the IE fluid behind the oval window. Also in reptiles and birds, the impedance of the IE is assumed to affect CFP vibrations (Gummer et al., 1989b) and the behavior of the ME in general (Manley, 1972b). To study the motions of the ossicles and the corresponding influence of the IE, measurement data are needed of the acoustic input impedance of the IE.

In humans and other mammals, the acoustic input impedance of the IE has been estimated and measured in several ways (e.g., Zwislocki, 1965; Lynch et al., 1982; Kringlebotn, 1988; Merchant et al., 1996; Puria et al., 1997; Aibara et al., 2001). The IE impedance of birds is presumably different from mammals because of differences in IE size and structure. The auditory portion of the IE in birds is not coiled but straight as opposed to the cochlea in mammals. Also, the architecture of the basilar membrane inside the cochlear duct is different, and the ratios of the surfaces of the round window and oval window are dissimilar, which is assumed to contribute to the IE impedance as well (Merchant et al., 1996).

In this study, the acoustic input impedance of the IE is determined in the common ostrich (*Struthio camelus*). In the acoustic frequency range, the IE impedance is determined with LDV and digital stroboscopic holography. As stimulation source, an electromagnetic induction solenoid and a magnet attached to the ossicle are used. In the quasi-static regime, a piezo transducer and force sensor are utilized to measure the IE impedance.

4.2 Materials and methods

4.2.1 Acoustic impedance

The method to measure the acoustic impedance of the IE (Z_{IE}) is similar to the approach followed in Merchant et al. (1996). With this approach, the acoustic impedance of the columella and the IE combined (Z_{C+IE}) is calculated from measurements of the columellar velocity (v_C) with intact IE in response to stimulation forces measured at the distal end of the columella (F_C). The acoustic impedance is defined as

$$Z = \frac{p_{\text{CFP}}}{U_{\text{CFP}}} = \frac{F_C}{v_C A_{\text{CFP}}^2}, \quad (4.1)$$

in which p_{CFP} is the pressure acting on the CFP in the oval window, U_{CFP} the volume velocity of the CFP and A_{CFP} the total surface area of motion of the CFP. This area includes the medial surface area of the bony CFP, but also a portion of the annular ligament that surrounds the CFP in the oval window and vibrates along with the CFP. The measurement procedure is repeated with an opened and drained IE to determine the acoustic impedance of the columella Z_C , which incorporates the impedance of the bony ossicle and the annular ligament. The acoustic impedance of the IE (Z_{IE}) is calculated by subtracting Z_C from $Z_{\text{C+IE}}$.

With the followed approach, several assumptions are made: (1) motions of the columella are piston-like in the current setup, (2) forces (resp. velocities) measured on the distal end of the columella are equal to the forces (resp. velocities) acting on CFP in the oval window, (3) velocities measured on the columella are in the linear response regime for the applied stimulus levels, and (4) the passive properties of the dead IE were not altered after the sample preparations.

In the human temporal bone study by Merchant et al. (1996) it was possible to stimulate the stapes acoustically and shield the round window from this stimulation. In most birds this is not possible as the round window is very large and is located in close vicinity of the CFP, so an acoustic stimulus would reach both structures. We therefore used different stimulation techniques which are explained in detail in the following sections.

4.2.2 *Sample preparation*

The ostrich was chosen as model species because it is the largest existing avian species, so the ear is large enough to perform the needed manipulations. The heads of eight ostriches, with ages between eighteen months and five years, were obtained from an ostrich farm. The samples were frozen one day after death and thawed right before measurement. Studies in human (Ravicz et al., 2000) have shown that it is possible for air to penetrate in the IE during the freezing and thawing process, which may alter the IE impedance. Therefore, each sample was checked for the presence of air bubbles behind the round window membrane before measurement. Subsequently, the ear canal, the TM and the cartilaginous extracolumella, which connects the TM to the columella, were removed. Also, half of the columellar shaft was cut from the distal side of the ossicle. To obtain optical access of the columella and the CFP, some of the surrounding bone and soft tissues were removed without breaking up the IE structures. Vibration measurements were performed after each of the following manipulations. First, the IE was left intact. Then, the round window membrane was perforated with a needle. Next, the IE was thoroughly drained with a suction tip through the perforation in the round window. Finally, the medial walls of the IE were

drilled to remove the remaining IE fluid that was left on the medial surface of the CFP.

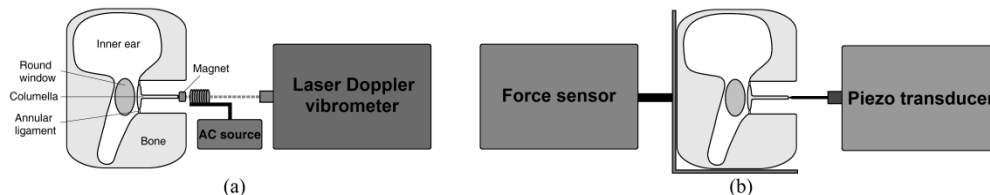


Figure 4.1. Schematic overview of the experimental setups. (a) Setup for the measurements in the acoustic regime. A magnet is placed on the distal end of the columella and stimulated by a miniature induction coil through which an alternating current is sent. A LDV system measures the induced columella vibration velocities on the magnet. (b) A piezo transducer stimulates the columella on the distal end with a needle at controlled displacement amplitude. The induced forces on the specimen are measured with a force sensor.

4.2.3 Experiments in the acoustic regime

4.2.3.1 Laser Doppler vibrometry

To induce columellar vibrations in the acoustic frequency range, magnetic stimulation of the ossicle was used, which is a technique that was previously applied to study ossicular fixation in human temporal bones (e.g., Peacock et al., 2013). A schematic overview of the experimental setup is shown in Figure 4.1 (a). A small gold-coated neodymium magnet with a mass of 3 mg was fixated with instant glue (Super Glue Precision, Loctite, Henkel, Düsseldorf, Germany) on the tip of the remaining distal part of the columella. Then, a miniature copper induction solenoid was placed over the magnet by using a translation stage to adjust the position of the coil in three directions. The force that the induction coil exerts on the electromagnet was calibrated using a scale with a precision of 1 μN . During the measurements, alternating sinusoidal currents were sent through the coil to stimulate the magnet, using stepwise frequencies between 0.25 and 4 kHz with sixteen lines per octave. At the same time, the induced vibration response of the columella was measured with a single-point 1D LDV system (OFV-534 sensor head and OFV-5000 controller, Polytec, Waldbronn, Germany) mounted on a surgical microscope (OPMI Sensera/S7, Carl Zeiss, Jena, Germany). Vibrations of the columella were measured on the lateral side of the electromagnet in a direction parallel to the columellar shaft and the induced magnetic field. To increase the reflection of the laser beam on the specimen, a small piece of reflective tape was placed on top of the magnet. To control and analyze the stimulation and response signals, a program was developed in Matlab (Mathworks, Natick, MA, USA) that interacted with a data-acquisition device (USB-6251 BNC, National Instruments, Austin, TX, USA) to generate the electromagnetic stimulus and to measure the stimulation and response signals simultaneously. The data-acquisition card was set at a sample rate of 48 kHz. Each signal was extended with 0.1 s to eliminate transient effects in the response. Subsequently, the amplitude of both

signals and the phase difference between the two signals was determined from the Fourier transform of the waveforms at the applied stimulus frequencies. Electronic phase delays in the experimental setup were accounted for.

4.2.3.2 *Digital stroboscopic holography*

In order to determine the IE impedance with the LDV setup and the electromagnetic stimulation, the assumption was made that columellar displacements are piston-like. To verify this assumption, the full-field out-of-plane displacements of the CFP were measured with digital stroboscopic holography. Very short laser pulses (8 ns) were synchronized with the phase of the vibrating object, so that full-field displacements of the object's surface could be calculated at the chosen phase. By cycling these pulses stepwise through the vibration period, the entire time-dependent motion of the surface was obtained. More details on the technique can be found in Cheng et al. (2010, 2013), Khaleghi et al. (2013) and De Greef et al. (2014). In the current holography setup, the columella is stimulated electromagnetically in the same way as in the LDV setup, but the displacement response is measured from the medial side of the CFP instead of from the lateral side. To expose the CFP, the IE needed to be removed for the measurements. To enhance reflectivity of the sample, the medial side of the CFP was coated with white make-up liquid (Aquacolor Soft Cream – White Wet Make-up, Product Code 01129/00, Kryolan, Berlin, Germany).

4.2.4 *Experiments in the quasi-static regime*

To study the quasi-static properties of the acoustic IE impedance, a piezo transducer (P-864.10, Physik Instrumente, Karlsruhe, Germany) was used to induce displacements of columella. A scheme of the measurement setup is shown in Figure 4.1 (b). The piezo transducer contains an embedded strain gauge that has an active feedback loop, so the displacements could be controlled to a precision better than 50 nm. The frequency dependence of the piezo system was calibrated by measuring its actual displacement amplitude with LDV. During measurement, the needle of the piezo transducer was positioned on the remaining distal end of the columella, in a direction parallel to the columellar shaft. The position of the needle was further adjusted under the microscope such that columellar displacements were purely piston-like. At the same time, the forces provoked by the displacements were measured with a force sensor (UF1 Force Sensor, LCM Systems Ltd, Newport, Isle of Wight, UK). The ear specimen was placed and glued on a holder connected to the force sensor, after dissecting the ear from the head. The sensor contains a load cell that can detect forces as small as 1 mN. The force sensor was integrated in the experimental setup using custom-made electronics. Forces that the specimen exerted on the force sensor were measured parallelly to the displacement stimulus of the piezo needle. To control and analyze the displacement stimulus and the force response, the same software was used as for the acoustic-frequency measurements.

The resulting columellar velocity v_C was determined by $v_C = i\omega x_C$, with i the imaginary unit, ω the angular frequency and x_C the measured columellar displacement.

4.2.5 Columellar footplate surface area

According to (4.1), the acoustic impedance of the IE depends on the square of the total surface area of the CFP. To determine this area accurately, microphotographs were made of the medial surface of the CFP with a high-resolution digital CCD camera (Fo442B /SC IEEE1394, Foculus, Aegis Electronic Group, Gilbert, AZ, USA) after vibration measurement of the sample. The camera has a resolution of 1392×1040 square pixels and the images were calibrated at $2.2 \mu\text{m}$ per pixel. Before the images were made, the columella was removed from the sample and positioned in front of the camera by means of a horizontal and vertical translation stage. In the analysis of the images, the surface of the bony CFP was extracted using a threshold filter. The remaining surrounding tissue of the annular ligament was not incorporated in this surface. As the annular ligament partially moves along with the CFP during vibration, it contributes to the total volume displacement in the oval window and hence the impedance of the IE. To quantify the volume displacement that is attributed to the annular ligament, full-field holography measurements were performed on the medial side of the CFP for a single sample, as described in Section 4.2.3.2. From the resulting full-field displacement map, the total volume displacement was determined as a function of the volume displacement that only belongs to the bony CFP.

4.3 Results

4.3.1 Columellar footplate surface area

Table 4.1 shows the surface area of the CFPs measured with microphotography. As can be deduced from the table, not each specimen was measured on both sides of the head. The mean surface area of all samples was equal to 3.03 mm^2 with a standard deviation of 0.41 mm^2 . Holography measurements performed on the CFP revealed that the total surface of motion in the oval window was equal to 165% of the area of bony CFP surface (data not shown), when averaged over multiple stimulus frequencies.

Table 4.1. Surface area of the medial side of the CFPs. The left column contains the specimen number, the second column shows the surface area on the left side of the head of the specimen, and the third column shows the CFP area on the right side of the head.

| Specimen number | Left side (mm^2) | Right side (mm^2) |
|-----------------|-----------------------------|------------------------------|
| 1 | 3.19 | 3.17 |
| 2 | 3.05 | 2.93 |
| 3 | 2.41 | 2.53 |
| 4 | 3.03 | 2.86 |
| 5 | | 2.69 |
| 6 | 3.36 | 3.42 |
| 7 | 3.54 | 3.74 |
| 8 | | 2.50 |

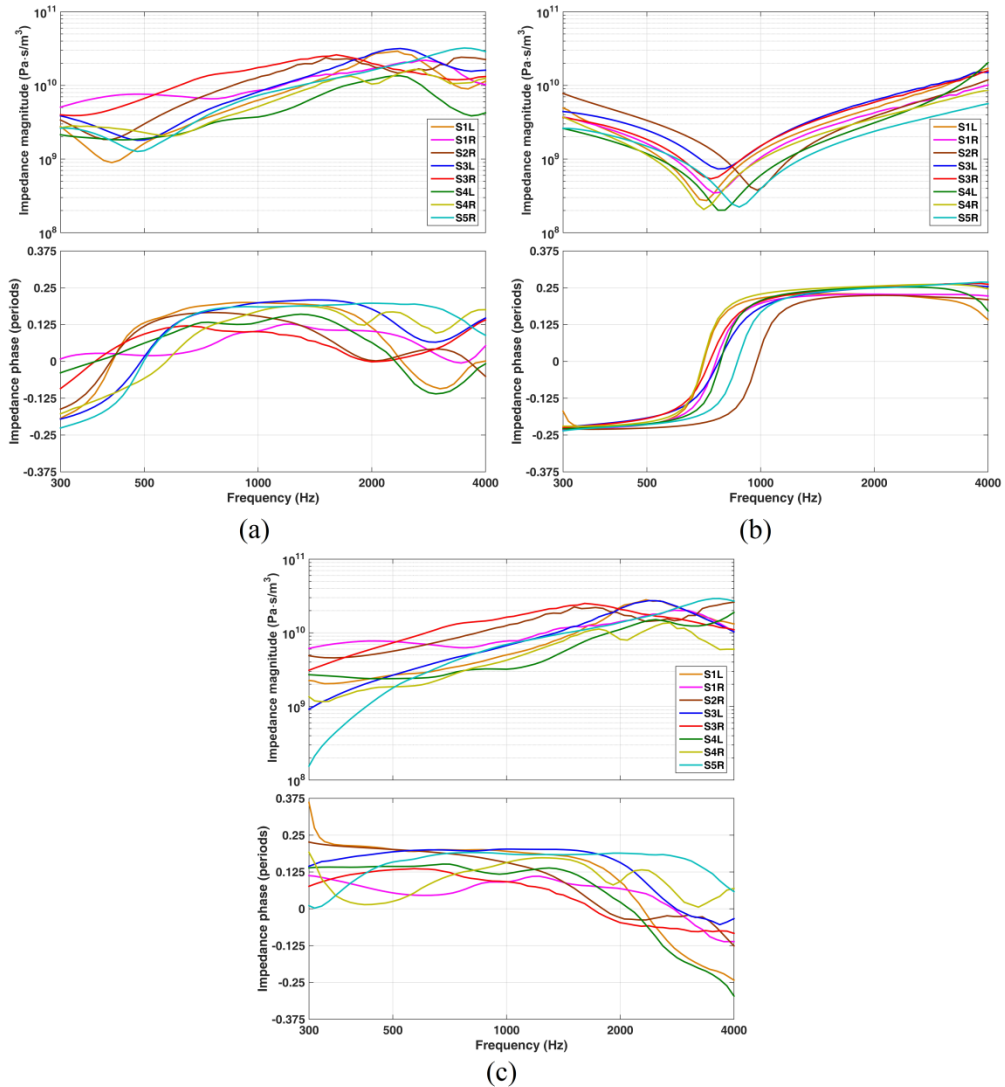


Figure 4.2. (a) Acoustic impedance magnitude (top) and phase (bottom) as a function of frequency, measured with (a) intact IE, (b) opened IE and (c) the difference between the two conditions for all measured ears.

4.3.2 Experiments in the acoustic regime

4.3.2.1 Laser Doppler vibrometry

LDV measurements were made for stimulus frequencies between 0.25 and 4 kHz, with sixteen lines per octave. The maximum frequency of 4 kHz was chosen in relation to the upper frequency limit of hearing in the emu (*Dromaius novaehollandiae*), which is a species closely related to the ostrich which we found in literature (Manley et al., 1997). The amplitude of the electromagnetic force stimulus was equal to 0.1 mN, resulting in CFP displacement amplitudes between 5 nm and 5 μ m. Figure 4.2 shows

the acoustic impedance calculated from the LDV measurements of (a) intact IE, (b) opened IE and (c) the difference of the two conditions that represents the impedance of the IE itself. Results from intermediate steps in the manipulation of the specimens are not shown and will not be discussed.

When comparing the impedance results of the intact and opened condition from Figure 4.2 (a), it is seen that impedance magnitudes are consistently higher when the IE is still intact. Only at the lowest and highest frequencies shown, magnitude values are similar. Peak magnitudes become sharper when the IE is opened, while being shifted to higher stimulus frequencies. This is also reflected in the phase response, in which the transition from -0.25 to $+0.25$ periods happens much more sudden in the opened condition, although being postponed to higher frequencies. In the high-frequency range, the magnitude and phase both decrease for certain specimens with intact IE, but not with opened IE. Also, the variability in the measurements with intact IE is larger. For the impedance of the IE itself, we observe from Figure 4.2 (c) that the magnitude and phase are similar to what is found for the intact condition in the mid-frequency range. For lower and higher frequencies, the IE impedance deviates from the impedance with intact IE.

4.3.2.2 Digital stroboscopic holography

Holography measurements were performed for frequencies between 0.05 and 12.8 kHz, with two lines per octave. The chosen amplitudes of the stimulation force varied between 0.014 and 0.217 mN. Figure 4.3 shows the experimental results of the full-field CFP displacement in the right CFP of specimen 5 with opened IE, for the selected frequencies of 0.1, 0.4, 0.8 and 1.9 kHz. Displacement magnitudes are normalized to the induced pressure of the electromagnetic stimulus, which was calculated from the force exerted on the magnet divided by the total area of motion in the oval window.

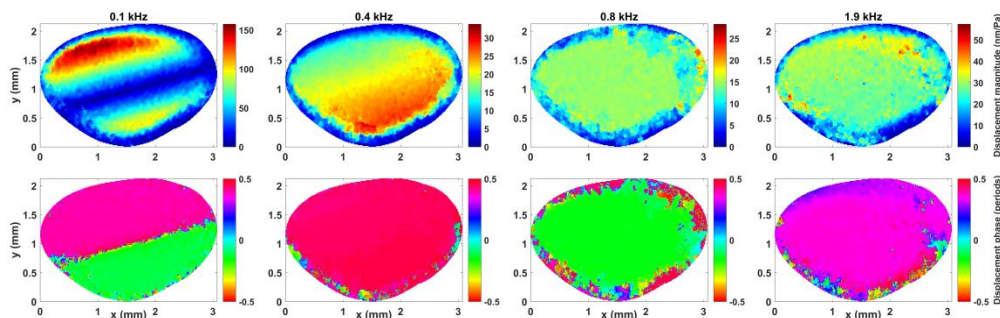


Figure 4.3. Full-field displacement response of the CFP in the right ear of specimen 5 with IE opened, at stimulus frequencies of 0.1, 0.4, 0.8 and 1.9 kHz. The displacement magnitude (top) is normalized to incident pressure and for the displacement phase (bottom) the reference phase was chosen arbitrary.

At 0.1 kHz, the CFP displacement magnitude contains two local maxima that have a relative phase difference of half a period, which shows that rocking motions are

present in the vibrations of the columella in the current setup. This type of displacement pattern was seen for all measured frequencies between 0.05 and 0.3 kHz. Above 0.3 kHz, the displacement pattern altered, as shown in Figure 4.3 for 0.4 kHz. At this frequency, the full-field displacement magnitude and phase are becoming more uniform, which is also the case for higher stimulus frequencies such as 0.8 and 1.9 kHz. This indicates that displacements at frequencies above 0.3 kHz are mostly piston-like. Because the motions are not piston-like below 0.3 kHz, we only present impedance data in the range of 0.3–4 kHz.

4.3.3 Experiments in the quasi-static regime

Measurements of columella vibrations in the quasi-static regime using the piezo and force transducer were performed for frequencies from 1 to 20 Hz, with one line per octave. The amplitude of the displacement stimulus imposed by the piezo transducer was chosen equal to 50 μm . Figure 4.4 shows the magnitude of the acoustic impedance resulting from the displacement and force measurements, both with (a) intact IE, (b) opened IE and (c) the difference of both conditions that represents the impedance of the IE itself. Results of intermediate steps in the manipulation of the specimen are again not shown. The phase difference between the displacement stimulus and force response was measured at 1 Hz and found to be zero. For increasing frequency, the results of the phase measurements deteriorated due to experimental constraints and are therefore not presented.

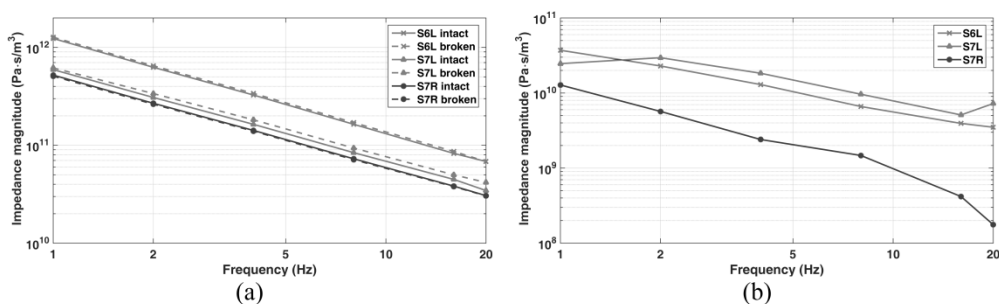


Figure 4.4. Acoustic impedance magnitude as a function of frequency for (a) intact IE (solid lines), opened IE (dashed lines) and (b) IE impedance. Measurements were performed on the left ear of specimen 6 and on both ears of specimen 7.

In Figure 4.4 (a) it is seen that the acoustic impedance in sample 6 is a bit larger than in sample 7. On the other hand, we observe that changes in the acoustic impedance after removal of the IE are almost negligible for each of the measured samples. This is also apparent from the IE impedance in Figure 4.4 (b), in which magnitudes are almost two orders smaller than in Figure 4.4 (a).

4.3.4 Acoustic impedance analysis

The mean of the acoustic-impedance measurements is shown in Figure 4.5 (a). Due to the rocking motions found with holography, we could not determine the impedance in the frequency range between 0.02 and 0.3 kHz. The mean experimental impedance Z_{exp} was fitted for both intact IE and opened IE by using a simple RLC model in series Z_{mod} as in Merchant et al. (1996). In this model, the impedance is described by three components, namely the stiffness reactance K that is dominant in the low-frequency range, the inertial impedance M that is dominant in the high-frequency range, and the damping resistance R that dominates the impedance near the resonance frequency. In theory, K can be determined from the low-frequency response by $K = \omega \text{Im}(Z)$, with ω a low-valued angular frequency and Z the impedance measured at that frequency. M can be found through $M = K/\omega^2$, with ω the resonance frequency in which the impedance phase becomes zero. R can be calculated from M at the resonance frequency via $R = \omega M/Q$, with Q the so-called Q factor that is defined as the ratio of the resonance frequency to the half-power bandwidth. To obtain the best fit the least-squares method was used, in which objective function χ^2 defined as

$$\chi^2(K) = \sum_i \left\{ \left[\log|Z_{\text{mod}}(\omega_i, K)| - \log|Z_{\text{exp}}(\omega_i)| \right]^2 + \left[\angle Z_{\text{mod}}(\omega_i, K) - \angle Z_{\text{exp}}(\omega_i) \right]^2 \right\} \quad (4.2)$$

was minimized with respect to K . In this equation, $|Z|$ is the impedance magnitude, $\angle Z$ the unwrapped impedance phase and ω_i the stimulus frequencies from the measurements over which is summed in (4.2). The components M and R in the impedance model depend on K as defined in the current section. The weight given to each term in the sum of (4.2) is proportional to the number of measurements performed at the corresponding frequency.

The components of the impedance were found to be $K_{\text{C+IE}} = 7.25 \cdot 10^{12} \text{ Pa/m}^3$, $M_{\text{C+IE}} = 0.952 \cdot 10^6 \text{ Pa} \cdot \text{s}^2/\text{m}^3$ and $R_{\text{C+IE}} = 2.02 \cdot 10^9 \text{ Pa} \cdot \text{s}/\text{m}^3$ for intact IE, and $K_{\text{C}} = 7.05 \cdot 10^{12} \text{ Pa/m}^3$, $M_{\text{C}} = 0.300 \cdot 10^6 \text{ Pa} \cdot \text{s}^2/\text{m}^3$ and $R_{\text{C}} = 0.54 \cdot 10^9 \text{ Pa} \cdot \text{s}/\text{m}^3$ for opened IE. For each component the difference of intact and opened IE was calculated, yielding $K_{\text{IE}} = 0.20 \cdot 10^{12} \text{ Pa/m}^3$, $M_{\text{IE}} = 0.652 \cdot 10^6 \text{ Pa} \cdot \text{s}^2/\text{m}^3$ and $R_{\text{IE}} = 1.57 \cdot 10^9 \text{ Pa} \cdot \text{s}/\text{m}^3$. The latter components represent the impedance of the IE itself, for which the corresponding RLC model is shown in Figure 4.5 (b).

In Figure 4.5 (a) we observe that the magnitudes of both models slightly overestimate the low-frequency measurements, while underestimating the high-frequency results. We also observe that the impedances with intact IE and opened IE strongly overlap in the low-frequency range, which is the case for both experiment and model. Between 0.3 and 1 kHz, the resonance peaks are nicely reflected in the models. For frequencies above 2 kHz, the sudden drop in the IE impedance magnitude of the intact condition cannot be reproduced by the model. The same is found for the impedance phase, in which the model fails to describe the intact IE for frequencies above 1 kHz. For opened IE, the phase is predicted well by our model. For the IE impedance itself,

shown in Figure 4.5 (b), the model describes the magnitudes well for low and mid frequencies, although it must be highlighted that standard deviations are large in the low-frequency range. For the highest frequencies above 1 kHz, the model is again unable to describe the experimental magnitude and phase.

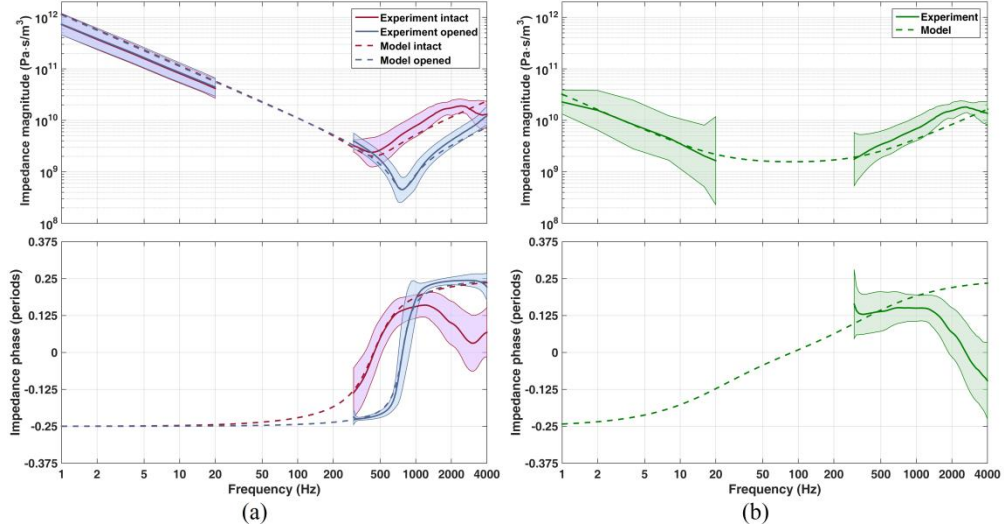


Figure 4.5. Acoustic impedance magnitude (top) and phase (bottom) for (a) intact and opened IE, and (b) the IE itself as a function of frequency. Full lines represent the mean of the measurements at each frequency for intact IE (red), opened IE (blue) and IE impedance (green), with standard deviations plotted as colored bands. The corresponding RLC models are shown as dashed lines.

4.4 Discussion

4.4.1 Experimental approach

The acoustic input impedance of the IE was determined using the approach of Merchant et al. (1996), which was based on measurements of the combined impedance of the stapes, oval window and IE. In other studies (e.g., Aibara et al., 2001), the IE impedance was assessed by measuring the pressure in the scala vestibuli directly using a hydrophone or another type of pressure sensor inserted in the IE. However, in our approach the IE was left intact during measurement as opposed to other techniques. Also, we can measure perpendicularly to the CFP, which is not possible with the other approaches for which an angle correction is required. In the experiments, only the piston-like component of the columellar vibrations was considered, as it was shown that it is the primary contributor to the pressure in the IE (Decraemer et al., 2007).

4.4.1.1 Sample preparation

Ravicz et al. (2000) studied the effect of freezing and thawing on the cochlear input impedance in human temporal bones. They found that air bubbles can penetrate the

IE after freezing and thawing of the fresh specimen. This event could reduce the magnitude of the IE impedance, compared to the measurements before freezing. However, when the IE was refilled with saline to remove the air bubbles, IE impedances were restored to the measurements observed in the fresh state. Therefore, we carefully checked each specimen for the presence of air bubbles behind the round window membrane before measurement. Nevertheless, air bubbles may have been present that were not observed, which may have some effect on the result.

Measurements of ME input immittance in human temporal bones were demonstrated to be similar to measurements in live ears (Rosowski et al., 1990). Also, no significant differences were found in that study between fresh bones and bones that were frozen and thawed. In literature, there are no studies available comparing IE input impedance measurements of live and dead specimens. It is known, however, that death results in an increased mobility of the basilar membrane (e.g., Kohllöffel, 1972), which according to Merchant et al. (1996) might decrease the IE impedance magnitude by a factor 2 under certain assumptions (Zwislocki, 1975). These findings were described for the human ear and may also apply to the ostrich.

4.4.1.2 Experiments in the acoustic regime

To determine the vibration velocity of the columella, the assumption was made that CFP vibrations are piston-like. From the full-field holography measurements with IE opened between 0.05 and 12.8 kHz it was found that this assumption is not consistently valid with electromagnetic stimulation of the columella: below frequencies of 0.3 kHz, the full-field displacement map of the CFP contains two maxima that move out of phase, indicating the presence of a vibration mode going along with rocking motions of the CFP. Apparently, small asymmetries in the geometry of the columella or the placement of the magnet and coil may cause the ossicle to vibrate asymmetrically in this frequency range. We therefore present impedance measurements in the acoustic frequency range above 0.3 kHz, for which it was found that CFP vibrations are mostly piston-like with IE opened. However, small asymmetric vibrations may still be present in the motions of the ossicle with IE intact, but according to Hato et al. (2003) and Gummer et al. (1989b) the IE only affects CFP motions in the high-frequency range. Yet, this technique has the advantage that only the oval window is stimulated as opposed to the RW.

4.4.1.3 Experiments in the quasi-static regime

The setup used for the quasi-static measurements is suited to measure frequencies up to 0.02 kHz. From visual observation, it was found that the CFP moves as a piston in this frequency range. Because the nature of this measurement method is mechanical instead of optical, the force and piezo transducers are unable to keep up with the imposed oscillations at stimulus frequencies above 0.02 kHz. Also, phase information is missing with this technique. Values of the impedance magnitude in the gap

between 0.02 and 0.3 kHz can be predicted from the impedance models, as is shown in Figure 4.5 (a), and the quasi-static results deliver the stiffness component of the impedance measurements.

For the piezo stimulation, columellar displacement amplitudes of 50 μm were used, which is about two orders of magnitude above naturally occurring motions in response to acoustic stimulation in the ostrich (Arechvo et al., 2013). Because of the extremely small reaction forces involved, it was not possible to get reliable force measurements with smaller displacements. Using the measurements of sound-induced columellar movements presented by Arechvo et al. (2013), we can estimate that a CFP motion amplitude of 50 μm corresponds to a stimulation of approximately 128 dB SPL. It has however been shown (e.g., Aerts and Dirckx, 2010; Peacock et al., 2015a) that even at such high sound pressures the nonlinear response of the ear is still more than 40 dB below the linear response. Also in birds (Saunders, 1985), it was found that the response of the ME was linear up to 120 dB SPL, and likely for even higher stimulus levels. Therefore, the measured forces can be linearly normalized, so the use of (4.1) is justified.

4.4.2 Experimental results

4.4.2.1 Acoustic impedance analysis

The RLC models in Figure 4.5 that were used to fit the experimental data with intact IE, opened IE and IE impedance slightly overestimate the magnitudes in the quasi-static regime, but underestimate the acoustic-frequency data. We presume that this is due to the limited number of measurement samples in the quasi-static frequency range, resulting in a larger uncertainty. Nevertheless, the models mostly remain within the experimental standard deviations. For frequencies above 1–2 kHz, the models fail to describe the experimental impedance for intact IE and the IE itself. The magnitude and phase suddenly drop in this regime, which was also observed in humans (Merchant et al., 1996). Apparently, the impedance cannot be described by a purely inertial component in this frequency range.

The components of the model impedance were calculated for intact IE (C+IE), opened IE (C) and the IE itself (IE). The component values are $K_{C+IE} = 7.25 \cdot 10^{12} \text{ Pa/m}^3$, $M_{C+IE} = 0.952 \cdot 10^6 \text{ Pa} \cdot \text{s}^2/\text{m}^3$ and $R_{C+IE} = 2.02 \cdot 10^9 \text{ Pa} \cdot \text{s}/\text{m}^3$ for intact IE, $K_C = 7.05 \cdot 10^{12} \text{ Pa/m}^3$, $M_C = 0.300 \cdot 10^6 \text{ Pa} \cdot \text{s}^2/\text{m}^3$ and $R_C = 0.54 \cdot 10^9 \text{ Pa} \cdot \text{s}/\text{m}^3$ for opened IE, and $K_{IE} = 0.20 \cdot 10^{12} \text{ Pa/m}^3$, $M_{IE} = 0.652 \cdot 10^6 \text{ Pa} \cdot \text{s}^2/\text{m}^3$ and $R_{IE} = 1.57 \cdot 10^9 \text{ Pa} \cdot \text{s}/\text{m}^3$ for the IE itself. Presumably, K_{IE} is insignificant as the difference between intact and opened IE was negligible in the stiffness-dominated region of low frequencies. K_C mainly represents the impedance of the annular ligament, while M_C represents the combined inertial impedance of the magnet, the columella and the annular ligament.

The mechanical stiffness k_C of the annular ligament can be calculated from $k_C = K_C \cdot A_{\text{CFP}}^2$, with A_{CFP} the mean surface of motion of the CFP, resulting in 64.7 N/m.

Similarly, the total mechanical mass m_C with IE opened can be determined, yielding 7.54 mg. The magnet has a mass of 3 mg, so the mass of the ligament and the columella should be equal to 4.54 mg, corresponding to an inertial impedance of $0.181 \cdot 10^6 \text{ Pa} \cdot \text{s}^2/\text{m}^3$. μCT scans of the right ear in specimen 8 reveal that the mass of the bony columella is equal to 1.65 mg for a volume of 0.749 mm^3 and mass density of $2.2 \cdot 10^3 \text{ kg}/\text{m}^3$ (data not shown). Therefore, 2.89 mg remains, which may be attributed to the annular ligament and hydration of the tissue. For M_{C+IE} the contribution of the magnet is also subtracted, yielding $0.833 \cdot 10^6 \text{ Pa} \cdot \text{s}^2/\text{m}^3$.

For M_{IE} the mechanical mass is found to be $m_{IE} = 16.4 \text{ mg}$, which is supposed to represent the mass of the fluid in the IE. This time, the mass of the magnet is not subtracted because it was already excluded when subtracting Z_C from Z_{C+IE} . The total mass inside the IE was estimated to be 111 mg from 3D scans of an ostrich head (Witmer and Ridgely, 2008) with a total IE volume of 111 mm^3 and an assumed fluid density of $10^3 \text{ kg}/\text{m}^3$. This value is 6.8 times larger than the measured value, indicating that only a small portion of the fluid in the IE influences motions of the columella. The sound input and exit of the IE via the oval window and round window only pass through the perilymphatic spaces of the IE (Manley, 1990a) which only comprise a fraction of the total IE volume. This partially explains the difference in the measured and estimated values of the inertial component of the IE impedance.

4.4.2.2 Comparison with measurements in mammals

The acoustic input impedance of the IE was studied previously in mammals, based on theoretical considerations (e.g., Zwislocki, 1962, 1965, 1975; Kringelbotn, 1988; Puria and Allen, 1991) and direct and indirect experimental data. These experiments include measurements on human (Merchant et al., 1996; Puria et al., 1997; Aibara et al., 2001; Puria, 2003; Nakajima et al. 2009), guinea pig (Dancer and Franke, 1980), cat (Lynch et al., 1982), chinchilla (Ruggero et al., 1990; Songer and Rosowski, 2007; Slama et al., 2010) and gerbil (Overstreet and Ruggero, 2002; Decraemer et al., 2007; de La Rochefoucauld et al., 2008). Measurements in the ostrich in this study show that the ostrich IE impedance is much smaller than what is found in each of these mammals. The magnitudes found in this study are in the order of 10^9 – $10^{10} \text{ Pa s}/\text{m}^3$, while in mammals the impedances were found to be one to two orders of magnitude higher (de La Rochefoucauld et al., 2008). In Merchant et al. (1996), the impedance components of the human cochlea were found to be $K_{C+IE} = 326 \cdot 10^{12} \text{ Pa}/\text{m}^3$ and $R_{C+IE} = 72 \cdot 10^9 \text{ Pa} \cdot \text{s}/\text{m}^3$ for intact IE ($C = \text{stapes}$ and $IE = \text{cochlea}$ in that study; M_{C+IE} was not considered), and $K_C = 219 \cdot 10^{12} \text{ Pa}/\text{m}^3$, $R_C = 5.7 \cdot 10^9 \text{ Pa} \cdot \text{s}/\text{m}^3$ and $M_C = 543 \cdot 10^6 \text{ Pa} \cdot \text{s}^2/\text{m}^3$ for drained IE. When comparing each individual component of the measurements in human to our results, it can be concluded that the components are consistently and considerably smaller in the ostrich ear.

At low frequencies, the difference between intact and opened IE is almost negligible, as can be deduced from Figure 4.4 (a) and Figure 4.5 (a). This is different from what is

found in mammals (e.g., Merchant et al., 1996), in which a small but detectable difference was found between the two conditions. This might be explained by a difference between mammals and birds in the area ratio of the round window to the oval window; the round window membrane is assumed to determine the stiffness reactance of the IE, but because in birds it has a much larger area than the oval window its contribution to the acoustic IE impedance is negligible.

4.4.2.3 Comparison with measurements in birds

So far, the static and dynamic motions of the avian ME have been measured in only a few species, using various techniques. The first study was performed by Gaudin (1968) who photographed vibrations of the columella using unspecified positive and negative pressures applied at the TM and observed rotational motions. Saunders and Johnstone (1972) measured the acoustic response of the TM and CFP in the Barbary dove using Mössbauer spectroscopy, while Saunders (1985) used a capacitive probe to compare the acoustic response at the TM of the chicken, pigeon, parakeet, canary and cowbird, and found a good correspondence between the audibility curves of the animals and their TM velocity responses. The latter study also reported quantitative information of ME anatomy of these species based on electron microscopy.

Gummer et al. (1989a) measured TM and CFP responses in the pigeon with the Mössbauer technique to determine the transformer ratio of the ME. In their companion paper (Gummer et al., 1989b) the CFP response was measured with intact IE, fenestrated IE and drained IE. With intact IE, they observed sharp or broadly tuned antiresonances in the CFP response at higher frequencies that exhibited positive slopes in the velocity phase. This behavior was assigned to the presence of a reflected wave in the IE that originates from motions of internal structures such as the basilar membrane. This wave would introduce an additional vibration mode that interferes with the presumed piston-like vibrations of the CFP. Also in our study, certain samples in Figure 4.2 (a) contain broad peaks in the magnitude of the impedance above 2 kHz (i.e., local minima in the velocity magnitude) with negative impedance phase slopes (i.e., positive velocity phase slopes) that are only observed with IE intact. This observation might indicate the presence of a similar mechanism in the ostrich IE.

The quasi-static motions of the ME were studied in the gull, pigeon, gannet and pheasant (Mills and Zhang, 2006; Mills et al. 2007). In these species, it was found that large static pressures at the TM are converted into a rocking displacement at the CFP to avoid excessive piston-like displacements into the scala vestibuli, thus serving as a protective mechanism. In the ostrich, the quasi-static and dynamic motions of the CFP under acoustic stimulation of the TM were measured by Arechvo et al. (2013) with LDV. In the acoustic frequency range, they found peak displacements between frequencies of 0.4 and 0.5 kHz with IE intact, which is similar to our findings with magnetic stimulation of the columella. Furthermore, LDV was used to measure the

internal coupling of MEs in starlings (Klump and Larsen, 1992), quails (Larsen and Popov, 1995), budgerigars (Larsen et al., 2006) and owls (Kettler et al., 2016) in the framework of directional hearing.

In future, the knowledge of the IE impedance in the ostrich that was acquired with this study will be used in FE analyses to examine the influence of the IE on columellar vibrations under acoustic stimulation of the TM. So far, the mechanical properties of the avian ME have only been studied with a rigid-rod model of the swiftlet ear (Thomassen et al., 2007) and with a FE model of the duck ME that was validated with vibration measurements (Muyshondt et al., 2016a; Chapter 3 of this thesis). Nevertheless, both studies did not include experimental information of the acoustic IE impedance. On the other hand, the quantitative information of the IE impedance that was obtained will be utilized to investigate sound power flow through the TM and the ME structures.

4.4.2.4 *Scaling to smaller bird species*

Generally, the acoustic input impedance of the IE is inversely related to the size of the IE. This is observed when comparing measurements of the cochlear input impedance in human to smaller mammals (de La Rochefoucauld et al., 2008). Theoretically, this observation can be explained by dividing the acoustic impedance into three components: stiffness, damping and mass. The (mechanical) mass m of an object is proportional to its volume or the 1D size x to the power three ($m \sim x^3$). The relation between the mechanical impedance z and the acoustic impedance Z and is $z = Z \cdot A^2$, with A the surface area of the CFP. If we assume that A scales together with the size of the IE, we obtain for the acoustic mass M that $M \sim 1/x$. Thus, the mass component of the acoustic impedance is inversely proportional to IE size. Similarly, for the stiffness component K we can estimate that $K \sim 1/x^3$ and for the damping component R that $R \sim 1/x^2$ under certain assumptions (Lynch et al., 1982). Therefore, the acoustic IE impedance is presumably larger in smaller birds. For instance, the Muscovy duck has an IE volume of 38 mm³ and a CFP surface area of 1.62 mm². For chickens, the IE volume is 32 mm³ and the CFP surface area is 1.42 mm² (obtained from μ CT data). Using these geometric relations, we can estimate that the mass component of the acoustic IE impedance in ducks would be 1.2 times larger than in the ostrich, while in chickens it would be 1.3 times larger. By extrapolation, one could expect that smaller bird species may also show higher IE impedances than the ostrich.

4.5 Conclusion

Measurements of the vibrations of the columella allowed us to determine the acoustic input impedance of the IE in the ostrich for frequencies between 1 Hz and 4 kHz. Due to experimental constraints, a gap is present in the data between 0.02 and 0.3 kHz. The mean values of the impedance measurements were fitted by means of a simple RLC model in series, resulting in a stiffness reactance of $K_{IE} = 0.20 \cdot 10^{12}$ Pa/m³, an

inertial impedance of $M_{IE} = 0.652 \cdot 10^6 \text{ Pa} \cdot \text{s}^2/\text{m}^3$ and a damping resistance of $R_{IE} = 1.57 \cdot 10^9 \text{ Pa} \cdot \text{s}/\text{m}^3$. These values are one to two orders of magnitude smaller than what is found in mammal ears. Measurements of the acoustic IE impedance revealed that at low frequencies, the difference of the impedance with intact and opened IE is negligible, suggesting that the round window does not contribute to the stiffness reactance. At high frequencies, we found that the IE impedance cannot be described by a purely inertial component. The inertial impedance of the IE fluids is found to be smaller than total inertia inside the IE.

CHAPTER 5 QUASI-STATIC AND DYNAMIC COLUMELLA FOOTPLATE MOTION IN OSTRICH

Abstract

The nature of the motion of the columella is still a matter of ongoing debate. Some sources propose that the columella performs largely longitudinal or piston-like motions, while others claim that rotating or rocking motions dominate. In this chapter, motions of the CFP were investigated experimentally and by means of FE modeling. In Chapter 4, the acoustic impedance of the IE was determined in the ostrich. In order to examine the influence of this impedance on CFP motion in the current chapter, we again focused on the ostrich. Quasi-static motions were measured with μ CT under positive and negative pressure of the MEs, and dynamic motions were measured with LDV and stroboscopic holography under acoustic stimulation of the TM. For quasi-static loads, the CFP performed largely piston-like motions under positive ME pressure, while the difference between piston-like and rocking motion was smaller under negative ME pressure. For dynamic loads, CFP motion was piston-like for frequencies below 1 kHz. The behavior was more complicated at higher frequencies, showing an increase of rocking motion. The IE load in the model further increased the rocking motion relative to the piston-like motion in this frequency range.

This chapter is based on:

Muyshondt, P.G.G., Claes, R., Aerts, P., Dirckx, J.J.J., 2018. Quasi-static and dynamic motions of the columellar footplate in ostrich (*Struthio camelus*) measured ex vivo. *Hear. Res.* 357, 10–24. doi:10.1016/j.heares.2017.11.005.

5.1 Introduction

Up till now, there has been uncertainty about the type of motions that the single ossicle in the ME of birds, the columella, performs under quasi-static and dynamic pressure loads of the TM. For dynamic loads, the nature of this motion is crucial as it determines the impedance matching function of the ME and because vibrations of CFP form the effective input to the IE. For quasi-static loads, the displacements are important as they contribute to ME pressure regulation. Currently, there are two conflicting theories regarding this motion.

The first theory, which was first proposed by Pohlman (1921) based on considerations of ME anatomy in the chicken, describes that rotations of the cartilaginous extracolumella, caused by TM displacements at the tip of the extrastapedial process where the extracolumella attaches to the TM, are converted into piston-like motions at the CFP. According to Pohlman (1921), this conversion takes place by relative rotation of the extracolumella and columella at the intracolumellar joint, functioning as a hinge. Norberg (1978), on the other hand, explained the origin of piston-like motion as follows: “The intracolumellar joint rotates about the axis of rotation of the extracolumella located at the rim of the TM. The outer end of the shaft of the columella thus moves along the arc of a circle centered at this axis. The spatial relations are such that a line from the extracolumella’s axis of rotation to the intracolumellar joint is about normal to the long axis of the extrastapedial process and columella. At small vibrations set up by sound, vibration of the joint then occurs essentially along the line of the axis of the columella. This is the geometry that calls for the least possible deformation of the joint.” Also Manley (1990b) expressed that the conversion of extrastapedial process rotations to piston-like CFP motions doesn’t take place by relative rotation at the intracolumellar joint, but within the flexible extracolumella itself.

The second theory, as proposed by Gaudin (1968), states that the columella doesn’t move longitudinally as a piston but rather side to side, which goes along with a rocking motion of the CFP rotating around the posterior edge of the oval window. Gaudin (1968) compared this motion of the CFP to “a musician’s foot tapping as it rests on the heel”. This proposal is based on visual observation of the columella under low-frequency high-pressure stimulation on the TM in samples of different species. According to the author, this movement occurs because of (1) the acute angle between the shaft of the columella and the TM plane, (2) the out-of-center attachment of the columellar shaft to the CFP, and (3) the asymmetrical anatomy of the annular ligament of the columella being widest at the anterior edge of the CFP.

Quasi-static and dynamic motions of the columella can be studied by investigating motions of the CFP. In humans and other mammals, motions of the stapedial footplate have been measured extensively using various approaches. In those studies,

it was found that the footplate performs mainly piston-like motions at low and mid frequencies, while at high frequencies the motions become more complicated, including an increase of the rocking components. In birds, out-of-plane CFP motions were measured for the first time in the Barbary dove using Mössbauer spectroscopy (Saunders and Johnstone, 1972). Later, Gummer et al. (1989b) used this technique to examine vibration modes of the CFP in the pigeon by comparing measurements of CFP response obtained under different angles. Their measurements implied the existence of additional vibration modes at higher frequencies alongside the presumed translational vibration mode. In the current study, motions of the CFP are investigated in the common ostrich. The choice for the ostrich is mainly inspired by the large ear size, which makes it more practical to measure certain mechanical properties of the single-ossicle ear when compared to smaller birds. The anatomy and mechanics of this ear have been examined in previous studies (Frank and Smit, 1976; Saiff, 1981; Starck, 1995; Vallejo Valdezate et al., 2007; Arechvo et al., 2013; Muyshondt et al., 2016b; Chapter 4 of this thesis), and it was proposed as a suitable model for total ossicular replacement prostheses in humans (Arechvo et al., 2013). In the present paper, quasi-static motions of the columella are studied with μ CT under static pressure of the MEs. Dynamic motions are investigated with digital stroboscopic holography to determine the full-field 1D out-of-plane displacement map of the CFP, and single-point LDV is used to determine the 1D frequency response on multiple locations of the CFP with a denser frequency resolution.

It has been shown that the load of the IE can affect footplate displacements in mammals, e.g., in cats (Allen, 1986) and in humans (Hato et al., 2003). The same was observed in one avian species, i.e., the pigeon (Gummer et al., 1989b). For this reason, measurements of footplate motion are usually performed with intact IE via the lateral side of the footplate. Unfortunately, the major surface area of the CFP in birds is inaccessible from outside as the columellar shaft runs through a narrow passage of the ME cavity, behind which the CFP is located. To keep the ME intact, measurements in this study are performed on the CFP from the medial side after opening and draining the IE, as was done on human ears (von Békésy, 1960; Kirikae, 1960). To study the influence of the intact IE on dynamic columellar motions, a 3D FE model of the ME is created that includes the IE load of the ostrich (Muyshondt et al., 2016b; Chapter 4 of this thesis). The outcome of the model is compared to the experimental results and used to predict CFP vibratory motion in the presence of an intact IE.

5.2 Materials and methods

5.2.1 Quasi-static motion

5.2.1.1 Sample preparation

Five adult ostrich heads (O1–O5) of animals with ages between fourteen and eighteen months were obtained from an ostrich farm and stored refrigerated at a temperature

of 5°C in a plastic bag for no more than five days before measurement. The ears were not stored frozen and thawed before measurement as this may result in a slightly modified ME response (Ravicz et al., 2000). Before preparing the samples for measurement, the TMs were visually inspected from the side of the external auditory meatus and they were found to be still hydrated. To put the ears under positive and negative static pressure, a custom-made pressure generator was used that was connected to the intracranial air space of the skull via a needle probe (0.8 mm diameter) inserted in the caudal side of the cranium. The intracranial air space forms a complex network of canals and air cells inside a large part of the skull, and is connected to both MEs pneumatically (Larsen et al., 2016). By putting the intracranial air space under a certain pressure, both MEs are put under the same pressure. To prevent tissue dehydration following the sample preparation procedure, the heads were covered with water-soaked paper during one night until right before measurement.

5.2.1.2 *Micro-computed tomography*

The ostrich heads were scanned at the UGCT using the High Energy CT Optimized for Research (HECTOR) scanner (Masschaele et al., 2013). The pressure generator that was used to maintain a specific pressure in the ears during scanning contains two air pumps (RENA Air 400, Aquarium Pharmaceuticals Inc., Chalfont, PA, USA) which, respectively, generate an over- and underpressure of 4 kPa in two plastic barrels. The barrels have the function of capacitors, suppressing pressure pulses from the pumps. Each barrel is connected to a regulated electromagnetic valve (Valve regulator Type 1093, Bürkert, Ingelfingen, Germany), which can open proportionally to a driving signal. The over- and underpressure delivered by these valves is connected in parallel to the output of the device, and the pressure at this output is measured by a calibrated pressure transducer (SCX01DN, Honeywell, Morris Plains, NJ, USA). A custom-built feedback circuit controls the signal going to the valves so the output pressure is maintained at the preset value. Because the system behaves as a current source, it can maintain this specified pressure level even in the presence of leaks. The pressure generator was located in the same room as the scanner, but it was not put inside the scanner together with the specimen. A flexible tube delivered the pressure from the device to the sample. The tube was flexible enough so it could twist over 360° during scanning without disturbing the specimen. Both ears were included in the field of view of the detector, so the quasi-static 3D deformation of both MEs could be captured. The MEs were consecutively put under zero static pressure, positive static pressure (+1 kPa) and negative static pressure (-1 kPa) and scans were made for each state. To record the MEs under zero static pressure, the pressure generator was disconnected from the needle probe in the skull. Before each scan, a waiting time of at least two minutes was introduced after putting the sample under pressure, so that any initial displacement or deformation could be released before the start of the scan. The

scanner made use of a cone beam with 360° image acquisition and an X-ray tube voltage of 160 kV. The scan time for each scan was 21 minutes. The image size of the resulting data sets was 997 × 997 × 830 pixels, each with a voxel size of 128 μm.

5.2.1.3 Image analysis

A semi-automatic image segmentation method was performed in Amira 6.2 (FEI, Hillsboro, OR, USA) to reconstruct the columella, extracolumella and IE from the scans in the different pressure states. To analyze and compare the ME deformation of the three pressure conditions, surface models of the reconstructed structures of the three data sets were realigned such that the surface models of the IE of the three data sets were overlapped the best. The overlapping was performed using a built-in function of Amira based on an iterative closest-point algorithm. Subsequently, several components of columellar motion were determined: the displacement of the center point of the CFP u_C (related to piston-like motion of the CFP); the rotational angle of the columella θ (related to rocking motion of the CFP); and the so-called rocking-to-piston ratio r , which is a measure of rocking motion relative to piston-like motion of the CFP (Heiland et al., 1999). Because no in-plane CFP translations were observed with the current resolution of the scans, u_C effectively coincided with the piston component of the CFP (i.e., the component of displacement of the CFP center point in a direction normal to the plane of the CFP). CFP rotations consistently occurred around a single axis close to the anterior-posterior direction. Therefore, the rocking-to-piston ratio for rotations around this axis is defined as

$$r = \left| \frac{u_S - u_I}{2u_C} \right| = \frac{d|\theta|}{2|u_C|} \quad (5.1)$$

In this equation, u_S and u_I are the displacement phasors on the edges of the CFP on approximately the superior and inferior side, respectively, d represents the distance between the edges, and θ is the rotational angle around an axis in approximately the anterior-posterior direction. Note that the rotational axis and the axis along which the distance d was measured did not coincide with the long and short axis of the CFP, respectively. The angle θ was calculated based on the rotation of the lateral end of the columellar shaft relative to the CFP center point, which is a valid approach if the shaft of the columella behaves as a rigid body. The absence of deformation in the columella was verified by aligning the reconstructions of the columella in the pressurized state to the corresponding reconstructions in the zero pressure state. Overlapping was performed using the same built-in function of Amira that was used to align the IEs. Visual inspection of the overlapped columellae did not reveal any deformations for the current resolution of the scans.

5.2.2 *Dynamic motion*

5.2.2.1 *Experiments*

5.2.2.1.1 *Sample preparation*

Six additional ostrich heads (O6–O11) from animals with ages between fourteen and eighteen months were obtained from an ostrich farm. They were stored frozen at a temperature of -20°C immediately after death. Prior to measurement, the heads were left to thaw for sixteen hours at a temperature of 5°C in a plastic bag. As mentioned, freezing and thawing can slightly change the ME response due to structural changes in the IE (Ravicz et al., 2000). Because the IE was drained for the experiments, this effect could be excluded. To expose the medial surface of the CFP, the caudal side of the head was removed using a bandsaw without damaging the ME structures, and the IE was drilled via the medial wall and drained thoroughly. All ME structures were left intact, including the ME muscles.

5.2.2.1.2 *Laser Doppler vibrometry*

The piston-like and rocking motions of the CFP were measured with single-point LDV by measuring the 1D velocity response on different points of the CFP. To achieve this, miniature pieces of reflective foil with a size of $0.4\text{ mm} \times 0.4\text{ mm}$ and a mass of less than 0.04 mg were positioned on the edges of the long and short axis of the CFP, i.e., on the inferior and superior side for the short axis and on the anterior and posterior side for the long axis. Some manual interpretation was needed to obtain two mutually orthogonal axes that more or less coincided with the longest and shortest edge of the CFP. An additional patch was placed in the center of the CFP on the intersection point of both axes at halfway their length. The mass of each reflective patch is about 1% of the columellar mass (3.88 mg), assuming a mass density and volume of the ossicle as used in the model (see Section 5.2.2.2). ME vibrations were induced by acoustic stimulation of the TM using a speaker placed at the entrance of the external auditory meatus. In front of the speaker, a pre-calibrated probe-tube microphone (Brüel & Kjør, Probe Microphone Type 4182, Nørum, Denmark) was positioned to record the SPL. The speaker and microphone were sealed in the external auditory meatus using modeling clay (Dreve Otoplastik, Otoform Ak, Unna, Germany). Stepwise pure-tone sinusoidal signals from 0.125 to 4 kHz , with at least eight frequencies per octave and a sample rate of 48 kHz , were sent to the speaker through a custom-made amplifier. The range of the frequency sweep corresponded to the auditory range of the emu (Manley et al., 1997), which is the species found in literature most closely related to the ostrich. At the entrance of the external auditory meatus, the SPL was recorded in a first step and corrected to 90 dB SPL for all frequencies in a second step. A LDV system (OFV-534 sensor head and OFV-5000 controller, Polytec, Waldbronn, Germany) that was mounted on a surgical microscope (Carl Zeiss, OPMI Sensera/S7, Jena, Germany) was used to measure the induced vibration velocity of the CFP. The beam of the laser was pointed perpendicularly to

the CFP surface (approximated through microscopic view) to measure the out-of-plane motions. The sound and vibration signals were recorded at the same sample rate as the input signal delivered to the speaker. To obtain correct phase information of the stimulation and response signals, phase delays in the setup were taken into account. These delays include the distance between the TM and the microphone at the entrance of the external auditory meatus, and the time delays set by the electronic devices. Signal generation and collection was performed using a 16-bit data-acquisition board (National Instruments, USB-6251 BNC, Austin, TX, USA) that was operated in Matlab (Mathworks, Natick, MA, USA). The steady-state magnitude and phase response of the signals at the excitation frequencies were obtained by means of a standard Fourier-analysis procedure. The measurements were gathered within five minutes per sample.

5.2.2.1.3 Digital stroboscopic holography

To obtain direct full-field out-of-plane displacement information of the CFP, digital stroboscopic holography was used to measure the vibration response of samples O6R and O7L at a selection of stimulus frequencies. The CFP was coated with a thin layer (~ 0.1 mm) of white make-up liquid (Aquacolor Soft Cream – White Wet Make-up, Product Code 01129/00, Kryolan, Berlin, Germany) to enhance diffuse light reflectivity. This coating gave the best combination of reflectivity, ease of application and delay of dehydration. The system was again stimulated acoustically via the TM using a speaker positioned at the entrance of the external auditory meatus, in front of which the SPL was recorded with a probe-tube microphone (Probe Microphone Type 4182, Brüel & Kjær, Nærum, Denmark). The camera that was used to record the displacement map was positioned perpendicularly to the medial CFP surface to capture the out-of-plane displacements. Displacement maps were recorded for stimulus frequencies from 0.05 to 4 kHz, with two frequencies per octave and for sound pressures between 70 and 100 dB SPL. For each stimulus frequency, the displacement magnitude and phase were calculated from the recorded displacement frames at eight phase instants in one vibration period. More details about digital stroboscopic holography can be found in e.g., Cheng et al. (2010, 2013) and Khaleghi et al. (2013) for a description of the technique, and in De Greef et al. (2014a) for a description of the experimental setup. The measurements were gathered within five minutes per sample.

5.2.2.2 Finite-element modeling

5.2.2.2.1 Morphology

The geometry of the model is based on the μ CT scan of a dissected left ostrich ear (O12L) from an animal that was eighteen months old. This ear was also scanned with the HECTOR scanner of the UGCT (Masschaele et al., 2013). To enhance contrast between the different soft tissue structures in the ME, the sample was stained in a daily refreshed 2.5% PTA solution in purified water for 48 hours before the scan. This solution resulted in the least amount of soft tissue shrinkage in a study of Buytaert et

al. (2014), with a linear shrinkage of 3.6%. The scans made use of a cone beam with 360° image acquisition. The image size of the resulting data sets was $1000 \times 1000 \times 840$ pixels with a voxel size of $43 \mu\text{m}$. Again, semi-automatic image segmentation was performed in Amira 6.2 (FEI, Hillsboro, OR, USA) to identify the different ME components. The segmented data set was converted into a surface model built up of triangles. This surface was exported under the STL format that could be imported into FE software (COMSOL Multiphysics 5.2a, Burlington, MA, USA). In Figure 5.1, the 3D geometry of the surface model is shown: the structures of the external auditory meatus, ME cavity and IE were excluded from this geometry.

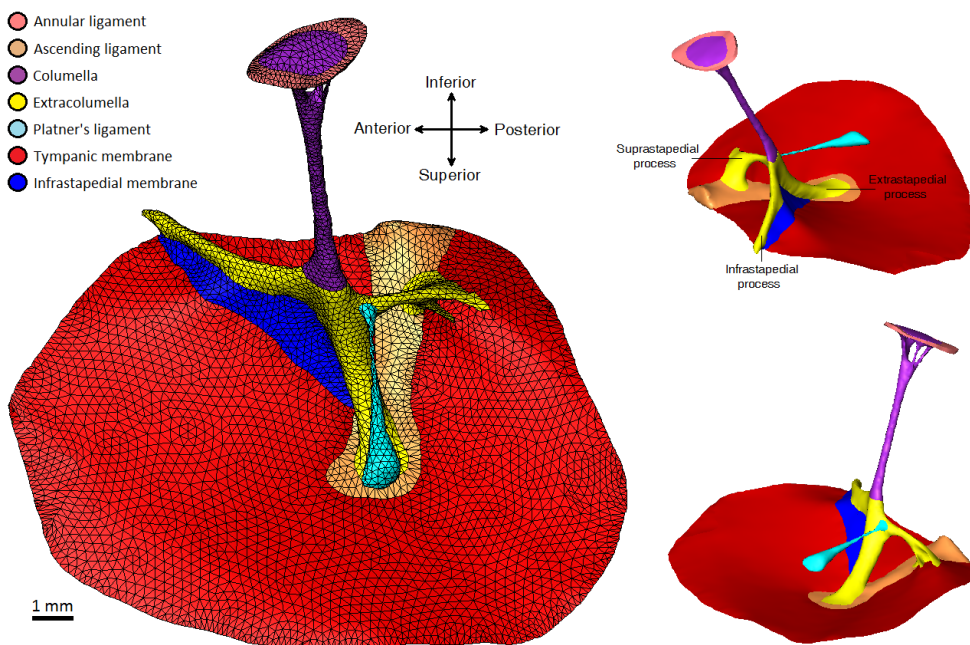


Figure 5.1. 3D surface model of the left ostrich ME of specimen O12 used as geometry for the FE model, shown in three different viewing directions. In the left panel, the different components of the ME are shown in the color legend and the anatomical directions are indicated as well.

The surface model includes the following structures: the TM that is slightly conical with the tip pointing into the external auditory meatus; the bony columella bounded by the annular ligament in the oval window; the cartilaginous extracolumella that consists of three arms: the infrastapedial, the extrastapedial and the suprastapedial processes, of which the infrastapedial process ends at periphery of the TM and the extrastapedial process in the conical tip of the TM; a membrane that spans the foramen between the TM and the infrastapedial and extrastapedial processes, which will be called the infrastapedial membrane; the ascending ligament that runs into the middle layer of the TM forming a string of collagen fibers; and Platner's ligament, which runs from the extracolumella to the otic process of the quadrate at the ME cavity wall. The stapedial and paratubal muscles as described by Starck (1995) were

not included in the model. The reason is that, without considering the specific case of muscle contraction, the muscles presumably only influence columellar motion through the boundary conditions of the TM, as they are attached to the TM periphery.

5.2.2.2.2 Model description

The TM was modeled using triangular shell elements. The nonuniform thickness distribution of the TM was defined onto the shell elements, and was calculated from the μ CT images of the same specimen (O12L) using the shortest-distance algorithm described in Van der Jeught et al. (2013). Figure 5.2 (a) shows the thickness distribution of the TM, from which the ascending ligament was excluded. In the bottom part of Figure 5.2 (a), the thickness map displays an area of increased thickness, which corresponds to the attachment location of the ME muscle (Starck, 1995). Note that the thickness in the figure is shown with saturation at 200 μm to make the thickness distribution on the TM more apparent. The maximal thickness near the attachment of the muscle is 607 μm , though it shows as 200 μm in the figure. The thickness distribution of the annular ligament is shown in Figure 5.2 (b). Platner's ligament was modeled using beam elements with a cylinder diameter of 125 μm , taking into account bending and torsion alongside contraction and elongation. All other structures in the geometry were modeled using tetrahedral solid elements. Beams, shells and solids shared translational and rotational degrees of freedom at their respective connections. The intracolumellar joint was modeled as a viscoelastic component on the joined nodes of the columella and extracolumella. This component decouples the motions between both sides of the boundary, which are connected by forces with equal size but opposite direction. The connective forces have an elastic and dissipation component and are defined by $F_C = -F_E = -k(1 + i\eta)(u_C - u_E)$, with F_C and F_E the force vectors on the columella and extracolumella side of the connection, respectively. The variables u_C and u_E are the corresponding displacement vectors, k is the isotropic spring constant of the joint, and η is the damping loss factor.

As boundary condition, Platner's ligament was fully clamped at its outer end. The surface of the annular ligament boundary was fixed by setting the displacement of its nodes to zero. The periphery of the TM was modeled as hinged instead of fully clamped, as the TM of the ostrich is not directly surrounded by bone but with nonrigid soft tissue (Starck, 1995; Arechvo et al., 2013). Also the outer end of the infrastapedial process was not fixed, as its surrounding tissue allows for movement (Starck, 1995). To incorporate the load of the IE, the complex acoustic IE input impedance Z , as experimentally obtained in the ostrich (Muyshondt et al., 2016b; Chapter 4 of this thesis), was imposed on the medial surface of the CFP. Z was modeled as a uniform pressure load p normal to this surface using $p = Z \cdot U$, with U the complex volume velocity of the CFP and annular ligament in the oval window. This definition is based on the concept that mainly piston-like motion contributes to scala vestibuli pressure, which was shown by Decraemer et al. (2007) and de La

Rochefoucauld et al. (2008) in gerbil, following the idea that, in theory, rocking motion does not lead to a net fluid displacement and hence pressure.

The sound stimulus was modeled as a uniform harmonic pressure of 1 Pa (i.e., 94 dB SPL) to the lateral TM surface. Modeling was performed in the frequency domain to study the steady-state response at a series of excitation frequencies. A convergence analysis was performed to determine the mesh size and number of degrees of freedom of the model, which were chosen in such a way that the relative error in the CFP velocity response of two consecutive mesh sizes was smaller than 0.5%.

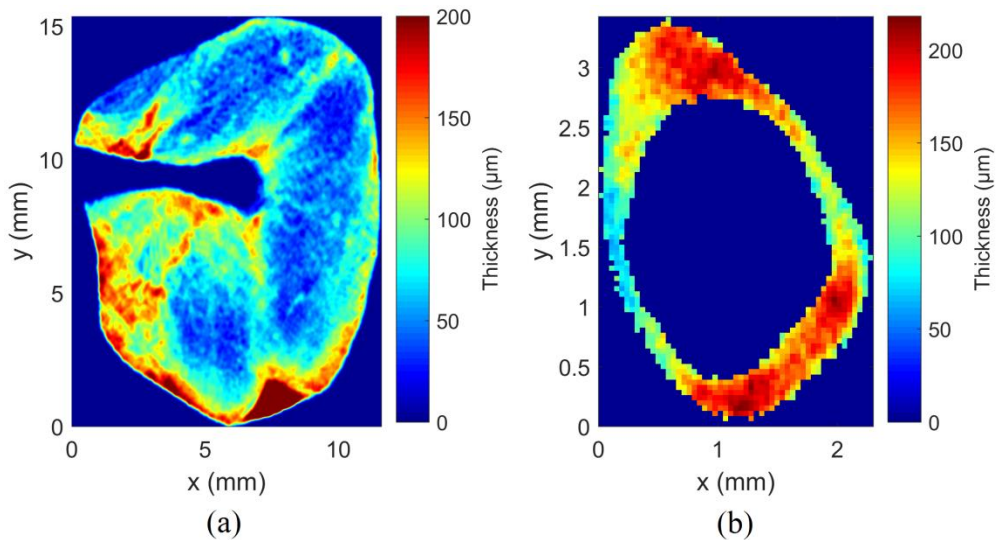


Figure 5.2. Smoothed thickness distribution of the left (a) TM and (b) annular ligament of specimen O12. The thickness distribution of the TM was defined onto the corresponding shell elements of the FE model.

5.2.2.2.3 Material properties

Constant, homogenous and isotropic Young's moduli E , Poisson's ratios ν , mass densities ρ and damping loss factors η were used for all structures, as listed in Table 5.1. Because quantitative information of material properties in the avian ME is largely lacking, parameter values were estimated, taken from ME models in literature, or adjusted within realistic bounds for the model to match most optimally with experimental data. The TM of the ostrich was modeled using isotropic elasticity parameters instead of an orthotropic description (e.g., Volandri et al., 2011) because preliminary investigations of the elastic fiber distribution of the TM could not detect a regular pattern of arrangement (Starck, 1995). The infrastapedial membrane was given the same parameter values as the TM. The extracolumella is made of hyaline cartilage that may ossify with age, which can drastically increase the stiffness, so the range of possible Young's moduli of the extracolumella is large. A value of 80 MPa gave a good match with experimental data. The ascending ligament is composed of collagen fibers that converge to form a string in the middle layer of the TM. Vallejo Valdezate et al.

(2007) described the ligament as solid and tense, which is the basis for the high Young's modulus of 80 MPa that was chosen. The Young's modulus of the columellar annular ligament E_{CAL} was calculated from the ligament's acoustic stiffness impedance in ostrich $K_{\text{CAL}} = 7.05 \cdot 10^{12}$ Pa/m³ (Muysshondt et al., 2016b; Chapter 4 of this thesis), using the expression of the annular ligament compliance subjected to a pure shear stress in Lynch et al. (1982):

$$E_{\text{CAL}} = \frac{3wA_{\text{CFP}}^2}{tp} K_{\text{CAL}}, \quad (5.2)$$

with $w = 0.39$ mm the average width of the annular space between the CFP and the oval window perimeter, $t = 0.14$ mm the average thickness of the annular ligament, $p = 8.79$ mm the perimeter of the oval window and A_{CFP} the surface area of the CFP. These geometrical parameters were inferred from the surface model. To compute A_{CFP} , the total surface area of the CFP was projected on the plane normal to the CFP piston axis, yielding a value of $A_{\text{CFP}} = 2.82$ mm². This value was multiplied with 1.65 to correct for the contribution of the annular ligament to the net volume velocity in the oval window (Muysshondt et al., 2016b; Chapter 4 of this thesis). All structures had the same Poisson's ratio and constant loss factor damping as a function of frequency, except for the columella having zero damping (e.g., De Greef et al., 2014b, 2017). The intracolumellar joint as defined in the current model requires a spring constant to describe its elastic properties instead of a Young's modulus and Poisson's ratio. This constant was chosen isotropic with a value of $2.25 \cdot 10^3$ N/m, which is based on estimations of the Young's modulus of the human incudostapedial joint (0.27 MPa) (Zhang and Gan, 2011; Maftoon et al., 2015) and on the thickness (~ 60 μm) and surface area (~ 0.50 mm²) of the ostrich intracolumellar joint. The damping loss factor of the joint was equal to 0.2.

Table 5.1. Material parameter values used in the FE model, including references for the Young's moduli. References: ^a Herrmann and Liebowitz (1972), ^b Thomassen et al. (2007), ^c Lynch et al. (1982), ^d Muysshondt et al. (2016b), ^e Kirikae (1960), ^f Maftoon et al. (2015), ^g De Greef et al. (2017). E , Young's modulus; ρ , mass density; η , damping loss factor; ν , Poisson's ratio. Parameters without reference were adjusted within realistic bounds for the model to match most optimally with experimental data.

| Component | E (MPa) | ρ (10^3 kg/m ³) | η | ν |
|-------------------------|----------------------|-------------------------------------|----------------|------------------|
| Columella | 14100 ^a | 2.2 ^e | 0 ^g | 0.3 ^g |
| Tympanic membrane | 8 | 1.1 ^f | 0.2 | 0.3 ^g |
| Infrastapedial membrane | 8 | 1.1 ^f | 0.2 | 0.3 ^g |
| Platner's ligament | 21 ^b | 1.1 ^f | 0.2 | 0.3 ^g |
| Annular ligament | 0.145 ^{c,d} | 1.1 ^f | 0.2 | 0.3 ^g |
| Ascending ligament | 80 | 1.1 ^f | 0.2 | 0.3 ^g |
| Extracolumella | 80 | 1.1 ^f | 0.2 | 0.3 ^g |

5.3 Results

5.3.1 Quasi-static motion

The results of the quasi-static experiments on specimens O1–O5 are summarized in Table 5.2. The table contains different components of CFP displacement under either positive or negative ME pressure of 1 kPa: the piston-like displacement u_C , the rotational angle θ and the rocking-to-piston ratio r . The final two rows show the mean and the standard deviation of the mean of each component. In Figure 5.3, the deformation of the columellar complex is shown for two illustrative specimens, O1 and O2.

Table 5.2. Components of quasi-static columellar motion in both ears of samples O1–O5 under positive and negative ME pressure. These components include the piston displacement u_C (mm), the rotational angle around approximately the anterior-posterior axis θ ($^\circ$) and the rocking-to-piston ratio related to rotations around this axis r . The two bottom rows show the mean $\langle x \rangle$ and the standard deviation of the mean $s_{\langle x \rangle}$ of each component.

| Sample | $p_{ME} < 0$ | | | $p_{ME} > 0$ | | |
|-------------------------|--------------|-----------------------|------|--------------|-----------------------|-------|
| | u_C (mm) | θ ($^\circ$) | r | u_C (mm) | θ ($^\circ$) | r |
| O1L | 0.30 | 4.9 | 0.27 | 0.24 | 1.0 | 0.07 |
| O1R | 0.30 | 3.6 | 0.24 | 0.27 | 2.0 | 0.15 |
| O2L | 0.23 | 0.5 | 0.04 | 0.27 | 2.4 | 0.16 |
| O2R | 0.29 | 0.7 | 0.04 | 0.24 | 3.1 | 0.23 |
| O3L | 0.20 | 10.2 | 0.89 | 0.37 | 1.1 | 0.05 |
| O3R | 0.18 | 7.3 | 0.67 | 0.34 | 1.1 | 0.05 |
| O4L | 0.06 | 13.9 | 3.79 | 0.24 | 3.0 | 0.22 |
| O4R | 0.07 | 12.9 | 3.02 | 0.27 | 2.0 | 0.12 |
| O5L | 0.17 | 9.6 | 0.89 | 0.21 | 0.2 | 0.02 |
| O5R | 0.17 | 7.7 | 0.87 | 0.21 | 0.3 | 0.03 |
| $\langle x \rangle$ | 0.197 | 7.1 | 1.07 | 0.226 | 1.62 | 0.110 |
| $s_{\langle x \rangle}$ | 0.028 | 1.5 | 0.41 | 0.017 | 0.33 | 0.025 |

For negative pressure, the CFP undergoes a displacement towards the medial direction as shown in the two top panels of Figure 5.3. At the same time, the extracolumella undergoes considerable bending in the extrastapedial process. For all samples, except for O2, a transverse displacement at the lateral end of the columellar shaft is observed towards the inferior direction that goes along with a rotation of the CFP, as shown for O1 in the top left panel of Figure 5.3. For O2 the situation is slightly different, as extracolumella rotation appears to be converted into a predominantly piston-like CFP motion. Great variation is observed for the rocking-to-piston ratio,

with a minimal value of 0.04 for O₂, indicating a largely piston-like motion, and a maximal value of 3.79 for O_{4L}, showing a predominantly rocking motion. For all other samples the ratio remains smaller than 1, indicating that the piston component is larger. However, for O₃ and O₅ a considerable rocking component is present as well.

For positive ME pressure, the 3D displacement of the columella looks similar for all samples. At the lateral end of the columellar shaft, a minor displacement towards the inferior direction is observed that is mostly smaller than for negative ME pressure, which is also noticed when comparing the bottom and top image in the left panel of Figure 5.3. Such a motion goes along with a CFP displacement that is slightly larger at the superior than at the inferior side. Rocking-to-piston ratios are smaller for positive than for negative ME pressure (except for O₂), with values that are much smaller than 1, showing that CFP motion is mostly piston-like. The out-of-plane displacement is on average larger for positive than for negative ME pressure.

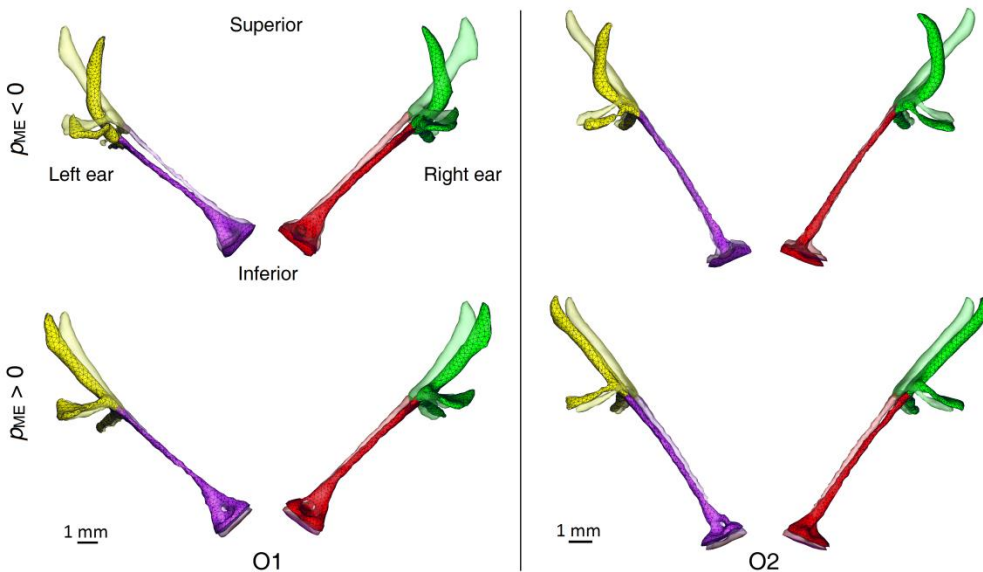


Figure 5.3. Posterior view of the quasi-static deformations of the columellar complex under negative (top) and positive (bottom) ME pressure for both ears of specimen O₁ (left panel) and O₂ (right panel). Transparent surfaces represent the undeformed state (with zero pressure) and opaque surfaces depict the deformed state (with positive or negative pressure). To distinguish the structures of the columella and the extracolumella, they are depicted in different colors.

5.3.2 Dynamic motion

5.3.2.1 Model validation

First, a convergence analysis was performed on the mesh of the FE model. The total number of degrees of freedom amounts to 187,824. Figure 5.4 displays the piston component of the CFP velocity magnitude resulting from the model, both with and without including the IE load. The results are compared to the average of the

measurements presented in Arechvo et al. (2013) on nine individual ostrich ears as reported with intact IE.

The average of the measurements is well represented by the model with IE load. The model matches well with the measurements for the low- and mid-frequency response up to 1 kHz. The magnitude peak occurs at 0.45 kHz for the model and at 0.47 kHz for the experimental average. The model contains small fluctuations at higher frequencies that are not seen in the mean of the experiments, which presents a smoother curve. However, individual experimental curves contain more variations as a function of frequency comparable to the model. The model stays within the experimental range for most frequencies, only around 1.2, 2.1 and 4 kHz it falls a little outside of this range. The response of the model without IE load has some characteristics different from the model with IE load, mostly at mid and high frequencies: magnitude values are higher without IE load beyond 0.4 kHz, including a sharper resonance at a frequency of 0.48 kHz.

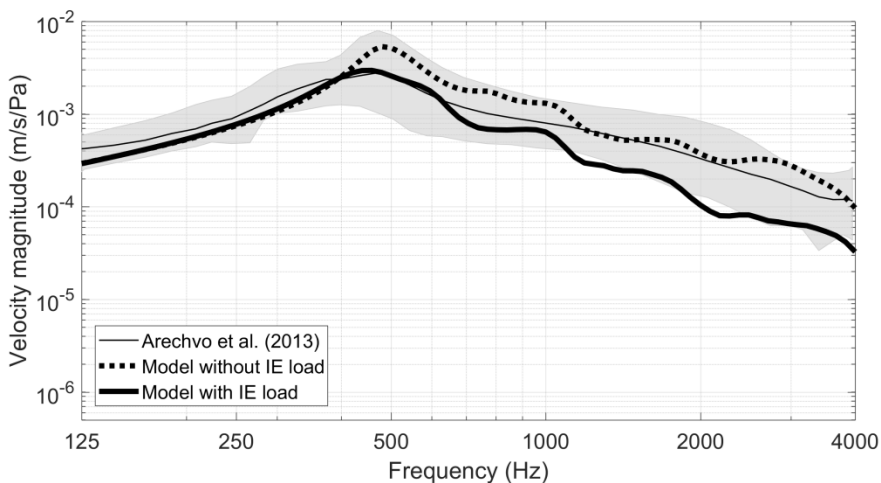


Figure 5.4. Piston component of the CFP vibration velocity magnitude (m/s/Pa) as a function of excitation frequency. The thin black line shows the mean of nine CFP displacement measurements converted to velocity (Arechvo et al., 2013). The gray band represents the measurement range. Bold black lines depict velocity magnitudes of the model with IE intact (solid) and IE drained (dashed).

5.3.2.2 Velocity response

In Figure 5.5, the magnitude and phase responses of the CFP velocity are shown for (a) the piston component, (b) the rocking component for rotation around the long CFP axis, and (c) the rocking component for rotation around the short CFP axis. The rocking component for rotation around the long (resp. short) axis is defined as the difference in complex numbers between the two edge velocities of the short (resp. long) axis of the CFP, divided by 2. For rotations around the long (resp. short) axis, the positive direction of rotation is given by the posterior (resp. superior) side of the

axis, as opposed to the anterior (resp. inferior) side. CFP responses are displayed for 7 measurement samples obtained with LDV and for the model without and with IE load. From here on, rocking components for rotation around the long and short axis of the CFP will be called long-axis and short-axis components, respectively.

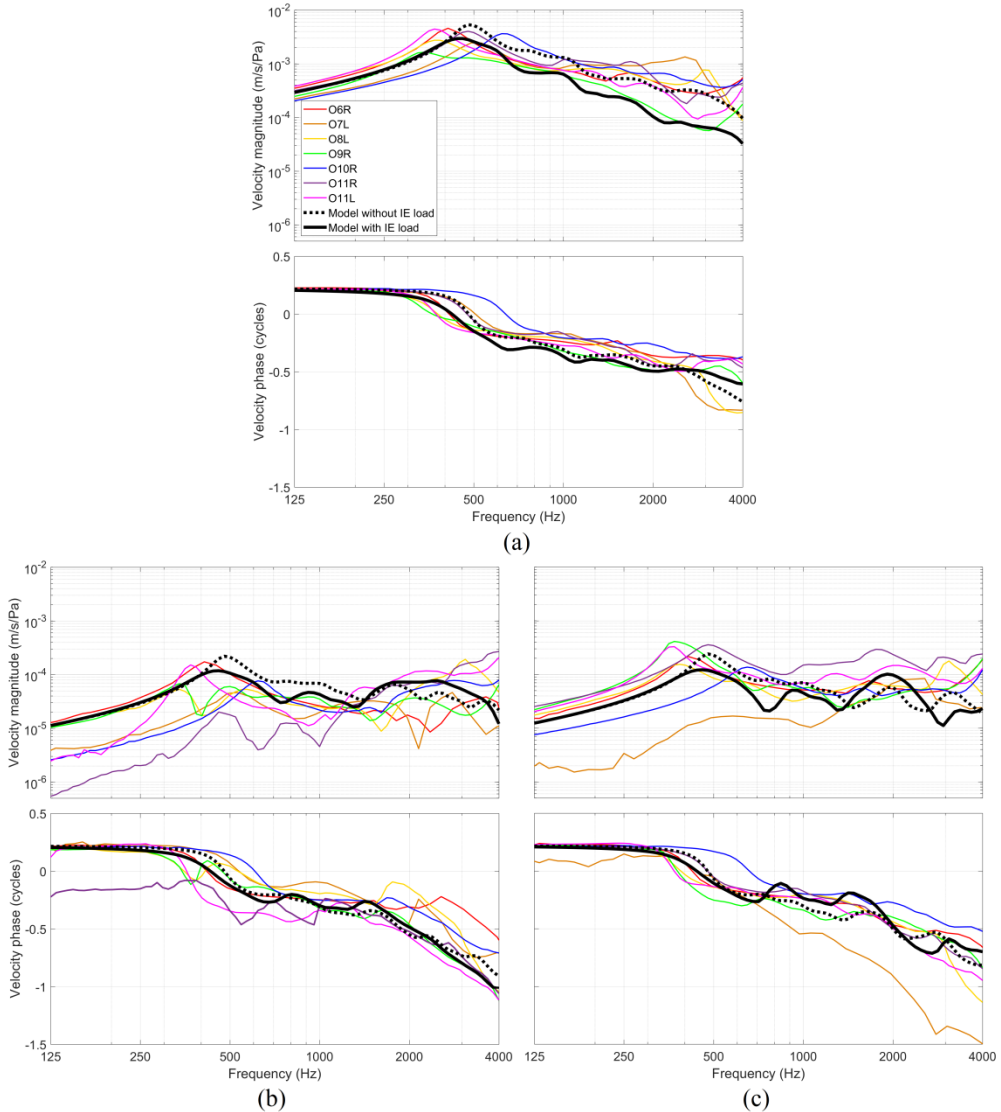


Figure 5.5. CFP velocity magnitude (m/s/Pa) and phase (cycles) as a function of frequency for (a) the piston component, (b) the rocking component for rotation around the long CFP axis (i.e., difference between two edge velocities of the short axis divided by 2), and (c) the rocking component for rotation around the short CFP axis (i.e., difference between two edge velocities of the long axis divided by 2). Velocities are shown for seven LDV measurements with drained IE (colored lines) and for the model without IE load (dashed) and with IE load (solid). Magnitudes are normalized to the stimulation pressure in the ear canal, and phases are taken relative to the phase of the incident pressure.

5.3.2.2.1 *Experimental results*

For the piston velocity in Figure 5.5 (a), we observe that there is considerable variability between different samples, which is also the case for the rocking components. For the piston component, the resonance frequency of the CFP response ranges between 0.34 and 0.62 kHz. The velocity magnitude remains smooth up until 1 kHz. Above this frequency, small and broadly tuned fluctuations become apparent in the decreasing velocity magnitude, and in two samples a second magnitude peak is observed around 3 kHz that goes along with a phase decrease of approximately half a period. For all other samples, the magnitude starts to increase above 3 kHz.

For the long-axis component, as shown in Figure 5.5 (b), we observe first of all that the magnitude is ten to hundred times smaller than the magnitude of the piston component. We also find that the long-axis component has a resonance at approximately the same frequency as the resonance of the piston component. In two specimens, a dip is observed within the peak of the resonance. Above the resonance frequency, the velocity magnitude decreases as a function of frequency, but starting from 1 kHz the magnitude begins to fluctuate and increase relative to the piston magnitude. For low and mid frequencies, phases are similar to the phase of the piston component. However, above 1 kHz the phase of the long-axis component decreases faster as a function of frequency, and it contains larger fluctuations than the piston phase. One specimen forms an outlier to the results of the long-axis component in the low-frequency range: the magnitude is very low and approaches the noise floor, while the phase differs half a period from the other measurements. However, above 1 kHz the velocity magnitude in this sample increases the most from all specimens, and the phase becomes comparable to the other measurements.

For the short-axis component, as depicted in Figure 5.5 (c), we also notice that the magnitude is ten to hundred times smaller than the contribution of the piston component. For most samples the low-frequency magnitude is higher than the magnitude of the long-axis component. The short-axis component also contains a resonance peak at a similar frequency as the piston component, and beyond this frequency the magnitude decreases up until 1 kHz. As was found for the long-axis component, the velocity magnitude starts to fluctuate and increase relative to the magnitude of the piston component above 1 kHz, while the phase decreases faster than the phase of the piston component. However, the increase of the magnitude as a function of frequency is more pronounced for the long-axis component. Also for the short-axis component there is one outlier to the results, different from the outlier of the long-axis component. This sample displays a very low magnitude at low frequencies, approaching the noise floor. Also the phase of this sample is lower than for the other measurements, decreasing faster as a function of frequency.

5.3.2.2.2 *Model results*

For the model without IE load we notice that the piston component lies within the range of measurements for most frequencies; only around the resonance it exceeds the experimental magnitude range between 0.44 and 0.57 kHz. Nevertheless, the resonance frequency of the model (0.48 kHz) lies within the range of measurements. Above 1 kHz, the model contains small and broadly tuned fluctuations in the decreasing velocity magnitude, which was also noticed for the measurements. The rocking components of the model mostly stay within the experimental range; only the magnitude of the long-axis component exceeds the measurement range between 0.44 and 1.25 kHz, while the magnitude of short-axis component underestimates the measurements between 2.1 and 2.8 kHz. However, the model is qualitatively similar to the experiments; the rocking components are considerably smaller than the piston component, and above 1 kHz they contain larger fluctuations and increase relative to the piston component. At low frequencies, the magnitude of the short-axis component is larger than the magnitude of the long-axis component, but only very little. The phase response of the model is very similar to most measurements.

For the model with IE load, the magnitude of the three velocity components is very similar to the model without IE load up to 0.4 kHz. For higher frequencies the magnitude is smaller with loaded CFP for the piston component, and around 0.46 kHz the model displays a resonance peak for all velocity components that is smaller and broader than with unloaded CFP. For both rocking components, the model shows a dip in the magnitude around 0.75 and 1.3 kHz that goes along with a small increase of the phase. The short-axis component has an additional magnitude dip near 3 kHz. Around 1.4 kHz, the magnitudes of the rocking components increase above the result of the model without IE load, but around 3.5 and 2.6 kHz they again decrease below the unloaded model result for the long-axis and short-axis component, respectively. Phase responses of the model without and with IE load are qualitatively similar. However, the phase decrease of half a period around the resonance evolves more slowly in the model with loaded CFP.

5.3.2.3 *Rocking-to-piston ratio*

Figure 5.6 displays the CFP rocking-to-piston ratio of the long-axis (top) and short-axis (bottom) components for the experiments with drained IE and for the model without and with IE load. For the model without IE load, we computed the effect of adding five mass loads to the CFP, representing the reflective patches, of which the result is also shown in the figure. Ratios were determined by dividing the magnitude of the rocking components by the magnitude of the piston component, which were presented in Figure 5.5, for the experiments and models respectively. In Figure 5.6, results of the ostrich are compared to the average of measurements in human with intact and drained IE for rotations around the long axis and short axis of the stapedial footplate (Hato et al., 2003). To quantify the change in CFP response of the specimens

over time, for instance due to dehydration, one specimen (O10R) was measured again fifteen minutes after the first measurement. The resulting effect on rocking-to-piston ratios was at the most 3.5 dB for all frequencies, but mostly less than 2 dB (data not shown).

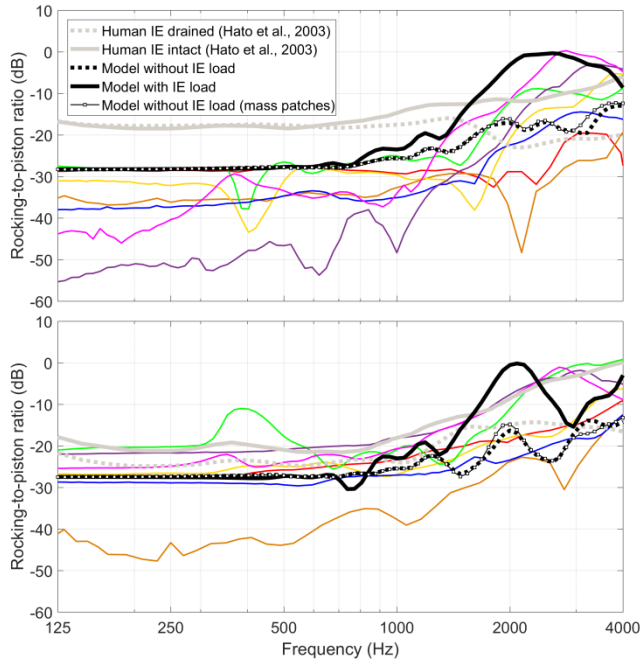


Figure 5.6. Components of the CFP rocking-to-piston ratio (dB) for rotations around the long axis (top) and short axis (bottom) as a function of frequency. Ratios are shown for the FE model (bold black lines) without IE load (dashed) and with IE load (solid) and for the LDV measurements (colored lines). Bold gray lines depict the average of human stapedial footplate measurements (Hato et al., 2003) with IE intact (solid) and drained (dashed).

5.3.2.3.1 Experimental results

For the long-axis component, as shown in the top panel of Figure 5.6, we observe that there is considerable variability between rocking-to-piston ratios, with a range of about 30 dB, as is the case for the individual velocity components. For low frequencies, the rocking-to-piston ratio mostly remains constant as a function of frequency, though in some samples a local dip or peak is apparent around the resonance frequency. The velocity of the long-axis component is at least 27.5 dB lower than the piston velocity, corresponding to a linear ratio of 0.042. In human, this value is on average -17 dB, or 0.14, for low frequencies with IE intact and drained. There is one outlier to the results, as for the long-axis component in Figure 5.5 (b), which displays a very low rocking-to-piston ratio down to -55 dB or 0.0018. Around 1 kHz, the rocking-to-piston ratio starts to increase for most samples, containing small fluctuations. In human, the ratio decreases on average with IE drained, but increases with IE intact. The ratio in ostrich never exceeds 0 dB; only one sample reaches a

value of 0 dB around 2.8 kHz. At the maximal frequency of 4 kHz, the rocking-to-piston ratio ranges between -24 dB and -4 dB, or 0.063 and 0.63 respectively.

The rocking-to-piston ratio of the short-axis component, depicted in the bottom panel of Figure 5.6, also shows considerable variability. At low frequencies, the ratio of the short-axis component remains mostly constant, and values are larger than the ratio of the long-axis component for most specimens. The short-axis component is at least 20 dB lower than the piston component, or a linear ratio of 0.1. In human, rocking-to-piston ratios are higher for rotations around the long axis than for rotations around the short axis at low frequencies. One of the ostrich specimens displays a local peak near the resonance. Another specimen forms an outlier to the rocking-to-piston ratios, as for the short-axis component in Figure 5.5 (c), reaching values down to -48 dB or 0.004. The rocking-to-piston ratio of the short-axis component starts to increase around 0.5 kHz, also containing small fluctuations, but the increase evolves more slowly as a function of frequency than for the ratio of the long-axis component. In human, an increase is observed for the ratio of the short-axis component for both IE intact and drained, but the increase is higher than for the ratio of the long-axis component. Rocking-to-piston ratios of the short-axis component in the current experiments do not exceed 0 dB; although one specimen reaches a value of 0 dB at 4 kHz. The ratio at 4 kHz ranges between -13 dB and 0 dB, or 0.22 and 1 respectively.

5.3.2.3.2 Model results

For the model without IE load, we observe that both rocking-to-piston ratios remain constant at low frequencies up until 0.7 kHz. At 0.125 kHz, the rocking-to-piston ratio is equal to -28 dB for the long-axis component and -27 dB for the short-axis component, or a linear ratio of 0.040 and 0.044 respectively. The model stays within the range of measurements in this frequency region; the ratio of the short-axis component of the model approaches the experimental average, while the ratio of the long-axis component almost reaches the upper bound of the experiments. Starting from 0.7 kHz, both ratios of the rocking components start to show an overall increase as a function of frequency up to 4 kHz, and the fluctuations are larger than in the experiments. At 4 kHz, maximal rocking-to-piston ratios of -13 dB (or 0.22) and -14 dB (or 0.20) are reached for the long-axis and short-axis component, respectively. Adding five point masses of 0.04 mg to the CFP surface in the model, representing the reflective patches, has minor influence on the results, as shown in Figure 5.6.

For the model with IE load, both ratios are the same as without IE load for frequencies below 0.6 kHz. For measurements in human, the rocking-to-piston ratio of the short-axis component is 4 dB higher with intact than with drained IE at low frequencies. Above 0.8 kHz, the ratios of the model with loaded CFP start to increase relative to the condition with unloaded CFP, reaching a maximum of 0 dB between 2-3 kHz, so that CFP motion can no longer be identified as purely piston-like or rocking. Beyond

the maximum, the ratio of the long-axis component for the model with IE load decreases slowly down to -9 dB or 0.35 towards 4 kHz. For the short-axis component the decrease is much larger (down to -15 dB or 0.18), but towards 4 kHz the ratio rises again up to -3 dB or 0.71 . For the average of measurements in human, a decrease is also observed beyond 6 kHz for both rocking components (data not shown).

5.3.2.4 Full-field displacement

Figure 5.7 shows the full-field 1D out-of-plane displacement magnitude and phase of the CFP, for the digital stroboscopic holography experiments measured in O6R and O7L with IE drained, and for the model without and with IE load. Displacement maps are shown for three selected frequencies of 0.2 , 0.8 and 3.2 kHz.

5.3.2.4.1 Experimental results

At 0.2 kHz, the magnitude and phase maps are almost entirely uniform for both specimens, corresponding to a piston-like motion. At 0.8 kHz, the displacements in O6R are a little larger at the posterior and inferior side of the CFP compared to the anterior and superior side. In O7L the displacement is neither completely uniform, but the largest displacement occurs on a different part of the CFP, i.e., at the posterior and superior side. For both specimens, the phase maps remain uniform. This behavior indicates a small increase of the rocking components, although the piston component remains clearly dominant. At 3.2 kHz, the rocking components appear to increase further relative to the piston component in O6R, because displacements on the posterior and inferior edges of the CFP are almost twice as large as on the anterior and superior edges. Also, the phase map is no longer completely uniform in this sample. In O7L, however, the displacement maps at 3.2 kHz are qualitatively similar to the maps at 0.8 kHz.

5.3.2.4.2 Model results

At 0.2 kHz, the displacement map is almost completely uniform for both the model without and with IE load. Also at 0.8 kHz, the displacement maps of the models remain largely uniform. Only at 3.2 kHz the behavior starts to change: as in O6R, the magnitude map of the model without IE load contains larger displacements in the inferior and posterior regions of the CFP than in the superior and anterior regions, and the phase remains uniform. For the model with IE load, a clear rocking component emerges and the phase is no longer uniform. Still, the piston component remains the largest at this frequency, as can be deduced from both panels of Figure 5.6. However, the overall dynamic motion of the columella in the model is too complicated to be described as purely piston-like or rocking. Adding a mass load of the coating to the CFP surface in the model, using a layer thickness of 0.1 mm and a mass density of 1000 kg/m³, has only minor effect on CFP displacements (data not shown).

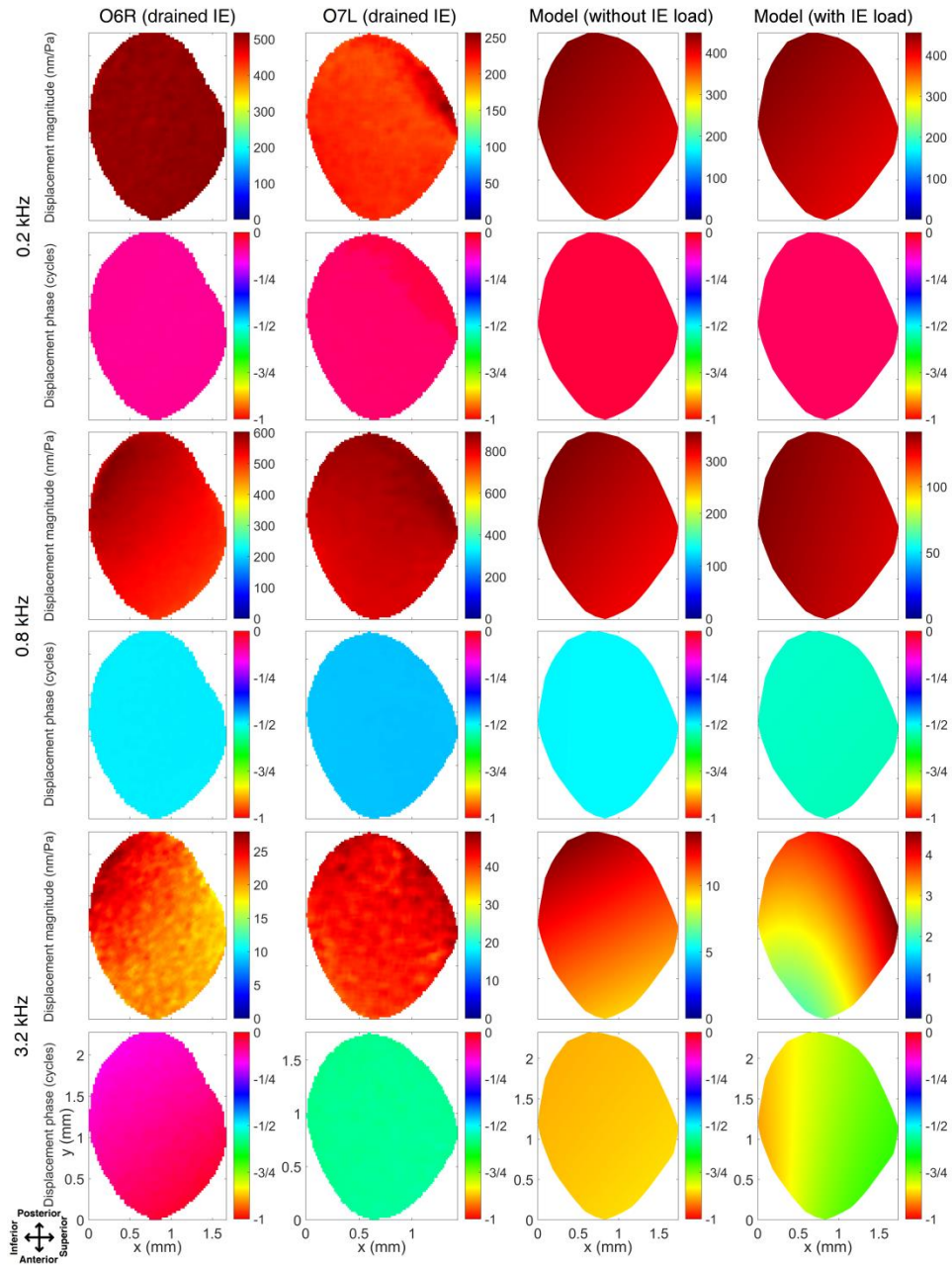


Figure 5.7. Full-field 1D out-of-plane displacement magnitude (nm/Pa) and phase (cycles) for three selected frequencies of 0.2, 0.8 and 3.2 kHz. Magnitudes are normalized to the stimulation pressure in the ear canal. The first two columns depict experimentally obtained displacement maps measured with digital stroboscopic holography in specimen O6R (mirrored) and O7L with IE drained. Experimental phase maps have arbitrary reference value. The last two columns show displacement maps of the model without and with IE load. For the models, phases are taken relative to the phase of the stimulation pressure. Approximate anatomical directions are indicated in the bottom-left part of the figure.

5.4 Discussion

5.4.1 Quasi-static motion

5.4.1.1 Experiments in literature

In the past, deformations of the columellar complex under the influence of quasi-static pressures have been measured in several bird species. Nevertheless, quantitative results of rocking relative to piston-like motion are lacking.

Gaudin (1968) made photographs of columellar displacement under low-frequency high-pressure simulation of the TM in different species by applying pressures in the external auditory meatus. The observed columellar displacements were side to side, perpendicular to the columellar shaft, and CFP displacements occurred mostly at the anterior edge of the oval window.

Mills and Zhang (2006) observed columellar displacements under static pressures of +1 and -1 kPa applied in the external auditory meatus of different birds, and found a tilting of the extracolumella and a flexion of the intracolumellar joint, which produced a rocking motion of the CFP around its anterior edge rather than a direct displacement into the scala vestibuli. Later, Mills et al. (2007) performed similar pressure experiments in the ear of the common guillemot, measuring CFP displacements of 100 μm at a positive pressure of 2 kPa in the external auditory meatus. No pronounced rocking motion of the CFP was observed.

Arechvo et al. (2013) measured displacements at the center point of the CFP in the ostrich as a function of positive input pressure applied in the external auditory meatus from 0 to 2 kPa. The average CFP displacement was equal to 270 μm at 1 kPa and 330 μm at 2 kPa. When a positive or negative pressure was applied in the external auditory meatus, considerable bending occurred in the extrastapedial process of the cartilaginous extracolumella, while Platner's ligament limited displacements of the CFP in and out of the oval window.

Thomassen et al. (2007) created a 3D FE model of the static displacements of the columellar complex in the cave swiftlet and 2D models of several other avian species. The 3D model of the cave swiftlet resulted in rocking motions of the CFP, behaving as a tapping foot as described by Gaudin (1968). The CFP displacements inferred from the 2D models were either rocking or piston-like in nature, depending on the ME geometry of the species.

5.4.1.2 Experimental results

In the current study, quasi-static columellar displacements in both ears of the ostrich were induced simultaneously by applying a positive or negative pressure of 1 kPa inside the intracranial airspace. Applying pressures via the inside or the outside of the ME doesn't result in different columellar displacements, as only the pressure gradient

over the TM is determinative for ME deformations. Piston-like and rocking motions of the CFP for both pressurized conditions were quantified by comparing μ CT scans of the head with and without pressure.

Based on the results we could conclude that, for positive ME pressure, CFP motion was predominantly piston-like, with only a small rocking component. Also for negative ME pressure, the piston component was mostly larger than the rocking component; only one sample (O₄) showed dominant rocking motion, and for two other specimens (O₃ and O₅) a considerable rocking component was present as well. The rocking-to-piston ratio was always larger for negative than for positive ME pressure, except for specimen O₂. The deviating result of O₂ may be related to a different geometry of the columellar complex, as can be deduced by comparing the undeformed shape of O₁ and O₂ in Figure 5.3: in O₁ the undeformed extrastapedial process has a curved shape with its distal end located medially to the elongated long axis of the columella, while in O₂ the distal end of the curved extrastapedial process is located laterally to this imaginary axis, possibly leading to a different CFP motion. The large rocking motion observed in O₄ for negative ME pressure, on the other hand, goes along with a large rotation of the extrastapedial process (i.e., a rotation caused by medial displacement of the distal part of the process) that leads to an almost straight angle between the long axes of the extrastapedial process and the columella (data not shown). Such a motion is associated with considerable buckling at the intracolumellar joint, but the behavior of this outlier may also represent a damaged ear. Displacements at the distal end of the columellar shaft that are transverse to the long axis of the shaft are an indication of rocking motion. However, because the columellar shaft of the ostrich is very long relative to the size of the CFP, the encountered transverse motions of the shaft involve only small CFP rotations as observed in most samples. Therefore, the rocking component remains small compared to the piston component in most cases, which is mostly in agreement with the observation of Mills et al. (2007) reporting piston-like behavior, and different from Gaudin (1968) and Mills and Zhang (2006) who reported rocking motion. Out-of-plane CFP displacements were on average 0.226 mm for positive and 0.197 mm for negative ME pressure. The latter result is considerably smaller than the average of 0.27 mm observed by Arechvo et al. (2013). The observation that piston-like motion is smaller for negative than for positive ME pressure may indicate the presence of a protective mechanism that minimizes excessive displacement of the CFP into the scala vestibuli, as proposed by Mills and Zhang (2006). The protective mechanism may reduce piston-like motion by partially converting it into rocking motion, which does not involve a net displacement into the scala vestibuli.

Rocking-to-piston ratios resulting from the quasi-static experiments, especially for negative ME pressure, were generally larger than the ratios obtained with the dynamic measurements at the lowest measured frequencies, which are discussed in the following section. This discrepancy is probably due to nonlinearity of the quasi-static

CFP displacements: at the applied static pressures of 1 kPa, CFP displacements become nonlinear (Arechvo et al., 2013), which differs from the dynamic CFP motions that remain well within the linear response regime at the stimulus pressure of 1 Pa. Nonlinearities may involve material nonlinearities of the columellar complex, but also geometric nonlinearities or nonlinearity of the IE load. In case of a geometric nonlinearity, the physics equations can no longer be formulated with respect to the object's undeformed state, but they depend on the effective deformation when becoming large. For example, the conical shape of the TM in the lateral direction could produce such nonlinearity: if the TM deforms in the lateral direction it may stretch and gain tension, while a medial deformation may lead to a loss in tension. At high quasi-static pressures these nonlinearities may lead to asymmetry in CFP displacement between positive and negative pressure, as was found for the rocking-to-piston ratios listed in Table 5.2.

5.4.2 *Dynamic motion*

5.4.2.1 *Experiments in literature*

In mammals, motions of the stapedial footplate have been measured and quantified extensively in different species, using various approaches. These species include human (e.g., von Békésy, 1960; Kirikae, 1960; Heiland et al., 1999; Huber et al., 2001; Hato et al., 2003; Sim et al., 2010), cat (Guinan and Peake, 1967; Decraemer et al., 2000), gerbil (Decraemer et al., 2007; Ravicz et al., 2008) and guinea pig (Huber et al., 2008; Eiber et al., 2012). The latter three used mechanical stimulation instead of acoustic stimulation to generate rocking motions on the footplate.

Full-field dynamic motions of the CFP in the single-ossicle ear have only been measured qualitatively in one reptile species, the alligator lizard (Rosowski et al., 1985), by using stroboscopic illumination with high stimulus levels (Guinan and Peake, 1967). The columella was shown to vibrate mostly as a piston.

In birds, Saunders and Johnstone (1972) measured CFP vibrations in the Barbary dove using Mössbauer spectroscopy. Gummer et al. (1989a) used the same technique to measure CFP responses in anesthetized pigeons along several axes. CFP vibrations were measured with IE intact, fenestrated and drained. The authors found a frequency dependence of the phase response on the spatial angle of the measurement axis. This frequency dependence provided direct evidence for vibration modes additional to the presumed piston-like mode. For high frequencies above 2 kHz, sharp and broadly tuned antiresonances were observed in the CFP response with IE intact, involving amplitude notches, large phase drops of up to two cycles and positive phase slopes.

More recently, Arechvo et al. (2013) measured the out-of-plane CFP displacement magnitude response in the ostrich with intact IE using LDV (Figure 5.4). Results of that study are similar to our measurements, with a resonance peak near 0.5 kHz. Our results show slightly higher magnitudes at high frequencies, which was probably due

to draining the IE. LDV was also used to measure the extrastapedial tip and CFP response in the mallard (Muysshondt et al., 2016a; Chapter 3 of this thesis). Extrastapedial tip vibrations were measured with IE intact and drained, and CFP vibrations with IE drained. After draining the IE, the extrastapedial tip response mainly changed in the mid- and high-frequency range, and the resonance peak shifted to higher frequencies. To determine the impedance of the IE in ostrich, the columellar response was measured by Muysshondt et al. (2016b; Chapter 4 of this thesis) with intact and drained IE under magnetic stimulation of the ossicle. Again, removing the IE fluids mainly influenced the response in the mid- and high-frequency range, and the resonance peak was shifted to higher frequencies.

5.4.2.2 *Experimental results*

In the current study, dynamic motions of the CFP were measured with LDV and digital stroboscopic holography in the ostrich after draining the IE. The measured specimens showed a large quantitative variation in the CFP velocity response, which was also the case for the rocking-to-piston ratios. Also in humans, large differences between samples were observed in motions of the stapedial footplate (Sim et al., 2010), which were presumed to be due to individual differences in ME anatomy. However, differences in vibration response may also indicate differences in material properties. Specific features to some specimens, such as dips in the response near the resonance frequency or outliers in magnitude and phase, may reflect small changes or differences in physiological condition. Qualitatively, the results of CFP motion were similar and the samples exhibited largely piston-like behavior at low frequencies below 1 kHz. Towards higher frequencies, the rocking components increased as a function of frequency, although never exceeding the piston component.

In many aspects, the results are qualitatively similar to what was found in the aforementioned experiments on mammalian ears. In Hato et al. (2003), stapedial footplate motions were measured in human from 0.1 to 10 kHz before and after draining the IE. With intact cochlea, the average footplate motion was piston-like below 1 kHz. Above 1 kHz, rocking motions for rotations around the long and short axis of the footplate started to increase, and around 4 kHz they became most dominant, reaching a peak at 6 kHz. With cochlea drained, the piston component increased for all frequencies, while the rocking components slightly increased for low frequencies and decreased for high frequencies. Due to the increase of the piston component after drainage, rocking-to-piston ratios decreased overall, leading to a predominant piston-like motion for all frequencies, which is in agreement with the presented ostrich measurements with IE drained.

5.4.2.3 *Model results*

To study the influence of the IE on displacements of the CFP, a FE model was constructed of the ME with an IE load model that is based on the net volume velocity

and uniform pressure of the IE fluid on the medial CFP surface. As rocking motion does normally not lead to a net fluid displacement, the pressures and velocities in this model are supposedly caused by piston-like motion. As a consequence, the load will mainly affect the piston component, as can be noticed in Figure 5.5 (a). Nevertheless, rocking motions have been shown to contribute to cochlear activation by changes in the compound action potential of the cochlea (Huber et al., 2008; Eiber et al., 2012). However, the activation threshold was higher and the sensitivity lower for the rocking components than the corresponding values of the piston component. A cochlear model of Edom et al. (2013) showed that rocking motion contributed to basilar membrane motion, but under normal conditions the piston component was dominant; while piston-like motion leads to a pressure wave that travels across the basilar membrane, rocking motion causes only a weak pressure wave compared to the pressure right behind the footplate. Decraemer et al. (2007) and de La Rochefoucauld et al. (2008) found no clear indication that rocking motion leads to pressure behind the footplate; the authors suspected that rocking motion causes the fluid to slosh back and forth in a small volume behind the footplate, and that this local fluid motion does not excite a pressure wave to propagate further into the cochlea. Therefore, despite that vestibular pressure caused by rocking motion is certainly present (Huber et al., 2008; Eiber et al., 2012), its magnitude must be small compared to the corresponding values of the piston component. As such, the impedance of piston-like motion must be influenced more by the status of the cochlea than the impedance of rocking motion, as suggested by Hato et al. (2003). Presumably, introducing a small load to the model related to rocking motion will slightly reduce the magnitude of rocking motion. In this sense, the current model with an IE load based on the net volume velocity and uniform pressure poses an upper bound on the effective rocking-to-ratios with intact IE.

For the model without IE load, we observed that the rocking-to-piston ratios belonging to rotations around both the long and short CFP axis remained constant as a function of frequency up to 0.7 kHz, which was similar to most measurements. At higher frequencies, the rocking-to-piston ratios exhibited an increase as a function of frequency, containing evident fluctuations. When comparing the CFP motion of the model with and without IE load, it was found that the frequency response of the piston component mainly changed at mid and high frequencies, as observed experimentally in different birds (Gummer et al., 1989b; Muyshondt et al., 2016a,b; Chapter 3 and 4 of this thesis).

When the IE load was included, the rocking components started to increase at 0.8 kHz relative to the situation with unloaded CFP. Around 2–3 kHz, rocking-to-piston ratios showed that CFP motion could not be identified as purely piston-like or rocking. Yet, the rocking components never exceeded the piston component. Also the 3D motion of the model outcome showed that columellar motions at higher frequencies were too complicated to be identified as purely piston-like or rocking,

which was also observed for the reported measurements of stapedial motion in mammals. In the human temporal bone measurements of Hato et al. (2003), rocking-to-piston ratios were also larger with intact IE than with drained IE for most frequencies. With intact IE, however, rotational motions of the footplate exceeded the piston-like motion at 4 kHz and higher, indicating a predominantly rocking motion.

Ideally, CFP motions under intact IE conditions are better addressed through measurement than by a model that makes assumptions about boundary conditions and isotropy and homogeneity of tissues. However, when we compare our model of the ostrich to measurements in human, we observe that the IE influences footplate motions in a similar way, which suggests that the model result is reliable to a certain extent. Nevertheless, to determine what lies at the origin of the observed motions, and how material properties, geometry and boundary conditions of the different ME structures contribute to this motion, sensitivity analyses should be performed in combination with FE modeling.

From the experiments and the model, it can be concluded that the CFP performs largely piston-like motions for sound pressures at low and mid frequencies, where the displacements are not yet too complicated. This implies that the description of rocking motion provided by Gaudin (1968) does at least not apply in the ostrich. When analyzing the piston-like motion of the CFP in the model, it seems that the situation in the ostrich is more complicated than the explanations provided by Pohlman (1921), Norberg (1978) or Manley (1990b): in the presented model, the deformable extracolumella and flexible joint convert the existing rotations of the extrastapedial process partially into piston-like motion of the columella. This conversion goes along with bending of the extracolumella and relative rotation at the joint, and the contribution of the joint is the largest. However, piston-like CFP motion is also observed when the extracolumella and joint are considered undeformable: for instance, when the columella, extracolumella and their connection are modeled as completely bony, the extrastapedial process produces mostly translations in and out of the TM plane that also lead to a piston-like CFP motion, without any conversion by bending. However, with a bony extracolumella the displacements of the extrastapedial tip and CFP become too small in magnitude compared to what is observed experimentally. This observation suggests that flexibility of the joint and extracolumella is needed to produce large enough CFP motion rather than to provide piston-like CFP motion, because the latter can also be demonstrated with undeformable ME components. Yet, further experimental and modeling analysis of the ME structures is needed to make a more conclusive statement.

5.5 Conclusion

When static pressures of +1 and -1 kPa were applied to the ME of the ostrich, both piston-like and rocking motion was observed at the CFP. In most cases, the rocking-

to-piston ratio was larger for negative than for positive ME pressure. For positive ME pressure, the motion was predominantly piston-like. For negative ME pressure, the piston component was mostly larger than the rocking component, but the difference was smaller; in one specimen, rocking motion was even dominant. For the dynamic pressure experiments with frequencies ranging from 0.125 to 4 kHz, the rocking components arising from rotations around the long and short axis of the CFP were mostly much smaller than the piston component. At frequencies below 1 kHz, rocking-to-piston ratios were constant as a function of frequency with values of less than 0.1. For higher frequencies, the rocking components increased relative to the piston component as a function of frequency, although never exceeding the piston component. The IE load affected CFP motions of the model in such a way that the rocking-to-piston ratio increased relative to the condition with unloaded CFP above 0.8 kHz. At higher frequencies, columellar motions could no longer be identified as purely piston-like or rocking.

CHAPTER 6 SOUND ATTENUATION IN THE CHICKEN EAR AS A RESULT OF BEAK OPENING

Abstract

This chapter is different from the previous two chapters in that it does not investigate the mechanical behavior of the avian ME components, but it studies a potential effect of beak opening on sound conduction in the ME of the chicken. As opposed to mammals, the ME of birds is not fully enclosed by the skull, as a part of it is connected to the kinetic quadrate bone. The quadrate is a part of the beak suspension that will rotate relative to the ME structures when the beak is opened. In collaboration with researchers of the biology department we found that quadrate rotations go along with a deformation of the TM, which was more pronounced in roosters than in hens. This observation led us to the hypothesis that beak opening in roosters serves as a protective mechanism against their own crowing by reducing the sound transmission ability of the deformed TM, and that this mechanism is less important in hens due to their smaller vocalization capacity. To test the hypothesis, vibrations of the CFP were measured with LDV in hens and roosters and compared for closed and maximally opened beak, with sounds introduced at the entrance of the ear canal. The average attenuation was 3.5 dB in roosters and only 0.5 dB in hens. To demonstrate the importance of a putative protective mechanism, audio recordings were performed of a crowing rooster. Huge SPLs of 133.5 dB were recorded near the ears of the animal. The results indicate a small but significant difference in sound attenuation between the sexes. However, the amount of attenuation in both hens and roosters is small and will contribute little to protection, so effective attenuation must be obtained by other protective mechanisms.

This chapter is based on:

Muysshondt, P.G.G., Claes, R., Aerts, P., Dirckx, J.J.J., 2017. Sound attenuation in the ear of domestic chickens (*Gallus gallus domesticus*) as a result of beak opening. *R. Soc. Open Sci.* 4, 171286. doi:10.1098/rsos.171286.

6.1 Introduction

As opposed to the ME of mammals that is built up of three ossicles, birds only have a single ossicle, the columella. Apart from this single bony ossicle, the avian ME contains a trifurcated cartilaginous extracolumella which joins the TM to the columella and of which the central arm, the extrastapedial process, gives the TM its conical shape with the apex pointing outwards into the ear canal. The ear also contains a single muscle, the ME muscle, that is innervated by a branch of the facial nerve and is located for the most part outside of the ME cavity (Smith, 1904). Furthermore, the system is suspended by a series of ligaments, such as the annular ligament surrounding the CFP, Platner's ligament that connects the columella to the quadratosquamosal articulation, the ascending ligament coupling the TM to the extrastapedial process, and some drum-tubal ligaments that support the TM (Pohlman, 1921).

In contrast to the mammalian ME, which is embedded in a single bony cavity within the temporal bone, the avian ME and TM are enclosed by two separate bony structures: the temporal bone of the neurocranium and the quadrate. The quadrate is a part of the beak suspension that can move relative to the neurocranium. Upper-jaw and quadrate movements are linked via the pterygoid-palatine complex and the jugal bone (e.g., Bock, 1964). Additionally, the TM is fixed at its rim by loose connective tissue in the ventrolateral part of the ME (Starck, 1995). Furthermore, the cavity of the avian ME is connected to the contralateral ME via the pharyngotympanic tube and a complex-shaped intracranial air space (e.g., Wada, 1924; Larsen et al., 2016). The geometry of the TM and the columella of the chicken and their relation to the quadrate and the beak are shown in Figure 6.1. The geometry is based on the reconstruction of μ CT images that were presented in Claes et al. (2017).

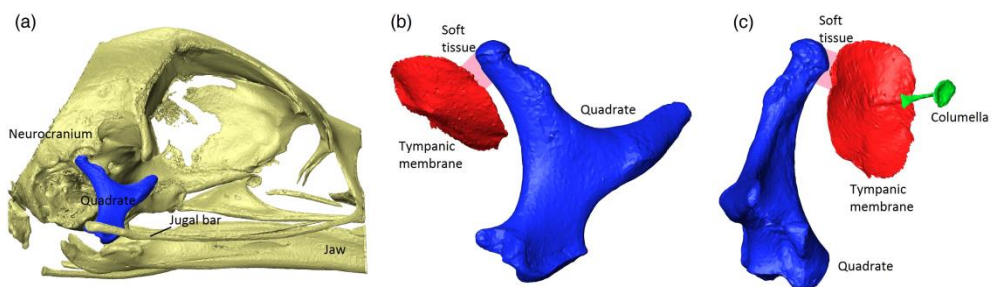


Figure 6.1. Geometry of the ear structures of the chicken's skull obtained from reconstructions of μ CT images presented in Claes et al. (2017). (a) Lateral view of the chicken's skull illustrating the geometric relation of the quadrate (blue) to the neurocranium, jaw and jugal bar (yellow). (b) Enlarged lateral view and (c) frontal view of the quadrate (blue), TM (red) and columella (green). The otic process of the quadrate attaches to the TM via soft tissue (pink-shaded area). Beak opening goes along with rotations of the quadrate via the jugal bar, which leads to deformation of the TM (relaxation or tension) by way of the soft tissue connection.

Sound transmission through the avian ear is influenced by the ME muscle, which was shown to react during self-generated vocalizations in the domestic chicken based on electromyography measurements (Counter and Borg, 1979). Grassi et al. (1990) later claimed that this muscle activation mostly plays a role in vocal development, rather than effectively protecting the animal from its own generated vocalizations. Interestingly, Counter and Borg (1979) concluded that mechanisms other than muscle activity must be present to account for the observed change in ME volume during vocalization, which influence ME function. Suggested explanations were muscle contractions in the outer ear, the insertion of air into the intracranial cavity via the pharyngotympanic tube or skull deformations during vocalization.

On top of these factors, additional mechanisms may play a role in the adaptation of ME function. Ewald (1889) discovered that IE pressure rises as a consequence of beak opening in pigeons. This happens due to the attachment of the TM to the skin of the ear canal, which is connected to the skin covering the lower jaw: when the beak opens the skin of the jaw is stretched, which further pulls on the TM. The so-established static pressure is transmitted to the IE by the columella. Bray and Thurlow (1942) investigated this hypothesis with cochlear potential measurements in pigeons, demonstrating an average drop of 20 dB in auditory sensitivity when the beak is widely opened.

As the TM is connected to the kinetic quadrate and loose connective tissue, as illustrated in Figure 6.1 (b)–(c), it was proposed by Starck (1995) that movements of the upper jaw, for instance during vocalization, may change the shape and tension of the TM and thus affect hearing in birds. Claes et al. (2017) compared the effect of maximal beak opening on the ME structures in the male and female domestic chicken using μ CT, given the large difference in vocalization capacity between the sexes. It was found that TM deformation, causing relaxation of the membrane, was more pronounced in roosters than in hens. These deformations may alter the vibroacoustic properties of the TM and could be part of a protective mechanism, possibly only present in roosters, which serves to prevent damage of the IE receptor cells during vocalization, as observed in pigeons (Bray and Thurlow, 1942).

To investigate this hypothesis, the transmission of sound through the ear of the domestic chicken is investigated and compared for different beak-opening configurations by measuring vibrations of the ME. Up till now, only a few studies have reported measurements of ME vibrations in bird species. The few techniques that were used in this context include macrophotography on different animals (Gaudin, 1968), Mössbauer spectroscopy on doves (Saunders and Johnstone, 1972) and pigeons (Gummer et al., 1989a,b), and capacitive probe to compare the TM response in pigeon, parakeet, canary, cowbird and neonatal chick (Saunders, 1985). More recently, LDV was used to measure TM response in the neonatal chick (Cohen et al., 1992). LDV was also used to study the internal coupling of MEs in the framework of

directional hearing in starlings Klump and Larsen, 1992), quails (Larsen and Popov, 1995), budgerigars (Larsen et al., 2006) and owls (Kettler et al., 2016). The same technique was used to study vibrations in the ME of the ostrich (Arechvo et al., 2013; Muysshondt et al., 2016b; Chapter 4 of this thesis) and the duck (Muysshondt et al., 2016a; Chapter 3 of this thesis). In the present study the vibration velocity of the CFP was measured with LDV *ex vivo* in response to sound pressures introduced at the entrance of the ear canal. These experiments are performed on both hens and roosters, and repeated for closed and maximally opened beak conditions. Because it is the aim of the present study to isolate the purely mechanical effect of beak opening, measurements are performed *ex vivo* so that other active mechanisms such as ME-muscle action are excluded.

To demonstrate the need of a protective mechanism against potentially very loud self-generated vocalizations, audio recordings of a crowing rooster are presented. The acoustic properties of the rooster's crows are studied by analyzing the amplitude and frequency content of the recordings. To verify their potential impact on the hearing of the animals, they are related to the results of the vibration experiments.

6.2 Materials and methods

6.2.1 Middle-ear vibration experiments

6.2.1.1 Sample preparation

The heads of five male and five female young adult domestic chickens (*Gallus gallus domesticus*) between three and thirteen months old were obtained from a poultry farm and were refrigerated at a temperature of 5°C for no more than five days before measurement. The subjects were euthanized in the function of the food industry, so no animals needed to be sacrificed for the current work. The adult males had a body weight of (2.4 ± 0.14) kg and females had a weight of (1.8 ± 0.12) kg. The domestic chicken was chosen because the species is widespread and well-studied, but also because of the large difference in vocalization capacity between the sexes. To measure ME vibrations at the medial side of the CFP, the skull was opened from the caudal side of the head using a band saw as shown in Figure 6.1 (a), without damaging the hearing organs or any structures associated with the bill. To gain optical access of the CFP, the medial wall of the IE was opened from the inside of the skull and the remaining IE fluid was removed from the surface of the CFP. Furthermore, the head was fixed in the experimental setup by inserting a screw in the upper part of the skull. For the experiments with an opened beak, a plastic rod of appropriate length was placed between the upper jaw (i.e., the maxilla and premaxilla) and the lower jaw (or mandible) to open the beak maximally.

6.2.1.2 *Experimental setup*

To induce ME vibrations, loudspeaker with a diameter of 10 cm (FR10 - 4 Ohm, Visaton, Haan, Germany) was used as an acoustic stimulation source. The sound generated by the speaker was concentrated by a funnel onto a small surface area of around 1 cm² to concentrate the acoustic input at the entrance of the ear canal. To prevent significant sound pressure from reaching the medial and lateral surface of the columella, modeling clay was used to seal the sound-source funnel to the ear canal. Stepwise pure-tone sinusoidal signals from 0.125 to 4 kHz, with sixteen lines per octave, were delivered to the speaker via a custom-made amplifier. The frequency range was chosen in accordance with the hearing range of chickens (Saunders and Salvi, 1993). A probe-tube microphone (Probe Microphone Type 4182, Brüel & Kjær, Nærum, Denmark), connected to a conditioning amplifier (Nexus Type 2690-A-OF2, Brüel & Kjær, Nærum, Denmark), was inserted between the speaker and the ear canal at the entrance of the canal to measure the SPL inside the sealed volume. To compensate for the frequency-dependent sensitivity of the speaker, the generated sound pressure was corrected to 90 dB SPL for all frequencies in a single iteration. The frequency-dependent response of the microphone was accounted for. Sound-induced vibrations of the CFP were measured from the medial side of the ear using a single-point 1D LDV system (OFV-534 sensor head and OFV-5000 controller, Polytec, Waldbronn, Germany) that was mounted on a surgical microscope (OPMI Sensera/S7, Carl Zeiss, Jena, Germany). By using the microscope, the beam of the laser was pointed at the center of the CFP perpendicularly to the CFP surface, and to increase reflection of the laser on the sample, a miniature piece of reflective foil was fixed on the surface of the CFP which was small enough to minimize inertial effects. To monitor how well the sound source was sealed in the ear canal, a second probe-tube microphone was positioned right in front of the medial CFP surface, of which the recorded SPL was compared to the sound pressure detected at the entrance of the ear canal. The resulting stimulation and response signals were retrieved using a custom-made Matlab program (Mathworks, Natick, MA, USA) that communicates with a data-acquisition module (USB-6251 BNC, National Instruments, Austin, TX, USA). The sample rate of the input and output signals was set at a frequency of 50 kHz. Each signal was extended for 0.1 s to exclude transient effects in the stimulation and response signals. Finally, the amplitude of each signal was calculated from the Fourier transform of the waveforms at the corresponding stimulus frequencies. This experimental procedure was performed on the heads of both hens and roosters, and repeated for closed and maximally opened beak conditions.

6.2.1.3 *Statistical analysis*

To determine whether the observed difference in attenuation between male and female chickens was statistically significant, a statistical analysis was performed in R 2.15.1 (R Core Team, Vienna, Austria). The data to be analyzed were the attenuations

in each specimen averaged over frequency. A Shapiro-Wilk normality test was performed to verify whether the data were distributed normally ($W > 0.9$). When normality could be confirmed, an F test was executed to compare variances ($p < 0.05$; variances not equal). Normality and equal variance were met for all data. Afterwards a one-way analysis of variance (ANOVA) was performed in which the p value was determined to verify whether or not the null hypothesis, i.e., no difference between the sexes, could be rejected. Additionally, the statistical power was determined for a significance level of 0.05 and the given sample size.

6.2.2 *Rooster vocalization experiments*

To study both the amplitude and frequency characteristics of a rooster's crow in the proximity of its own ears, a miniature audio recorder (Wristband Voice Recorder, J&R Electronics, Hong Kong, China) was used to record vocalizations of an adult domestic rooster. The sensitivity of the device was attenuated so that SPLs up to 140 dB SPL could be measured without saturation. The rooster was five years old and had a body weight of 3.2 kg. The audio recorder was incorporated in a wristband that was suspended loosely around the neck of the animal right under the head, with the microphone positioned near the ear. The wristband was put on in the evening so the animal was accustomed to it before crowing at dawn. The audio recorder had a sample rate of 16 kHz and a bit depth of 16 bit, and was calibrated using a pre-calibrated microphone (Probe Microphone Type 4182, Brüel & Kjær, Nærum, Denmark) by measuring the SPL of stepwise pure-tone sound signals generated by a loudspeaker. In this procedure, the audio recorder and microphone were positioned at the same location at a distance of 20 cm from the loudspeaker to measure the SPL under free-field conditions. As a result, the frequency-dependent calibration curve of the audio recorder could be obtained by comparing the magnitudes of both signals. Subsequently, the total SPL of the vocalization signal as a function of time was calculated by means of a standard Fourier-analysis procedure.

6.3 Results

6.3.1 *Middle-ear vibration experiments*

6.3.1.1 *Female specimens*

The results of the LDV experiments that were performed on the heads of five hens (H₁R, H₂R, H₃L, H₄R and H₅R; H = hen; L = left ear and R = right ear) are shown in Figure 6.2. The five top panels in Figure 6.2 show the magnitude of the vibration velocity of the CFP in response to sound pressures introduced at the entrance of the ear canal as a function of frequency. Solid lines represent the measurements performed on a head with a closed beak, while the measurements with a maximally opened beak are depicted by dashed lines. Maximal beak opening in hens corresponds to a lower jaw depression of 34.1° and an upper jaw elevation of 12.7° (Claes et al.,

2017). When inspecting the results, we observe that each sample contains a peak in the velocity magnitude around a frequency of 0.55 kHz for both a closed and opened beak. There is one exception to this rule, namely sample H2R, which exhibits a peak resonance near 0.9 kHz. The maximum peak amplitude is around 1 mm/s/Pa. In some specimens, a minor second peak is found between 1 and 2 kHz and a third one above 2 kHz. To quantify the loss in CFP vibration amplitude of the opened beak configuration with respect to the closed beak configuration, the ratio of the velocity magnitude of both conditions was calculated for each specimen, as is shown in the bottom panel of Figure 6.2. The black dashed line in this graph represents the mean velocity ratio of all samples. Ratios are shown in dB, which allows easy interpretation in terms of hearing loss. First of all, the graphs show that the difference in velocity magnitude between a closed and opened beak is small for each sample. Only for specimen H5R, we note that a small decrease in vibration response is seen for the results with an opened beak, but the observed drop in this sample remains smaller than 3 dB over all frequencies. All other samples exhibit a negligible loss of vibration response. The mean velocity ratio over all samples of opened to closed beak is as small as 1 dB or less for all frequencies, with an average value of around 0.5 dB over frequency.

6.3.1.2 *Male specimens*

The results of the same experiments performed on the heads of five roosters (R1R–R5R; first R = rooster; second R = right ear) are shown in Figure 6.3. In roosters, maximal beak opening corresponds to a lower jaw depression of 32.7° and an upper jaw elevation of 18.5° (Claes et al., 2017). As in hens, a peak resonance is observed around approximately 0.55 kHz for all specimens in the five top panels of Figure 6.3. In some samples, a second resonance is prominent above 2 kHz. In contrast to hens, however, there is a drop in the velocity magnitude of the opened to closed beak measurements in roosters. When comparing the velocity ratios in the ME of roosters in the bottom panel of Figure 6.3, we detect some variability across the samples below the first resonance, with sample R4R showing no loss in vibration and other samples such as R1R and R2R displaying a decrease of 5 dB or more. For frequencies above the resonance, the velocity ratio is more consistent. Specimens R1R and R2R, however, contain a sudden drop in vibration response at isolated frequencies of 0.37 and 0.85 kHz, respectively. This behavior is seen in both the velocity magnitude and the velocity ratio of the involved specimens. The mean velocity ratio over all samples ranges between 1.5 and 6 dB, with an average value of 3.5 dB over frequency.

6.3.1.3 *Statistical analysis*

The one-way ANOVA results in a p value of 0.0015225, which is within the region of $p \leq 0.05$ for which the null hypothesis is commonly rejected. The coefficient of determination $R^2 = 0.7018$, and the statistical power of the test is equal to 0.9836.

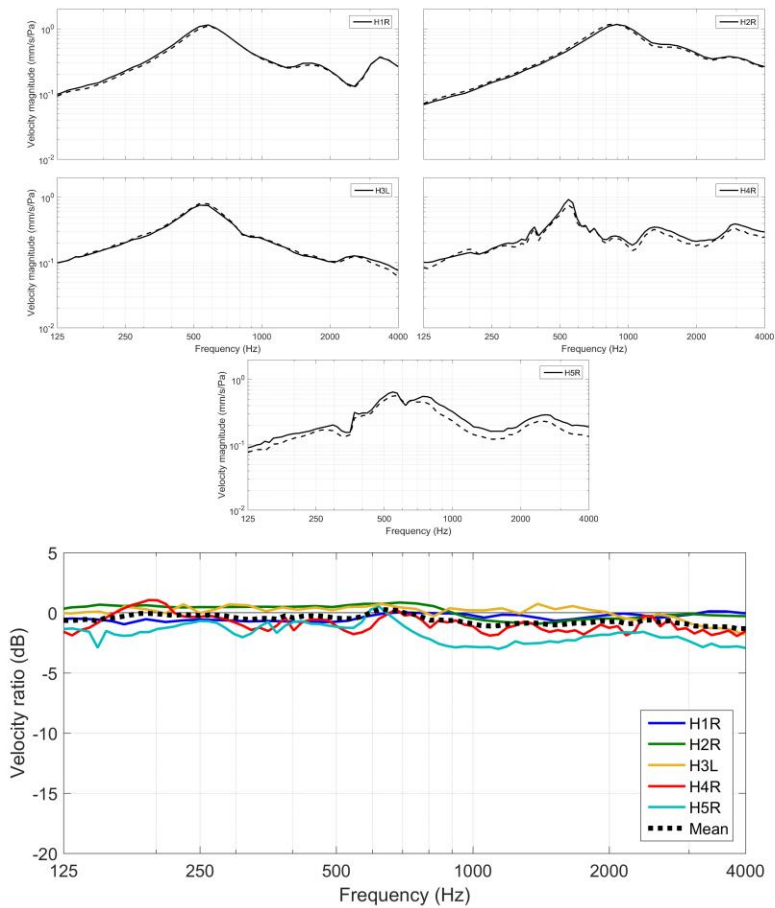


Figure 6.2. CFP vibration in hens in response to sound pressures applied at the entrance of the ear canal. Five top panels: magnitude of the vibration velocity normalized to incident pressure (mm/s/Pa) as a function of frequency, measured with a closed beak (solid lines) and maximally opened beak (dashed lines) for each sample individually. Bottom panel: ratio of the velocity magnitude (dB) of opened to closed beak for all specimens. The black dashed line represents the mean velocity ratio of all samples.

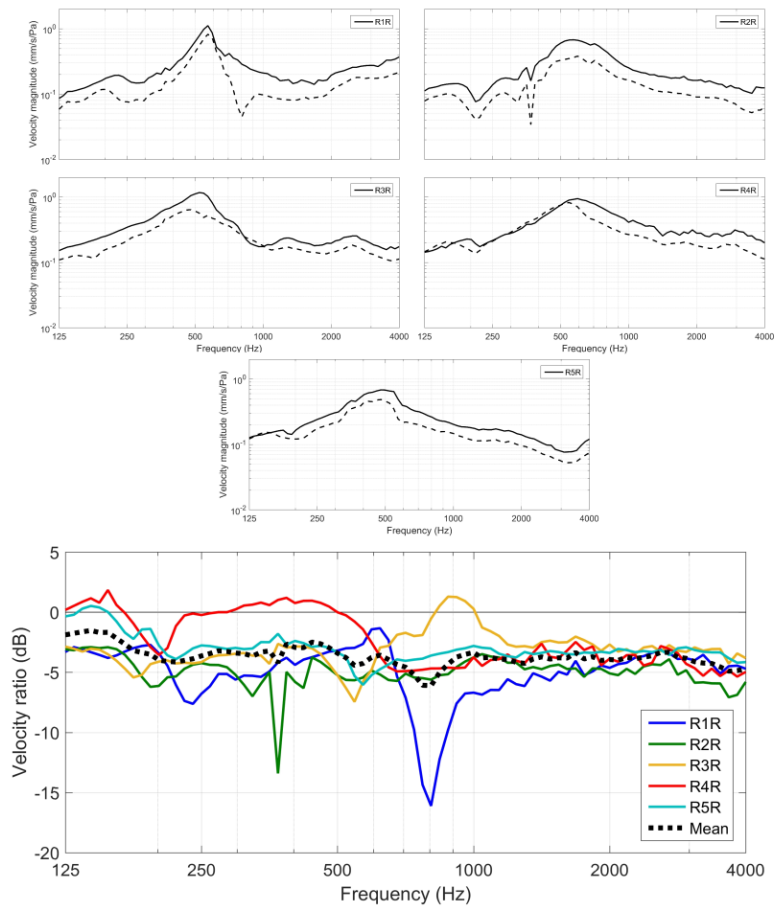


Figure 6.3. CFP vibration in roosters in response to sound pressures applied at the entrance of the ear canal. Five top panels: magnitude of the vibration velocity normalized to incident pressure (mm/s/Pa) as a function of frequency, measured with a closed beak (solid lines) and maximally opened beak (dashed lines) for each sample individually. Bottom panel: ratio of the velocity magnitude (dB) of opened to closed beak for all specimens. The black dashed line represents the mean velocity ratio of all samples.

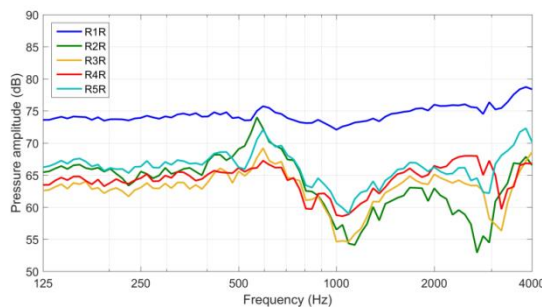


Figure 6.4. Level of sound stimulus at the CFP in roosters when 90 dB SPL stimulation occurred in the ear canal. This secondary stimulus was at least 15 and generally 25 dB smaller than the ear canal stimulus.

6.3.2 Rooster vocalization experiments

The rooster used for the vocalization experiments was recorded during multiple vocalization cycles. The spectrogram of such a cycle is shown in Figure 6.5 (a), after it was corrected for the calibration curve of the audio recorder. The shade in the plot represents the magnitude of the sound pressure expressed in dB SPL (re 20 μ Pa) as a function of frequency and time. The spectrogram is shown for frequencies between 0.25 and 4 kHz, as this range includes the audible range of chickens.

First of all, we observe multiple peaks arising in the magnitude of the spectrogram: each peak component is a multiple or harmonic of the fundamental frequency, also called the first harmonic or pitch. The fundamental frequency fluctuates between 0.4 and 0.65 kHz in the beginning and middle of the cycle, and reaches a stable value in the second half around 0.6 kHz. The most prominent peaks in the spectrogram are the first and second harmonic, thus being the primary contributors to the total SPL of the vocalization signal.

From the spectrogram in Figure 6.5 (a), the total SPL of the vocalization could be calculated as a function of time. In Figure 6.5 (b), the frequency spectrum is shown of the time fragment in the signal for which the total SPL is maximal, i.e., after around 0.4 s. In Figure 6.5 (b), we can discriminate the six different harmonics whose sinusoidal contributions – each with correct amplitude and phase – are summed to compute the total SPL as the root mean square of this signal. As mentioned in the previous paragraph, the first and second harmonics are the largest in magnitude. With peak frequencies of 0.65 and 1.3 kHz and peak amplitudes of 125 and 131.5 dB SPL, respectively, they are the primary contributors to the total SPL of the vocalization signal at maximal sound intensity.

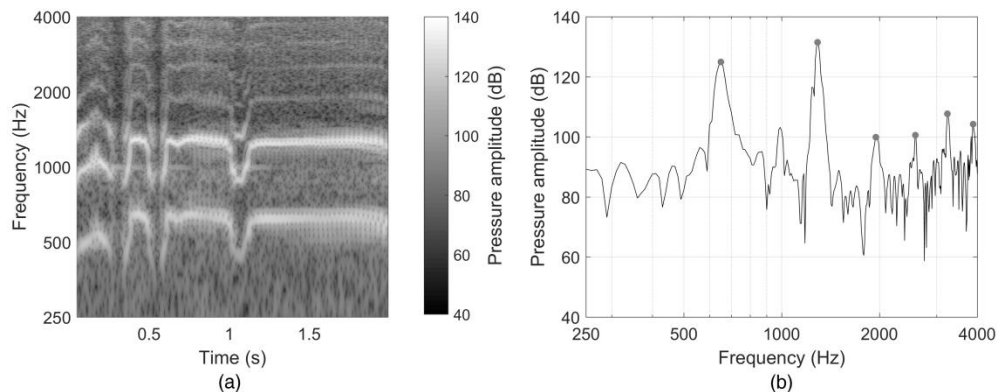


Figure 6.5. Spectral decomposition of the rooster's crow. (a) Calibrated spectrogram of the sound pressure signal (dB SPL re 20 μ Pa) as a function of time and frequency. (b) Frequency spectrum of the time fragment for which the total SPL was maximal, occurring at approximately 0.4 s in the crowing cycle. Dots annotate the location of the amplitude peaks that are used to calculate the total SPL.

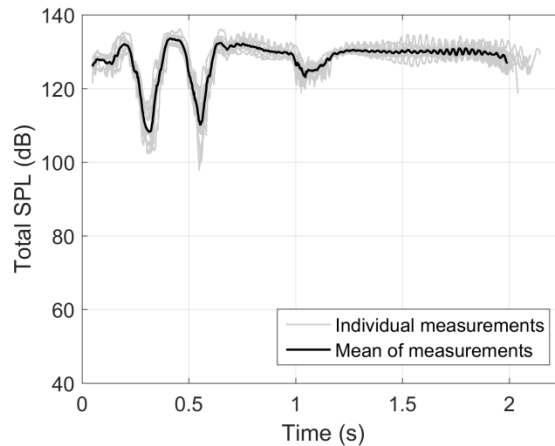


Figure 6.6. Total sound pressure amplitude (dB SPL re 20 μ Pa) of all vocalizations produced by the rooster as a function of time.

The total SPL of all vocalizations produced by the rooster is shown in Figure 6.6 as a function of time. The curves show that the vocalization signal is very reproducible: each cycle contains two distinctive SPL minima after 0.3 and 0.55 s, and one moderate minimum after 1.1 s. On average, the rooster produced maximal pressure amplitude levels of 133.5 dB SPL close to the ear of the animal after 0.4 s in the crowing cycle. Individual cycles even reached values of 136 dB SPL.

6.4 Discussion

6.4.1 Middle-ear vibration experiments

6.4.1.1 Experimental approach

The ex-vivo ME vibration experiments allowed us to rule out ME-muscle activity during measurement, as the current study is concerned with purely mechanical processes in the ear. However, it is well known that after death, the structure of soft tissue changes, which can affect the mechanical properties of parts of the system. The presented experiments are impossible to perform in vivo, so we are unable to compare the ex-vivo measurements to in-vivo results. However, studies of the ME input admittance in humans (e.g., Rosowski et al., 1990) have shown that changes after death are generally small if the preparations are kept moist and cool, which suggests that the chosen post-mortem approach is justified.

In order not to influence the natural shape of the ear canal, or the possible change of shape after beak opening, ME vibrations were not measured on the lateral surface of the TM but on the medial surface of the CFP. To reach the medial CFP surface, the skull was opened caudally and the IE was opened and drained, which also guaranteed that no additional quasi-static pressures were acting on the TM that could alter ME response. By sealing the sound source in the ear canal, the acoustic crosstalk defined

as the ratio of sound pressure between near the CFP and the closed ear canal is at least -25 dB. In sample R1R, however, the SPL at the CFP was only 15 dB lower than at the ear canal, which could be caused by a leaky sealing of the speaker. Even a crosstalk of as little as -15 dB should produce an increase in stapes motion of less than 0.1 dB. Moreover, the possible effect of the sound stimulation between opened and closed beak on the velocity ratio is nonexistent, as the acoustic crosstalk was the same with a closed and opened beak, and because the bird ME was shown to behave linearly up to stimulus levels of 120 dB SPL (Saunders, 1985).

Opening and draining the IE alters the vibration response of the CFP. For instance, the resonance frequency in the vibration response of the CFP is shifted to higher frequencies due to the presence of the IE, as has been reported on ostrich ears (Muyschondt et al., 2016b; Chapter 4 of this thesis). In the current paper, however, we are investigating the attenuation of an opened with respect to closed beak due to mechanical effects on the ear. When in a linear system the input sound pressure is lowered, the output (in this case the CFP velocity) will be lowered to the same degree. It has been demonstrated that ME nonlinearities exist (e.g., Aerts and Dirckx, 2010) but the effect is very small. On the other hand, removing the IE impedance will neither influence this part of the attenuation effect as long as it behaves linearly. Different from what is found in mammals, motions of the basilar membrane in the bird IE do not show any nonlinear behavior (Gummer et al., 1987), which suggests that the IE load is also linear. Therefore, it is reasonable to assume that the system behaves linearly for the sound pressures encountered during vocalization.

For the attenuation caused by mechanical changes in the ME and IE, the situation is more complicated. Even when the ME and IE behave linearly, the transfer of motion between the input (the TM) and the output (the CFP) depends on the acoustic impedance of the ME and IE, and on how their impedances changes due to the beak opening. It might be that the columella and extracolumella show more bending when coupled to a stiff IE than when acting upon an unloaded CFP. In such case, the reduction of columellar movement due to beak opening may be different in the case of an intact IE than in the case of a removed IE. It has been shown, however, that the avian IE impedance, as measured in ostrich, is ten to hundred smaller than the IE impedance measured in mammals (Muyschondt et al., 2016b; Chapter 4 of this thesis). In other words, the bird IE is a rather compliant structure. Nevertheless, it should be noted that the attenuation of CFP motion caused by beak opening in absence of the IE is not necessarily identical to the attenuation with the IE intact.

To measure the effect of beak opening, the beak was opened maximally during measurement. In certain birds it has been shown that louder sounds are produced with larger gaping (e.g., Williams, 2001; Goller et al, 2004), and that larger gapes are related to the production of higher frequencies (e.g., Hausberger, 1991; Westneat et al., 1993; Podos et al., 1995). It is not certain that these findings also apply to roosters

and, if so, whether they are associated with maximal beak opening during highest sound production.

In the presented experiments, sound pressures were introduced at the entrance of the ear canal. Yet, there remains a possibility that vocally evoked sounds are transmitted by the pharyngotympanic tubes to the medial TM surfaces. However, the pharyngotympanic tubes of chickens are closed most of the time and only open occasionally when swallowing (Larsen et al., 2016). Also in humans the tubes are normally closed and only occasionally open to pass gas between the ME cavity and the nasal cavity (e.g., Sadé and Ar, 1997; Dirckx et al., 2013). In humans, a clinical condition exists in which the Eustachian tubes are permanently open. People with this condition often hear their own voice very loudly due to internal sound transmission. In healthy people with a closed Eustachian tube, we can estimate the SPL reaching the medial TM surface relative to the lateral membrane surface due to self-generated sounds. Kawase et al. (2006) found that the SPL in healthy subjects was around 20 dB higher in the nasal cavity than in the ear canal. Measurements in patients with open Eustachian tube have shown an increase in the auditory threshold of 40 dB after treatment of the tube (i.e., by closing the tube) in response to sound pressures introduced in the nasal cavity (Kano et al., 2004; Hori et al., 2006). When we assume that the SPL behind the TM is as large as the SPL in the nasal cavity in people with an *open* Eustachian tube, then the SPL in subjects with *closed* tubes will be around 20 dB higher in front of the TM than behind the TM. In people with an open Eustachian tube, however, the actual sound pressure in the ME will be lower than the SPL in the nasal cavity due to attenuation of internal transmission. Therefore, the difference of 20 dB for closed tubes is merely a lower bound, so the effect of internal transmission remains limited.

6.4.1.2 *Experimental results*

In roosters, the decrease in vibration response of the CFP was shown to be significantly larger than the decrease observed in hens, i.e., 3.5 dB in roosters against 0.5 dB in hens on average. The possible source of the observed decrease in vibration response is a change in tension of the TM. In chickens, the skull is prokinetic, which implies that movements of the bill are a combination of lower jaw depression and upper jaw elevation (Van Den Heuvel, 1991). According to Ewald (1889), the skin covering the lower jaw pulls on the skin of the ear canal due to beak opening, which in turn pulls on the TM and changes its tension. On the other hand, the quadrate performs rotations that are associated with elevations of the upper jaw (Van Den Heuvel, 1991; Bout and Zweers, 2001), which could lead to changes in TM shape and tension (Starck, 1995). Claes et al. (2017) compared craniokinesis of the sexes in the domestic chicken and found a difference in upper jaw elevation, with roosters displaying a greater upper jaw lift than hens. As a result, roosters potentially exhibit larger gaping moderated by the quadrate. The more pronounced upper jaw elevation

in roosters goes along with larger rotational angles of the quadrate, potentially leading to greater structural changes to the ear of roosters. Claes et al. (2017) also observed clear differences in TM displacements in both ears of one hen and one rooster. In hens, the shape of the conical TM remained unchanged and the conical tip of the membrane did not move when the beak was opened. In roosters a substantial change in position of the conical tip of the TM was detected, corresponding to a flattening of the membrane. The observed displacements produced a relaxation of the membrane, which can be a cause of the observed 3.5 dB decrease in vibration velocity.

Another possible mechanism is related to the shape of the ear canal. The canal wall contains an erectile auditory pad – a semicircular worm-like elevation composed of connective tissue and venous spaces, which is better developed in male than in female chickens (Pohlman, 1921). This structure was first described by Wurm (1885) and von Graaf (1885) in capercaillie, arguing that it is responsible for the temporary deafness during sexual excitement by plugging the ear canals. Later, von Békésy (1949) observed that the entrance and the cross-sectional area of the rooster's ear canal become visibly smaller while raising the head during vocalization. The ear canal connected to the closed volume of the ME could act as a low-pass filter; decreasing the diameter of the canal increases its resistance, which lowers the cutoff frequency. Therefore, high-frequency sound components could be attenuated more when the ear canal becomes narrower. However, during the current experiments it could not be observed whether the opening of the ear canal effectively became smaller, due to the acoustic seal made of modeling clay applied around the canal entrance. Therefore it is likely that the attenuation observed is only related to a mechanical effect on the TM.

Despite the significant difference in attenuation between hens and roosters, the attenuation observed in the current study remains limited, providing little effective protection to the IEs. Therefore, effective protection from self-generated vocalizations in roosters must be more importantly obtained through other mechanisms. Ewald (1889) suggested a possible role of beak opening on the static IE pressure, which may result in a decrease of the cochlear response. Bray and Thurlow (1942) concluded from their measurements on pigeons that the observed 20 dB drop in cochlear response is a result of a rise in IE pressure alongside a change in TM tension. Therefore, the difference between the presented decrease of 3.5 dB and the drop of 20 dB observed by Bray and Thurlow (1942) may be partially due to a change in IE pressure, which was eliminated in the current experiments as the IE was drained. Additionally, it has been shown that ME-muscle activity in roosters causes attenuations of up to 20 dB (Counter and Borg, 1979, 1982; Borg and Counter, 1989). Therefore, the presently described effect is clearly inferior in magnitude. Another potential mechanism is that roosters open their pharyngotympanic tubes while crowing, allowing sound to pass through, which leads to transtympanic pressure loads that destructively interfere with (and thus attenuate) the direct pressure load on the TM. The existence of such a mechanism, however, remains speculative at present.

6.4.2 Rooster vocalization experiments

The experiments show that the maximal sound pressure produced by the rooster measured close to the ear of the animal amounts to 133.5 dB when averaged over multiple vocalizations. Individual vocalizations even reach values of 136 dB. Brackenbury (1977) recorded rooster vocalization at a distance of one meter from the animal and obtained values of 100 dB, which corresponds to an average sound power that is approximately 27 times larger than the maximal speech power produced during very loud human conversation (Gaunt et al., 1976). Borg and Counter (1989) reported a SPL of 130 dB measured at the head of the rooster, which is similar to our presented results. Such high pressure levels are above the commonly considered threshold of pain, which amounts to 120 dB, and is potentially harmful to the IE receptor cells. This result gives suggestive evidence for the need of protective mechanisms in the ear of roosters. As hens do not crow, they are less in need of such a mechanism in response to self-generated vocalizations.

Vocalizations are made up of harmonic series with a fundamental frequency around 0.6 kHz in the second half of the vocalization cycle. The two most prominent peaks in the spectrogram are the first and second harmonic. When relating the results of the vocalization recordings to the ME vibration experiments, it is observed that the first harmonic in the crowing signal at the maximal SPL (Figure 6.5 (b)) approaches the first resonance of the CFP response in the rooster ME (five top panels in Figure 6.3), which is around 0.55 kHz. The frequency of best hearing in chickens is located around 1.41 kHz (Saunders and Salvi, 1993), which is closer to the second harmonic in the vocalization signal (Figure 6.5 (b)). As overly loud sounds associated with vocalization are in the sensitive region of the chicken, some degree of auditory protection is needed. Sound attenuation related to beak opening shows no preferred frequency region, because the velocity loss of the CFP vibrations during beak opening is constant as a function of frequency (bottom panel in Figure 6.3). ME-muscle activity, on the other hand, has been shown to mainly influence low frequencies (Borg and Counter, 1989), so the total effect will be strongest around the first and second harmonic in the vocalization signal.

6.5 Conclusion

CFP vibration attenuation as a result of beak opening is fairly constant as a function of frequency, with an average vibration loss of 3.5 dB in roosters and 0.5 dB in hens. Although also in roosters the loss is small, the difference between hens and roosters is statistically significant. As observed by Claes et al. (2017), the dissimilarity between the sexes may be related to a difference in upper jaw elevation, and hence quadrature motion. The interpretation for the origin of the attenuation is the following: the kinetic quadrature causes change in shape and tension of the TM (Claes et al., 2017), which changes the transmission properties of the ME. Vocalization recordings show

maximal sound pressures of 133.5 dB SPL on average, and a frequency content that is in accordance with the hearing range of highest sensitivity in chickens. The obtained values are above the threshold of pain and are potentially harmful to the IE receptor cells, thus suggesting that a protective mechanism is needed against self-generated vocalizations. The attenuation related to beak opening is limited to about 3.5 dB, which will provide little effective protection to the IEs. Therefore, effective protection from loud self-generated vocalizations must be obtained by combining the mechanical effect of beak opening with other mechanisms such as ME-muscle activity.

CHAPTER 7 LASER VIBROMETRY TO STUDY THE REPAIR OF HUMAN MALLEUS FRACTURES

Abstract

This final chapter differs from the other chapters as it doesn't focus on the ME of birds, but on reconstructive surgery in the ME of humans after a fracture in the malleus. In the literature, several surgical methods have been reported that aim to improve hearing in patients with malleus fractures. However, it is still not clear which method gives the best results. In this study, LDV was used to compare the outcome of different surgical methods on malleus fractures in freshly frozen human temporal bones. Fractured malleus shafts were repaired with bone cement, with a malleus prosthesis from cortical bone, or with a PORP from cortical bone. The best result was achieved with the bone cement only, applied directly at the site of the fracture. The malleus prosthesis and the PORP gave similar results. As a conclusion, this chapter illustrates the use of ossicular prosthesis to restore the sound conduction of the damaged human ME chain, which can benefit of understanding of the single-ossicle ear of birds.

Major contributions to the development of the experimental setup and the analysis of the data. Minor contributions to the execution of the experiments and the writing of the paper. This chapter is based on:

Niklasson, A., Rönnblom, A., Muyschondt, P., Dirckx, J., von Unge, M., Tano, K., 2016. Ossiculoplasty on isolated malleus fractures: a human temporal bone study using laser Doppler vibrometry. *Otol. Neurotol.* 37, 895–901. doi:10.1097/mao.0000000000001086.

7.1 Introduction

According to the literature, isolated malleus fractures are not very common. In articles published during the latest thirty years only about forty such fractures are described (Niklasson and Tano, 2010). The main cause of this type of fracture is the withdrawal of a wet finger from the ear canal after taking a bath. Because isolated malleus fractures are not easy to find, if not specifically looked for, we believe that these fractures are often missed because the symptoms are rather diffuse. In the county of Norrbotten, Sweden, with a population of 250,000, we have identified approximately one case of isolated malleus fractures every year for the past eight years. This gives an incidence of about four in a million every year. The symptoms of an isolated malleus fracture are as follows: after pulling out a wet finger from the ear canal, the patient usually suffers from a short painful sensation and a permanent mild hearing loss or dullness in the ear. Occasionally, there is a tinnitus, usually of high frequency, that sometimes becomes permanent. Objective findings are a conductive hearing loss as seen in an audiogram that is usually in the mid and high frequencies, and hypermobility observed with tympanometry. If otomicroscopy is performed, a fracture line is sometimes seen, and with pneumatic otoscopy a hypermobile malleus shaft/umbo is often evident. Gentle palpation on the malleus shaft can also be useful in revealing this hypermobility. Watchful waiting, a hearing aid or an ossiculoplasty are options available for these patients.

The ossiculoplasty methods that have been used to treat isolated malleus fractures are, for example, fixation of the broken shaft with bone cement (Hato et al., 2007; Delrue et al., 2015), or ossiculoplasty with either a PORP (Chien et al., 2007; Blanchard et al., 2011) or a TORP (Abo-Khatwa et al., 2006). Different methods of ossiculoplasty have also been tried to spare the ossicular chain, as for example stabilization of the fracture with bone chips (Harris and Butler, 1985; Casale et al., 2010) or with cartilage (Chang et al., 2011). Because of the infrequent cases of isolated malleus fractures, it is nearly impossible to design a prospective study for comparing different ossiculoplasty methods to evaluate which methods give the best hearing results.

LDV is a method that has been previously used in numerous studies on patients with ME pathology and in temporal bone studies (Alian et al., 2010). The LDV method detects the velocity of the movements of the ossicular chain, which makes it possible to estimate the loss/gain of sound transmission. It is a noncontact method that allows repeated measurements without disturbing the sound transmission. Furthermore, the velocity of tiny vibrating structures such as the stapes footplate can be measured by determining the Doppler frequency shift of a low-intensity laser beam (21 mW) (Peacock et al., 2014).

In regard to the use of thawed temporal bones that had been freshly frozen, it was shown that the freezing process has minimal influence on vibroacoustic behavior (Rosowski et al., 1990).

The aim of the present study was to examine three different ossiculoplasty methods with LDV to evaluate which one of these methods would be best for restoring the sound transmission after an isolated malleus fracture.

7.2 Materials and methods

Fifteen freshly frozen human temporal bones, donated for research purposes, were used in the present study. The bones were prepared while still frozen by cutting away the cochlea, thus exposing the stapes footplate from the medial side. Furthermore, an access into the ME cavity from the middle fossa was drilled to visualize the TM and the ossicular chain (Figure 7.1). After this preparation, the bones were stored at -20°C . Before the measurements, the bones were thawed and a closed cavity containing an earphone speaker and a microphone was attached with screws to the bony ear canal. The manipulations of the ossicular chain were made under an operating microscope (OPMI Sensera/S7, Carl Zeiss, Jena, Germany).

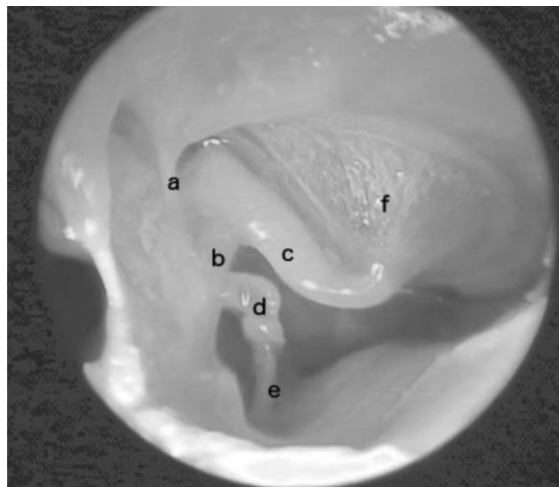


Figure 7.1. Picture of the drilled opening in the temporal bone and the access to the ME. The TM and the ossicular chain are intact. *a* = anterior ligament, *b* = tensor tympani tendon, *c* = malleus shaft, *d* = long process of the incus, *e* = stapes, *f* = TM.

During the whole procedure the TM was kept intact. The temporal bones were kept moistened with article towels soaked with saline. The LDV measurements were made within hours after thawing of the temporal bones, and care was taken that the stapes footplate was moistened repeatedly during the measurements. Each measurement was repeated two or three times to make sure stable results were obtained. Differences between repeated recordings were minimal, so in order not to unnecessary overload the figures the repeated measurements are not shown.

To determine the effect on the LDV measurements after several hours of waiting, one temporal bone was intentionally left without hydration and was remoistened during the experiments.

7.2.1 Description of the laser Doppler vibrometry method

A semi-closed cavity containing an earphone speaker and a condenser microphone was placed with its open end over the ear canal. The cavity was screwed to the temporal bone and the space between the temporal bone and the cavity was then sealed with plastic paste (Otoform AKX, Dreve Otoplastic, Unna, Germany), so that the earphone speaker was able to comfortably produce the desired SPL. Each temporal bone was equipped with its own sound-generating cavity. Microphones were calibrated against a probe microphone with a flat frequency response and a traceable calibration certificate (Probe Microphone Type 4182, Brüel & Kjær, Nærum, Denmark). For each measured frequency, the sound pressure was adjusted to 90 dB SPL with an accuracy better than 1 dB. The vibration of the stapes was measured with a LDV system (OFV-534 sensor head and OFV-5000 controller, Polytec, Waldbronn, Germany). The head of the vibrometer was mounted on an operation microscope, and the beam could be positioned and focused within the field of view by a motorized mirror and focusing lens (a detailed drawing of the setup can be found in Peacock et al., 2014). A patch of reflective material was put on the medial side of the footplate to obtain sufficient optical reflection for the vibrometer. Patches were about 0.4 mm × 0.4 mm in size, and had a mass of less than 0.04 mg, which is less than 1.5% of the stapes mass (2.73 ± 0.28 mg, De Greef et al., 2015). Vibration response of the stapes footplate was measured in a frequency range of 0.5 to 4 kHz at eight frequency lines per octave.

Three different types of simulated ossiculoplasty were performed on the temporal bones and measured with LDV:

1. Ossiculoplasty using only bone cement to stabilize the fractured malleus shaft. The bone cement, Otomimix (Olympus, Jacksonville, FL, USA), is a two-component cement that has been used clinically in otosurgery. A temporal bone was prepared as described above. With a backbiting forceps the malleus shaft was cut just distal to the tensor tendon (Figure 7.2 (a)). The fractured parts of the malleus were positioned near each other with a small piece of foam rubber that was put on the lateral surface of the TM via the ear canal. The TM was left intact and adherent to the malleus shaft and was not perforated. Bone cement was put on the medial surface of the malleus shaft and over the fracture. The foam rubber was removed after ten minutes, after which the bone cement had hardened before the measurements. LDV measurements were performed before and after surgery. Figure 7.2 (b) shows the fixation of the broken malleus shaft with bone cement.

2. Ossiculoplasty using a malleus-shaft prosthesis. A temporal bone was prepared as described above and a similar malleus fracture was made as above. The distal end of the fractured malleus shaft was carefully removed, avoiding any perforation of the TM. After cutting the anterior ligament of the malleus, a malleus prosthesis was put in place on the malleus neck and on the proximal part of the fractured malleus shaft to elongate the broken malleus shaft (Figure 7.3 (a)). The prosthesis was cut from cortical bone in the shape of a needle with a hole to fit around the short process of the malleus, and a groove to fit on the malleus (Figure 7.3 (b)). The prosthesis was fixed onto the malleus with bone cement and measurements were performed after at least ten minutes of hardening. The TM was fixed to the malleus prosthesis with fibrin tissue glue (Tisseel, Baxter, Deerfield, IL, USA) or commercial instant glue (Super Glue Precision, Loctite, Henkel, Düsseldorf, Germany). LDV measurements were performed before and after surgery. The removal of the anterior ligament of the malleus did not affect the velocity measurements (data not shown).
3. Ossiculoplasty with a PORP. A temporal bone was prepared as described above and a similar malleus fracture was made as above. The fractured distal end was carefully removed from the medial attachment to the TM, without damaging the TM. A PORP of cortical bone, about 3.5 mm in height, was placed from the stapes head to the TM (Figure 7.3 (c)). The PORP did not make any contact with the malleus shaft. The TM was attached to the PORP with tissue glue or instant glue to get a good contact between the PORP and the TM. LDV measurements were performed before and after surgery.

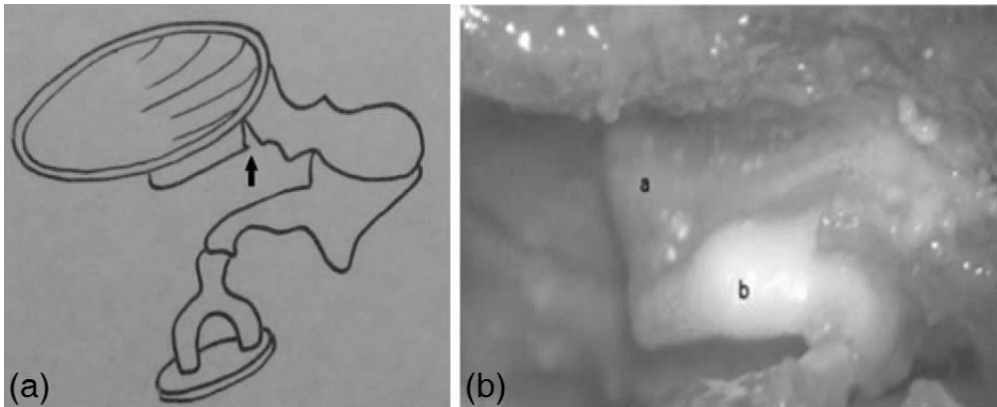


Figure 7.2. (a) Arrow shows the site of a proximal malleus fracture. (b) a = medial side of the TM. b = the repaired malleus shaft with bone cement.

To investigate the influence of the site of the malleus fracture on the sound transmission, the malleus shaft was cut at three different distances from the umbo – a distal (1 mm), a medial (2 mm), and a proximal (3 mm) fracture just distal to the tensor tympani tendon. LDV measurements were performed after each fracture. The

stapes velocity was also measured within a 24-hour time span, keeping the temporal bone at room temperature and after remoistening the stapes footplate.

All procedures involving the temporal bones used in the study were approved by the ethical committee of Umeå University, dnr 2014-352-31.

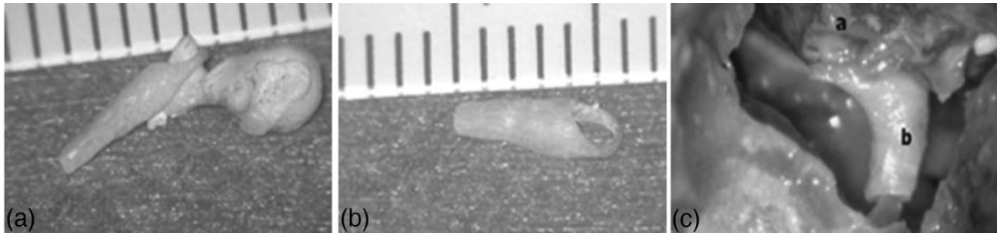


Figure 7.3. (a) The malleus prosthesis in position. Vertical bars = 1 mm. (b) Photograph of the malleus prosthesis made from cortical bone. There is a groove on the side of the prosthesis that is placed alongside the broken shaft to stabilize the prosthesis against the proximal remnant of the malleus shaft. (c) PORP sculptured from incus. a = medial side of the TM after removal of the distal end of the fractured malleus shaft. b = PORP in place on top of the stapes head.

7.3 Results

Figure 7.4–Figure 7.6 show changes in stapes velocity for a certain manipulation of the temporal bones, relative to the stapes velocity in the intact situation. Changes in velocity are depicted as velocity ratios that are considered relative to the line of zero velocity ratio, which represents the intact situation.

Figure 7.4 shows changes in stapes vibration response for different positions of the malleus fracture. An increasing loss of velocity is seen the more proximal the fracture is along the malleus shaft. The distal fracture shows a loss of velocity of about 5 dB in the higher frequencies (around 3 kHz) and in the medial fracture the loss of velocity is even more pronounced in the higher frequencies – about 10 to 20 dB loss of velocity. The proximal fracture showed a significant loss of velocity of about 35 dB, especially in the mid-frequency range (around 2 kHz) and about 15 dB loss in the higher frequencies.

The change of the stapes velocity within 21 hours was no more than 3 dB (Figure 7.5 (a)) when the specimen was rehydrated before the LDV measurements. However, there was a rapid deterioration of the velocity if the footplate was not rehydrated before the LDV measurements (Figure 7.5 (b)).

Detaching the malleus shaft from the TM, except at the umbo and short process, had a minimal effect on the stapes velocity (data not shown). Thus, it seemed that the most important attachment between the malleus and TM was at the short process and umbo.

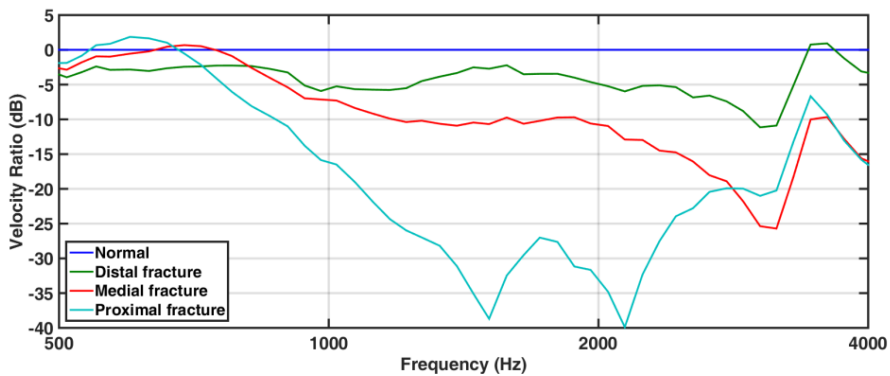


Figure 7.4. Change of stapes vibration response as a function of frequency for different positions of the malleus fractures. The zero line depicts the situation before the fractures were made. The loss of velocity in the medial and distal fractures is most pronounced in the higher frequencies, and in the proximal fracture there is a significant loss especially in the mid frequencies.

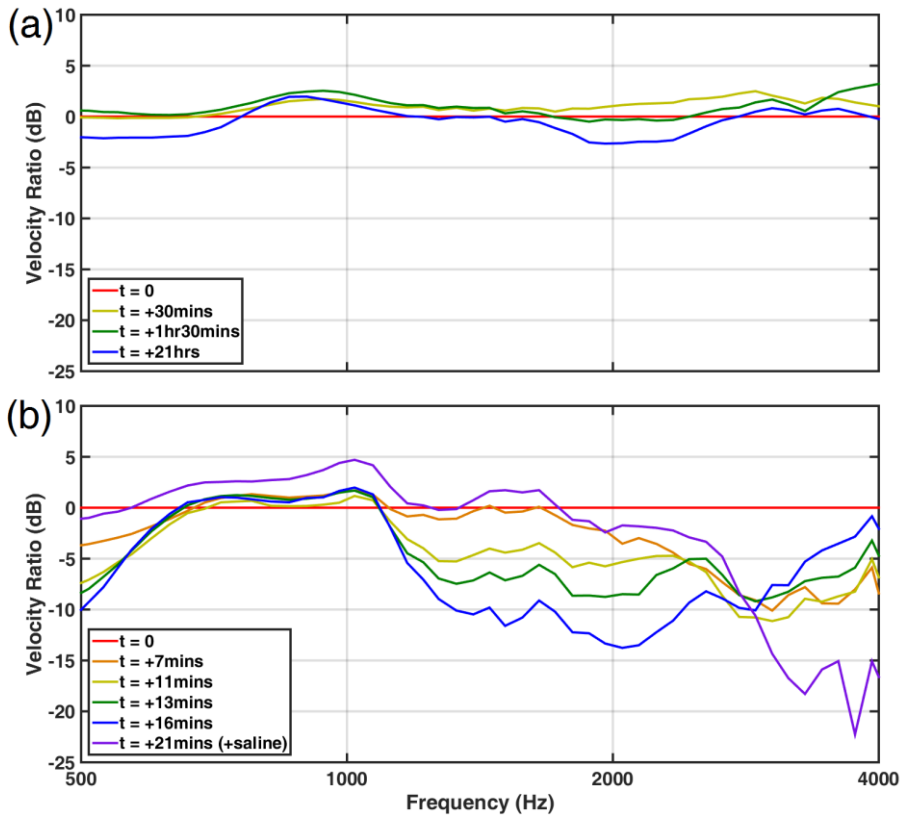


Figure 7.5. (a) Change of stapes velocity over a 21-hour time span. The maximal loss of velocity of nearly 3 dB is found at 2 kHz after 21 hours. LDV measurements for the experiments were made within a few hours after thawing. (b) Change of stapes velocity as a function of time, without rehydration of the specimen. This figure displays the importance of keeping the stapes footplate hydrated before each measurement, as a progressive loss of velocity is already observable after ten to fifteen minutes. When the footplate was rehydrated (+21 min + saline), the velocity recovered.

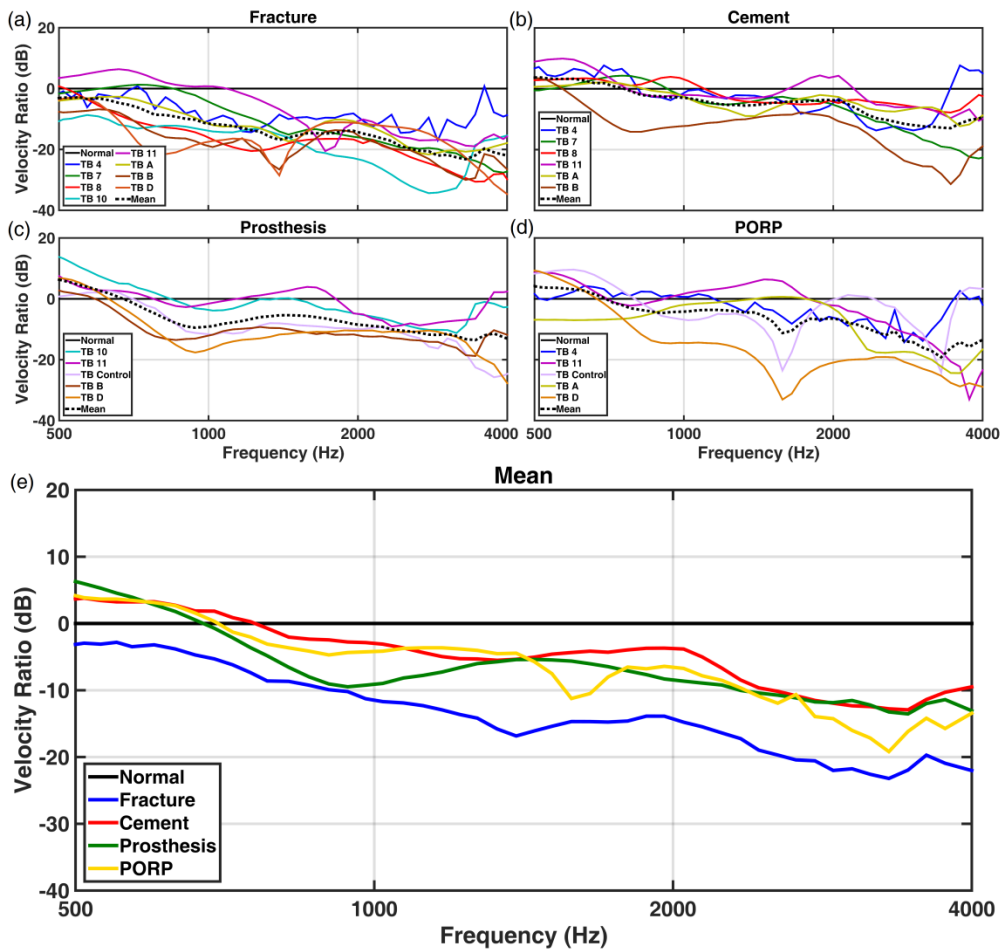


Figure 7.6. Changes in stapes velocity after manipulation of the sample, presented as velocity ratios (dB) relative to the condition before the fracture was made (line of 0 dB). (a) Effect of a proximal isolated malleus fracture on the change in stapes velocity, measured in eight different temporal bones (TB). There is a clear increasing trend in the loss of velocity towards higher frequencies, which is also found in clinical cases with a similar fracture. (b) Effect of treating the isolated malleus fractures with bone cement after attaching the fractured parts as close as possible to each other. The mean recovery at 1 and 2 kHz is about 10 dB compared with the fractured situation. (c) Effect of treating the isolated malleus fractures with a malleus prosthesis. The mean recovery at 1 and 2 kHz is only about 5 dB compared with the fractured situation. The best result is seen in the mid-frequency range. (d) Effect of treating the isolated malleus fractures with a PORP made of cortical bone (see Figure 7.3 (c)). The mean recovery at 1 and 2 kHz is between 5 and 10 dB compared with the fractured situation. The best result with the PORP is observed in the lower and mid frequencies. (e) Graphical plot of mean values of the above procedures.

Figure 7.6 shows the effect of different restoration procedures on the stapes velocity. Figure 7.6 (a) shows the stapes velocity change because of a malleus fracture, measured in eight temporal bones. When an isolated malleus fracture is created just distal to the tensor tympani tendon (= proximal fracture), a loss of velocity is seen

which is more pronounced at the higher frequencies. The mean loss of velocity, compared with the normal situation, is 12 dB at 1 kHz, 14 dB at 2 kHz, and 23 dB at 4 kHz. Although the fracture was made in the same way in all of the eight temporal bones, there is a wide range regarding the loss of velocity, so the loss of velocity at 4 kHz varies between 10 and 35 dB. Repairing the fractured malleus shaft with bone cement only (Figure 7.6 (b)) shows nearly no loss of velocity up to about 2 kHz, although the mean value declines by 10 dB at 4 kHz. The mean loss of velocity with the bone-cement method is 3 dB at 1 kHz, 3 dB at 2 kHz, and 10 dB at 4 kHz. The malleus-prosthesis method (Figure 8.6 (c)) already shows a loss of 10 dB from 1 kHz and onwards. The mean loss of velocity with the malleus prosthesis is 10 dB at 1 and 2 kHz and 13 dB at 4 kHz. The PORP method (Figure 7.6 (d)) shows a decline of 10 dB after 1.5 kHz and shows the worst results of the three methods in the higher frequency range. The mean loss of velocity with the PORPs is 5 dB at 1 kHz, 7 dB at 2 kHz, and 14 dB at 4 kHz. All three methods show good results in the lower frequency range, but the results of the PORP method have the largest spread, while the other two ossiculoplasty methods show more predictable results across the different temporal bones. Figure 7.6 (e) shows the mean values of the results depicted in Figure 7.6 (a)–(d). The bone cement method thus showed a slightly better result compared with the other two methods.

7.4 Discussion

Isolated fractures of the malleus are easily missed in the clinic. As they are quite rare, it is difficult to gather enough clinical material for randomized clinical studies of treatment methods. The multitude of different suggested methods in the literature might be explained by this difficulty to perform clinical trials. The present study aimed to compare the vibroacoustic outcome of three different ossiculoplasty methods *in vitro*: one that has recently been used clinically with good results, namely the bone-cement method (Delrue et al., 2015), a new method designed by one of the authors (AN) called the malleus-prosthesis method, and finally the PORP method, which is the most commonly used ossiculoplasty method when the stapes superstructures are intact. One drawback of the PORP method, in contrast to the other two methods, is that it requires the removal of the incus and subsequently the destruction of the ossicular chain.

By using freshly frozen human temporal bones and the LDV method, we were able to perform the ossiculoplasty operations under controlled conditions to compare the efficacy of each of the methods for restoring hearing. The LDV method has been used previously on temporal bones for such purposes (e.g., Peacock et al., 2013, 2015b). In the present study the velocity was measured at the medial side of the stapes footplate, which is a well accessible measurement site and relevant for assessing acoustic energy transmission to the IE. Moreover, thereby the highest measurement sensitivity is obtained. Manipulations on the ossicular chain can be done, and the laser beam can

be easily repositioned to the same location and under the same angle between subsequent manipulations of the temporal bone. Furthermore, by measuring footplate motion from the medial side, there is no need for an additional opening to the ME cavity to access the footplate with the laser beam. This access to the ME and IE allowed us to keep both the TM and the remnants of the ossicular chain intact. Removal of the cochlea evidently changes the acoustic impedance of the system, but as all measurements are done under this same condition this can be accepted for the benefit of the advantages mentioned.

The created proximal malleus fractures caused a loss of velocity that is in accordance with the clinical situation of patients with isolated malleus fractures that carry a conductive hearing loss which increases towards the higher frequencies. Also in the clinical situation the degree of hearing loss varies, even when fractures have similar locations on the handle of the malleus. The reason for this is unclear, but further studies possibly including the use of digital holography might shed light on this.

The present study showed that stabilization of the fractured malleus handle with bone cement yielded the best velocity restoration, and could therefore be recommended as a method of choice in the clinic, although many imponderabilia still prevail in this issue. The results were in accordance with reports from Hato et al. (2007) and of Delrue et al. (2015) who also reported good results after ossiculoplasty with bone cement. PORP placement is a conventional ossiculoplasty method, but it involves further destruction of the ossicular chain and often leaves an air-bone gap of about 10 dB (O'Reilly et al., 2005). The PORP method also showed the largest variation in velocity recordings, which corresponds well with clinical reports on a wide range of postoperative hearing outcomes (Galy-Bernadoy et al., 2014). In some of the patients with isolated malleus fractures that had been on watchful waiting for a longer time, our experience is that the distal part of the fractured malleus could be degenerated and atrophied. In such a situation, the bone cement method is probably not ideal, and the PORP or malleus prosthesis method could be an alternative.

7.5 Conclusion

Isolated malleus fractures in freshly frozen and thawed temporal bones lead to stapes velocity changes that resemble the changes in hearing sensitivity as observed in the clinical situation, namely a conductive hearing loss that increases towards higher frequencies. The treatment when the fractured handle of the malleus was stabilized with bone cement only showed a slightly better result than using a PORP or specially designed malleus prosthesis from cortical bone.

GENERAL CONCLUSIONS

This dissertation revolves around the functioning of the single-ossicle ME of birds and the research techniques to investigate it. Only Chapter 7 differs from this scope as it focuses on the human ME. In the current chapter, the most important conclusions from each chapter are summarized, and an outlook for future directions in the same research field is provided.

Summary of conclusions

In Chapter 3, the acoustic response and mechanical properties of the single-ossicle ME of birds was investigated in mallard duck. This study was conducted by combining the results of FE simulations and vibration experiments acquired with stroboscopic holography and LDV. Similarly to the mammalian ME it was found that TM vibrations were mostly influenced by the Young's modulus of the TM. The velocity response function at the CFP mostly depended on the Young's moduli of the annular ligament, the TM and the extracolumella, in that order. By using the full-field vibration measurements of the TM, the TM Young's modulus was determined by inverse analysis and found to be equal to 33.0, 41.9 and 72.6 MPa in three respective specimens, showing considerable interindividual variability. Our results suggest that, similar to mammals, moderate damping in the TM needs to be present to describe the measured full-field vibration phase patterns on the TM. The velocity response functions of the extrastapedial tip and CFP are around ten times larger in magnitude than what is generally found in mammals. The velocity ratio of the extrastapedial tip to the CFP ranges from 1.5 to 2.5, denoting a positive lever action of the single-ossicle ME apparatus.

Chapter 4 covered a study of the acoustic input impedance of the avian IE, measured in ostrich. This impedance was determined by means of vibration measurements on the columella and by comparing the response before and after draining the IE. For acoustic frequencies between 0.3 and 4 kHz, the columella was stimulated directly with a miniature magnet and the resulting vibrations were measured with LDV. The quasi-static response from 1 to 20 Hz was assessed by using a piezo displacement transducer combined with a force sensor. The mean values of the obtained impedance curves were fitted by means of a simple RLC model, resulting in a stiffness reactance of $K_{IE} = 0.20 \cdot 10^{12}$ Pa/m³, an inertial impedance of $M_{IE} = 0.652 \cdot 10^6$ Pa·s²/m³ and a damping resistance of $R_{IE} = 1.57 \cdot 10^9$ Pa·s/m³. These values were one to two orders of magnitude smaller than what is found in mammal ears. At low frequencies, the

difference of the measured impedance between intact and opened IE was negligible, showing that the round window does contribute little to the stiffness reactance. At high frequencies, the inertial impedance of the IE fluids was smaller than the total inertia of the IE, although the impedance behavior deviated from a purely inertial component in this frequency range.

In Chapter 5, the motions of the CFP were determined in response to both quasi-static and dynamic (acoustic) pressures. The quasi-static motion was measured by means of μ CT when the MEs were subjected to pressures of either -1 or $+1$ kPa. In these measurements, both piston-like and rocking motion was observed at the CFP. Piston-like motion was mostly dominant, although the ratio of rocking-to-piston motion was larger for negative than for positive ME pressure. In the dynamic pressure experiments, acoustically induced CFP vibrations were measured with LDV from 0.125 to 4 kHz on the medial surface of the CFP after opening and draining the IE. At frequencies below 1 kHz, rocking-to-piston ratios were constant as a function of frequency with values of less than 0.1. For higher frequencies, the rocking motion increased relative to the piston component, although the piston component quantitatively remained the largest. A FE model was created to validate the experimental results and to investigate the influence of the IE impedance, which was determined in the preceding chapter. This load caused the rocking-to-piston ratio of CFP motion to increase relative to the result with unloaded CFP, but only above 0.8 kHz. At higher frequencies, the model showed that columellar motions could no longer be identified as purely piston-like or rocking.

Chapter 6 investigated the influence of beak opening on sound transmission in the ME of chickens. This was achieved by measuring ME vibrations with LDV and comparing the results between closed and maximally opened beak. In this way the hypothesis could be tested that the vibration attenuation is larger in loudly vocalizing males than in more silent females, which should be less in need of a possible protective mechanism. CFP vibration attenuation as a result of beak opening was fairly constant with frequency, showing an average vibration loss of 3.5 dB in roosters and 0.5 dB in hens. In both cases the attenuation was small, contributing little to sound attenuation, although the difference between males and females was shown to be statistically significant. The dissimilarity between the sexes may be related to the difference in upper jaw elevation, and hence also the motion of the quadrate bone. Possibly, the kinetic quadrate causes a change in shape and tension of the TM, altering ME sound transmission. Sound recordings of a crowing rooster showed maximal sound pressures of 133.5 dB SPL close to its own ears. These values are above the threshold of pain (commonly considered in humans) and are potentially harmful to the IE receptor cells, suggesting that a protective mechanism is needed for self-generated vocalizations. As the observed attenuation related to beak opening is limited, effective protection must be obtained by combination with other mechanisms.

In Chapter 7, the effect of a fracture in the handle of the malleus on ME sound conduction was investigated in human temporal bone experiments. This effect was assessed by measuring the vibration response at the stapedial footplate, and by comparing the result before and after surgically applying a fracture. It was found that the vibration velocity response resembled the clinical situation, i.e., a conductive hearing loss that increases with acoustic frequency. Different surgical methods to reconstruct the broken ossicular chain were applied on the measured specimens and compared to each other. The treatment when the fractured malleus handle was stabilized with only bone cement showed a slightly better result than when using a PORP or specially designed malleus prosthesis from cortical bone.

Future directions

In Chapter 3, the most relevant mechanical parameter values of the TM were determined, i.e., the Young's modulus. In future, it would be interesting to determine the value of the Young's modulus not only at a single acoustic frequency but at a range of frequencies to investigate how it varies with frequency due to viscoelasticity. Possibly, the loss modulus characterizing the viscous portion of the TM's mechanical behavior could also be determined. Instead of only considering acoustic frequencies, one could also examine the viscoelastic deformation of the TM in response to large quasi-static pressures variations, where the elastic behavior of the ME typically becomes nonlinear. Beside the mechanical parameters of the TM, there are other structures in the avian ME of which the parameter values are very uncertain. For instance, the extracolumella, which is believed to buffer quasi-static pressure variations in the avian ear, consists of cartilage that typically ossifies with age. An interesting idea would be to determine the Young's modulus of this structure by means of point indentation measurements, or by pressurizing the ME apparatus and measure the stiffness of the extracolumella in situ. By performing these experiments on specimens of different ages, it could be verified how the elasticity of this structure changes over time.

In Chapter 4, CFP vibration velocities were measured before and after draining the IE to determine the acoustic impedance of the IE. However, the impedance can also be determined by assessing the CFP vibration velocity only with IE intact and by simultaneously measuring the acoustic pressure in the IE fluid right behind the CFP. For validation, it should be examined whether both methods indeed yield the same result. In the current experiments, the IE impedance was only determined for motions in the piston direction. However, it could be valuable to also measure the impedance related to rocking motion, and investigate whether it can indeed be neglected as assumed. From our results it was concluded that the IE impedance is one to two orders of magnitude smaller in ostrich than in humans and other mammals. A simple estimation suggested that the impedance is higher for smaller birds, but that this scaling is not sufficient to explain the difference between birds and mammals. To

further explore this, the IE impedance should also be determined in smaller bird species. In this way it can be investigated whether birds are indeed less in need of impedance matching between the outer ear and IE than mammals, given the smaller avian IE impedance.

In Chapter 5 the motions of the CFP were investigated in ostrich, and it was found that the motion was mostly piston-like but that small rocking motions were also present. However, it would be interesting to examine whether these results also apply to other avian species. Perhaps it is possible in other birds to measure CFP vibration from the lateral side on multiple positions, so the IE does not need to be drained in order to characterize CFP motion. On the other hand, we only investigated piston-like and rocking motions in the current experiments. However, translations and rotations in the plane of the CFP may also be present, although they are usually neglected. In birds, which have relatively wide annular ligaments compared to mammals, it is possible that these motions are not negligible as they potentially give the CFP more freedom to move. These in-plane motions could be quantified by measuring CFP vibrations on different points and under different angles with LDV. Beside the dynamic motions, the quasi-static motions were determined in this work for ME pressures of +1 and -1 kPa. However, at such large pressures ME deformations typically become nonlinear. This behavior could be examined by measuring the motion at a range of pressures, which has recently been done on chicken ears. These experiments resulted in nonlinear deformation of the extrastapedial tip and CFP, and for both anatomical locations the deformation curves were different for positive than for negative ME pressure. In contrast to mammals, however, the deformations were larger in the medial direction (negative ME pressure) than in the lateral direction (positive ME pressure). This difference is likely due to the inverted cone shape of the avian TM. In future, model calculations to compare the TM deformation between birds and mammals could be executed to attempt to explain this difference.

In Chapter 6, the effect of beak opening on acoustic transmission through the chicken ME was investigated. Despite the fact that the observed attenuation is too small to effectively contribute to protection for self-generated rooster vocalizations, the observed difference between roosters and hens was statistically significant. This effect was attributed to a difference in deformation of the TM through its connection with the kinetic quadrangle, leading to a different membrane tension. To quantify the change in TM shape, full-field deformation and strain measurements can be performed by using optical techniques such as 3D digital image correlation (DIC). Also here it would be interesting to investigate whether such an attenuating effect is also present in other avian species, as was already observed in pigeons (Ewald, 1889) and whether it is functional in these other birds.

In Chapter 7, different types of prostheses were implanted in the human ossicular chain, such as a PORP, to restore a fracture in the handle of the malleus. As discussed

earlier, single-ossicle prostheses such as a TORP have difficulties to buffer sudden external pressure changes. By learning from nature, we could attempt to develop an ideal single-ossicle prosthesis based on the functional principles of the single-ossicle ear of birds. As explained, one property that is typical for single-ossicle ears is that the TM is shaped as a cone with the tip pointing outwards, which differs from the three-ossicle ear of mammals where the conical TM points inwards. Because it is very probable that the ideal TM shape for a single-ossicle ear is outward oriented, it could be very promising to use this principle in ME surgery in patients with a single-ossicle prosthesis. Beside the principle of the inverted TM, it is an interesting idea to design a prosthesis with compliant elements based on the cartilaginous extracolumella of birds, which are able to handle external pressure changes. Before these principles can be applied in clinical surgery, they first need to be tested by ex-vivo experiments and computer modeling.

NEDERLANDSTALIGE SAMENVATTING

Het vermogen om te horen is een essentieel aspect in ons dagelijks leven. Volgens de Wereldgezondheidsorganisatie lijdt meer dan 5% van de wereldbevolking – 360 miljoen mensen – aan een vorm van gehoorverlies. Een geschikte behandeling vinden voor gehoorverlies is dus één van de meest relevante medische uitdagingen in onze tijd. Het oor bestaat uit drie hoofdonderdelen: het buitenoor, het middenoor en het binnenoor. Het menselijk middenoor bevat een trommelvlies en drie kleine gehoorbeentjes. Bij sommige gehoorsaandoeningen is deze keten van beentjes niet in staat om geluid verder te geleiden naar het binnenoor, hetgeen soms alleen kan worden opgelost door de beentjes chirurgisch terug aan elkaar te koppelen of te vervangen. In sommige gevallen wordt een prothese geïmplantéerd die één of meerdere beentjes vervangt. Een prothese die het trommelvlies rechtstreeks verbindt met het binnenoor heet een TORP ('total ossicular replacement prothesis') en wordt ook wel eens een éénbeentjes- of pistonprothese genoemd. Dit soort prothese functioneert redelijk goed, maar ze mist de nodige flexibiliteit om grote en plotse drukveranderingen op te vangen die kunnen optreden in het dagelijks leven. Dit gebrek aan buigzaamheid kan ervoor zorgen dat de prothese te diep in het binnenoor dringt, ontwricht of zich ontkoppelt van de middenoorketen.

Zoogdieren, waaronder mensen, zijn de enige klasse van gewervelde dieren met drie beentjes in hun middenoor. Amfibieën, reptielen en vogels hebben zo maar één gehoorsbeentje – de columella – om geluidsenergie te transporteren van het buitenoor naar het binnenoor toe. Het is nog steeds een raadsel hoe de natuur erin is geslaagd om een éénbeentjesoor te ontwikkelen dat de flexibiliteit heeft om grote drukveranderingen te kunnen opvangen, zonder dat het vermogen om geluidsenergie te geleiden wordt aangetast. Dit doctoraatsproefschrift focust op het middenoor van vogels om de mechanische werking van éénbeentjesoren te onderzoeken. Van de dieren met een éénbeentjesoor hebben vogels grotendeels het sterkste gehoor, terwijl ze net het meest zijn blootgesteld aan externe drukveranderingen. Het mechanische gedrag en materiaalparameters van dit type oor onder invloed van quasi-statische en dynamische drukken zijn echter grotendeels onbekend. Nieuwe inzichten in de mechanische functie van het vogeloor zouden uiteindelijk zeer nuttig kunnen blijken voor het ontwikkelen van verbeterde éénbeentjesprothesen voor mensen.

Dit proefschrift is opgedeeld in twee delen. **Deel I** omvat twee hoofdstukken met een algemene inleiding tot de onderwerpen en technieken die worden behandeld in de vijf hoofdstukken van Deel II. Hoofdstukken 1 en 2 kunnen door de lezer worden

geraadpleegd als een referentiegeds tot de terminologie, de theoretische principes en de onderzoekstechnieken die worden gebruikt in de latere hoofdstukken. In **Deel II** worden de algemene resultaten van dit proefschrift besproken in vijf hoofdstukken die sterk zijn gebaseerd op verschillende onderzoekspapers.

Hoofdstuk 1 introduceert de basisprincipes van geluid en gehoor, en geeft een samenvattend overzicht van de structuur en functie van het oor van vogels. De anatomie en fysiologie van het buitenoor, middenoor en binnenoor worden besproken, al wordt het middenoor in meer detail besproken dan de andere twee onderdelen. **Hoofdstuk 2** geeft een overzicht van de theorie van structurele mechanica relevant voor dit werk, de computationele technieken om het middenoor te modelleren en de toegepaste experimentele methoden om de morfologie en het vibratiegedrag van het middenoor te meten. **Hoofdstuk 3** is het eerste hoofdstuk over mijn onderzoek en bestudeert de vibroakoestische respons en de mechanische eigenschappen van het middenoor van de wilde eend. De meest invloedrijke materiaalparameters van het trommelvlies worden bepaald door de uitkomst van het computermodel aan te passen aan meetdata van vibraties in het middenoor. **Hoofdstuk 4** levert de allereerste meetdata van de akoestische inputimpedantie van het vogelbinnenoor, gemeten in struisvogels. Het binnenoor is gevuld met vloeistoffen die een zekere belasting of impedantie aan de middenoorcomponenten opleggen. Deze impedantie is een belangrijke grootte omdat ze het vibratiegedrag en dus ook de geluidstransmissie van het middenoor beïnvloedt. In **Hoofdstuk 5** worden de quasi-statische en dynamische bewegingen van het enkele gehoorsbeentje in de struisvogel bepaald. Het dynamische vibratiegedrag wordt gemeten in afwezigheid van het binnenoor. Vervolgens wordt een computermodel ontwikkeld om de gemeten beweging te valideren en om het effect van de belasting van het binnenoor op deze beweging te onderzoeken. **Hoofdstuk 6** onderzoekt het effect van bekopening op de akoestische transmissie in het oor van kippen door de verandering in middeeroorvibraties te meten, en er wordt een vergelijking gemaakt tussen hanen en hennen. De hypothese is dat de afname van akoestische transmissie groter is in mannetjes dan in vrouwtjes, gezien het grote verschil in vocalisatievermogen tussen beide geslachten. De geluidsintensiteit van de kraai van een haan wordt gemeten dichtbij zijn eigen oren om te illustreren dat hij mogelijk een mechanisme nodig heeft om zich te beschermen tegen zijn eigen gekraai. **Hoofdstuk 7** bestudeert het effect van een breuk in de manubrium van de malleus – het eerste beentje in het menselijk middenoor – op de vibroakoestische transmissie. Er worden vibratiemetingen uitgevoerd op menselijke oorspecimens, en verschillende chirurgische methoden om de breuk te herstellen worden vergeleken. Dit hoofdstuk verschilt qua onderwerp van de anderen, maar het illustreert hoe prothesebeentjes worden gebruikt om de middenoorketen te herstellen, hetgeen zijn voordeel kan doen bij een betere begrip van de werking van het middenoor van vogels.

BIBLIOGRAPHY

- Abo-Khatwa, M., Addams-Williams, J., Vincent, R., Osborne, J., 2006. Malleus-handle fracture: literature review and a new surgical approach. *Internet J. Otorhinolaryngol.* 4, 1–6. doi:10.5580/20e.
- Aernouts, J., 2012. Mechanical properties of the tympanic membrane: measurement and modeling. Ph.D. thesis, University of Antwerp, Antwerp.
- Aernouts, J., Aerts, J.R.M., Dirckx, J.J.J., 2012. Mechanical properties of human tympanic membrane in the quasi-static regime from in situ point indentation measurements. *Hear. Res.* 290, 45–54. doi:10.1016/j.heares.2012.05.001.
- Aerts, J.R.M., Dirckx, J.J.J., 2010. Nonlinearity as a function of frequency and sound pressure. *Hear. Res.* 263, 26–32. doi:10.1016/j.heares.2009.12.022.
- Aibara, R., Welsh, J.T., Puria, S., Goode, R.L., 2001. Human middle-ear sound transfer function and cochlear input impedance. *Hear. Res.* 152, 100–109. doi:10.1016/S0378-5955(00)00240-9.
- Alian, W.A., Majdalawieh, O.F., van Wijhe, R.G., Ejnell, H., Bance, M., 2010. Prosthetic reconstruction from the tympanic membrane to the stapes head or to the stapes footplate? A laser Doppler study. *Hear. Res.* 263, 236–237. doi:10.1016/j.heares.2010.03.021.
- Allen, J.B., 1986. Measurement of eardrum acoustic impedance. In: Allen, J.B., Hall, J.L., Hubbard, A.E., Neely, S.T., Tubis, A. (Eds.), *Peripheral Auditory Mechanisms. Lecture Notes in Biomathematics.* Springer-Verlag, Berlin, Heidelberg, pp. 44–51. doi:10.1007/978-3-642-50038-1_6.
- American Society of Mechanical Engineers (ASME), 2006. *Guide for verification and validation in computational solid mechanics.* American Society of Mechanical Engineers, New York.
- Arechvo, I., Zahnert, T., Bornitz, M., Neudert, M., Lasurashvili, N., Simkunaite-Rizgeliene, R., 2013. The ostrich middle ear for developing an ideal ossicular replacement prosthesis. *Eur. Arch. Otorhinolaryngol.* 270, 37–44. doi:10.1007/s00405-011-1907-1.
- Banks, H.T., Hu, S., Kenz, Z.R., 2011. A brief review of elasticity and viscoelasticity for solids. *Adv. Appl. Math. Mech.* 3, 1–51. doi:10.4208/aamm.10-m1030.
- Blanchard, M., Abergel, A., Verillaud, B., Williams, M.T., Ayache, D., 2011. Isolated malleus-handle fracture. *Auris Nasus Larynx* 38, 439–443. doi:10.1016/j.anl.2010.11.011.
- Bock, W.J., 1964. Kinetics of the avian skull. *J. Morphol.* 114, 1–42. doi:jmor.1051140102.

- Bonet, J., Wood, R.D., 1997. *Nonlinear Continuum Mechanics for Finite Element Analysis*. Cambridge University Press, Cambridge. doi:10.1017/CBO9780511755446.
- Borg, E., Counter, S.A., 1989. The middle-ear muscles. *Sci. Am.* 261, 74–80. doi:10.1038/scientificamericano889-74.
- Bout, R.G., Zweers, G.A., 2001. The role of cranial kinesis in birds. *Comp. Biochem. Physiol. A Mol. Integr. Physiol.* 131, 197–205. doi:10.1016/S1095-6433(01)00470-6.
- Brackenbury, J.H., 1977. Physiological energetics of cock-crow. *Nature* 270, 433–435. doi:10.1038/270433a0.
- Bray, C.W., Thurlow, W.R., 1942. Temporary deafness in birds. *The Auk* 59, 379–387. doi:10.2307/4079207.
- Buytaert, J.A.N., 2010. *New optical tomographic & topographic techniques for biomedical applications*. Ph.D. thesis, University of Antwerp, Antwerp.
- Buytaert, J.A.N., Goyens, J., De Greef, D., Aerts, P., Dirckx, J.J.J., 2014. Volume shrinkage of bone, brain and muscle tissue in sample preparation for micro-CT and light sheet fluorescence microscopy (LSFM). *Microsc. Microanal.* 20, 1208–1217. doi:10.1017/S1431927614001329.
- Casale, M., De Franco, A., Rinaldi, V., Zini, C., Salvinelli, F., 2010. Isolated fracture of the malleus handle: A video clip. *Laryngoscope* 120, 813–814. doi:10.1002/lary.20783.
- Counter, S.A., Borg, E., 1979. Physiological activation of the stapedius muscle in *Gallus gallus*. *Acta Otolaryngol.* 88, 13–19. doi:10.3109/00016487909137134.
- Counter, S.A., Borg, E., 1982. The avian stapedius muscle. *Acta Otolaryngol.* 94, 267–274. doi:10.3109/00016488209128913.
- Chang, Y.N., Hung, C.C., Lee, J.C., Wang, C.H., 2011. Isolated malleus-handle fracture surgical repair using tragal cartilage. *Am. J. Otol.* 32, 77–79. doi:10.1016/j.amjoto.2009.09.005.
- Cheng, J.T., Aarnisalo, A.A., Harrington, E., del Socorro Hernandez-Montes, M., Furlong, C., Merchant, S.N., Rosowski, J.J., 2010. Motion of the surface of the human tympanic membrane measured with stroboscopic holography. *Hear. Res.* 263, 66–77. doi:10.1016/j.heares.2009.12.024.
- Cheng, J.T., Hamade, M., Merchant, S.N., Rosowski, J.J., 2013. Wave motion on the surface of the human tympanic membrane: holographic measurement and modeling analysis. *J. Acoust. Soc. Am.* 133, 918–937. doi:10.1121/1.4773263.
- Chien, W., McKenna, M.J., Rosowski, J.J., Merchant, S.N., 2007. Isolated fracture of the manubrium of the malleus. *J. Laryngol. Otol.* 122, 898–904. doi:10.1017/S0022215107000990.
- Chin, K., Kurian, R., Saunders, J.C., 1997. Maturation of tympanic membrane layers and collagen in the embryonic and post-hatch chick (*Gallus domesticus*). *J. Morphol.* 233, 257–266. doi:10.1002/(SICI)1097-4687(199709)233:3<257::AID-JMOR5>3.0.CO;2-o.

- Claes, R., Muysshondt, P.G.G., Van Hoorebecke, L., Dhaene, J., Dirckx, J.J.J., Aerts, P., 2017. The effect of craniokinesis on the middle ear of domestic chickens (*Gallus gallus domesticus*). *J. Anat.* 230, 414–423. doi:10.1111/joa.12566.
- Cohen, Y.E., Rubin, D.M., Saunders, J.C., 1992. Middle ear development. I: Extra-stapedius response in the neonatal chick. *Hear. Res.* 58, 1–8. doi:10.1016/0378-5955(92)90002-5.
- Dancer, A., Franke, R., 1980. Intracochlear sound pressure measurements in guinea pigs. *Hear. Res.* 2, 191–205. doi:10.1016/0378-5955(80)90057-x.
- Dawson, M.M., Metzger, K.A., Baier, D.B., Brainerd, E.L., 2011. Kinematics of the quadrate bone during feeding in mallard ducks. *J. Exp. Biol.* 214, 2036–2046. doi:10.1242/jeb.047159.
- De Arantes E Oliveira, E.R., 1968. Theoretical foundations of the finite element method. *Int. J. Solids Struct.* 4, 929–952. doi:10.1016/0020-7683(68)90014-0.
- De Greef, D., Soons, J.A.M., Dirckx, J.J.J., 2014a. Digital stroboscopic holography setup for deformation measurement at both quasi-static and acoustic frequencies. *Int. J. Optomechatroni.* 8, 275–291. doi:10.1080/15599612.2014.942928.
- De Greef, D., Aernouts, J., Aerts, J., Cheng, J.T., Horwitz, R., Rosowski, J.J., Dirckx, J.J.J., 2014b. Viscoelastic properties of the human tympanic membrane studied with stroboscopic holography and finite element modeling. *Hear. Res.* 312, 69–80. doi:10.1016/j.heares.2014.03.002.
- De Greef, D., Buytaert, J.A.N., Aerts, J.R.M., Van Hoorebecke, L., Dierick, M., Dirckx, J., 2015. Details of human middle ear morphology based on micro-CT imaging of phosphotungstic acid stained samples. *J. Morphol.* 276, 1025–1046. doi:10.1002/jmor.20392.
- De Greef, D., Pires, F., Dirckx, J.J.J., 2017a. Effects of model definitions and parameter values in finite element modeling of human middle ear mechanics. *Hear. Res.* 344, 195–206. doi:10.1016/j.heares.2016.11.011.
- De Greef, D., 2017. The human middle ear – A multidisciplinary study by means of tomographic imaging, stroboscopic holography and dynamic finite element modeling. Ph.D. thesis, University of Antwerp, Antwerp.
- de La Rochefoucauld, O., Decraemer, W.F., Khanna, S.M., Olson, E.S., 2008. Simultaneous measurements of ossicular velocity and intracochlear pressure leading to the cochlear input impedance in gerbil. *JARO* 9, 161–177. doi:10.1007/s10162-008-0115-1.
- Decraemer, W.F., Khanna, S.M., Funnell, W.R.J., 2000. Measurement and modeling of the three-dimensional vibration of the stapes in cat. In: Wada, H., Takasaka, K., Ikeda, K., Phiyama, K., Koike, T. (Eds.), *Proceeding of the Symposium on Recent Developments in Auditory Mechanics*. World Scientific Press, Singapore, pp. 36–43. doi:10.1142/9789812793980_0006.
- Decraemer, W.F., de La Rochefoucauld, O., Dong, W., Khanna, S.M., Dirckx, J.J.J., Olson, E.S., 2007. Scala vestibuli pressure and three-dimensional stapes velocity

- measured in direct succession in gerbil. *J. Acoust. Soc. Am.* 121, 2774–2791. doi:10.1121/1.2709843.
- Delrue, S., De Foer, B., van Dinther, J., Zarowski, A., Somers, T., Casselman, J., Offeciers, E., 2015. Handling an isolated malleus handle fracture: current diagnostic work-up and treatment options. *Ann. Otol. Rhinol. Laryngol.* 124, 244–249. doi:10.1177/0003489414550240.
- Dirckx, J.J.J., Marcusohn, Y., Gaihede, M.L., 2013. Quasi-static pressures in the middle ear cleft. In: Puria, S., Fay, R.R., Popper, A.N. (Eds.), *The Middle Ear: Science and Applications*. Springer Handbook of Auditory Research. Springer-Verlag, New York, pp. 93–133. doi:10.1007/978-1-4614-6591-1_5.
- Dooling, R.J., Lohr, B., Dent, M.L., 2000. Hearing in birds and reptiles. In: Dooling, R.J., Fay, R.R., Popper, A.H. (Eds.), *Comparative Hearing: Birds and Reptiles*. Springer Handbook for Auditory Research. Springer-Verlag, New York, pp. 308–359. doi:10.1007/978-1-4612-1182-2_7.
- Dooling, R.J., 2002. Avian hearing and the avoidance of wind turbines. Ph.D. thesis, University of Maryland, Maryland.
- Edom, E., Obrist, D., Henninger, R., Kleiser, L., Sim, J.H., Huber, A.M., 2013. The effect of rocking stapes motions on the cochlear fluid flow and on the basilar membrane motion. *J. Acoust. Soc. Am.* 134, 3749–3758. doi:10.1121/1.4824159.
- Eiber, A., Huber, A.M., Lauxmann, M., Chatzimichalis, M., Sequeira, D., Sim, J.H., 2012. Contribution of complex stapes motion to cochlea activation. *Hear. Res.* 284, 82–92. doi:10.1016/j.heares.2011.11.008.
- Ewald, J.R., 1889. Zur Physiologie der Bogengänge. Fortsetzung. Ueber Bewegungen der Perilymphe. *Pflüger, Arch.* 44, 319–326. doi:10.1007/bf01789785.
- Fletcher, N.H., 1992. *Acoustic systems in biology*. Oxford University Press, New York.
- Frank, G.H., Smit, A.L., 1976. The morphogenesis of the avian columella auris with special reference to *Struthio camelus*. *Afr. Zool.* 11, 159–182. doi:10.1080/00445096.1976.11447522.
- Funnell, W.R.J., Laszlo, C.A., 1977. Modeling of the cat eardrum as a thin shell using the finite-element method. *J. Acoust. Soc. Am.* 63, 1461–1467. doi:10.1121/1.381892.
- Funnell, W.R.J., Maftoon, N., Decraemer, W.F., 2012. Mechanics and modelling for the middle ear.
- Funnell, W.R.J., Maftoon, N., Decraemer, W.F., 2013. Modeling of Middle-Ear Mechanics. In: Puria, S., Fay, R.R., Popper, A.N. (Eds.), *The Middle Ear: Science, Otosurgery, and Technology*. Springer Handbook of Auditory Research. Springer-Verlag, New York, pp. 1–35. doi:10.1007/978-1-4614-6591-1.
- Galy-Bernadoy, C., Akkari, M., Mathiolon, C., Mondain, M., Uziel, A., Venail, F., 2014. Comparison of early hearing outcomes of type 2 ossiculoplasty using hydroxyapatite bone cement versus other materials. *Eur. Ann. Otorhinolaryngol. Head Neck Dis.* 131, 289–292. doi:10.1016/j.anorl.2013.03.009.

- Gaudin, E.P., 1968. On the middle ear of birds. *Acta Otolaryngol.* 65, 316–326. doi:10.3109/00016486809120971.
- Gaunt, A.S., Gaunt, S.L.L., Hector, D.H., 1976. Mechanics of the syrinx in *Gallus gallus*. I. A comparison of pressure events in chickens to those in oscines. *Condor* 78, 208–223. doi:10.2307/1366856.
- Gleich, O., Fischer, F.P., Köppl, C., Manley, G.A., 2004. Hearing organ evolution and specialization: Archosaurs. In: Manley, G.A., Popper, A., Fay, R.R. (Eds.), *Evolution of the Vertebrate Auditory System*. Springer-Verlag, New York, pp. 224–255. doi:10.1007/978-1-4419-8957-4_8.
- Goller, F., Mallinckrodt, M.J., Torti, S.D., 2004. Beak gape dynamics during song in the zebra finch. *J. Neurobiol.* 59, 289–303. doi:10.1002/neu.10327.
- Golubeva, T.B., 1972. The reflex activity of the tympanal muscle in the owl *Asio otus*. *Zhurn. Evol. Biol. Fisiol.* 8, 173–181.
- Gorissen, D., Couckuyt, I., Demeester, P., Dhaene, T., Crombecq, K., 2010. A surrogate modeling and adaptive sampling toolbox for computer based design. *J. Mach. Learn. Res.* 11, 2051–2055.
- Grassi, S., Ottaviani, F., Bambagioni, D., 1990. Vocalization-related stapedius muscle activity in different age chickens (*Gallus gallus*), and its role in vocal development. *Brain. Res.* 529, 158–164. doi:10.1016/0006-8993(90)90823-t.
- Guinan, J.J., Peake, W.T., 1967. Middle-ear characteristics of anesthetized cats. *J. Acoust. Soc. Am.* 41, 1237–1261. doi:10.1121/1.1910465.
- Gummer, A.W., Smolders, J.W.T., Klinke, R., 1987. Basilar membrane motion in the pigeon measured with the Mössbauer technique. *Hear. Res.* 29, 63–92. doi:10.1016/0378-5955(87)90206-1.
- Gummer, A.W., Smolders, J.W.T., Klinke, R., 1989a. Mechanics of a single-ossicle ear: I. The extra-stapedius of the pigeon. *Hear. Res.* 39, 1–14. doi:10.1016/0378-5955(89)90077-4.
- Gummer, A.W., Smolders, J.W.T., Klinke, R., 1989b. Mechanics of a single-ossicle ear: II. The columella footplate of the pigeon. *Hear. Res.* 39, 15–25. doi:10.1016/0378-5955(89)90078-6.
- Harris, J.P., Butler, D., 1985. Recognition of malleus handle fracture in the differential diagnosis of otologic trauma. *Laryngoscope* 95, 665–670. doi:10.1288/00005537-198506000-00006.
- Hato, N., Stenfelt, S., Goode, R.L., 2003. Three-dimensional stapes footplate motion in human temporal bones. *Audiol. Neurotol.* 8, 140–152. doi:10.1159/000069475.
- Hato, N., Okada, M., Hakuba, N., Hyodo, M., Gyo, K., 2007. Repair of a malleus-handle fracture using calcium phosphate bone cement. *Laryngoscope* 117, 361–363. doi:10.1097/01.mlg.0000246952.85668.24.
- Hausberger, M., Black, J.M., Richard, J-P., 1991. Bill opening and sound spectrum in barnacle goose loud calls: individuals with ‘wide mouths’ have higher pitched voices. *Anim. Behav.* 42, 319–322. doi:10.1016/s0003-3472(05)80565-2.

- Heiland, K.E., Goode, R.L., Asai, M., Huber A.M., 1999. A human temporal bone study of stapes footplate movement. *Am. J. Otol.* 20, 81–86. doi:10.5167/uzh-8371.
- Herrmann, G., Liebowitz, H., 1972. Mechanics of bone fracture. In: Liebowitz, H. (Ed.), *Fracture of Nonmetals and Composites*. Academic Press, New York, pp. 771–840. doi:10.1016/b978-0-12-449707-8.50014-2.
- Homma, K., Du, Y., Shimizu, I., Puria, S., 2009. Ossicular resonance modes of the human middle ear for bone and air conduction. *J. Acoust. Soc. Am.* 125, 968–976. doi:10.1121/1.3056564.
- Homma, K., Shimizu, Y., Kim, N., Du, Y., Puria, S., 2010. Effects of ear-canal pressurization on middle-ear bone- and air-conduction responses. *Hear. Res.* 263, 204–215. doi:10.1016/j.heares.2009.11.013.
- Hori, Y., Kawase, T., Hasegawa, J., Sato, T., Yoshida, N., Oshima, T., Suetake, M., Kobayashi, T., 2006. Audiometry with nasally presented masking noise: Novel diagnostic method for patulous Eustachian tube. *Otol. Neurotol.* 27, 596–599. doi:10.1097/01.mao.0000226301.21080.1c.
- Kreis, T., 2005. *Handbook of Holographic Interferometry: Optical and Digital Methods*. Wiley-VCH Verlag GmbH & Co. KGaA. doi:10.1002/3527604154.
- Huber, A.M., Linder, T., Ferrazzini, M., Schmid, S., Dillier, N., Stoekli, S., Fisch, U., 2001. Intraoperative assessment of stapes movement. *Ann. Otol. Rhinol. Laryngol.* 110, 31–35. doi:10.1177/000348940111000106.
- Huber, A.M., Sequeira, D., Breuninger, C., Eiber, A., 2008. The effect of complex stapes motion on response of the cochlea. *Otol. Neurotol.* 29, 1187–1192. doi:10.1097/mao.0b013e31817ef49b.
- Kano, S., Kawase, T., Baba, Y., Sato, T., Kobayashi, T., 2004. Possible new assessment of patulous Eustachian tube function: Audiometry for tones presented in the nasal cavity. *Acta Otolaryngol.* 124, 431–435. doi:10.1080/00016480410016306.
- Kawase, T., Kano, S., Otsuka, T., Hamanishi, S., Koike, T., Kobayashi, T., Wada, H., 2006. Autophony in patients with patulous Eustachian tube. *Otol. Neurotol.* 24, 600–603. doi:10.1097/01.mao.0000226294.26918.1d.
- Kettler, L., Christensen-Dalsgaard, J., Larsen, O.N., Wagner, H., 2016. Low frequency eardrum directionality in the barn owl induced by sound transmission through the interaural canal. *Biol. Cybern.* 110, 333–343. doi:10.1007/s00422-016-0689-3.
- Khaleghi, M., Lu, W., Dobrev, I., Cheng, J.T., Furlong, C., Rosowski, J.J., 2013. Digital holographic measurements of shape and three-dimensional sound-induced displacements of tympanic membrane. *Opt. Eng.* 52, 101916. doi:10.1117/1.OE.52.10.101916.
- Kirikae, I., 1960. *The structure and function of the middle ear*. Tokyo, University of Tokyo Press.
- Klump, G.M., Larsen, O.N., 1992. Azimuthal sound localization in the European starling (*Sturnus vulgaris*): I. Physical binaural cues. *J. Comp. Physiol. A* 170, 243–251. doi:10.1007/BF00196906.

- Klump, G.M., 2000. Sound localization in birds. In: Dooling, R.J., Fay, R.R., Popper, A.N. (Eds.), *Comparative Hearing: Birds and Reptiles*. Springer-Verlag, New York, pp. 249–307. doi:10.1007/978-1-4612-1182-2_6.
- Kohllöffel, L., 1972. A study of basilar membrane vibrations. III. The basilar membrane frequency response curve in the living guinea pig. *Acustica* 27, 82–89.
- Köppl, C., 2015. Avian hearing. In: Scanes, C.G. (Ed.), *Sturkies Avian Physiology – Sixth Edition*. Elsevier, pp. 71–87. doi:10.1016/b978-0-12-407160-5.00006-3.
- Kreithen, M.L., Keeton, W.T., 1974. Detection of changes in atmospheric pressure by the homing pigeon, *Columba livia*. *J. Comp. Physiol.* 89, 73–82. doi:10.1007/BF00696164.
- Kreithen, M.L., Quine, D.M., 1979. Infrasound detection by the homing pigeon: a behavioral audiogram. *J. Comp. Physiol.* 129, 1–4. doi:10.1007/bfoo679906.
- Kringlebotn, M., 1988. Network model for the human middle ear. *Scand. Audiol.* 17, 75–85. doi:10.3109/01050398809070695.
- Larsen, O.N., Popov, A.V., 1995. The interaural canal does enhance directional hearing in quail (*Aves; Coturnix Coturnix japonica*). In: Burrows, M., Matheson, T., Newland, P.L., Schupe, H. (Eds.), *Nervous Systems and Behaviour. Proceedings of the 4th International Congress of Neuroethology*. Georg Thieme Verlag, New York, p. 313.
- Larsen, O.N., Dooling, R.J., Michelsen, A., 2006. The role of pressure difference reception in the directional hearing of budgerigars (*Melopsittacus undulatus*). *J. Comp. Physiol. A* 192, 1063–1072. doi:10.1007/s00359-006-0138-1.
- Larsen, O.N., Christensen-Dalsgaard, J., Jensen, K.K., 2016. Role of intracranial cavities in avian directional hearing. *Biol. Cybern.* 110, 319–331. doi:10.1007/s00422-016-0688-4.
- Lynch, T.J., 3rd, Nedzelnitsky, V., Peake, W.T., 1982. Input impedance of the cochlea in cat. *J. Acoust. Soc. Am.* 72, 108–130. doi:10.1121/1.387995.
- Maftoon, N., Funnell, W.R.J., Daniel, S.J., Decraemer, W.F., 2015. Finite-element modelling of the response of the gerbil middle ear to sound. *JARO* 16, 547–567. doi:10.1007/s10162-015-0531-y.
- Manley, G.A., 1972a. The middle ear of the Tokay gecko. *J. Comp. Physiol.* 81, 239–250. doi:10.1007/BF00693629.
- Manley, G.A., 1972b. Frequency response of the middle ear of geckos. *J. Comp. Physiol.* 81, 251–258. doi:10.1007/BF00693630.
- Manley, G.A., 1990a. The peripheral hearing organ of birds. In: Manley, G.A. (Ed.), *Peripheral Hearing Mechanisms in Reptiles and Birds. Zoophysiology*. Springer-Verlag, Berlin, Heidelberg, pp. 206–252. doi:10.1007/978-3-642-83615-2_13.
- Manley, G.A., 1990b. Overview and outlook. In: Manley, G.A. (Ed.), *Peripheral Hearing Mechanisms in Reptiles and Birds. Zoophysiology*. Springer-Verlag, Berlin, Heidelberg, pp. 253–273. doi:10.1007/978-3-642-83615-2_14.

- Manley, G.A., Köppl, C., Yates, G.K., 1997. Activity of primary auditory neurons in the cochlear ganglion of the emu *Dromaius novaehollandiae*: spontaneous discharge, frequency tuning, and phase locking. *J. Acoust. Soc. Am.* 101, 1560–1573. doi:10.1121/1.418273.
- Masschaele, B., Cnudde, V., Dierick, M., Jacobs, P., Van Hoorebeke, L., Vlassenbroeck, J., 2007. UGCT: new X-ray radiography and tomography facility. *Nucl. Instr. Meth. Phys. Res.* 580, 266–269. doi:10.1016/j.nima.2007.05.099.
- Masschaele, B., Dierick, M., Van Loo, D., Boone, M.N., Brabant, L., Pauwels, E., Cnudde, V., Van Hoorebeke, L., 2013. HECTOR: A 240 kV micro-CT setup optimized for research. *J. Phys. Conf. Ser.* 463, 012012. doi:10.1088/1742-6596/463/1/012012.
- Merchant, S.N., Ravicz, M.E., Rosowski, J.J., 1996. Acoustic input impedance of the stapes and cochlea in human temporal bones. *Hear. Res.* 97, 30–45. doi:10.1016/S0378-5955(96)80005-0.
- Mills, R., Zhang, J., 2006. Applied comparative physiology of the avian middle ear: the effect of static pressure changes in columellar ears. *J. Laryngol. Otol.* 120, 1005–1007. doi:10.1017/S0022215106002581.
- Mills, R., Zadrozniak, M., Jie, Z., 2007. Ossicular motion during changes in static pressure in the avian middle ear. In: Huber, A.M., Eiber, A. (Eds.), *Middle Ear Mechanics in Research and Otolaryngology*. Proceedings of the 4th International Symposium. World Scientific Publishing, Singapore, pp. 21–25. doi:10.1142/9789812708694_0003.
- Muyshondt, P.G.G., Soons, J.A.M., De Greef, D., Pires, F., Aerts, P., Dirckx, J.J.J., 2016a. A single-ossicle ear: Acoustic response and mechanical properties measured in duck. *Hear. Res.* 340, 35–42. doi:10.1016/j.heares.2015.12.020.
- Muyshondt, P.G.G., Aerts, P., Dirckx, J.J.J., 2016b. Acoustic input impedance of the avian inner ear measured in ostrich (*Struthio camelus*). *Hear. Res.* 339, 175–183. doi:10.1016/j.heares.2016.07.009.
- Nakajima, H.H., Dong, W., Olson, E.S., Merchant, S.N., Ravicz, M.E., Rosowski, J.J., 2009. Differential intracochlear sound pressure measurements in normal human temporal bones. *JARO* 10, 23–36. doi:10.1007/s10162-008-0150-y.
- Niklasson, A., Tano, K., 2010. Self-inflicted negative pressure of the external ear canal: a common cause of isolated malleus fracture. *Acta Otolaryngol.* 130, 410–416. doi:10.1080/00016480903177521.
- Norberg, R.Å., 1978. Skull asymmetry, ear structure and function, and auditory localization in Tengmalm's owl, *Aegolius funereus* (Linné). *Phil. Trans. R. Soc. B* 282, 325–410. doi:10.1098/rstb.1978.0014.
- Norberg, R.Å., 2002. Independent evolution of outer ear asymmetry among five owl lineages: morphology, function and selection. In: Newton, I., Kavanagh, R., Olsen, J., Taylor, I. (Eds.), *Ecology and Conservation of Owls*. CSIRO Publishing, Collingwood, Victoria, pp. 329–342.

- O'Reilly, R.C., Cass, S.P., Hirsch, B.E., Kameron, D.B., Bernat, R.A., Poznanovic, S.P., 2005. Ossiculoplasty using incus interposition: hearing results and analysis of the middle ear risk index. *Otol. Neurotol.* 26, 853–858. doi:10.1097/oi.mao.0000185054.92265.b7.
- Oakley, J., O'Hagan, A., 2004. Probabilistic sensitivity analysis of complex models: a Bayesian approach. *J. R. Stat. Soc. Series B. Stat. Methodol.* 66, 751–769. doi:10.1111/j.1467-9868.2004.05304.x.
- Oeckinghaus, H., Schwartzkopff, J., 1983. Electrical and acoustical activation of the middle ear muscle in a songbird. *J. Comp. Physiol. A* 150, 61–67. doi:10.1007/bfo0605288.
- Overstreet, E.H., 3rd, Ruggero, M.A., 2002. Development of wide-band middle ear transmission in the Mongolian gerbil. *J. Acoust. Soc. Am.* 111, 261–270. doi:10.1121/1.1420382.
- Padurariu, S., De Greef, D., Jacobsen, H., Nlandu Kamavuako, E., Dirckx, J.J.J., Gaihede, M., 2016. Pressure buffering by the tympanic membrane. In vivo measurements of middle ear pressure fluctuations during elevator motion. *Hear. Res.* 340, 113–120. doi:10.1016/j.heares.2015.12.004.
- Peacock, J., von Unge, M., Dirckx, J., 2013. Measurement of the vibration of the middle ear ossicles with removed eardrum: A method for quantification of ossicular fixation. *Med. Eng. Phys.* 35, 1786–1792. doi:10.1016/j.medengphy.2013.07.012.
- Peacock, J., Dirckx, J., von Unge, M., 2014. Magnetically driven middle ear ossicles with laser vibrometry as a new diagnostic tool to quantify ossicular fixation. *Acta Otolaryngol.* 134, 352–357. doi:10.3109/00016489.2013.841990.
- Peacock, J., Pintelon, R., Dirckx, J., 2015a. Nonlinear vibration response measured at umbo and stapes in the rabbit middle ear. *JARO* 16, 569–580. doi:10.1007/s10162-015-0535-7.
- Peacock, J., Dirckx, J., von Unge, M., 2015b. Towards quantitative diagnosis of ossicular fixation: measurements of stapes fixation using magnetically driven ossicles in human temporal bones. *Acta Otolaryngol.* 135, 880–885. doi:10.3109/00016489.2015.1015605.
- Pianosi, F., Beven, K., Freer, J., Hall, J.W., Rougier, J., Stephenson, D.B., Wagener, T., 2016. Sensitivity analysis of environmental models: A systematic review with practical workflow. *Environ. Modell. Softw.* 79, 214–232. doi:10.1016/j.envsoft.2016.02.008.
- Podos, J., Sherer, J.K., Peters, S., Nowicki, S., 1995. Ontogeny of vocal tract movements during song production in song sparrows. *Anim. Behav.* 50, 1287–1296. doi:10.1016/0003-3472(95)80044-1.
- Pohlman, A.G., 1921. The position and functional interpretation of the elastic ligaments in the middle-ear of Gallus. *J. Morphol.* 35, 228–262. doi:10.1002/jmor.1050350106.

- Poon, T.-C., 2007. Optical Scanning Holography with MATLAB®. Springer, US. doi:10.1007/978-0-387-68851-0.
- Puria, S., Allen, J.B., 1991. A parametric study of cochlear input impedance. *J. Acoust. Soc. Am.* 89, 287–309. doi:10.1121/1.400675.
- Puria, S., Peake, W.T., Rosowski, J.J., 1997. Sound-pressure measurements in the cochlea vestibule of human cadaver ears. *J. Acoust. Soc. Am.* 101, 2754–2770. doi:10.1121/1.418563.
- Puria, S., 2003. Measurements of human middle ear forward and reverse acoustics: Implications for otoacoustic emissions. *J. Acoust. Soc. Am.* 113, 2773–2789. doi:10.1121/1.1564018.
- Quine, D.B., 1978. Infrasonic detection and ultralow frequency discrimination in the homing pigeon (*Columba livia*). *J. Acoust. Soc. Am.* 63, S75. doi:10.1121/1.2016815.
- Ravicz, M.E., Merchant, S.N., Rosowski, J.J., 2000. Effect of freezing and thawing on stapes-cochlear input impedance in human temporal bones. *Hear. Res.* 150, 215–224. doi:10.1016/S0378-5955(00)00200-8.
- Rosowski, J.J., Peake, W.T., Lynch, T.J., 3rd, Leong, R., Weiss, T.F., 1985. A model for signal transmission in an ear having hair cells with free-standing stereocilia. II. Macro-mechanical stage. *Hear. Res.* 20, 139–155. doi:10.1016/0378-5955(85)90165-0.
- Rosowski, J.J., Davis, P.J., Merchant, S.N., Donahue, K.M., Coltrera, M.D., 1990. Cadaver middle ears as models for living ears: comparisons of middle-ear input immittance. *Ann. Otol. Rhinol. Laryngol.* 99, 403–412. doi:10.1177/000348949009900515.
- Rosowski, J.J., Chien, W., Ravicz, M.E., Merchant, S.N., 2007. Testing a method for quantifying the output of implantable middle ear hearing devices. *Audiol. Neurootol.* 12, 265–276. doi:10.1159/000101474.
- Relkin, E.M., 1988. Introduction to the analysis of middle-ear function. In: Jahn, A.F., Santos-Sacchi, J. (Eds.), *Physiology of the Ear*. Raven Press, New York, pp. 103–123.
- Ruggero, M.A., Rich, N.C., Robles, L., Shivapuja, B.G., 1990. Middle-ear response in the chinchilla and its relationship to mechanics at the base of the cochlea. *J. Acoust. Soc. Am.* 87, 1612–1629. doi:10.1121/1.399409.
- Sadd, M., 2005. *Elasticity: theory, applications, and numerics*. Elsevier.
- Sadé, J., Ar, A., 1997. Middle ear and auditory tube: Middle ear clearance, gas exchange, and pressure regulation. *Otolaryngol. Head Neck Surg.* 116, 499–524. doi:10.1016/s0194-5998(97)70302-4.
- Saiff, E.I., 1981. The middle ear of the skull of birds: the ostrich, *Struthio camelus* L., *Zool. J. Linn. Soc.* 73, 201–212. doi:10.1111/j.1096-3642.1981.tb01593.x.
- Saunders, J.C., Johnstone, B.M., 1972. A comparative analysis of middle-ear function in non-mammalian vertebrates. *Acta Otolaryngol.* 73, 353–361. doi:10.3109/00016487209138952.

- Saunders, J.C., 1985. Auditory structure and function in the bird middle ear: An evaluation by SEM and capacitive probe. *Hear. Res.* 18, 253–268. doi:10.1016/0378-5955(85)90042-5.
- Saunders, J.C., Duncan, R.K., Doan, D.E., Werner, Y.L., 2000. The middle ear of reptiles and birds. In: Dooling, R.J., Fay, R.R., Popper, A.H. (Eds.), *Comparative Hearing: Birds and Reptiles*. Springer Handbook for Auditory Research. Springer-Verlag, New York, pp. 13–69. doi:10.1007/978-1-4612-1182-2_2.
- Saunders, S.S., Salvi, R.J., 1993. Psychoacoustics of normal adult chickens: Thresholds and temporal integration. *J. Acoust. Soc. Am.* 94, 83–90. doi:10.1121/1.406945.
- Schnars, U., Jüptner, W.P.O., 2002. Digital recording and numerical reconstruction of holograms. *Meas. Sci. Technol.* 13, R85–R101. doi:10.1088/0957-0233/13/9/201.
- Schwer, L. E., 2007. An overview of the PTC 60/V&V 10: Guide for verification and validation in computational solid mechanics. *Eng. Comput.* 23, 245–252.
- Slama, M.C.C., Ravicz, M.E., Rosowski, J.J., 2010. Middle ear function and cochlear input impedance in chinchilla. *J. Acoust. Soc. Am.* 127, 1397–1410. doi:10.1121/1.3279830.
- Smith, G., 1904. The middle ear and columella of birds. *Quart. J. Microsc. Sci.* 48, 11–22.
- Songer, J.E., Rosowski, J.J., 2007. Transmission matrix analysis of the chinchilla middle ear. *J. Acoust. Soc. Am.* 122, 932–942. doi:10.1121/1.2747157.
- Spahn, G., Wittig, R., 2003. Biomechanical properties (compressive strength and compressive pressure at break) of hyaline cartilage under axial load. *Zentralbl. Chir.* 128, 78–82. doi:10.1055/s-2003-37325.
- Starck, J.M., 1992. Towards a model of the functional morphology of the avian middle ear – The transfer function. *Zool. Jahrb. Anat.* 122, 287–302.
- Starck, J.M., 1995. Comparative anatomy of the external and middle ear of palaeognathous birds. *Adv. Anat. Embryol. Cell Biol.* 131, 1–137. doi:10.1007/978-3-642-79592-3.
- Sim, J.H., Chatzimichalis, M., Lauxmann, M., Rösli, C., Eiber, A., Huber, A.M., 2010. Complex stapes motions in human ears. *JARO* 11, 329–341. doi:10.1007/s10162-010-0207-6.
- Tanaka, K., Smith, C.A., 1975. Structure of the avian tectorial membrane. *Ann. Otol. Rhinol. Laryngol.* 84, 287–296. doi:10.1177/000348947508400302.
- Thomassen, H.A., Gea, S., Maas, S., Bout, R.G., Dirckx, J.J.J., Decraemer, W.H., Povel, G.D.E., 2007. Do Swiftlets have an ear for echolocation? The functional morphology of Swiftlet's middle ears. *Hear. Res.* 225, 25–37. doi:10.1016/j.heares.2006.11.013.
- Tonndorf, J., Khanna, S.M., 1970. The role of the tympanic membrane in middle ear transmission. *Ann. Otol. Rhinol. Laryngol.* 79, 743–753.
- Trainer, J.E., 1946. The auditory acuity of certain birds. Ph.D. thesis, Cornell University, Ithaca.

- Vallejo Valdezate, L.A., Gil-Carcedo Sañudo, E., Gil-Carcedo Sañudo, M.D., Pablos López, M., Gil-Carcedo García, L.M., 2007. The avian middle ear (*Struthio camelus*). Data for the physiology of sound transmission in systems with a single ossicle in the chain. *Acta Otorrinolaringol. Esp.* 58, 246–251. doi:10.1016/s2173-5735(07)70343-5.
- Van Den Heuvel, W.F., 1991. Kinetics of the skull in the chicken (*Gallus gallus domesticus*). *Neth. J. Zool.* 42, 561–582. doi:10.1163/156854292x00071.
- Van der Jeught, S., Dirckx, J.J.J., Aerts, J.R.M., Bradu, A., Podoleanu, A.G., Buytaert, J.A.N., 2013. Full-field thickness distribution of human tympanic membrane obtained with optical coherence tomography. *JARO* 14, 483–494. doi:10.1007/s10162-013-0394-z.
- Volandri, G., Di Puccio, F., Forte, P., Carmignani, C., 2011. Biomechanics of the tympanic membrane. *J. Biomech.* 44, 1219–1236. doi:10.1016/j.jbiomech.2010.12.023.
- von Bartheld, C.S., Giannessi, F., 2011. The paratympanic organ: a barometer and altimeter in the middle ear of birds? *J. Exp. Zool. Mol. Dev. Evol.* 316, 402–408. doi:10.1002/jez.b.21422.
- von Békésy, G., 1949. The structure of the middle ear and the hearing of one's own voice by bone conduction. *J. Acoust. Soc. Am.* 21, 217–232. doi:10.1121/1.1906501.
- von Békésy, G., 1960. *Experiments in Hearing*. New York, McGraw-Hill.
- von Graaf, L., 1885. Zur Naturgeschichte des Auerhahnes (*Tetrao urogallus* L.). *Z. Wiss. Zool.* 41, 107–115.
- von Helmholtz, H., 1873. *The mechanism of the ossicles of the ear and membrana tympani*. William Wood & Co., New York.
- Wada, Y., 1924. Beiträge zur vergleichenden Physiologie des Gehörorganes. *Pflüg. Arch.* 202, 46–69. doi:10.1007/bf01723478.
- Westneat, M.W., Long, J.H., Hoese, W., Nowicki, S., 1993. Kinematics of birdsong: functional correlation of cranial movements and acoustic features in sparrows. *J. Exp. Biol.* 182, 147–171.
- Williams, H., 2001. Choreography of song, dance and beak movements in the zebra finch (*Taeniopygia guttata*). *J. Exp. Biol.* 204, 3497–3506.
- Witmer, L.W., Ridgely, R.C., 2008. The paranasal air sinuses of predatory and armored dinosaurs (Archosauria: Theropoda and Ankylosauria) and their contribution to cephalic structure. *Anat. Rec.* 291, 1362–1388. doi:10.1002/ar.20794.
- Wurm, W., 1885. Die Taubheit des schleifenden Auerhahnes. Eine Erwiderung. *Z. Wiss. Zool.* 41, 728–730.
- Yodlowski, M.L., 1980. *Infrasonic sensitivity in pigeons (Columba livia)*. Ph.D. thesis, Rockefeller University, New York.
- Zhang, X., Gan, R.Z., 2010. Dynamic properties of human tympanic membrane – experimental measurement and modeling analysis. *Int. J. Exp. Comput. Biomech.* 1, 252–270. doi:10.1186/2193-1801-2-527.

- Zhang, X., Gan, R.Z., 2011. Experimental measurement and modeling analysis on mechanical properties of incudostapedial joint. *Biomech. Model. Mechanobiol.* 10, 713–726. doi:10.1007/s10237-010-0268-9.
- Zienkiewicz, O.C., Taylor, R.L., 2000a. *The Finite Element Method: Solid Mechanics*, 5th ed. Butterworth-Heinemann.
- Zienkiewicz, O.C., Taylor, R.L., 2000b. *The Finite Element Method: The Basis*, 5th ed. Butterworth-Heinemann.
- Zwislocki, J., 1962. Analysis of the middle-ear function. I. Input impedance. *J. Acoust. Soc. Am.* 34, 1514–1523. doi:10.1121/1.1918382.
- Zwislocki, J., 1965. Analysis of some auditory characteristics. In: Luce, R.D., Bush, R.R., Galanter, E. (Eds.), *Handbook of Mathematical Physiology*. Wiley, New York, pp. 3–46.
- Zwislocki, J., 1975. The role of the external and middle ear in sound transmission. In: Tower, D.B. (Ed.), *The Nervous System, Vol. 3. Human Communication and Its Disorders*. Raven Press, New York, pp. 45–55.

ABBREVIATIONS

| | |
|-------------|---|
| (μ)CT | (micro-)computed tomography |
| ANOVA | analysis of variance |
| C | columella |
| CAL | columellar annular ligament |
| CFP | columellar footplate |
| EST | extrastapedial tip |
| EXC | extracolumella |
| FE | finite element |
| HECTOR | High-Energy CT Optimized for Research scanner |
| IE | inner ear |
| LDV | laser Doppler vibrometry |
| ME | middle ear |
| nD | n-dimensional |
| PORP | partial ossicular replacement prosthesis |
| PTA | phosphotungstic acid |
| SPL | sound pressure level |
| STL | stereolithography file format |
| TM | tympanic membrane |
| TORP | total ossicular replacement prosthesis |
| UGCT | University of Ghent's Center for X-ray Tomography |

PUBLICATIONS

Journal publications with peer review

- Cambré, S., **Muysbondt, P.**, Federicci, R., Wenseleers, W., 2015. Chirality-dependent densities of carbon nanotubes by in situ 2D fluorescence-excitation and Raman characterisation in a density gradient after ultracentrifugation. *Nanoscale* 7, 20015–20024. doi:10.1039/c5nr0602of.
- Muysbondt, P.G.G.**, Soons, J.A.M., De Greef, D., Pires, F., Aerts, P., Dirckx, J.J.J., 2016. A single-ossicle ear: Acoustic response and mechanical properties measured in duck. *Hear. Res.* 340, 35–42. doi:10.1016/j.heares.2015.12.020.
- Muysbondt, P.G.G.**, Aerts, P., Dirckx, J.J.J., 2016. Acoustic input impedance of the avian inner ear measured in ostrich (*Struthio camelus*). *Hear. Res.* 339, 175–183. doi:10.1016/j.heares.2016.07.009.
- Niklasson, A., Rönnblom, A., **Muysbondt, P.**, Dirckx, J., von Unge, M., Tano, K., 2016. Ossiculoplasty on isolated malleus fractures: a human temporal bone study using laser Doppler vibrometry. *Otol. Neurotol.* 37, 895–901. doi:10.1097/mao.0000000000001086.
- Rothberg, S.J., Allen, M.S., Castellini, P., Di Maio, D., Dirckx, J.J.J., Ewins, D.J., Halkon, B.J., **Muysbondt, P.**, Paone, N., Ryan, T., Steger, H., Tomasini, E.P., Vanlanduit, S., Vignola, J.F., 2016. An international review of laser Doppler vibrometry: making light work of vibration measurement. *Opt. Lasers Eng.* 99, 11–22. doi:10.1016/j.optlaseng.2016.10.023.
- Claes, R., **Muysbondt, P.G.G.**, Van Hoorebeke, L., Dhaene, J., Dirckx, J.J.J., Aerts, P., 2016. The effect of craniokinesis on the middle ear of domestic chickens (*Gallus gallus domesticus*). *J. Anat.* 230, 414–423. doi:10.1111/joa.12566.
- Gladiné, K., **Muysbondt, P.G.G.**, Dirckx, J.J.J., 2017. Human middle-ear nonlinearity measurements using laser Doppler vibrometry. *Opt. Lasers Eng.* 99, 98–102. doi:10.1016/j.optlaseng.2017.03.001.
- Salih, W.H., **Muysbondt, P.G.G.**, Dirckx, J.J.J., 2017. Tympanic membrane pressure buffering at quasi-static and low-frequency pressure variations. *Hear. Res.* 353, 49–56. doi:10.1016/j.heares.2017.07.010.
- Muysbondt, P.G.G.**, Claes, R., Aerts, P., Dirckx, J.J.J., 2017. Sound attenuation in the ear of domestic chickens (*Gallus gallus domesticus*) as a result of beak opening. *R. Soc. Open Sci.* 4, 171286. doi:10.1098/rsos.171286.

- Muysshondt, P.G.G.**, Claes, R., Aerts, P., Dirckx, J.J.J., 2018. Quasi-static and dynamic motions of the columellar footplate in ostrich (*Struthio camelus*) measured ex vivo. *Hear. Res.* 357, 10–24. doi:10.1016/j.heares.2017.11.005.
- Claes, R., **Muysshondt, P.G.G.**, Dirckx, J.J.J., Aerts, P., 2018. Deformation of avian middle ear structures under static pressure loads, and potential regulation mechanisms. *J. Zool.* 126, 128–136. doi:10.1016/j.zool.2017.11.003.
- Claes, R., **Muysshondt, P.G.G.**, Dirckx, J.J.J., Aerts, P., 2018. Do high sound pressure levels of crowing in roosters necessitate passive mechanisms for protection against self-vocalization? *J. Zool.* 126, 65–70. doi:10.1016/j.zool.2017.12.002.

Conference contributions

^(P) Presenting author

- Muysshondt, P.**, De Greef, D. ^(P), Soons, J.A.M., Dirckx, J.J.J., 2014. Optical techniques as validation tools for finite element modeling of biomechanical structures, demonstrated in bird ear research. 11th International Conference on Vibration Measurements by Laser and Noncontact Techniques – AIVELA 2014, Ancona. AIP Conf. Proc. 1600, 330–337. doi:10.1063/1.4879599.
- Muysshondt, P.** ^(P), De Greef, D., Soons, J.A.M., Peacock, J., Dirckx, J.J.J., 2014. Determination of the mechanical properties in the avian middle ear by inverse analysis. Proceedings of the 2014 COMSOL Conference, Cambridge, September 2014.
- Muysshondt, P.G.G.** ^(P), De Greef, D., Soons, J.A.M., Dirckx, J.J.J., 2016. Optical interferometry and finite element modeling as input techniques for inverse analysis on the mechanical properties of the avian middle ear. In: Dirckx, J.J.J. (Ed.), *Optical Measurement Techniques for Systems & Structures III*, Antwerp. Shaker Publishing B.V., Maastricht, p. 384.
- Muysshondt, P.** ^(P), Soons, J.A.M., De Greef, D., Aerts, P., Dirckx, J.J.J., 2015. A single-ossicle ear: acoustic response and mechanical properties measured in duck. 7th International Symposium on Middle Ear Mechanics in Research and Otology, Aalborg, p. 27.
- Claes, R. ^(P), **Muysshondt, P.**, Dirckx, J., Aerts, P., 2015. The effect of craniokinesis on the avian middle ear. 6th International Meeting on Cranio-cervical Systems in Vertebrates, Ghent, July 2015.
- Muysshondt, P.** ^(P), De Greef, D., Soons, J., Dirckx, J.J.J., 2015. Study of the mechanical properties of the avian middle ear by optical interferometry and finite element modeling. BSSM's 10th International Conference on Advances in Experimental Mechanics, Edinburgh, September 2015.
- Claes, R. ^(P), **Muysshondt, P.**, Van Hoorebeke, L., Dhaene, J., Dirckx, J., Aerts, P., 2016. The effect of upper bill elevation on hearing in domestic chickens (*Gallus gallus domesticus*). Bruker Micro-CT User Meeting, Brussels, pp. 199–202.

- Dirckx, J.^(P), **Muyshondt, P.**, Pires, F., De Greef, D., 2016. Stroboscopic digital holography combined with laser vibrometry and X-ray tomography to study mechanics of the middle ear. International Conference on Combined Digital Optical & Imaging Methods Applied to Mechanical Engineering, Ascona, May 2016.
- Muyshondt, P.G.G.**^(P), Aerts, P., Dirckx, J.J.J., 2016. The columella and the footplate in the middle ear of birds. IUTAM Symposium on Advances in Biomechanics of Hearing, Stuttgart, pp. 28–29.
- Pires, F.^(P), **Muyshondt, P.G.G.**, Dirckx, J.J.J., Paul, S., Cordioli, J., 2016. Sensitivity analysis of material properties on a human middle ear model based on the finite element method. IUTAM Symposium on Advances in Biomechanics of Hearing, Stuttgart, pp. 60–61.
- Muyshondt, P.G.G.**^(P), Pires, F., Dirckx, J.J.J., 2016. LDV measurement of bird ear vibrations to determine inner ear impedance and middle ear power flow. 12th International Conference on Vibration Measurements by Laser and Noncontact Techniques – AIVELA 2014, Ancona. AIP Conf. Proc. 1740, 050001. doi:10.1063/1.4952665.
- Gladiné, K.^(P), **Muyshondt, P.**, Dirckx, J., 2016. LDV measurement of small nonlinearities in flat and curved membranes. A model for eardrum nonlinear acoustic behaviour. 12th International Conference on Vibration Measurements by Laser and Noncontact Techniques – AIVELA 2014, Ancona. AIP Conf. Proc. 1740, 050005. doi:10.1063/1.4952669.
- Claes, R., **Muyshondt, P.**, Van Hoorebeke, L., Dhaene, J., Dirckx, J., Aerts, P.^(P), 2016. The effect of craniokinesis on the middle ear of domestic chickens (*Gallus gallus domesticus*). International Congress of Vertebrate Morphology, Washington DC, July 2016.
- Muyshondt, P.**^(P), 2016. Acoustic impedance measurement in the bird inner ear. 15 Years Polytec Benelux Anniversary, Antwerp, October 2016.
- Muyshondt, P.**^(P), Claes, R., Aerts, P., Dirckx, J., 2017. The single-ossicle ear of birds: motions of the columella and the role of the inner-ear load. WAS-dag, Eindhoven, May 2017.

DANKWOORD – ACKNOWLEDGMENTS

Deze thesis had nooit tot stand kunnen komen door het werk van mij alleen. Daarom wil ik een aantal mensen expliciet bedanken die mij hierbij de afgelopen jaren hebben geholpen en bijgestaan.

Om te beginnen wil ik de hoofdpromotor van mijn doctoraat bedanken, professor Joris Dirckx. Vanaf het begin van mijn Bachelor-thesis, zes en een half jaar geleden, tot nu wordt ik al door Joris begeleid. Gedurende die periode stond hij altijd klaar om mij te helpen wanneer het nodig was, maar ik kreeg van hem ook de vrijheid om mijn onderzoek te doen op mijn manier. Voor dit voor nog veel andere dingen: bedankt!

Ten tweede wil ik ook mijn co-promotor bedanken, professor Peter Aerts. Met Peter had ik minder rechtstreeks contact tijdens mijn doctoraat, maar tijdens de gezamenlijke vergaderingen kon ik altijd rekenen op zijn expertise en kritische blik vanuit biologisch oogpunt, waarvoor dank!

Daarnaast wil ik mijn (ex-)collega's van Bimef bedanken. Mijn voormalige collega's en Bachelor- en Master-thesisbegeleiders Jef, Joris en Daniël hebben mij veel van hun expertise bijgebracht, hetgeen mijn werk naar een hoger niveau heeft getild. Ook mijn vroegere bureaugenoten Adriaan en John wil ik bedanken voor de fijne sfeer in het begin van mijn doctoraat.

Van de huidige collega's wil ik in de eerste plaats Raf bedanken. Onze gezamenlijke experimenten en vooral de lange scandagen, met bijkomende files, waren vaak vermoeiend, maar verliepen altijd in vlotte samenwerking. Daarnaast wil ik ook mijn huidige collega-doctoraatsstudenten op Bimef – Kilian, William en Felipe – bedanken voor de interessante onderlinge brainstormsessies, maar ook voor de leuke niet-werkgerelateerde conversaties. Ook bedankt aan de huidige post-docs Sam en Jana, die mij als ervaringsdeskundigen konden helpen wanneer ik er nood aan had.

Voor de technische expertise kon in altijd rekenen op William en Fred, en intussen ook Wim. Daarnaast wil ik ook Arne en Tine bedanken voor de ondersteuning en feilloze organisatie van het practicum Fysica. De gezellige gesprekken tijdens de koffiepauzes zorgden altijd voor een leuke sfeer op het labo. Ook Greet wil ik bedanken als mijn vroegere wiskundeleerkracht en tegenwoordig soms ook als voorziener van lekkere zelfgebakken cake tijdens de pauzes. Ook op de mensen van het secretariaat Fysica – Hilde, Gert en Nathalie – kon ik altijd terecht voor hulp bij administratieve aangelegenheden.

Er zijn nog een aantal externe onderzoeksinstituten waar ik tijdens mijn doctoraat mee heb samengewerkt. Zo wil ik de mensen van het x-stralen tomografie labo van UGent (UGCT) bedanken, met name Manuel Dierick, Pieter Vanderniepen en Iván Josipovic, voor het opstellen en uitvoeren van de scans die werden gebruikt in mijn onderzoek. I also want to thank Anders Niklasson, Krister Tano and Anton Rönnblom of Umeå University Hospital for our successful collaboration.

I also want to honor the members of my doctoral jury: internal jury members Prof. Jan Sijbers and Prof. Joke Hadermann, and external jury members Prof. Steve Vanlanduit, Prof. Michael Fagan and Prof. Magnus von Unge. Thank you for taking the time to read my thesis and discussing it with me during the predefense of my PhD.

Also thanks to all the reviewers and editors who critically reviewed my publications. I especially want to thank co-editor of Hearing Research, John Rosowski, for his valuable comments and efforts to guide the reviewing process.

Ik wil ook Vincent en Jeroen bedanken voor de vele gezellige middagpauzes, die altijd een aangenaam rustpunt waren tussen de werkuren.

Tenslotte wil ik ook graag mijn familie bedanken voor hun interesse in mijn onderzoek en voor hun praktische en mentale steun tijdens mijn doctoraat. Specifiek wil ik mijn broer Matthias en zijn vrouw Sigourney bedanken voor de leuke momenten samen in België en in Japan, en last but not least mijn ouders, Dirk en Martine. Ik heb zowat alles aan jullie te danken, en zonder jullie had ik nooit gestaan waar ik nu sta.

Aan iedereen vermeld hierboven, en aan iedereen die ik moest vergeten zijn,

Bedankt!

Pieter